

NASA
TP
1521
c.1

NASA Technical Paper 1521

LOAN COPY: RETURN TO
AFWL TECHNICAL LIBRARY
KIRTLAND AFB, N. M.

2284570



TECH LIBRARY KAFB, NM

Fuselage and Nozzle Pressure Distributions on a 1/12-Scale F-15 Propulsion Model at Transonic Speeds

Odis C. Pendergraft, Jr.

NOVEMBER 1979





0134822

NASA Technical Paper 1521

Fuselage and Nozzle Pressure
Distributions on a 1/12-Scale F-15
Propulsion Model at Transonic Speeds

Odis C. Pendergraft, Jr.
Langley Research Center
Hampton, Virginia



National Aeronautics
and Space Administration

Scientific and Technical
Information Branch

1979

SUMMARY

Static-pressure distributions on the forebody, afterbody, and nozzles of a 1/12-scale F-15 propulsion model have been determined in the Langley 16-foot transonic tunnel for Mach numbers from 0.60 to 1.20, angles of attack from -1° to 9° , and ratio of jet total pressure to free-stream static pressure from 1 (jet off) up to about 5, depending on Mach number. The effects of nozzle power setting and horizontal-tail deflection angle on the pressure distributions were also investigated. Reynolds number per meter varied from about 1.0×10^7 to 1.3×10^7 , depending on Mach number.

Results of the wind-tunnel test program indicate that the flow field surrounding the nozzles is very complex, always resulting in nonuniform pressure distributions around the circumference of the nozzles and quite often resulting in separated flow regions, especially for the dry-power nozzles. Deflection of the horizontal tails, in spite of their outboard and partly shielded location, has surprisingly strong effects on integrated nozzle axial force.

INTRODUCTION

The reduction of propulsion system losses for twin engines installed in a fighter type aircraft has been a difficult problem because of the inability to adequately predict the effect of the jet engine exhaust flows on the airframe. Even current computer technologies cannot adequately handle the masses of data input needed to model the very complex flow fields surrounding the exhaust nozzles and adjacent airframe components.

One of the best ways to gain further understanding of this complex flow field is to conduct both subscale wind-tunnel tests and full-scale flight tests with configurations and instrumentation as nearly identical as possible. In practice, this rarely occurs, since the evolution of flight hardware usually involves substantial changes from the models used in the development stages of the design. Further differences usually arise because of simplification of details on subscale models, such as elimination of small inlets, vents, antennas, and steps on the model surfaces.

In 1975, Langley Research Center obtained an existing 1/12-scale F-15 propulsion model which would be available indefinitely and could be modified as needed for the tests. At about the same time, Dryden Flight Research Center received the number 2 and number 8 prototype aircraft for a program to investigate interactions between the propulsion system and the airframe. With the proper modifications to the existing 1/12-scale model along with newly instrumented nozzle hardware for both the model and the aircraft, an opportunity was presented to obtain both subscale and full-scale data on identical configurations (except for the inlets, which on the model were faired over) with identical external pressure-orifice locations and also to obtain data at the same test parameters (except for Reynolds number).

The model was modified to incorporate the larger production vertical tails, notched horizontal-tail leading edges, and raked wing tips. Ventral fins on the afterbody were removed, and some small details, such as the vertical-tail antenna fairings, were added. Three new axisymmetric nozzle sets were fabricated with geometries to match those expected on the full-scale aircraft at flight conditions matching those possible in the wind tunnel. The static-pressure orifices on the model nozzles were located so that structural characteristics of the full-scale nozzles would not prevent similarly located orifices.

The purpose of this wind-tunnel investigation was to establish a data base of static-pressure distributions and integrated nozzle axial force to be used for comparison with that from the full-scale flight tests (ref. 1). Three nozzle configurations representing maximum dry power (power lever angle (PLA) = 83°), intermediate afterburning power (PLA = 112°), and maximum afterburning power (PLA = 130°) were tested. Nozzle exhaust flow was simulated by using high-pressure air at about room temperature (294 K).

This investigation was conducted in the Langley 16-foot transonic tunnel at Mach numbers of approximately 0.60, 0.80, 0.87, 0.90, and 1.20 at angles of attack from -1° to 9° , depending on anticipated steady-state and maneuver conditions for the full-scale aircraft. Jet total-pressure ratio was varied from approximately 1 (jet off) to about 5, depending on Mach number and the nozzle configuration used. Horizontal-tail deflection angle was set at 0° and at -10° (leading edge down) to determine the effects on nozzle and afterbody static-pressure distributions.

SYMBOLS

$A_{n,i}$	incremental nozzle axially projected area assigned to an orifice ($i = 1$ to 42)
A_{REF}	reference area of model; reference wing area (0.3923 m^2)
a	mean-line designation; fraction of the chord from leading edge over which loading is uniform at the ideal angle of attack, $\frac{x_w}{c}$
$C_{A,n}$	integrated axial-force coefficient for one nozzle, $\frac{1}{A_{REF}} \sum_{i=1}^{42} (C_{p,n,i}) A_{n,i}$ (positive in the drag direction)
$C_{p,boom}$	tail-boom pressure coefficient, $\frac{p_\ell - p_\infty}{q_\infty}$
$C_{p,f}$	fuselage pressure coefficient, $\frac{p_\ell - p_\infty}{q_\infty}$
$C_{p,n}$	nozzle pressure coefficient, $\frac{p_\ell - p_\infty}{q_\infty}$

$C_{p,nac}$	nacelle pressure coefficient, $\frac{p_l - p_\infty}{q_\infty}$
c	local chord length, m
l	reference length from nose of model to tip of booms (158.689 cm)
M	free-stream Mach number
p_l	local static pressure, Pa
$p_{t,j}$	jet total pressure, Pa
p_∞	free-stream static pressure, Pa
q_∞	free-stream dynamic pressure, Pa
x	longitudinal distance measured downstream from model nose (see fig. 3(a)), cm
x_n	longitudinal distance upstream from nozzle exit (see fig. 4), cm
x_w	longitudinal distance from surface leading edge, positive rearward, m
x'	longitudinal distance downstream from nozzle connect station, or F.S. 165.423 (see fig. 4), cm
α	angle of attack, deg
δ_h	horizontal-tail deflection angle, positive L.E. up, deg
ϕ	meridian angle, measured from top of model in clockwise direction when looking upstream, deg

Abbreviations:

A/B	afterburning
AFT	afterbody pressure orifices, aft of metric break (1 to 15)
B.L.	buttock line, spanwise distance from vertical plane of symmetry, cm
FF	fuselage pressure orifices, forward of metric break (1 to 21)
F.S.	fuselage station (see fig. 1), cm
L.E.	leading edge
max	maximum
PLA	power lever angle (throttle position)

PR jet total-pressure ratio (also $p_{t,j}/p_\infty$)

W.L. water line, vertical distance from horizontal reference plane, cm

Subscripts:

bot bottom orifice row

top top orifice row

350 approximate meridian angle (i.e., 350 denotes 349.85°)

APPARATUS AND PROCEDURE

Wind Tunnel and Tests

This investigation was conducted in the Langley 16-foot transonic tunnel, a single-return, continuous-flow, atmospheric wind tunnel with a slotted, octagonal test section measuring 4.8 m diametrically to midflat center line. With the aid of a compressor system, which draws air out through slots in the test section for $M > 1.05$, the test section airspeed is continuously variable between Mach numbers of 0.20 and 1.30. Further details on dimensions and the operating characteristics of the 16-foot transonic tunnel can be found in reference 2.

Model data were taken at Mach numbers of 0.60, 0.80, 0.87, and 0.90 for the dry-power nozzle configuration. Data were also taken at these Mach numbers and at $M = 1.20$ for both afterburning power nozzle configurations. Reynolds number per meter varied from about 1.0×10^7 to about 1.3×10^7 for the Mach number range tested. Model angle of attack varied from -1° to 9° corresponding to anticipated steady-state and maneuver conditions for the full-scale aircraft at the Mach numbers indicated above. Sideslip angle was zero throughout the test program. The ratio of jet total pressure to free-stream static pressure was varied from approximately 1 (jet off) to about 5, depending on Mach number and nozzle power setting (geometry and throat area), in an attempt to cover the operational range of nozzle pressure ratio for the full-scale aircraft. Because of limitations of the model high-pressure air system, this was not always possible. Therefore, to get a reasonable number of jet-on points for the afterburning-power nozzle configurations, it was necessary to take additional jet-on points below the nozzle choke value ($p_{t,j}/p_\infty < 1.89$). Horizontal-tail deflection angle δ_h was set at 0° and at -10° (leading edge down) during separate tunnel runs to determine the effect on afterbody and nozzle pressure distributions.

Boundary-layer transition was fixed on the model by means of 0.13- to 0.20-cm-wide strips of No. 120 carborundum grains. The transition strips (or boundary-layer trips) were located 1.78 cm downstream of the wing leading edge, 1.02 cm downstream of the horizontal-stabilizer leading edge, 0.89 cm downstream of the twin-vertical-tail leading edges, and in a ring around the nose 7.62 cm downstream of the nose apex (F.S. 24.613). The methods described in

references 3 and 4 were used to determine the locations for these trips and the grain size.

Model and Support System

Sketches showing the principal dimensions of the 1/12-scale F-15 model are shown in figure 1, and photographs of the model, mounted in the Langley 16-foot transonic tunnel with dry-power nozzles, are shown in figure 2. The dashed diagonal line across the closed inlet fairing on the side view (fig. 1) indicates the location of the inlet side plate leading edges on the aircraft. The model inlet fairings were blended into the external inlet surfaces at the inlet leading edges (fig. 2(c)). The inlet fairings on the model were constructed to represent an inlet rotation angle of 0° on the full-scale aircraft. Further details of the model and aircraft geometry can be found in table I and in references 5 and 6.

High-pressure air was used to simulate the exhausts of the twin-jet configuration. Compressed air was routed through a 3.97-cm-diameter passage drilled through the strut and into a high-pressure plenum (6.895 MPa max.) located in the model. Air was throttled through 25 orifices, each having a diameter of 0.7938 cm (12.371 cm^2 total area), to a low-pressure plenum (1.034 MPa max.) and then divided into two flow passages (45.604 cm^2 each) for the twin, closely spaced exhaust nozzles. The model also contained a six-component afterbody balance which measured forces and moments on the afterbody (metric break at F.S. 138.107, see fig. 1), including the tails and external boattails of the nozzles. Data for this balance system were taken during separate wind-tunnel runs with the manifolds for the external pressure orifices disconnected at the metric break to unlock the balances. Further information on these data and tests can be found in reference 7.

The locations of the external static-pressure orifices on the forebody and afterbody of the fuselage are shown in the model sketches of figure 3. The axial locations of the fuselage orifices are also given in table II, along with span locations (B.L.) and water line locations (W.L.), where necessary to define positions on the model surface.

Sketches of the various nozzles showing their geometry are given in figure 4. These nozzle configurations were designs corresponding to actual power settings on the full-scale engines. The geometry of the dry-power nozzle (fig. 4(a)) corresponds very closely to all low Mach number ($M < 1.10$) dry-power settings (actual geometry is for $\text{PLA} = 83^{\circ}$); the configurations for intermediate- and maximum-afterburning power settings correspond to the power lever angles (PLA) indicated for $M \geq 1.10$. Note that the dry-power nozzles ($\text{PLA} = 83^{\circ}$) have a smooth external surface contour, whereas both afterburning power nozzles ($\text{PLA} = 112^{\circ}$ and $\text{PLA} = 130^{\circ}$) have a "kink" in their surfaces at F.S. 167.828. (See fig. 4.) The coordinates of the external nozzle boattails are given in table III for each configuration, and the locations of the 42 nozzle static-pressure orifices are given for each power setting in table IV. All external boattail static-pressure orifices were incorporated in the left-hand nozzle, looking upstream. Some irregularities in the orifice locations resulted from consideration of mounting locations on the full-scale nozzles (fig. 5).

Instrumentation

Two 48-port pressure-scanning devices, referenced to the wind-tunnel static pressure, were used to measure 8 of the 42 nozzle static pressures, 15 afterbody static pressures, and 21 forebody static pressures. The other 34 nozzle static pressures were measured directly with individual gages. The pressure-scanning devices were cycled through in approximately 1 minute with a dwell time of 1/2 second on each port. Gages used with the pressure-scanning devices were mounted on the scanner bodies, resulting in almost instantaneously stabilized pressures to the gages. The jet total pressure in the tail pipes was measured with individual gages, and jet total temperature was measured with an iron-constantan stagnation thermocouple probe. Combined mass flow for the two jet exhausts was measured with an electronic turbine flowmeter.

Data Reduction

The recorded external static-pressure data were used to compute standard pressure coefficients. The external pressure axial-force coefficients on the nozzle boattails were obtained by a numerical summation of the local nozzle static-pressure coefficients multiplied by an axially projected area assigned to each of the 42 nozzle orifices and all divided by the reference area:

$$C_{A,n} = \frac{1}{A_{REF}} \sum_{i=1}^{42} C_{p,n,i} A_{n,i} \quad (1)$$

RESULTS

The results of the investigation are presented in the following figures:

Figure

Static-pressure distributions for various rows around the fuselage; $\delta_h = 0^\circ$	6 to 10
Static-pressure distributions on dry-power nozzle for several Mach numbers and angles of attack; $\delta_h = 0^\circ$ and -10°	11 and 12
Static-pressure distributions on intermediate A/B power nozzle for several Mach numbers and angles of attack; $\delta_h = 0^\circ$ and -10°	13 and 14
Static-pressure distributions on max. A/B power nozzle for several Mach numbers and angles of attack; $\delta_h = 0^\circ$ and -10°	15 and 16
Isobar contours on dry-power nozzle at $\delta_h = 0^\circ$	17

Figure

Integrated axial-force coefficients for one nozzle	18
Comparison of nozzle axial-force coefficients for two horizontal-tail deflection angles	19

DISCUSSION

In the following discussion, many of the figures of C_p versus x/l contain dashed lines between two values of x/l . This indicates an area of uncertainty where the data were faired on the basis of other data or experience, rather than being faired between the points shown.

Fuselage Pressure-Coefficient Distributions

Typical pressure-coefficient distributions along the top of the fuselage at span station 0 (center line) are presented in figure 6 at $M = 0.60$ and 0.894 for the model with dry-power nozzles and at $M = 1.19$ for the model with max. A/B power nozzles. Increasing angle of attack causes a general decrease in pressure along the upper fuselage, but jet total-pressure ratio has only a small effect - and, as expected, only on the pressures farthest aft. Similar pressure-coefficient distributions along the bottom surface at the fuselage center line are presented in figure 7. For this figure, two Mach numbers are given for each nozzle power setting. Increasing angle of attack causes a general increase in the level of pressure coefficients - and, as expected, an opposite effect from that found on the top surface. Initial jet operation generally causes a significant increase in the pressure coefficients at the orifices farthest aft, but further increases in jet total pressure have only small effects (e.g., fig. 7(a) for $M = 0.894$ and $\alpha = 1.11^\circ$).

Figures 8 and 9 present typical pressure-coefficient distributions on the top and bottom surfaces, respectively, of the engine nacelles and nozzle boattails. Locations of the forebody/afterbody metric break, start of the nozzle boattail, kink in the nozzle surface, and nozzle exit are indicated by tick marks on the bottom border of the left-hand plot of figure 8(a). The nozzle surface kink (F.S. 167.828) occurs between the variable nozzle external flaps (variable only on the full-scale nozzle) and the fixed external nozzle surface when the nozzle exit and throat areas are opened up for A/B power modes (figs. 4(b) and 4(c)). From a comparison of parts (b) and (c) of figures 8 and 9, for the A/B power nozzles, with part (a) of figures 8 and 9, for the dry-power nozzles, it is evident that this sudden change in slope at the kink has a detrimental effect on the subsonic pressure recovery. A more detailed discussion of this is given in the section "Intermediate A/B Power Nozzles," where nozzle boattail pressure data are presented for all meridian angles around the nozzles.

For the nozzle boattail pressures, as with the fuselage center line pressures, jet operation causes a slight increase in the static-pressure coefficients at the nozzle orifices farthest aft. The effects of increasing angle of

attack on the nacelle and nozzle pressure coefficients are also similar to the effects on the fuselage center line surface pressures. That is, the pressures on the upper surface (fig. 8) generally decrease and the pressures on the lower surface (fig. 9) generally increase with increasing angle of attack.

Typical pressure-coefficient distributions along the top inside surface of the left-hand horizontal-tail boom (see fig. 3(b) for orifice locations) are presented in figure 10. Small pressure-coefficient increases along this surface are generally indicated for increasing jet total pressures. A significant change in curve shape occurs between $M = 0.90$ and $M = 1.20$ (figs. 10(b) and 10(c)). More significant is the low level of pressure in this region, probably caused by the low-pressure field between the twin vertical tails in combination with the expansion process between the vertical tail and adjacent nacelle/nozzle side. For aircraft with twin vertical tails, some alleviation of this problem is usually possible by adjusting the toe angles of the vertical tails, but this must be a compromise between subsonic and supersonic requirements.

Nozzle Pressure-Coefficient Distributions

Dry-power nozzles.- Static-pressure-coefficient distributions on the dry-power nozzles at eight meridian angles around the nozzles are presented in figures 11 and 12 for horizontal-tail angles δ_h of 0° and -10° , respectively. Each page represents a specific combination of Mach number and angle of attack, and the different symbols define the jet total-pressure ratios. A view looking upstream of the left-hand dry-power nozzle showing the locations of the orifice rows relative to the tail boom fairing and nozzle interfairing is given in figure 5. Note that the free-stream flow is at least partially blocked by the presence of the fairings for the orifice rows at $\phi = 85.85^\circ$ and 277.85° , especially at positive angles of attack, whereas the rows experiencing the least interference from surrounding structure would be those at $\phi = 181.85^\circ$ and 349.85° .

For all angles of attack at $M = 0.60$, the flow exhibits good pressure recovery except in the area around the nozzle interfairing ($\phi = 61.85^\circ$, 85.85° , and 133.85°). The tapering of the side-by-side nozzles (boattail angles of 18.445°) creates a rapidly diverging channel between the nozzles and appears to produce flow separation in this region, even at a Mach number this low (figs. 11(a) to 11(c)). This problem appears to grow worse with increasing Mach numbers, showing up to a lesser extent adjacent to the outboard tail-boom fairing at $M \approx 0.80$ (figs. 11(d) to 11(f)). At $M \approx 0.90$, it is quite evident that flow separation has progressed to the point that it covers nearly the entire nozzle (figs. 11(j) to 11(m)). For this Mach number, attached flow generally is evident only on the bottom surface ($\phi = 181.85^\circ$) of the nozzles at jet-on conditions. The largest effects of jet total-pressure ratio occur between the jet-off and the first jet-on points, and only small effects occur with further increases in jet total-pressure ratio.

The pressure-coefficient distributions in figure 12 for $\delta_h = -10^\circ$ are very similar in every respect to the distributions in figure 11 for $\delta_h = 0^\circ$, except that those for $\delta_h = -10^\circ$ are consistently lower at all Mach numbers,

angles of attack, and meridian angles. Since the result of this effect is most evident for the integrated axial-force values, it is discussed in the subsequent section "Nozzle Integrated Axial-Force Coefficients."

Intermediate A/B power nozzles.- Static-pressure-coefficient distributions on the intermediate A/B power nozzles at eight meridian angles around the nozzles are presented in figure 13 for $\delta_h = 0^\circ$ and in figure 14 for $\delta_h = -10^\circ$. As indicated previously in the discussion of the afterbody pressure-coefficient data, the kink in the nozzle boattail for A/B power modes produces a strong disturbance in the flow over the nozzle surface. For the intermediate A/B power nozzles, the disturbance does not appear to produce a shock at subsonic Mach numbers, but at $M \approx 1.20$ for the rows at $\phi = 349.85^\circ$, 61.85° , and 181.85° (figs. 13(n) and 13(o)), the sharp pressure peak at $x/l = 0.904$ indicates a possible shock at this location. As with the dry-power nozzles, initial operation of the jet for the intermediate A/B power nozzles causes a significant increase in the static-pressure coefficients over the nozzle boattail at subsonic speeds, but further increases in jet total-pressure ratio generally produce only small effects. For $M \approx 1.20$, these trends are not consistent with the subsonic data. This difference may be attributable in part to the first jet-on points being unchoked instead of choked as they are for the subsonic Mach numbers. Also at supersonic speeds, jet interference can only feed upstream through the boundary layer which would account for the generally smaller effects of jet operation. Jet operation may affect separated regions (see for example $\phi = 61.85^\circ$ and 301.85° in fig. 13(n), and $\phi = 133.85^\circ$ in fig. 13(o)) and would account for larger (and erratic) effects in these regions. Jet operation may also affect nozzle terminal shock location and this would also appear as jet interference. As with the dry-power nozzles, deflection of the horizontal tails to $\delta_h = -10^\circ$ (fig. 14) has little or no effect on the general shape of the nozzle pressure-coefficient distributions on the intermediate A/B power nozzles but causes a general decrease in the level of pressure, which will increase nozzle drag.

Maximum A/B power nozzles.- Static-pressure-coefficient distributions on the maximum A/B power nozzles at eight meridian angles around the nozzles are presented in figure 15 for $\delta_h = 0^\circ$ and in figure 16 for $\delta_h = -10^\circ$. For this configuration, the nozzle boattail angle is only about 2.5° (fig. 4(c)); thus, the kink in the nozzle boattail is much more severe than for the intermediate A/B power nozzles, where the boattail angle is about 7.5° . For this reason, the pressure peaks on the nozzle occur even for $M \approx 0.60$, although they do not necessarily indicate flow-field shocks around the nozzles at this location. In many cases for all three nozzle configurations, the maximum pressure could occur between the orifices, so that no pressure peak would be revealed by the distribution of static-pressure values. The effects of jet total-pressure ratio and horizontal-tail angle are similar to those for the intermediate A/B power nozzles. The most significant difference between the pressure-coefficient distributions for the max. A/B power nozzles and the intermediate A/B power nozzles is the general overall increase in static pressure around the max. A/B power nozzles due to a lower nozzle boattail angle. However, the very low pressures associated with the fixed upstream part of the nozzle boattail are still evident for several rows on the nozzle at $M > 0.80$.

Isobar Contours on Dry-Power Nozzle

Isobar contours on the left-hand, dry-power nozzle for $M = 0.60$ and $M = 0.87$ are shown in figure 17 to illustrate the effects of Mach number (figs. 17(a) and 17(b)), angle of attack (figs. 17(b) and 17(c)), and jet operation (figs. 17(c) and 17(d)). It is evident that flow around the vertical-tail surfaces at $M = 0.60$ creates a low-pressure region in the upper left-hand quadrant of the nozzle, whereas for $M = 0.87$ at the same conditions, the flow seems nearly symmetrical from left to right. This illustrates the compromise necessary when "tuning" the toe angle of the twin vertical tails for minimum drag. Different vertical-tail toe angles would probably be required for minimum drag at each flight condition. Higher pressure recovery occurs on the nozzles at $M = 0.60$ than at $M = 0.87$, as evidenced by the disappearance of a large positive pressure region near the nozzle exit at $M \approx 0.87$. At $\alpha = 0.08^\circ$ and $M = 0.87$ (fig. 17(b)), the lowest pressures on the top and bottom nozzle surfaces are equal and cover nearly the same area. Increasing angle of attack (compare figs. 17(c) and 17(b)) produces a more unsymmetrical and lower pressure field over the entire nozzle, especially on the bottom surface of the nozzle for $M = 0.87$. Operation of the jet (compare figs. 17(d) and 17(c)) seems to smooth out the isobar patterns somewhat, and at the same time significantly increases the pressure levels over the entire nozzle boattail.

Nozzle Integrated Axial-Force Coefficients

Nozzle axial-force coefficients for all three nozzle power settings, all angles of attack, and all Mach numbers tested are plotted in figure 18 as a function of jet total-pressure ratio. Axial force on the left-hand nozzle was obtained by assigning incremental longitudinal projected areas to each orifice and then summing incremental forces to obtain nozzle axial force. When orifices were plugged or leaking, the area assigned to such orifices was divided among adjacent orifices. The dashed lines between the jet-off and first jet-on points for the dry-power and intermediate A/B power nozzle configurations show an approximation of the drag level with the characteristic dip below the choke point. This drag "bucket" is evident from the data for the max. A/B power nozzles, since several data points were taken for jet total-pressure ratios near choke values (see figs. 18(e) and 18(f)).

Deflection of the horizontal-tail surfaces, in spite of their outboard and partly shielded location, has surprisingly strong effects on integrated nozzle axial force. One of these effects can be readily observed by comparing the data at $M = 0.87$ for the intermediate A/B power nozzles (figs. 18(c) and 18(d)). For $M = 0.87$, deflection of the horizontal tails to -10° causes a reversal of the effect of increasing angle of attack shown for $\delta_h = 0^\circ$. Since the horizontal-tail load is increasing (tail angle increasing relative to free stream, fig. 18(c)) in one case and decreasing (tail angle decreasing relative to free stream, fig. 18(d)) for the other, one must conclude that the horizontal tails have a stronger influence on nozzle axial force than angle of attack. This increase in nozzle axial force with horizontal tail angle is summarized in figure 19 for all five Mach numbers tested, for $\alpha \approx 3^\circ$ and $p_{t,j}/p_\infty = 3.0$. As shown by figure 19, the effect of horizontal-tail deflection is consistent

for all three nozzle configurations at all Mach numbers tested. The effect on nozzle axial force of changing nozzle configuration can be seen by comparing the three plots in figure 19. Projected axial area of the nozzle boattails decreases with increasing nozzle power setting (looking at plots from left to right) and causes nozzle axial force to decrease, as expected.

SUMMARY OF RESULTS

Static-pressure-coefficient distributions on the forebody, afterbody, and nozzles of a 1/12-scale F-15 propulsion model have been determined in the Langley 16-foot transonic tunnel for Mach numbers from 0.60 to 1.20, angles of attack from -1° to 9° , and jet total-pressure ratios from 1 (jet off) up to about 5, depending on Mach number. The effects of nozzle power setting and horizontal-tail deflection angle on the pressure-coefficient distributions were also investigated. Reynolds number per meter varied from about 1.0×10^7 to 1.3×10^7 , depending on Mach number.

The wind-tunnel investigation to determine static-pressure-coefficient distributions on the F-15 model in the presence of operating jets has produced the following results:

1. Forebody and afterbody pressures were affected by both angle of attack and Mach number but were little affected by variation of nozzle jet total-pressure ratio.
2. Initial operation of the twin jets caused significant positive increases in the fuselage and nozzle pressures farthest aft, but further increases in jet total pressure generally had only small effects.
3. The sharp angle change between the fixed part of the nozzle and the movable nozzle boattail flaps, created when the nozzles are opened up for afterburning power, has a detrimental effect on subsonic pressure recovery, and at a Mach number of approximately 1.2 causes a sharp pressure peak, indicating a possible shock wave standing over the nozzle surface.
4. The combination of twin vertical tails and expansion flow over the nozzle boattail closures produces extremely low pressure coefficients in the upper, outboard quadrant of the nozzles. This is evidenced not only by the nozzle pressures but also by the upper-surface pressures on the boom, just inboard of the left-hand vertical tail.
5. Deflection of the horizontal-tail surfaces, in spite of their outboard and partly shielded location, has surprisingly strong effects on the integrated nozzle boattail axial force.

6. The flow field surrounding the nozzles is very complex, always resulting in nonuniform pressure distributions around the nozzles and often resulting in separated flow regions, especially for the dry-power nozzles.

Langley Research Center

National Aeronautics and Space Administration

Hampton, VA 23665

October 5, 1979

REFERENCES

1. Nugent, Jack; Taillon, Norman V.; and Pendergraft, Odis C., Jr.: Status of a Nozzle-Airframe Study of a Highly Maneuverable Fighter. AIAA Paper 78-990, July 1978.
2. Corson, Blake W., Jr.; Runckel, Jack F.; and Igoe, William B.: Calibration of the Langley 16-Foot Transonic Tunnel With Test Section Air Removal. NASA TR R-423, 1974.
3. Braslow, Albert L.; Hicks, Raymond M.; and Harris, Roy V., Jr.: Use of Grit-Type Boundary-Layer Transition Trips on Wind-Tunnel Models. NASA TN D-3579, 1966.
4. Braslow, Albert L.; and Knox, Eugene C.: Simplified Method for Determination of Critical Height of Distributed Roughness Particles for Boundary-Layer Transition at Mach Numbers From 0 to 5. NACA TN 4363, 1958.
5. Berrier, Bobby L.; and Maiden, Donald L.: Effect of Nozzle-Exhaust Flow on the Longitudinal Aerodynamic Characteristics of a Fixed-Wing, Twin-Jet Fighter Airplane Model. NASA TM X-2389, 1971.
6. Maiden, Donald L.; and Berrier, Bobby L.: Effect of Airframe Modifications on Longitudinal Aerodynamic Characteristics of a Fixed-Wing, Twin-Jet Fighter Airplane Model. NASA TM X-2523, 1972.
7. Pendergraft, O. C.: Comparison of Axisymmetric and Nonaxisymmetric Nozzles Installed on the F-15 Configuration. AIAA Paper No. 77-842, July 1977.

TABLE I.- MODEL DETAILS

Wing geometry:

Airfoil sections	NACA 64AXXX with modified conical camber leading edge
At B.L. 16.299 (root section)	NACA 64A(5.5)(05.9) a = 0.8 modified
At B.L. 32.809	NACA 64A(5.5)(04.6) a = 0.8 modified
At B.L. 47.567	NACA 64A2(03.5) a = 0.8 modified
At B.L. 54.364 (tip section)	NACA 64A203 a = 0.8 modified
Reference area, m ²	0.3923
Span, cm	108.727
Mean aerodynamic chord, cm	40.498
Tip chord, cm	14.464
Taper ratio	0.250
Aspect ratio	3.007
L.E. sweep angle, deg	45.0
Dihedral angle, deg	-1.0

Horizontal-stabilizer geometry:

Airfoil sections	Modified NACA 000X-64
At B.L. 14.817 (root section)	NACA 0005.5-64
At B.L. 19.050	NACA 0003.5-64
At B.L. 34.723 (tip section)	NACA 0002.5-64
Area (each), m ²	0.0359
Span, cm	71.755
Root chord, cm	29.041
Tip chord, cm	9.851
Taper ratio	0.339
Aspect ratio	2.046
L.E. sweep angle, deg	50.0
Dihedral angle, deg	0.0
Twist, deg	0.0

Vertical tail geometry:

Airfoil sections	NACA 000X-64
At W.L. 27.517 (root section)	NACA 0005-64
At W.L. 53.729 (tip section)	NACA 0003.5-64
Area (each), m ²	0.0404
Span, cm	26.213
Root chord, cm	24.333
Tip chord, cm	6.481
Taper ratio	0.266
Aspect ratio	1.70
L.E. sweep angle, deg	36.57
Toe angle (L.E. out), deg	2.0
Twist, deg	0.0

TABLE II.- FUSELAGE ORIFICE LOCATIONS FOR THE
1/12-SCALE F-15 PROPULSION MODEL

Orifice number	Fuselage station, cm	Buttock or water line, cm
FF 1	F.S. 36.779	B.L. 0.0
FF 2	F.S. 49.213	
FF 3	F.S. 59.030	
FF 4	F.S. 71.679	
FF 5	F.S. 85.217	
FF 6	F.S. 96.977	
FF 7	F.S. 109.423	
FF 8	F.S. 121.564	
FF 9	F.S. 133.175	
FF 10		B.L. 5.961
FF 11		W.L. 21.229
FF 12		B.L. 5.961
FF 13		B.L. 0.0
FF 14	F.S. 109.423	B.L. 6.030
FF 15	F.S. 121.564	B.L. 6.030
FF 16	F.S. 133.175	B.L. 5.961
FF 17	F.S. 121.564	W.L. 21.229
FF 18	F.S. 133.175	W.L. 21.229
FF 19	F.S. 109.423	B.L. 6.030
FF 20	F.S. 121.564	B.L. 6.030
FF 21	F.S. 133.175	B.L. 5.961
AFT 1	F.S. 152.819	B.L. 0.0
AFT 2	F.S. 158.323	
AFT 3	F.S. 169.418	
AFT 4	F.S. 152.819	
AFT 5	F.S. 158.323	
AFT 6	F.S. 169.418	
AFT 7	F.S. 152.819	B.L. 5.687
AFT 8	F.S. 158.750	B.L. 5.839
AFT 9	F.S. 163.096	B.L. 5.547
AFT 10	F.S. 158.323	B.L. 12.106
AFT 11	F.S. 163.096	B.L. 12.106
AFT 12	F.S. 169.418	B.L. 12.106
AFT 13	F.S. 152.819	B.L. 5.687
AFT 14	F.S. 158.750	B.L. 5.687
AFT 15	F.S. 163.096	B.L. 5.547

TABLE III.- COORDINATES OF THE NOZZLE EXTERNAL CONTOURS

Maximum dry power PLA = 83°			Intermediate A/B power PLA = 112°			Maximum A/B power PLA = 130°		
x', cm (a)	Radius, cm	Remarks	x', cm (a)	Radius, cm	Remarks	x', cm (a)	Radius, cm	Remarks
0.000	4.907		0.000	4.907		0.000	4.907	
.234	4.897		.234	4.895		.234	4.895	
.445	4.879		.445	4.879		.445	4.882	
.655	4.862		.655	4.859		.655	4.862	
.869	4.836		.869	4.834		.869	4.839	
1.080	4.806		1.080	4.806	Blend for smooth contour	1.080	4.811	
1.290	4.775	Blend for smooth contour	1.290	4.770		1.290	4.780	Blend for smooth contour
1.504	4.737		1.504	4.732		1.504	4.744	
1.715	4.694		1.715	4.689		1.715	4.704	
1.925	4.651		1.925	4.643		1.925	4.658	
2.139	4.600		2.139	4.590		2.139	4.608	
2.350	4.547		2.350	4.534		2.350	4.552	
2.560	4.491		2.405	4.519	Change of slope	2.405	4.534	Change of slope
2.774	4.432		2.560	4.509	Blend for smooth contour	2.560	4.536	Blend for smooth contour
2.985	4.366		2.774	4.488		2.985	4.531	
3.129	4.315	Tangent point	2.985	4.468		3.124	4.526	Tangent point
7.739	2.776	Straight taper	3.099	4.450	Tangent point	7.981	4.305	Straight taper
			7.915	3.792	Straight taper			

^aMeasured downstream from F.S. 165.423.

TABLE IV.- AXIAL LOCATIONS OF NOZZLE BOATTAIL

STATIC-PRESSURE ORIFICES

Maximum dry power: PLA = 83°

ϕ , deg	Nozzle orifice row at axial location x_n^a , cm, of -						
	0.676	1.176	1.740	2.301	3.145	4.270	b_5 5.410
349.85		6		5	4	3	2
61.85		12		11	10	9	8
85.85		16		15		14	
133.85		20		19	18	17	
181.85		26		25	24	23	22
229.85		30		29		28	
277.85		34		33		32	
301.85	42	41	40	39	38	37	36

Intermediate A/B power: PLA = 112°

ϕ , deg	Nozzle orifice row at axial location x_n^a , cm, of -						
	0.706	1.229	1.819	2.405	3.287	4.460	b_5 5.649
349.85		6		5	4	3	2
61.85		12		11	10	9	8
85.85		16		15		14	
133.85		20		19	18	17	
181.85		26		25	24	23	22
229.85		30		29		28	
277.85		34		33		32	
301.85	42	41	40	39	38	37	36

Maximum A/B power: PLA = 130°

ϕ , deg	Nozzle orifice row at axial location x_n^a , cm, of -						
	0.719	1.247	1.839	2.431	3.320	4.503	b_5 5.700
349.85		6		5	4	3	2
61.85		12		11	10	9	8
85.85		16		15		14	
133.85		20		19	18	17	
181.85		26		25	24	23	22
229.85		30		29		28	
277.85		34		33		32	
301.85	42	41	40	39	38	37	36

^aMeasured upstream from nozzle exit. See figure 5 for orifice locations.^bAll orifices at this station offset 0.107 cm clockwise looking upstream.

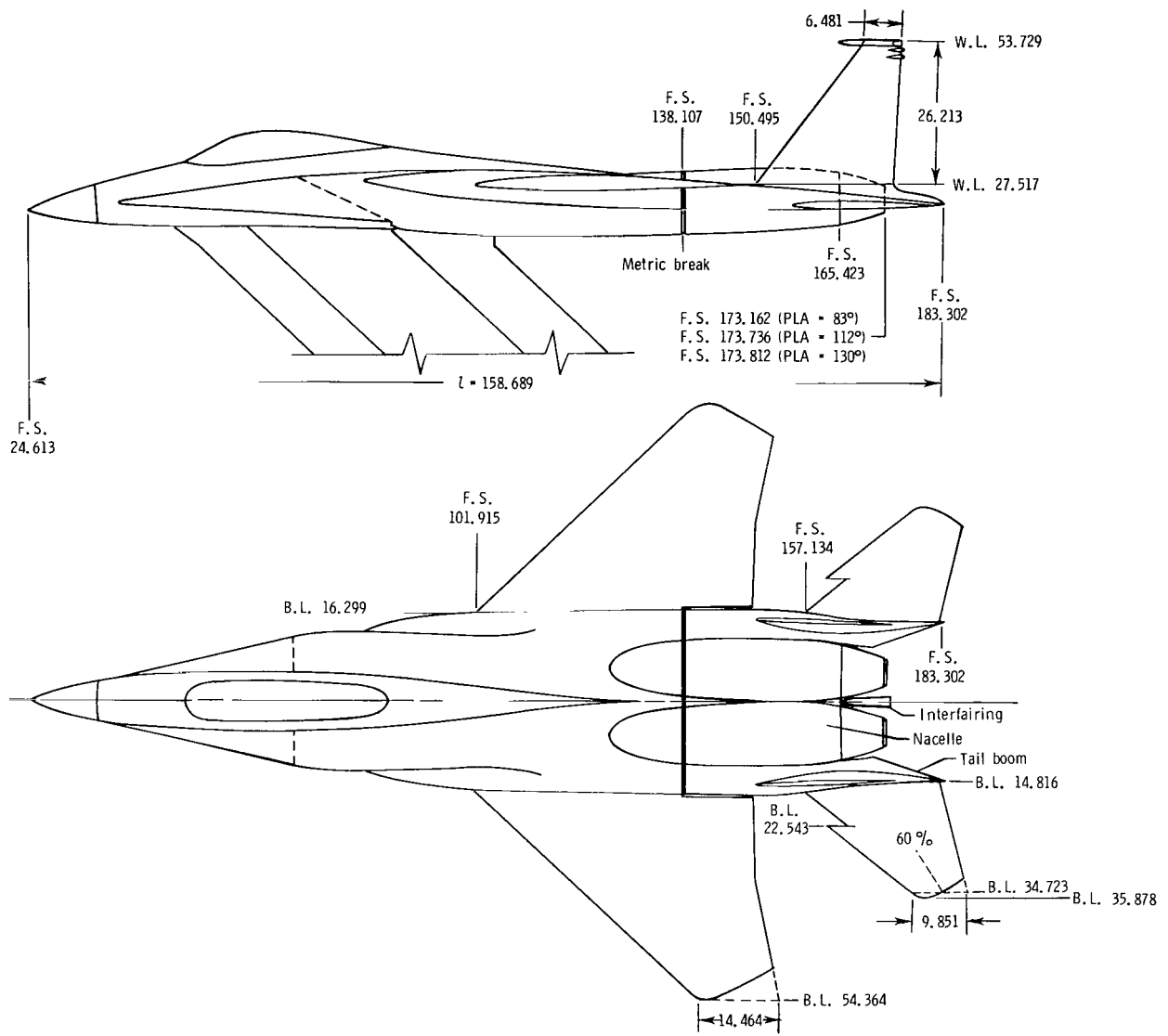


Figure 1.- Details of model geometry. (See also table I.)
All linear dimensions are in centimeters.



(a) Overall view of model.

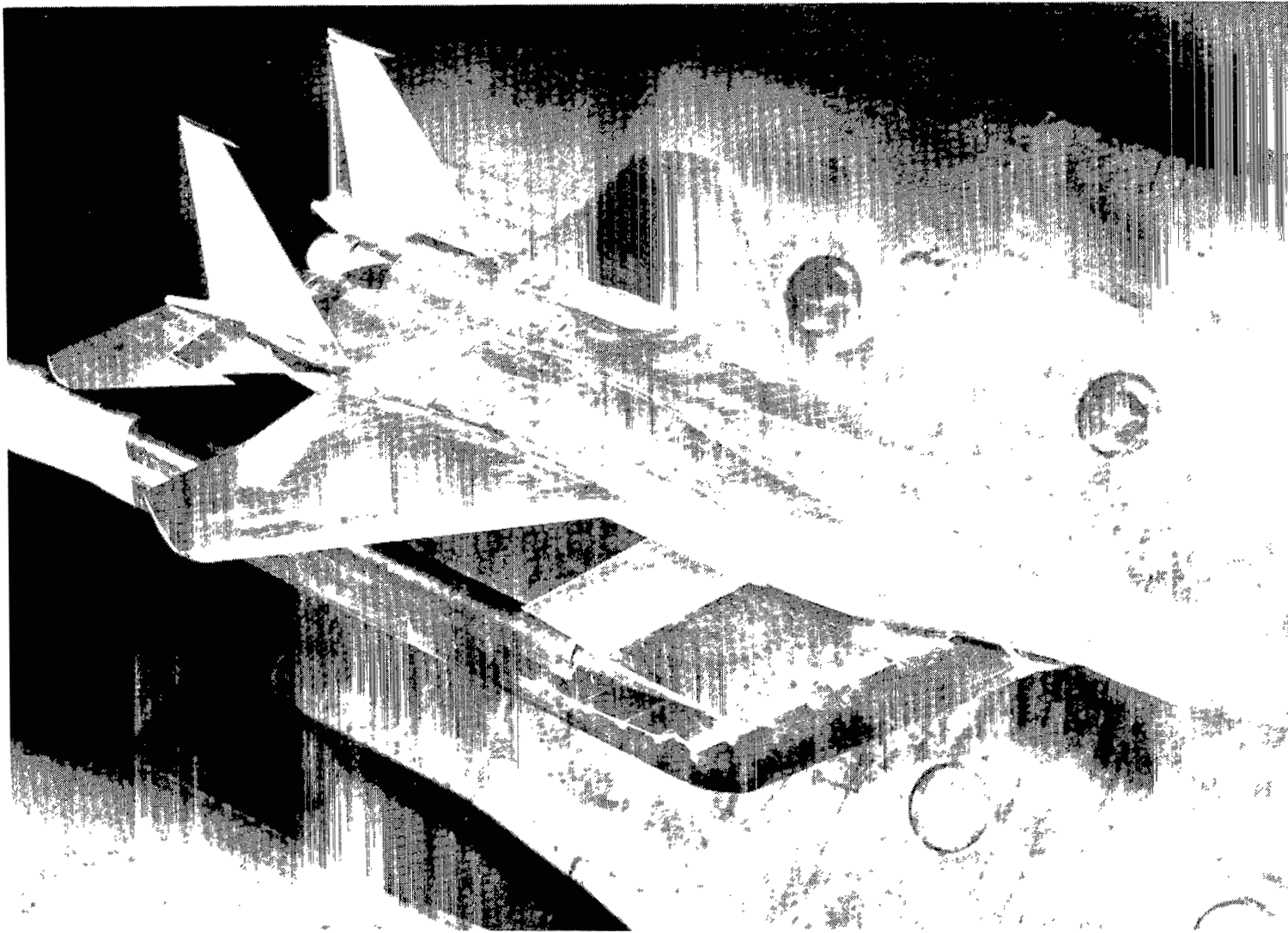
Figure 2.- Photographs of 1/12-scale F-15 propulsion model installed
in 16-foot transonic tunnel.



L-76-3414

(b) Detailed view of aft-end, showing dry-power nozzles.

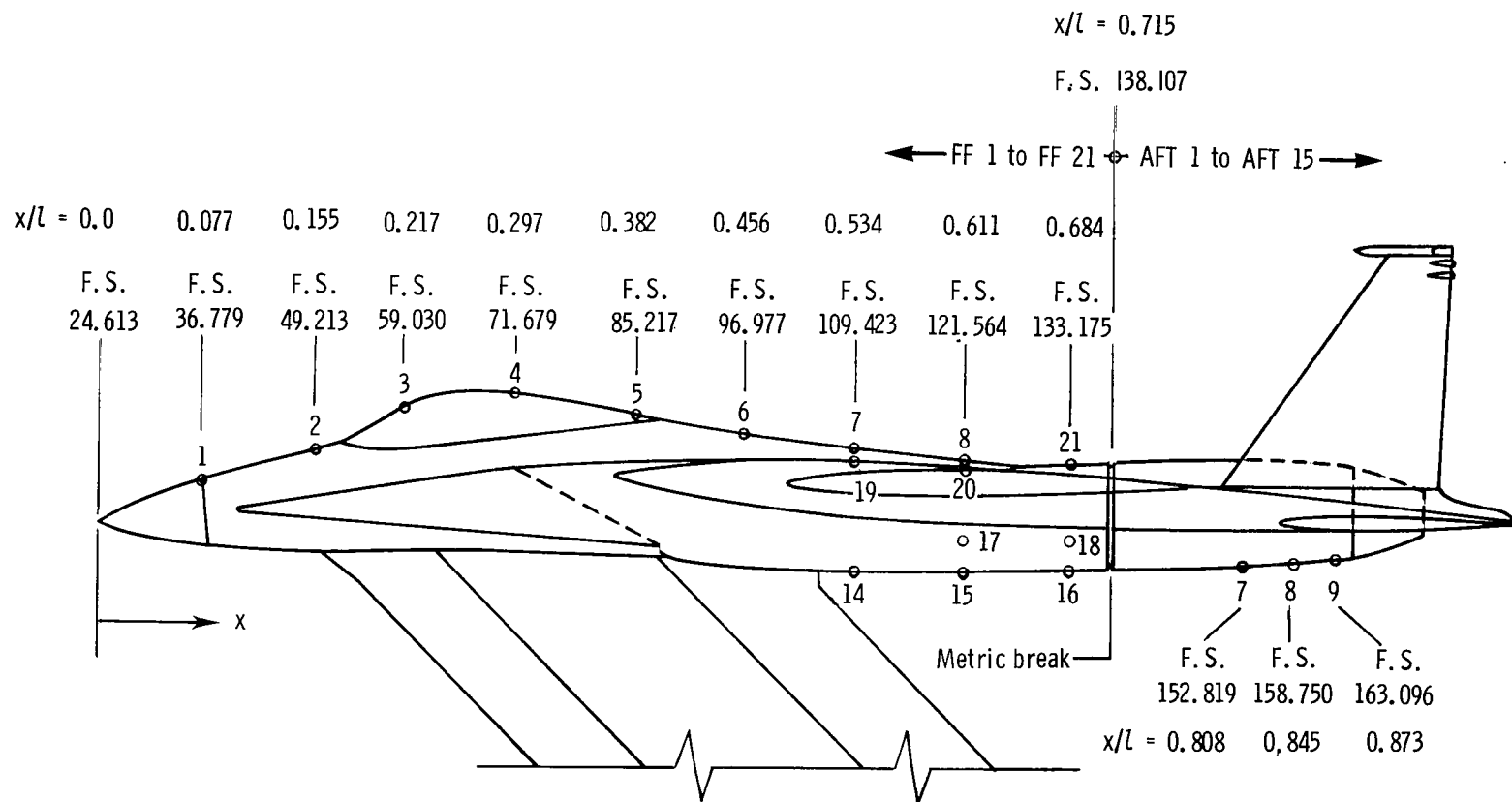
Figure 2.- Continued.



(c) Detailed view showing inlet fairing.

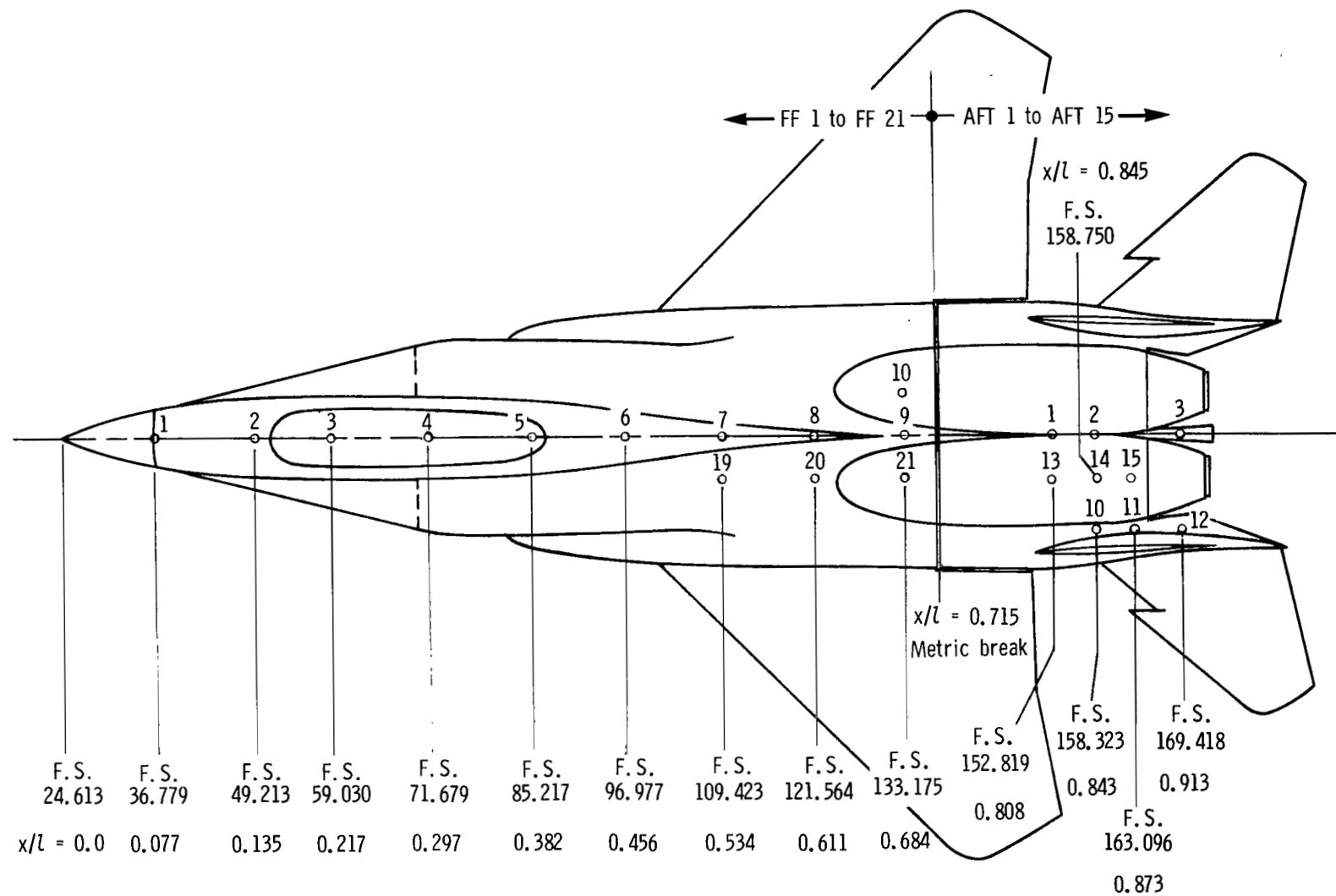
Figure 2.- Concluded.

L-76-3412



(a) Side view.

Figure 3.- Sketches of model showing static-pressure orifice locations on forebody and afterbody. All dimensions are in centimeters.



(b) Top view.

Figure 3.- Continued.

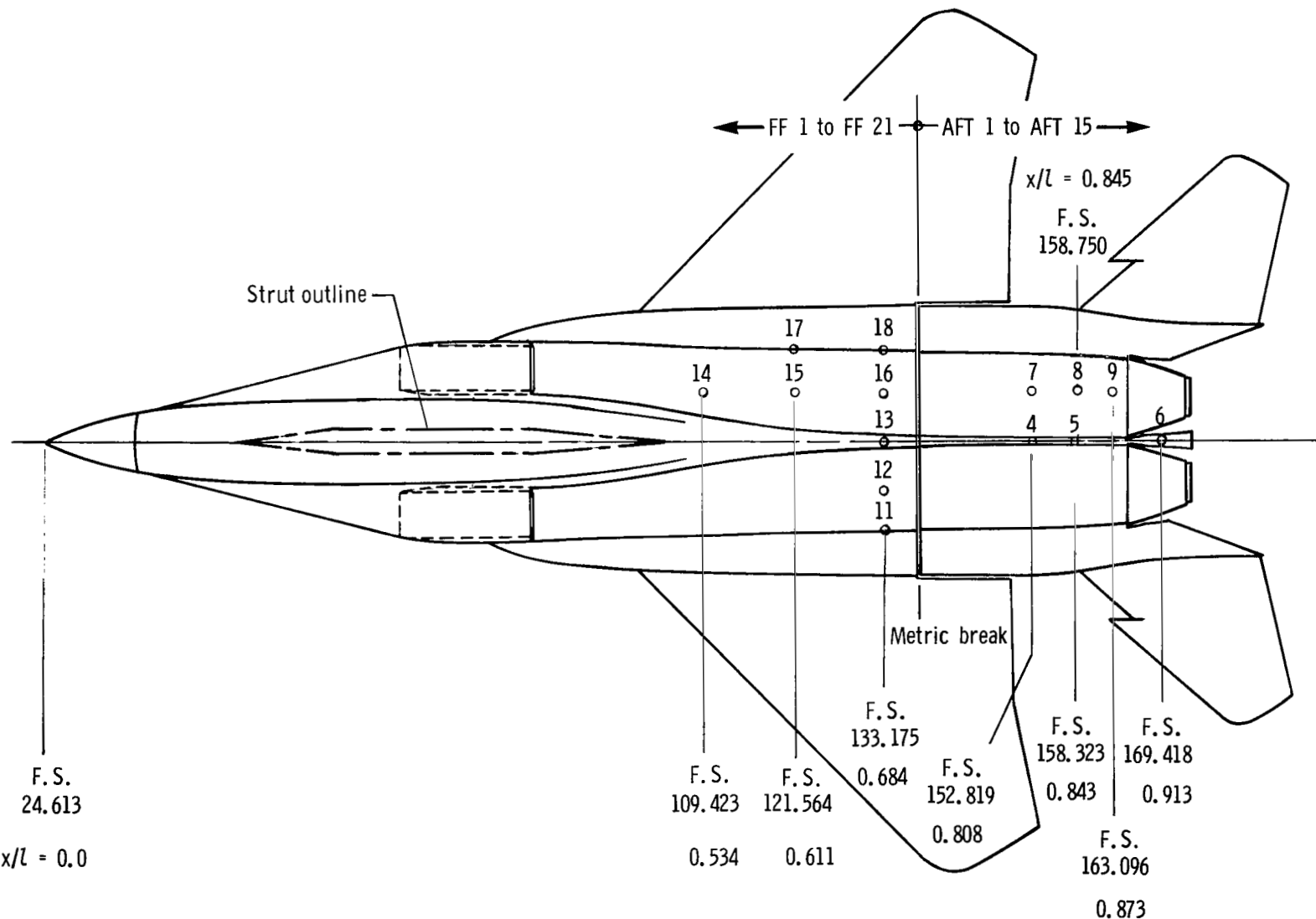
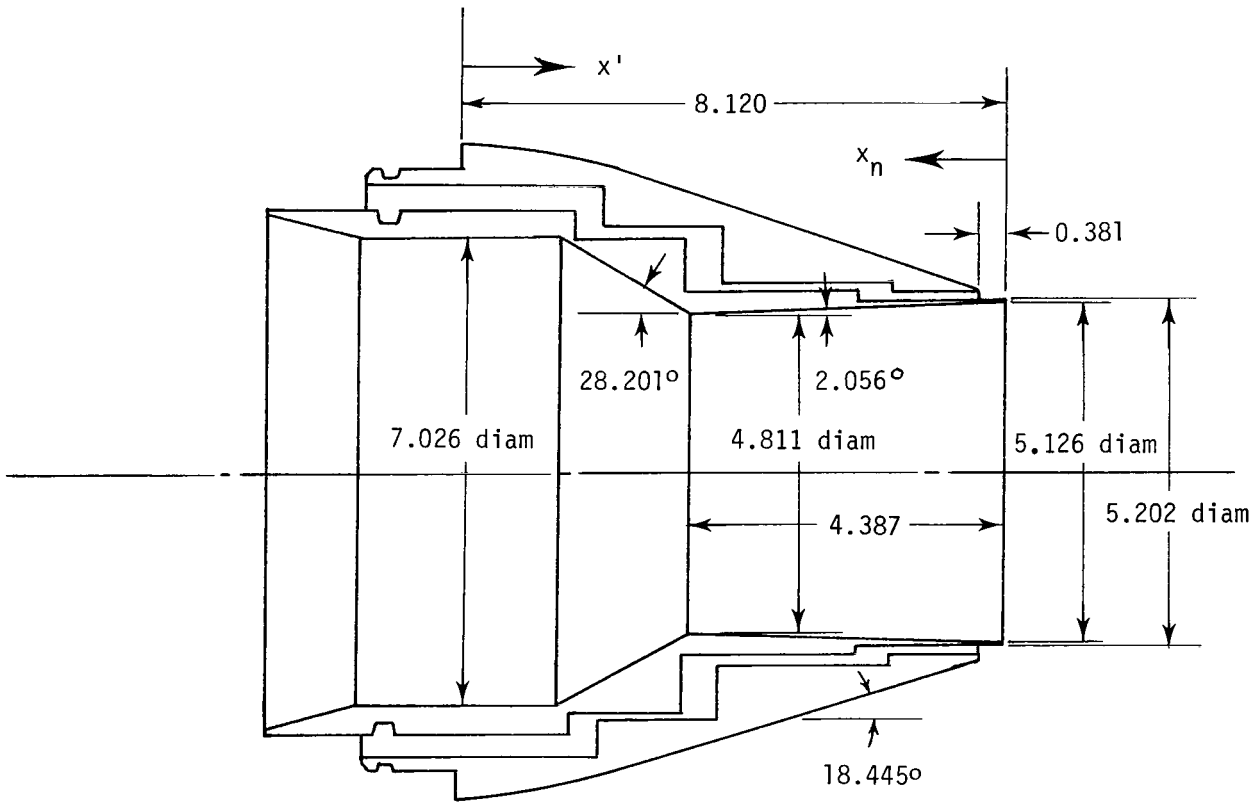


Figure 3.- Concluded.

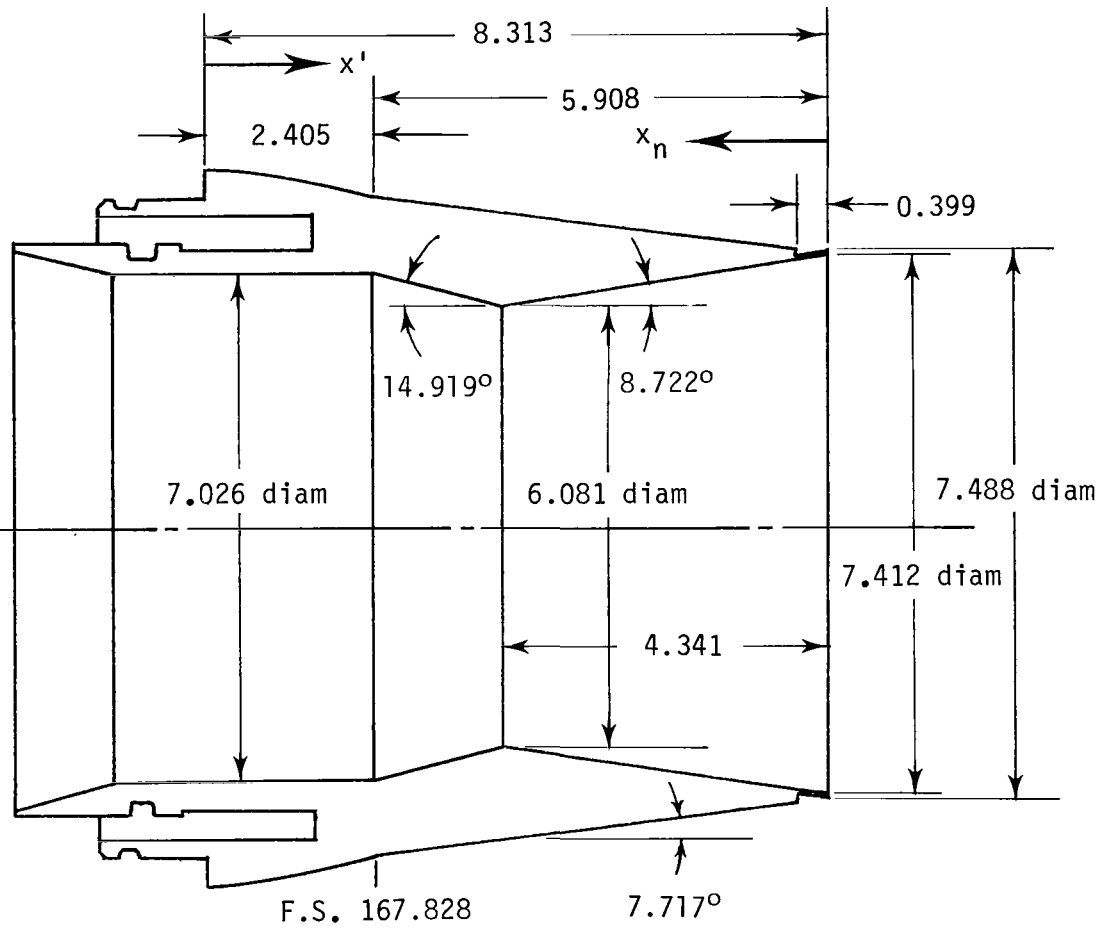
F.S. 165.423



(a) Maximum dry power: PLA = 83°.

Figure 4.- Sketches of the various nozzle configurations.
All linear dimensions are in centimeters.

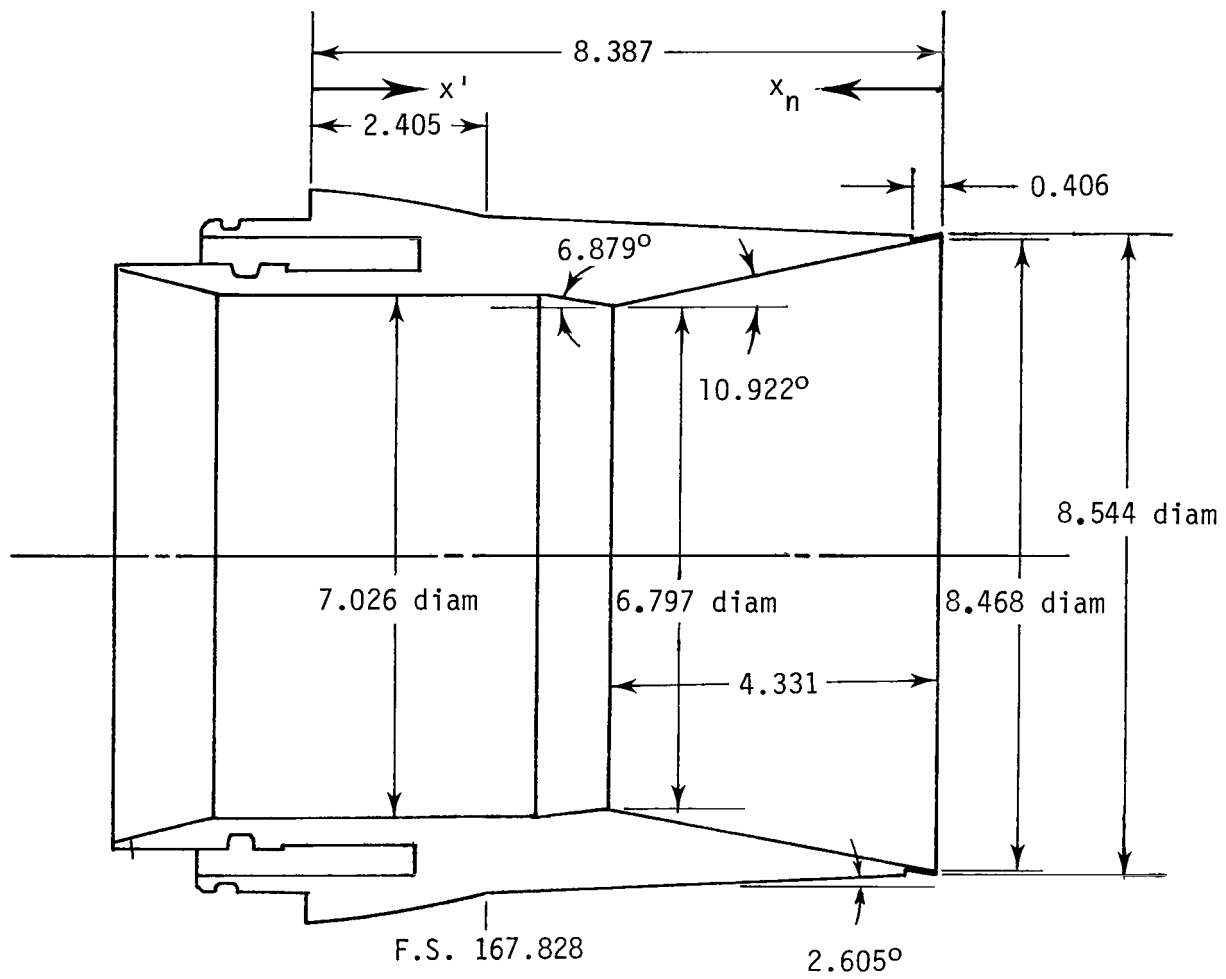
F.S. 165.423



(b) Intermediate A/B power: PLA = 112°.

Figure 4.- Continued.

F.S. 165.423



(c) Maximum A/B power: PLA = 130°.

Figure 4.- Concluded.

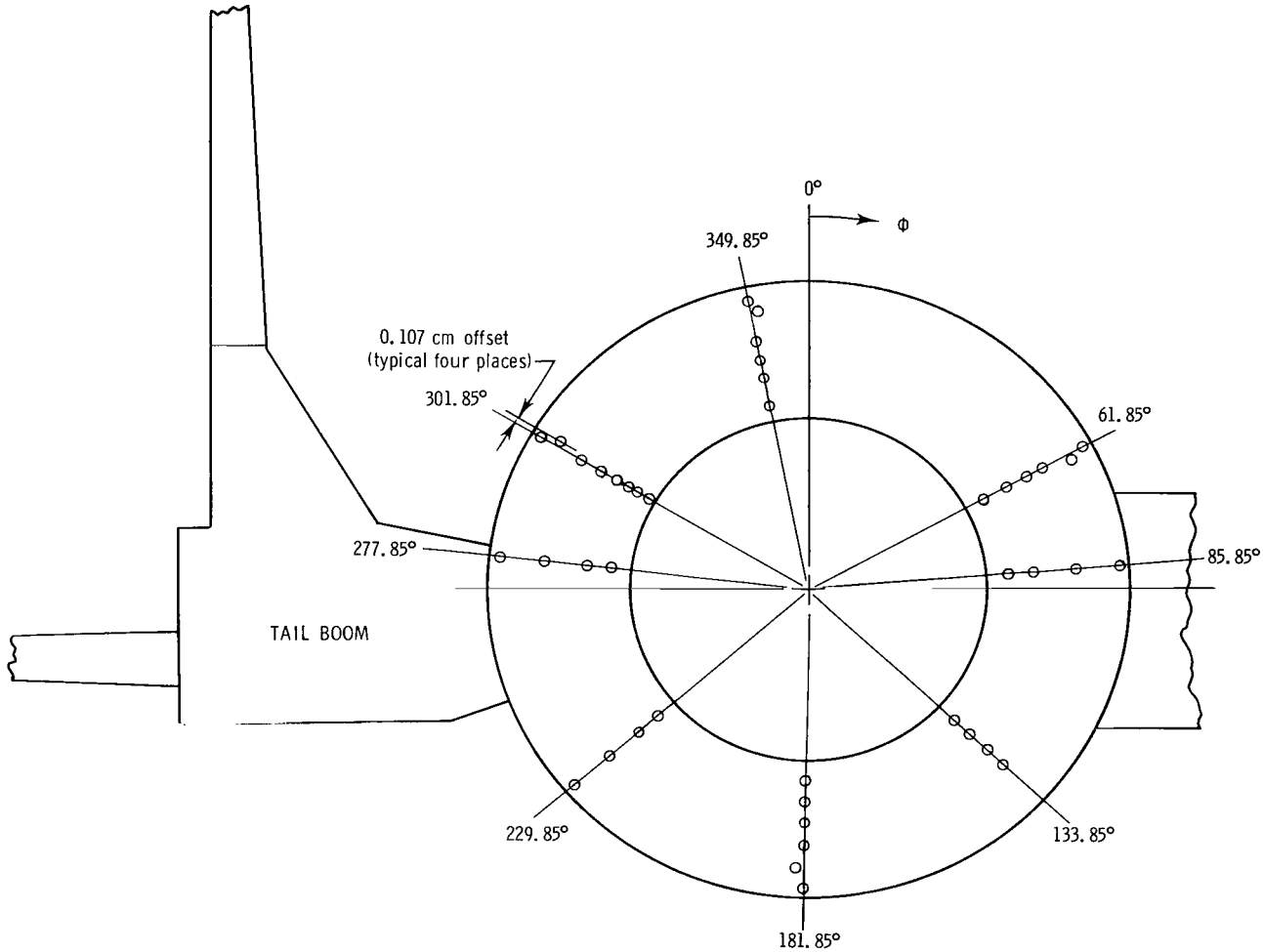
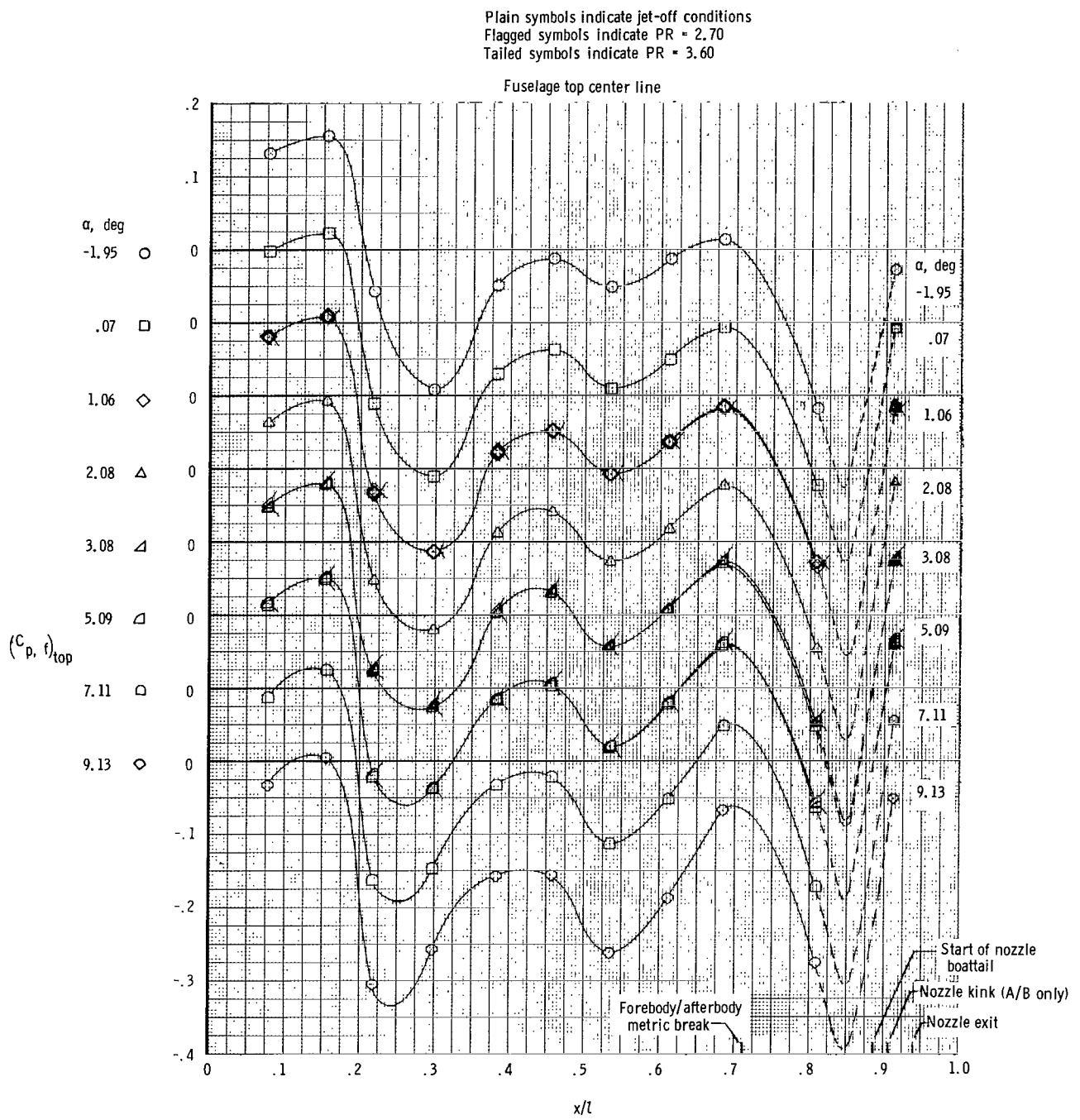
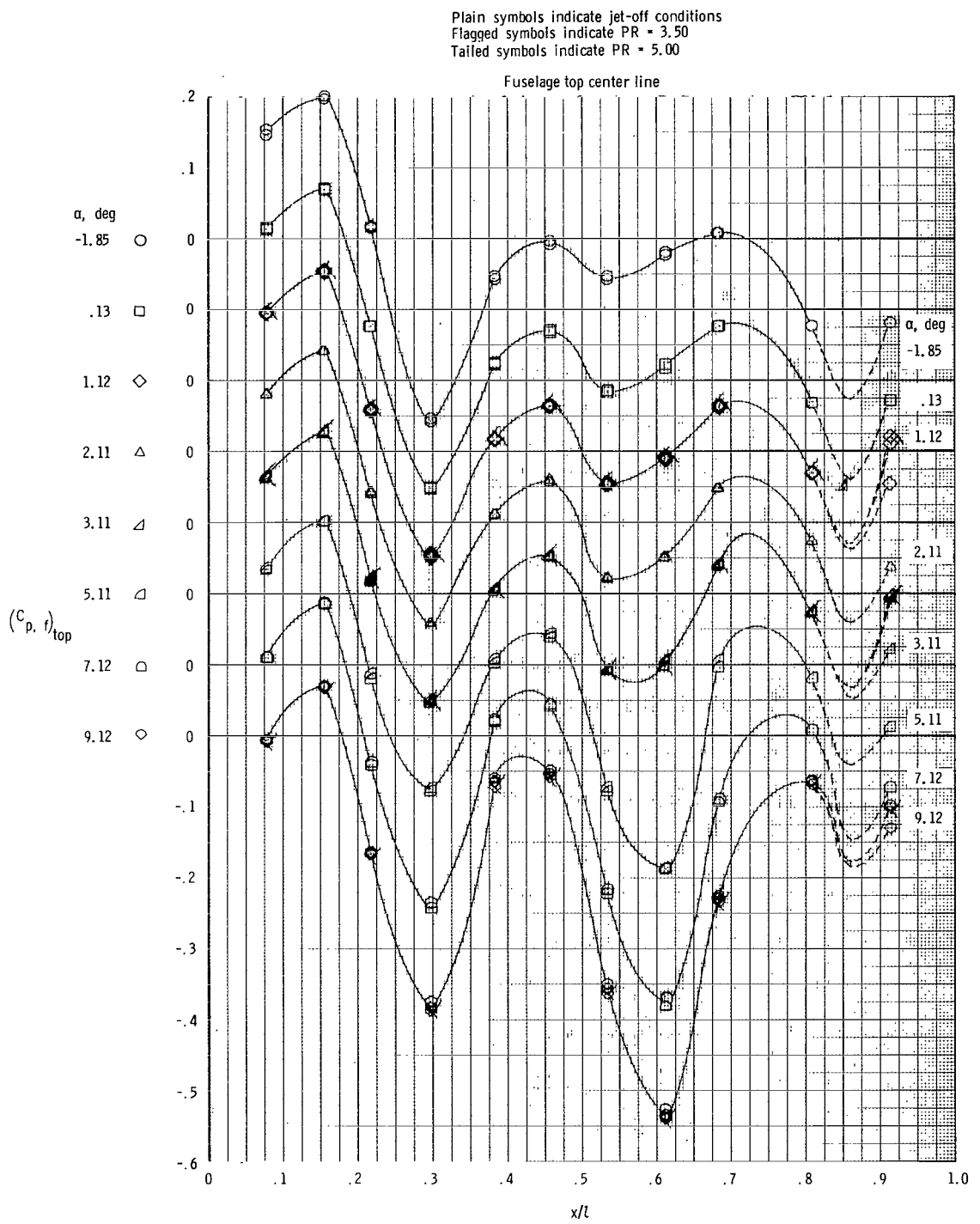


Figure 5.- Location of static-pressure orifices on nozzle boattail (left-hand nozzle only). View of left-hand, dry-power nozzle looking upstream. All linear dimensions are in centimeters.



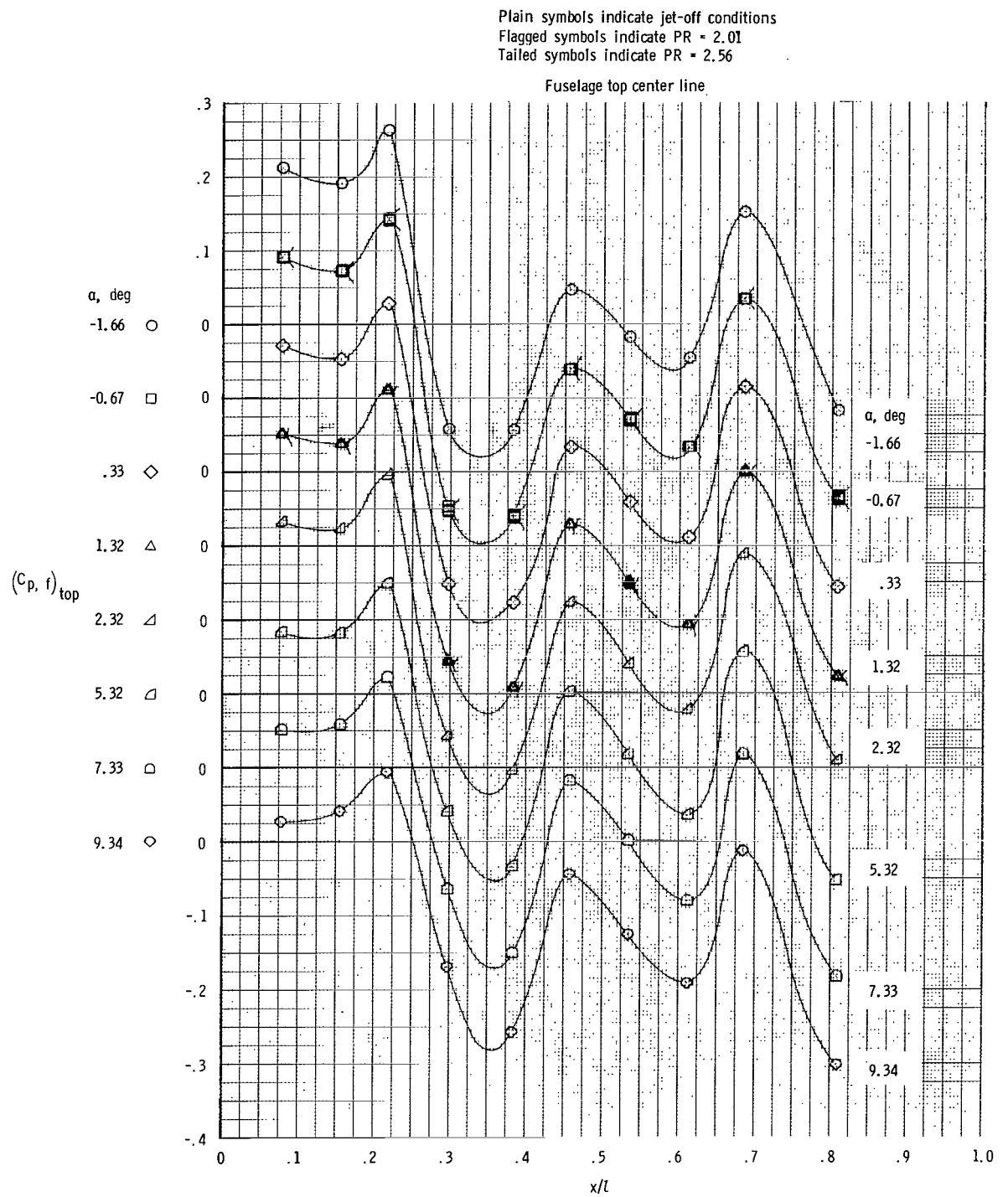
(a) $M = 0.600$; dry power.

Figure 6.- Static-pressure distributions on top of fuselage center line.
 $\delta_h = 0^\circ$.



(b) $M = 0.894$; dry power.

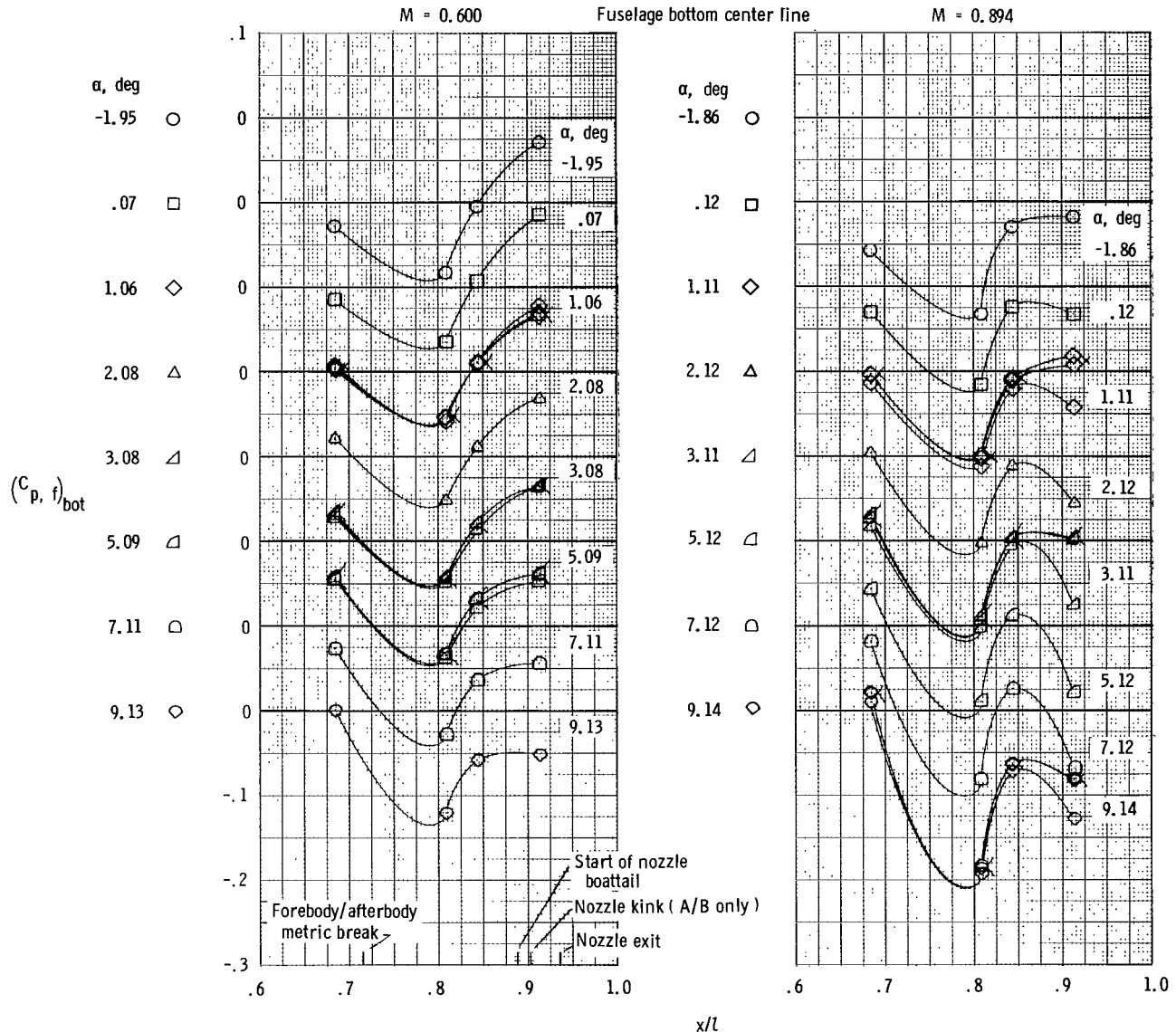
Figure 6.- Continued.



(c) $M = 1.190$; max. A/B power.

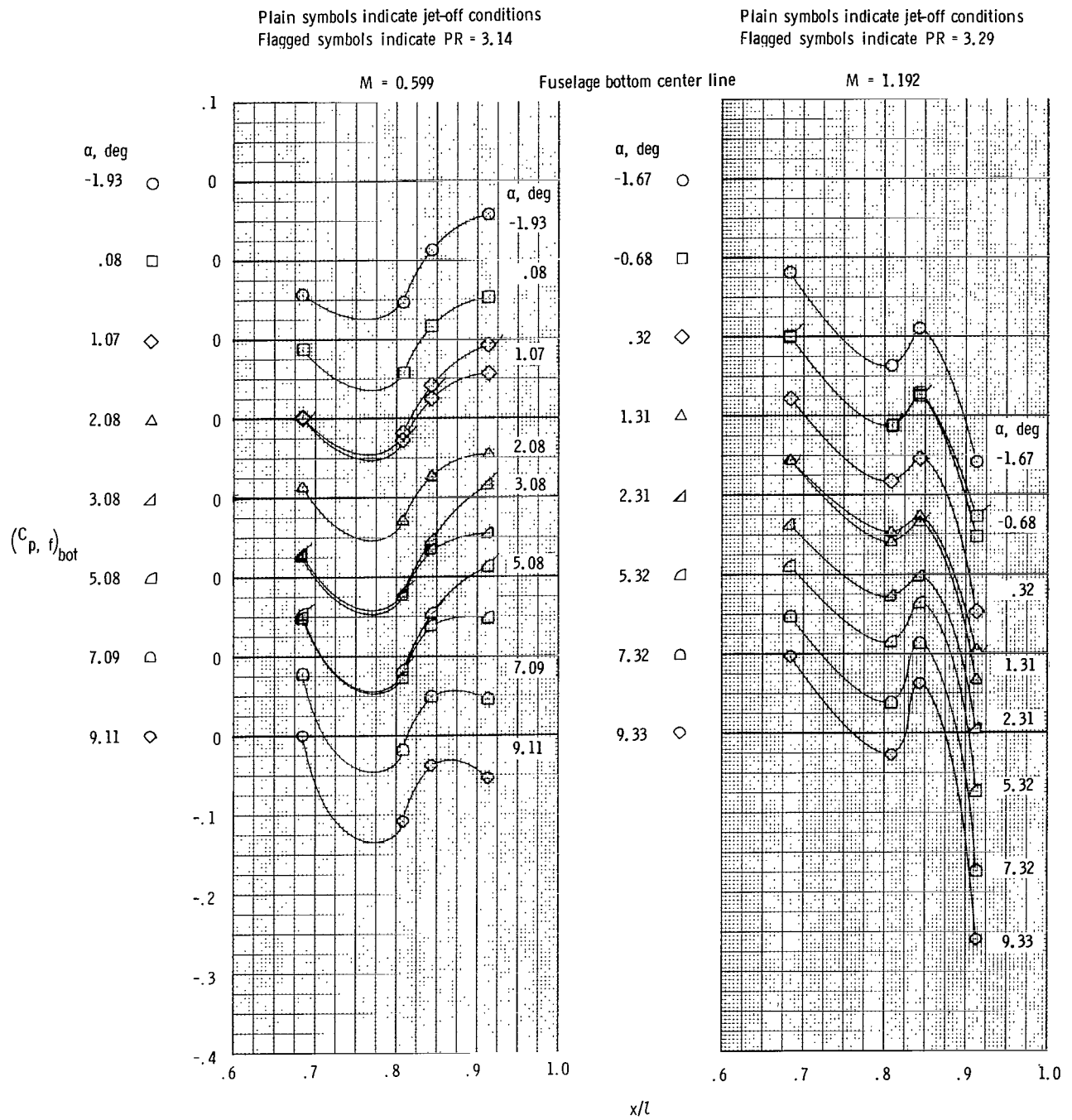
Figure 6.- Concluded.

Plain symbols indicate jet-off conditions
 Flagged symbols indicate PR = 2.70
 Tailed symbols indicate PR = 3.60



(a) Dry power.

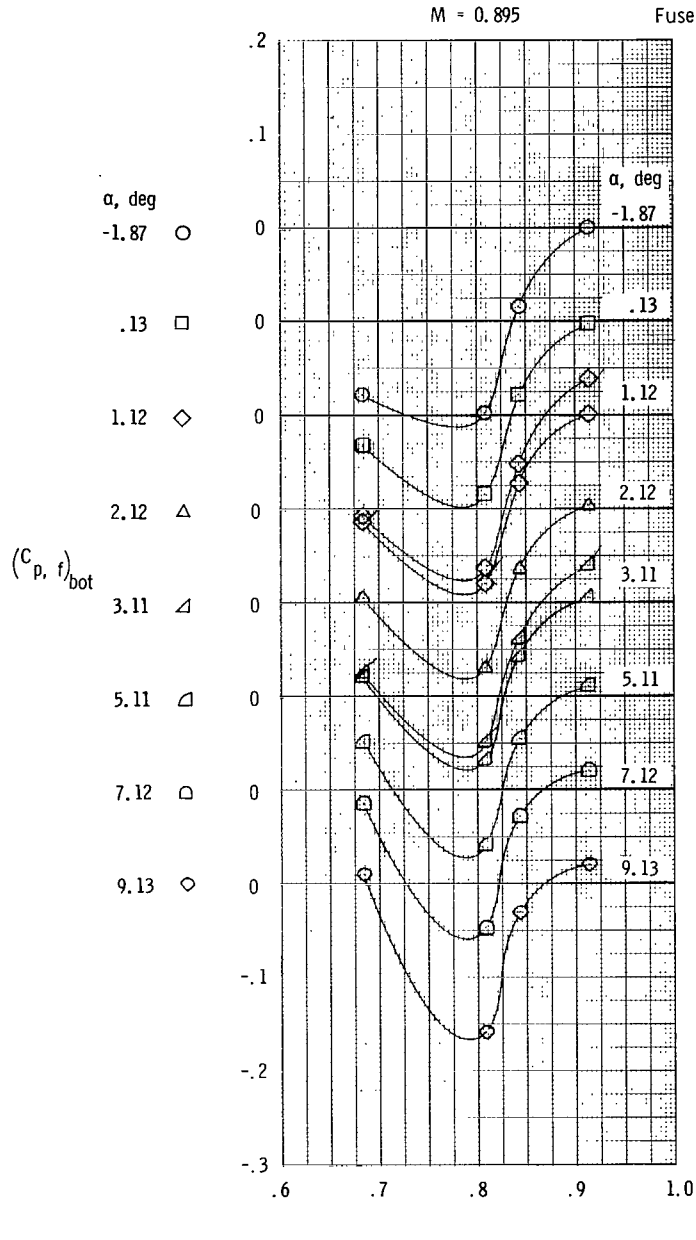
Figure 7.- Static-pressure distributions on bottom of fuselage engine interfairing at center line. $\delta_h = 0^\circ$.



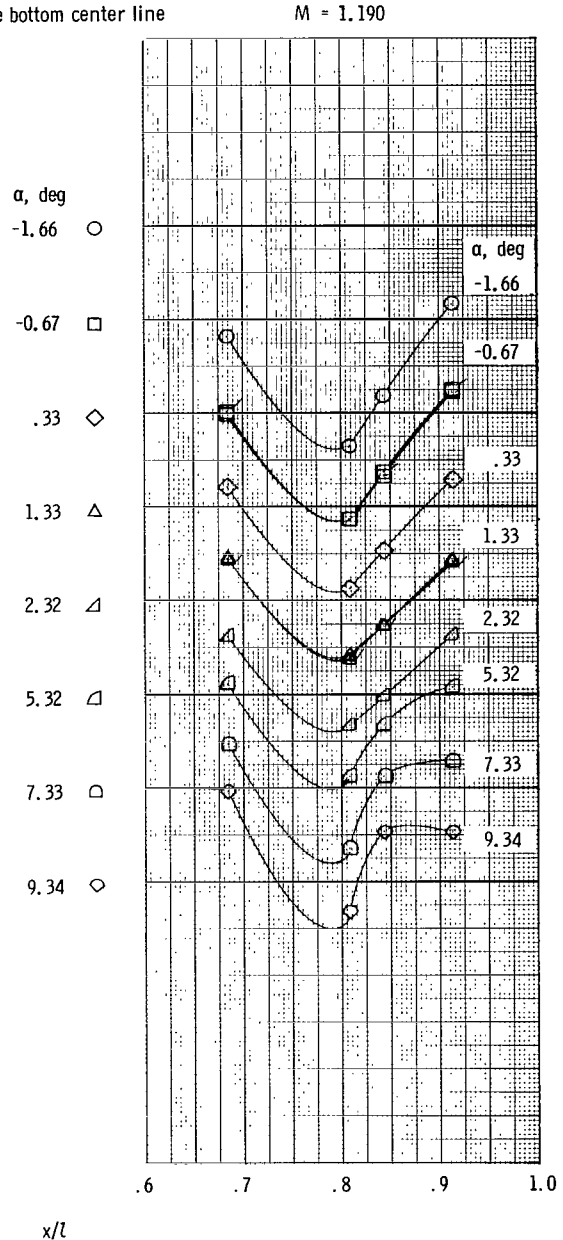
(b) Intermediate A/B power.

Figure 7.- Continued.

Plain symbols indicate jet-off conditions
 Flagged symbols indicate PR = 2.93



Plain symbols indicate jet-off conditions
 Flagged symbols indicate PR = 2.56



(c) Max. A/B power.

Figure 7.- Concluded.

Plain symbols indicate jet-off conditions
 Flagged symbols indicate PR = 2.70

Plain symbols indicate jet-off conditions
 Flagged symbols indicate PR = 3.50

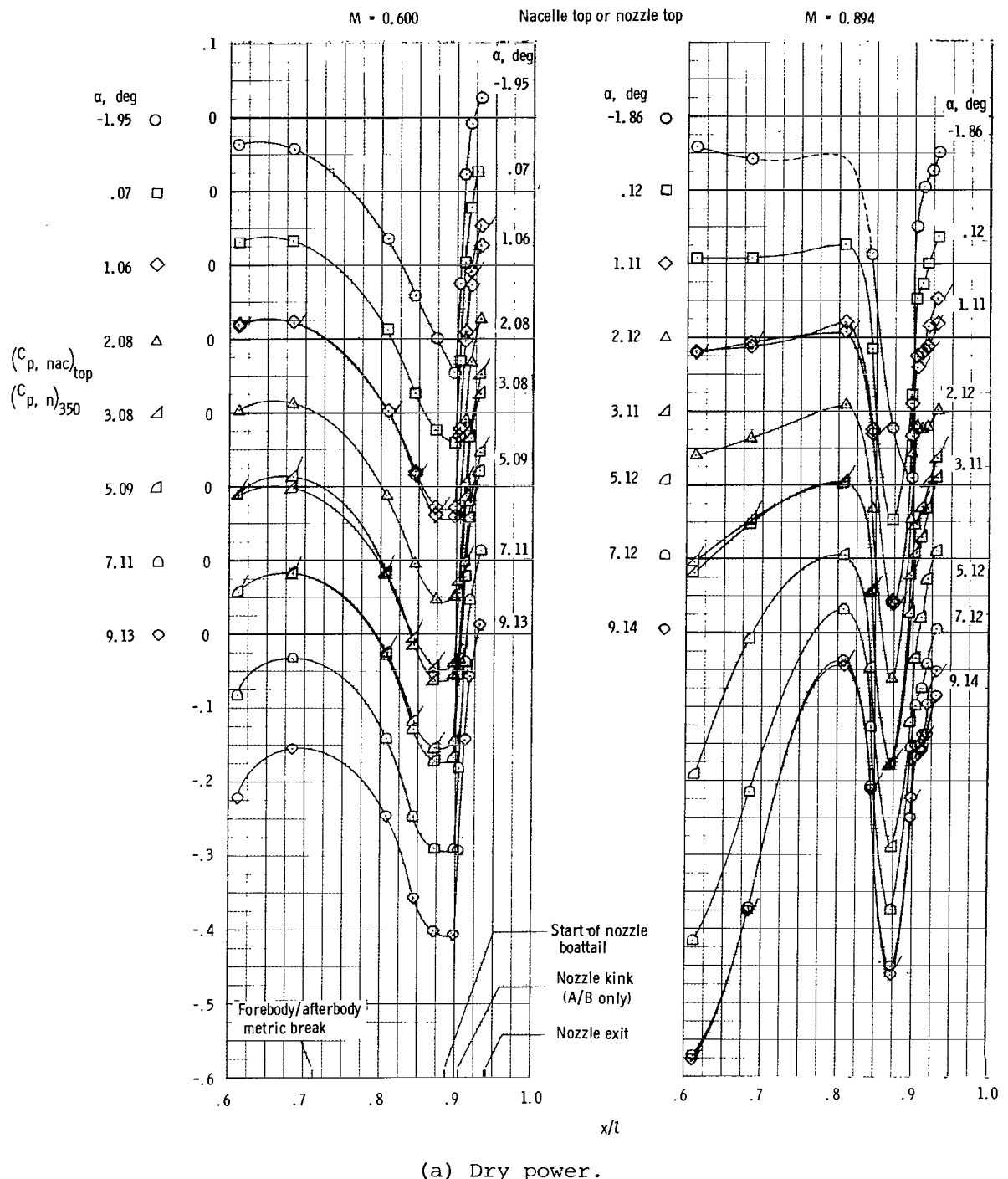
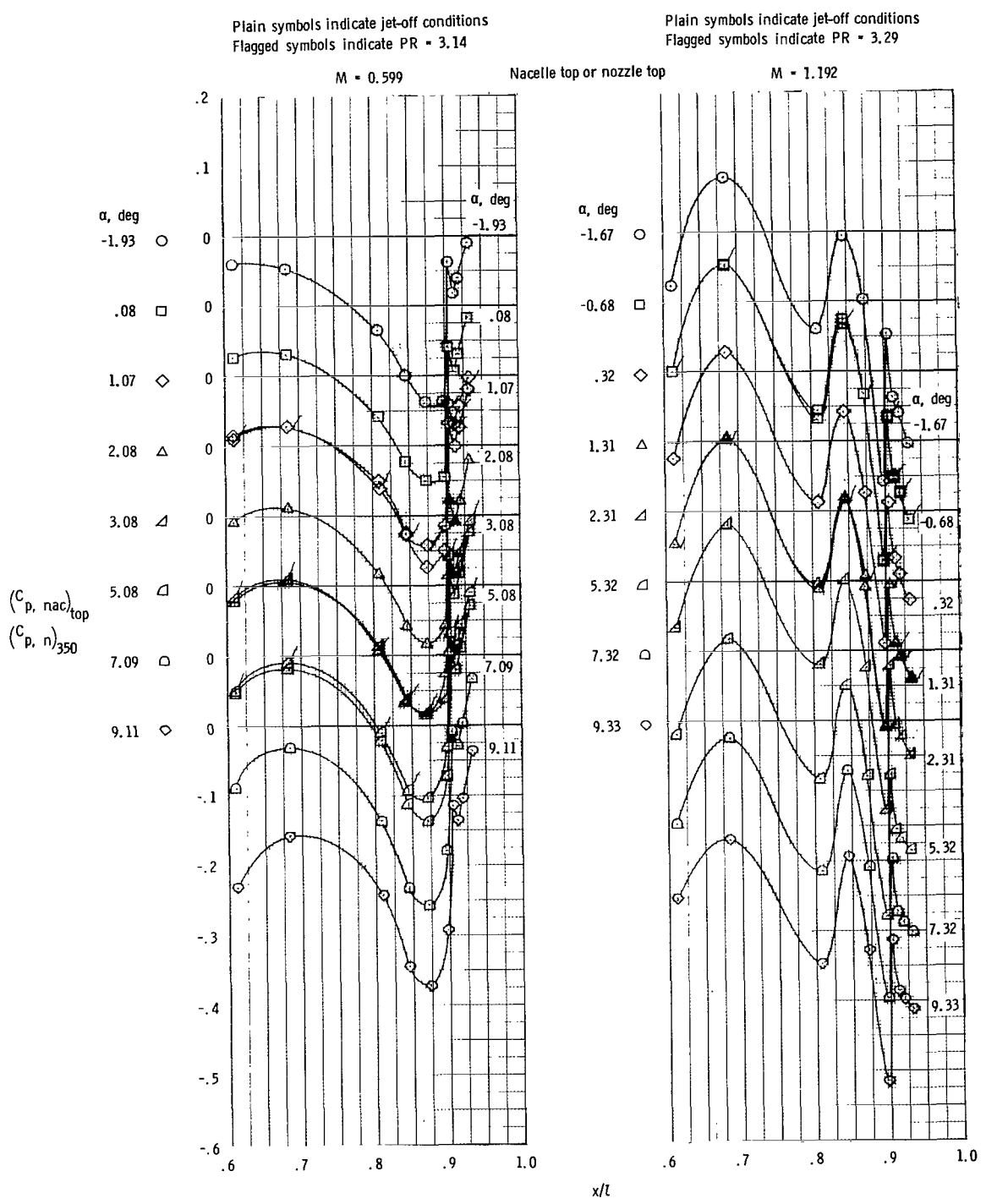
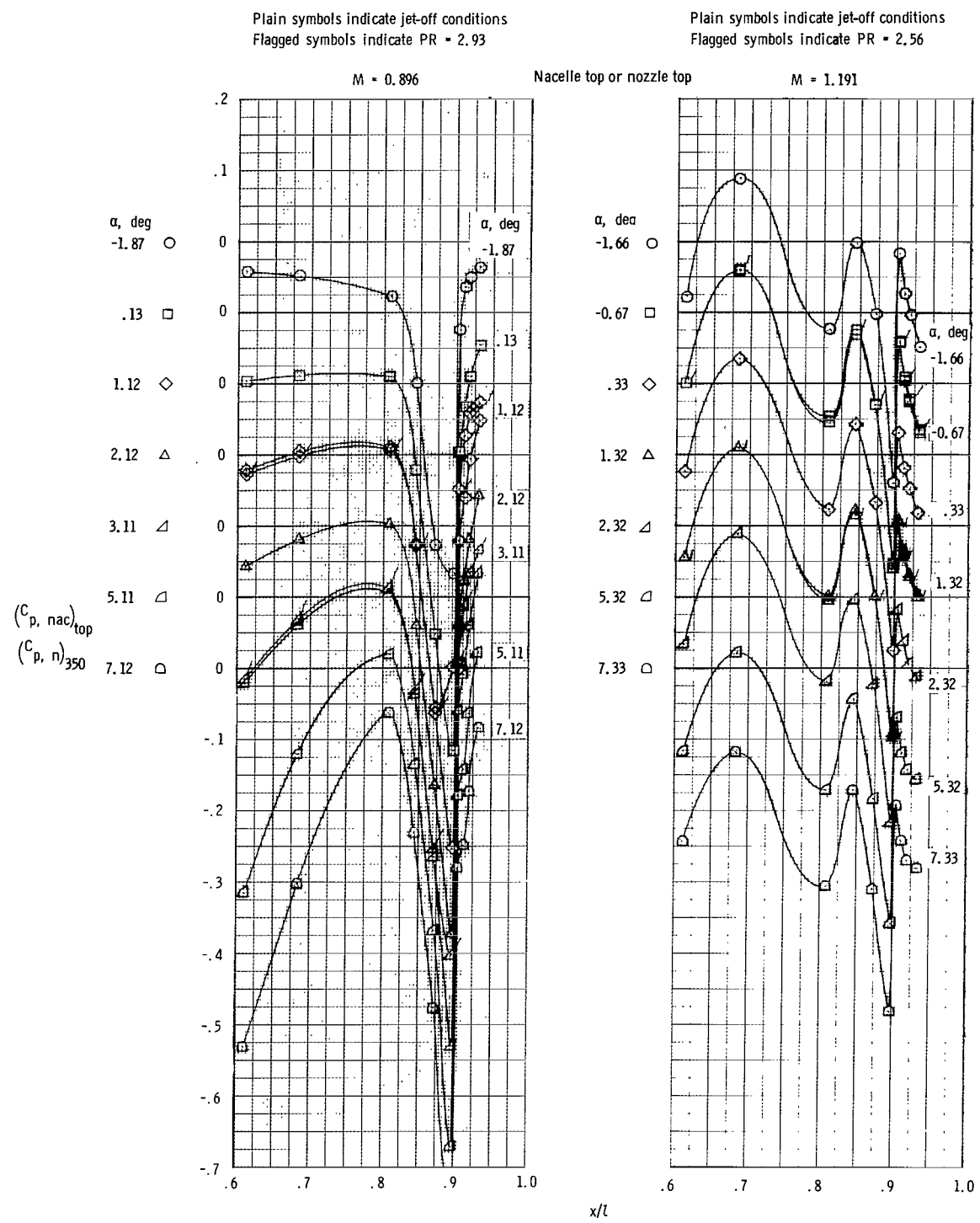


Figure 8.- Static-pressure distributions on top of nacelle and nozzle. $\delta_h = 0^\circ$.



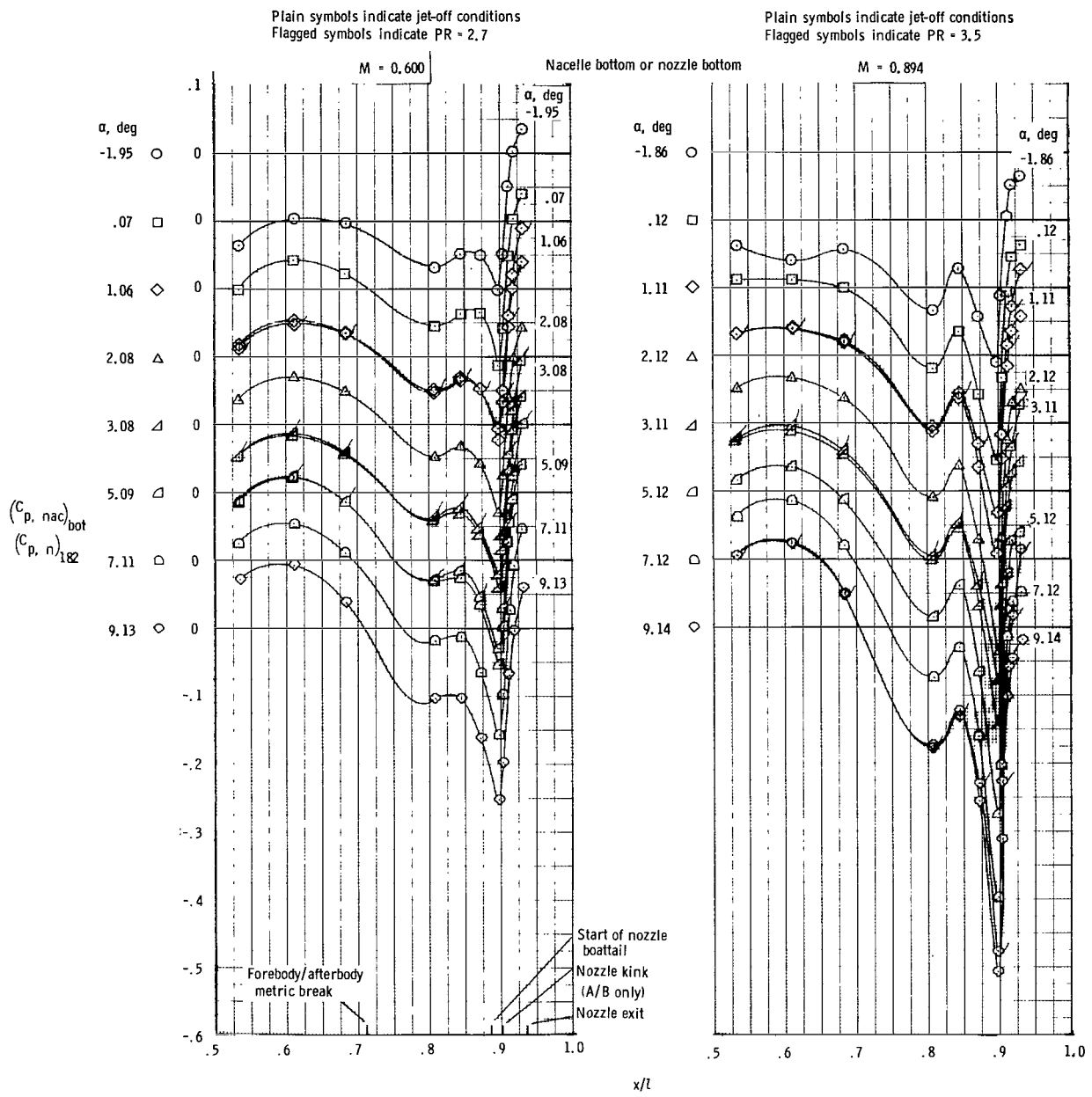
(b) Intermediate A/B power.

Figure 8.- Continued.



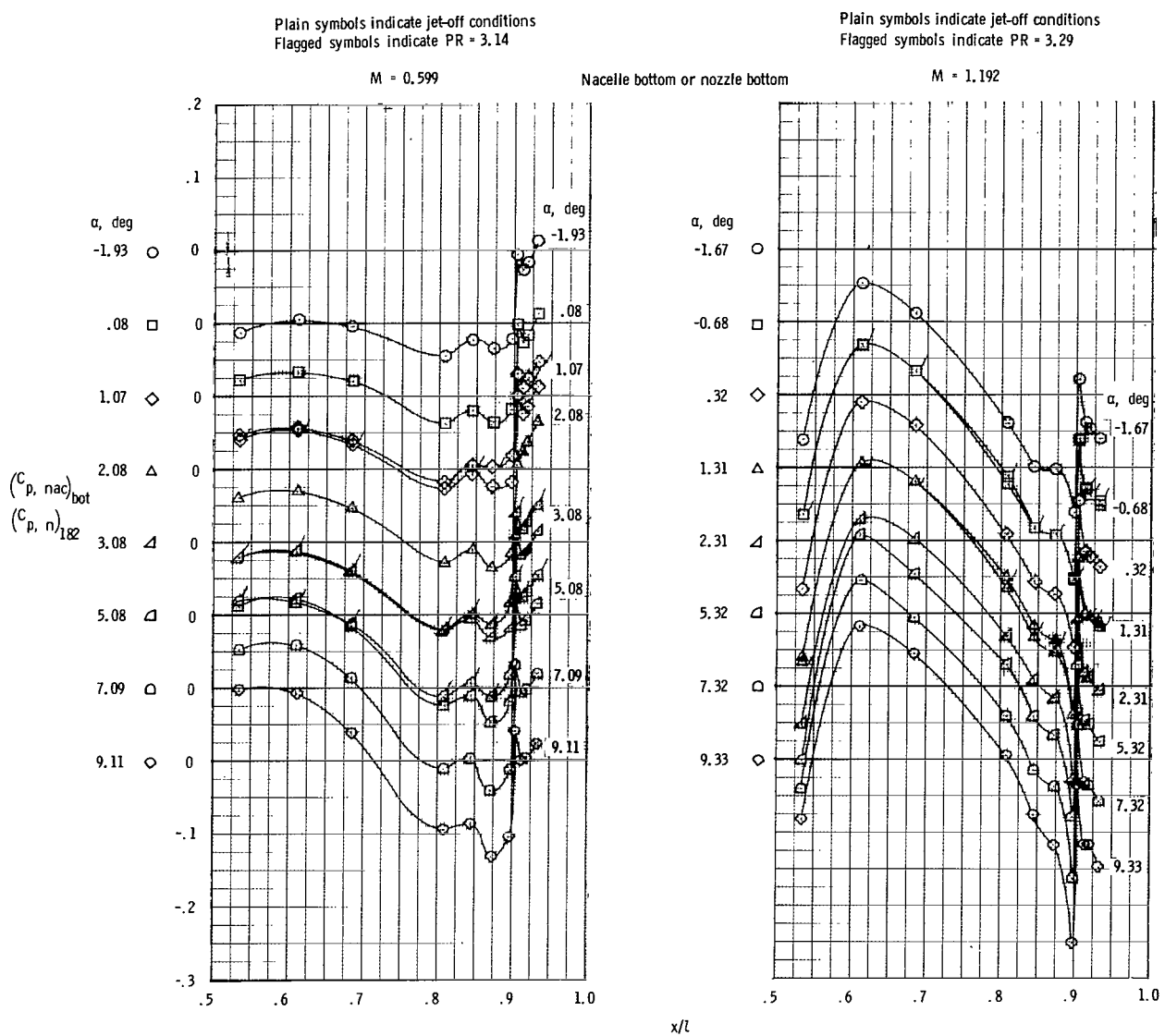
(c) Max. A/B power.

Figure 8.- Concluded.



(a) Dry power.

Figure 9.- Static-pressure distributions on bottom of nacelle and nozzle.
 $\delta_h = 0^\circ$.

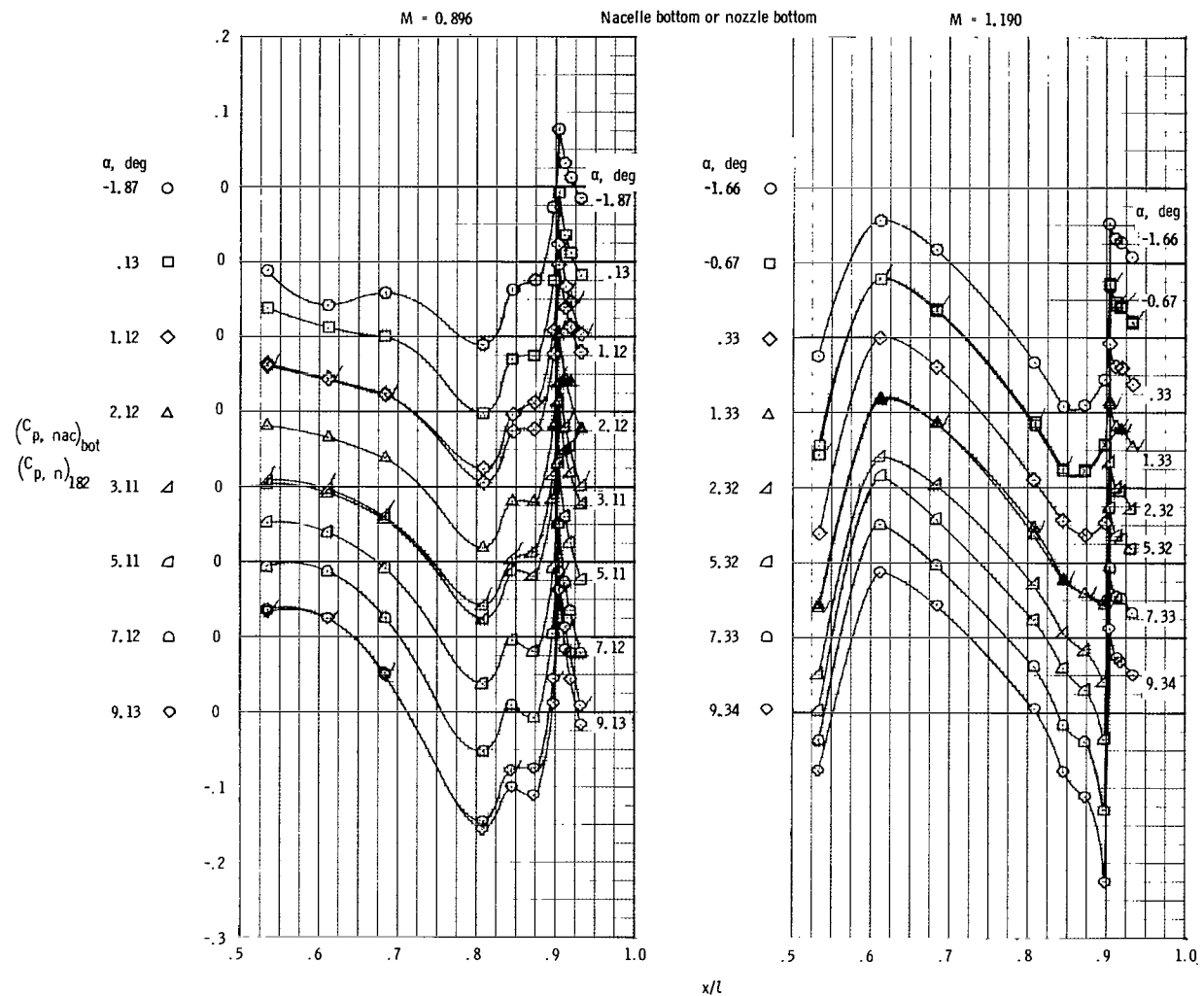


(b) Intermediate A/B power.

Figure 9.- Continued.

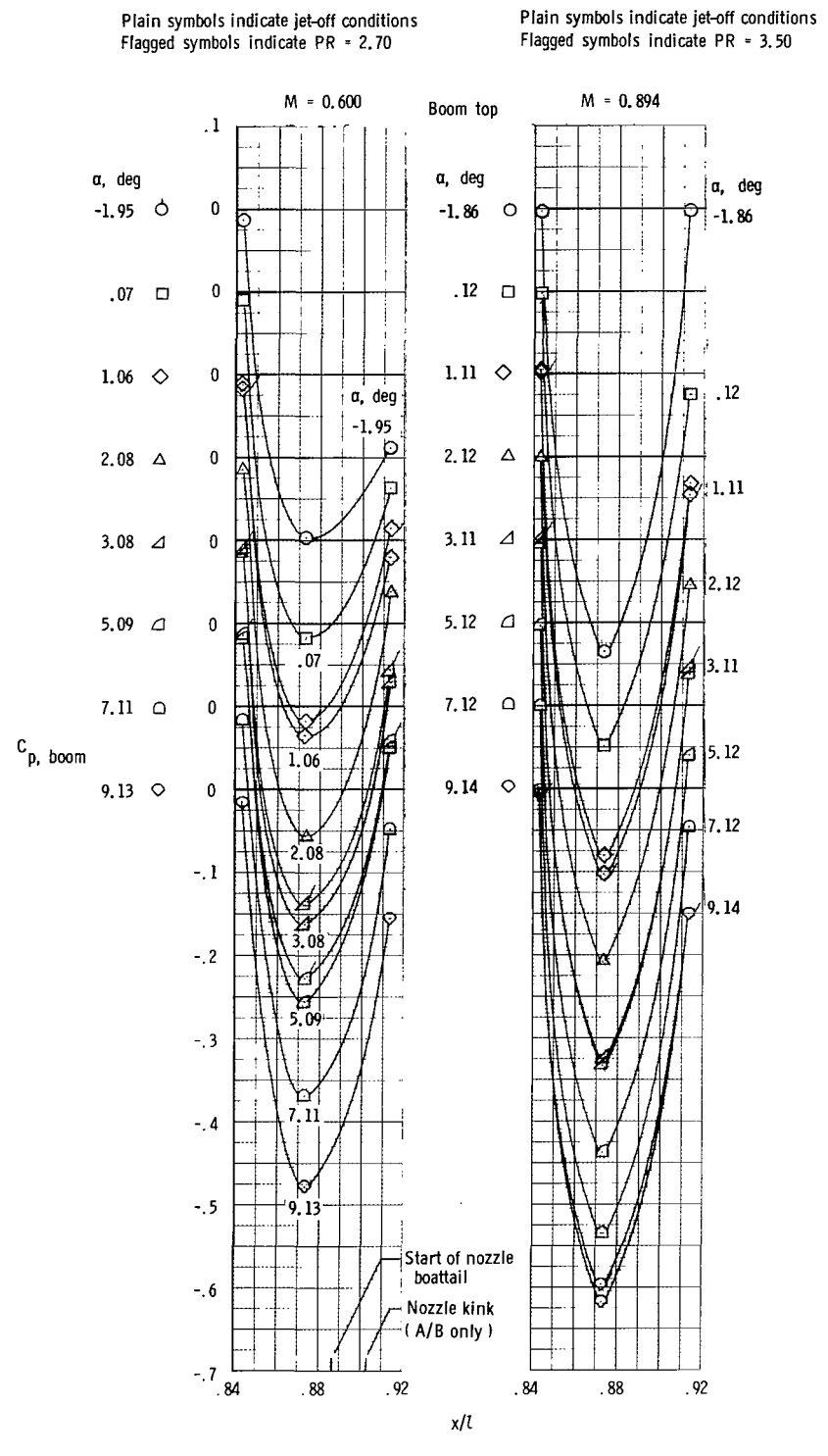
Plain symbols indicate jet-off conditions
Flagged symbols indicate PR = 2.93

Plain symbols indicate jet-off conditions
Flagged symbols indicate PR = 2.56



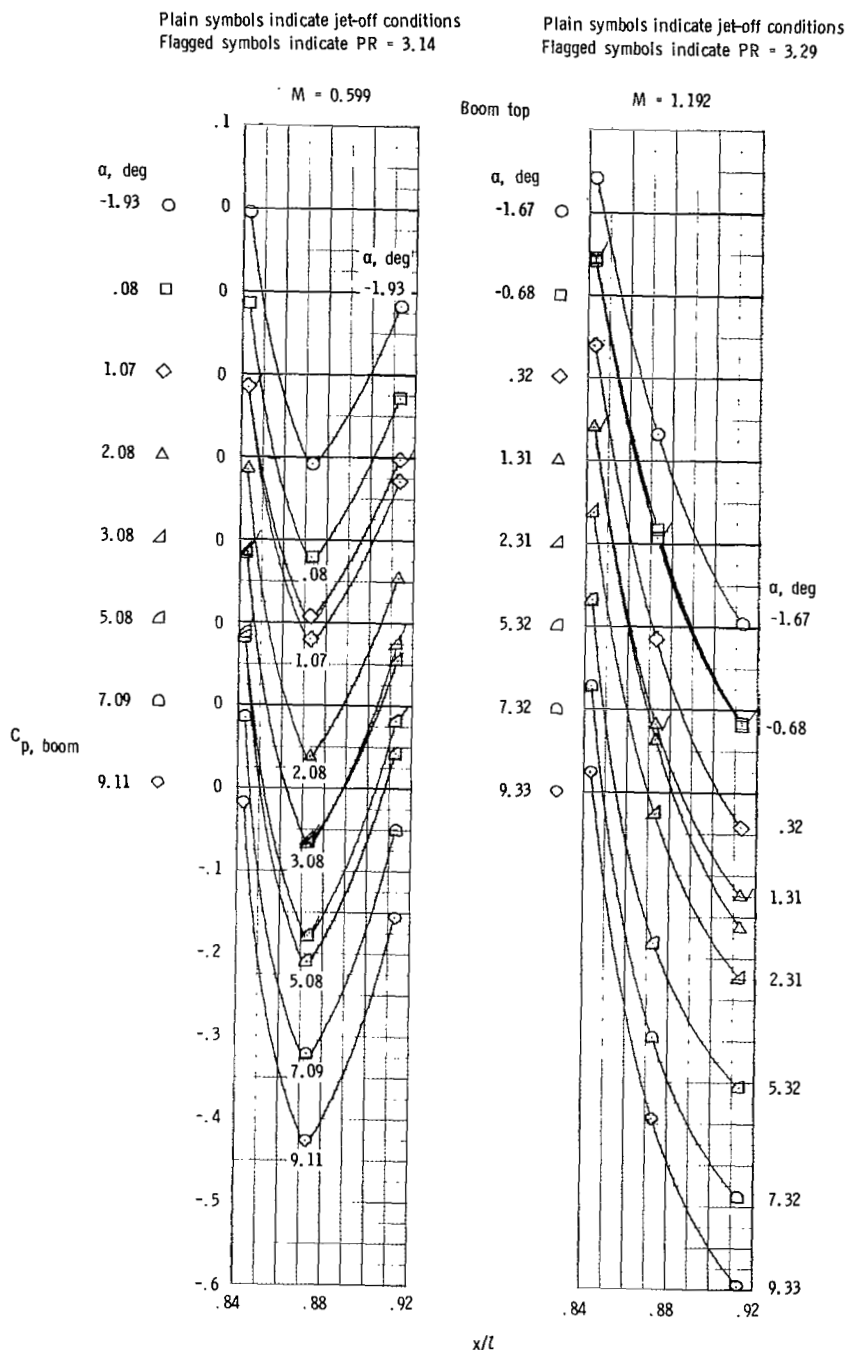
(c) Max. A/B power.

Figure 9.- Concluded.



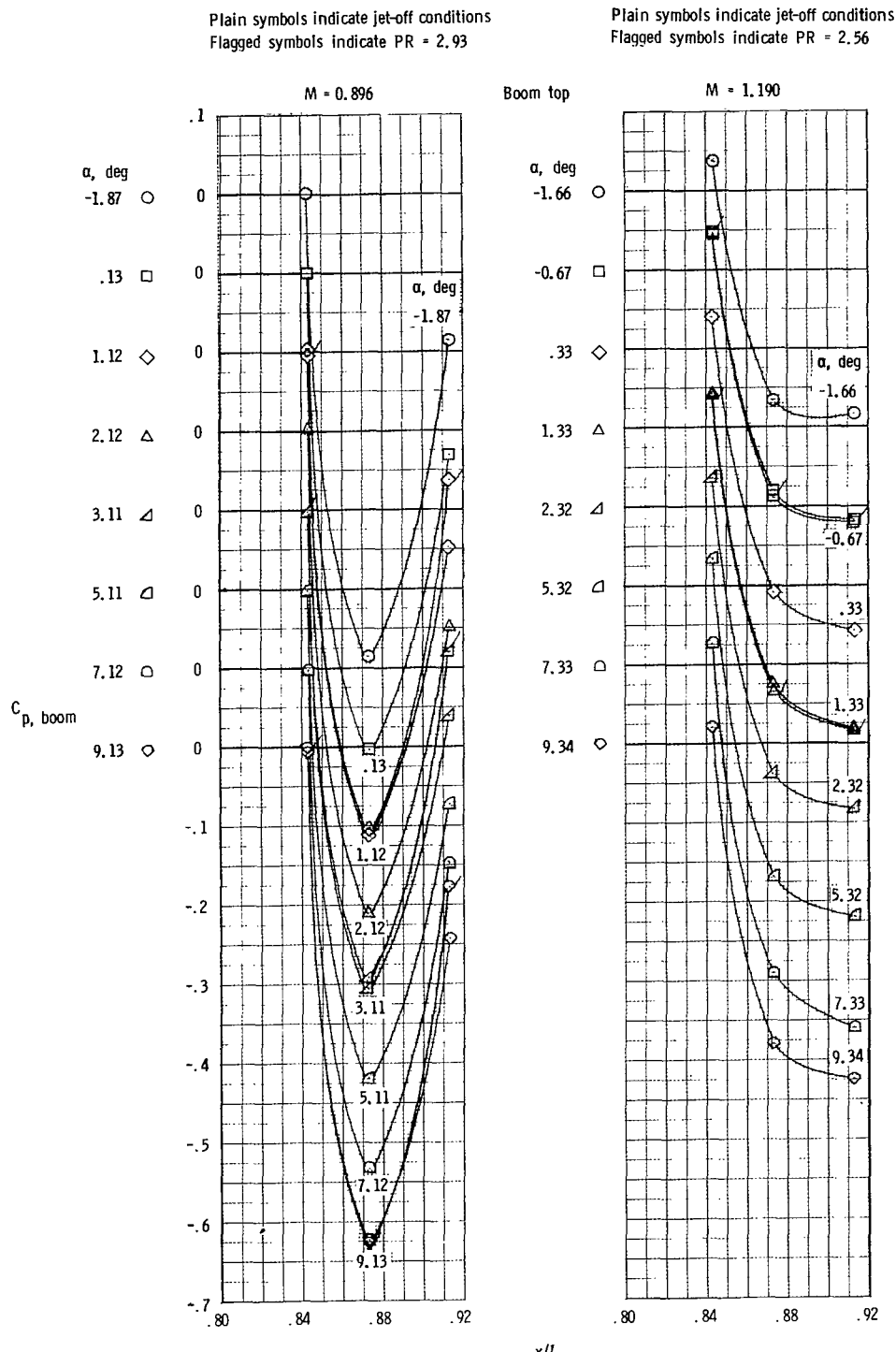
(a) Dry power.

Figure 10.- Static-pressure distribution on top of horizontal-tail boom. $\delta_h = 0^\circ$.



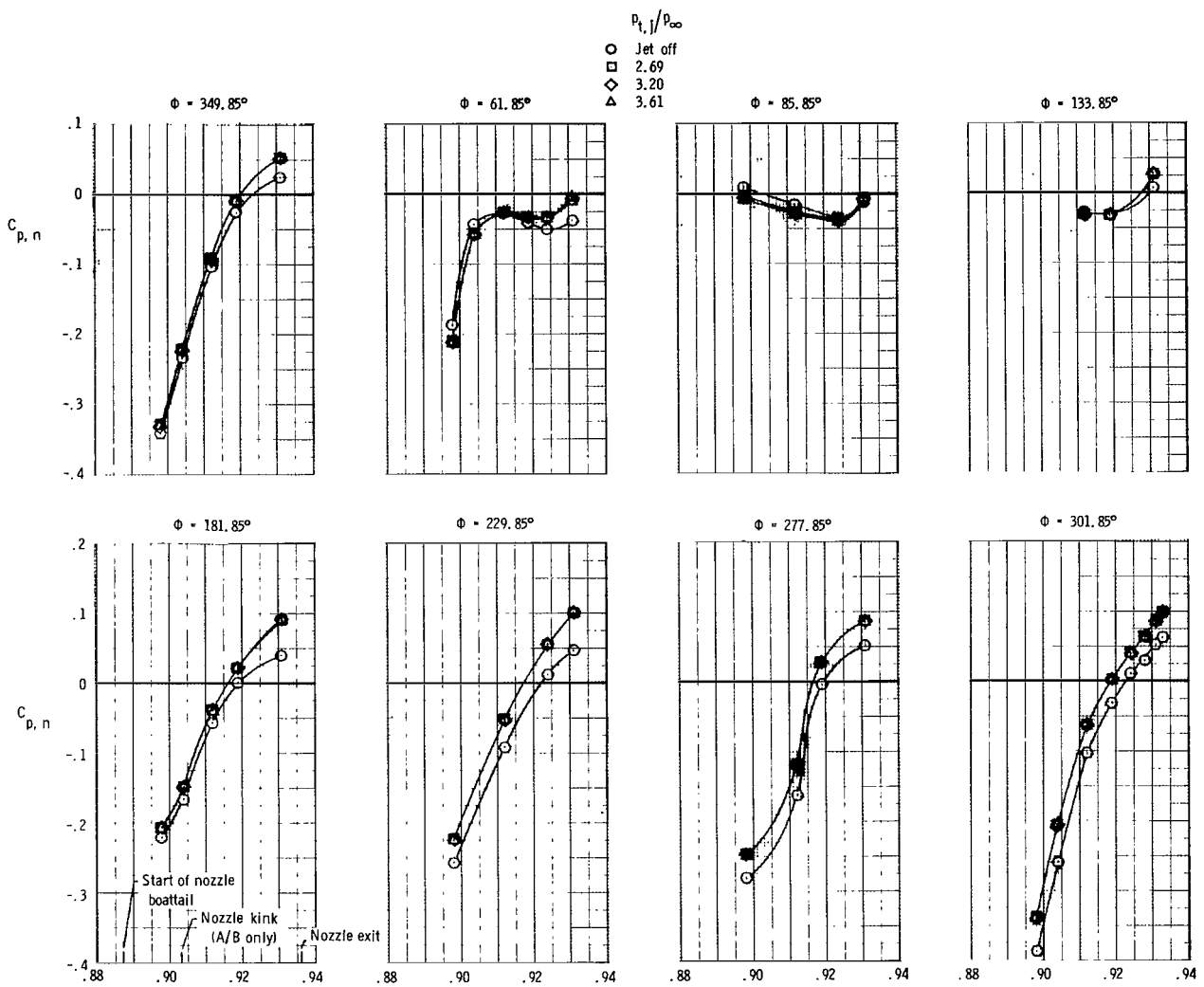
(b) Intermediate A/B power.

Figure 10.- Continued.



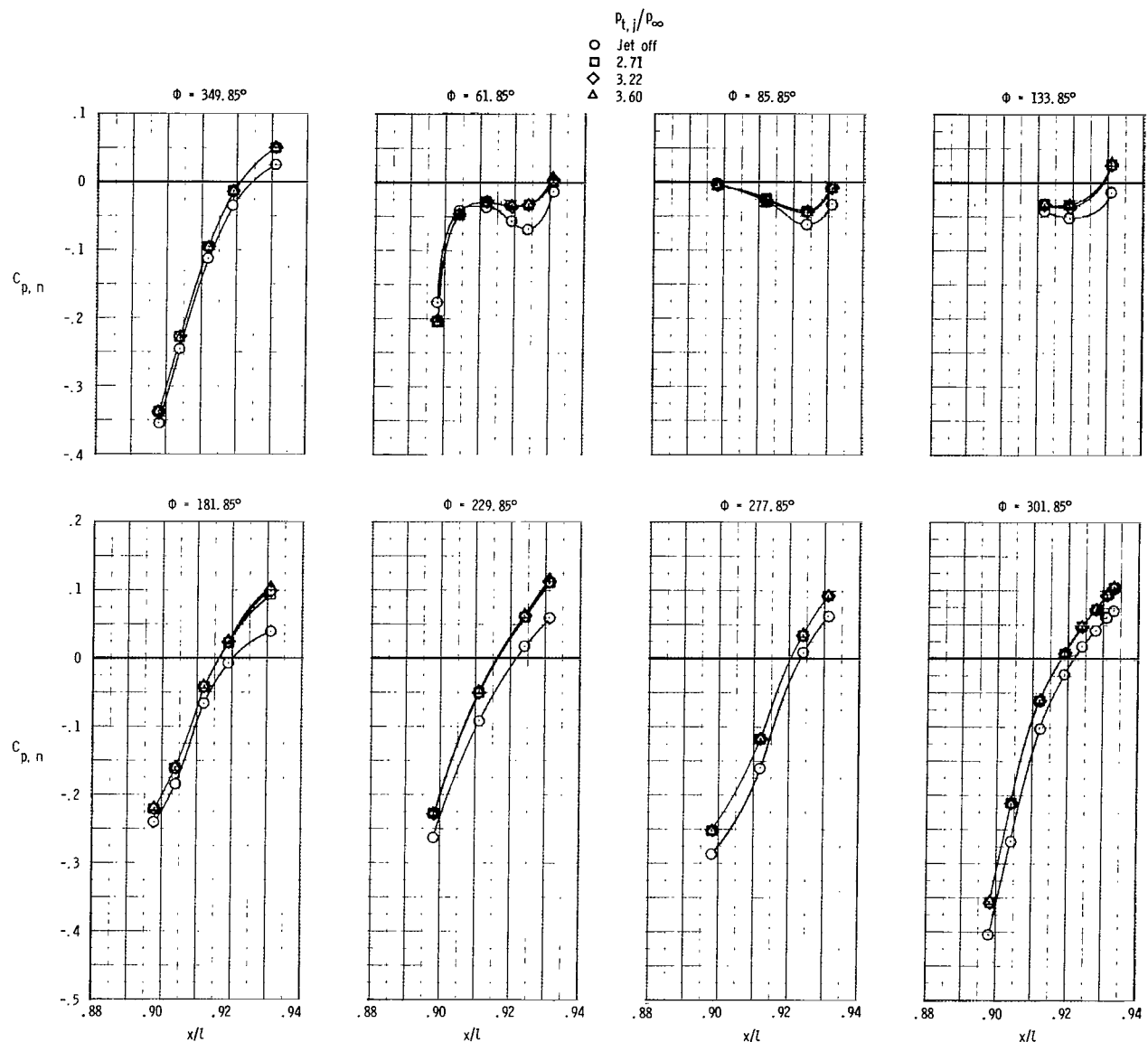
(c) Max. A/B power.

Figure 10.- Concluded.



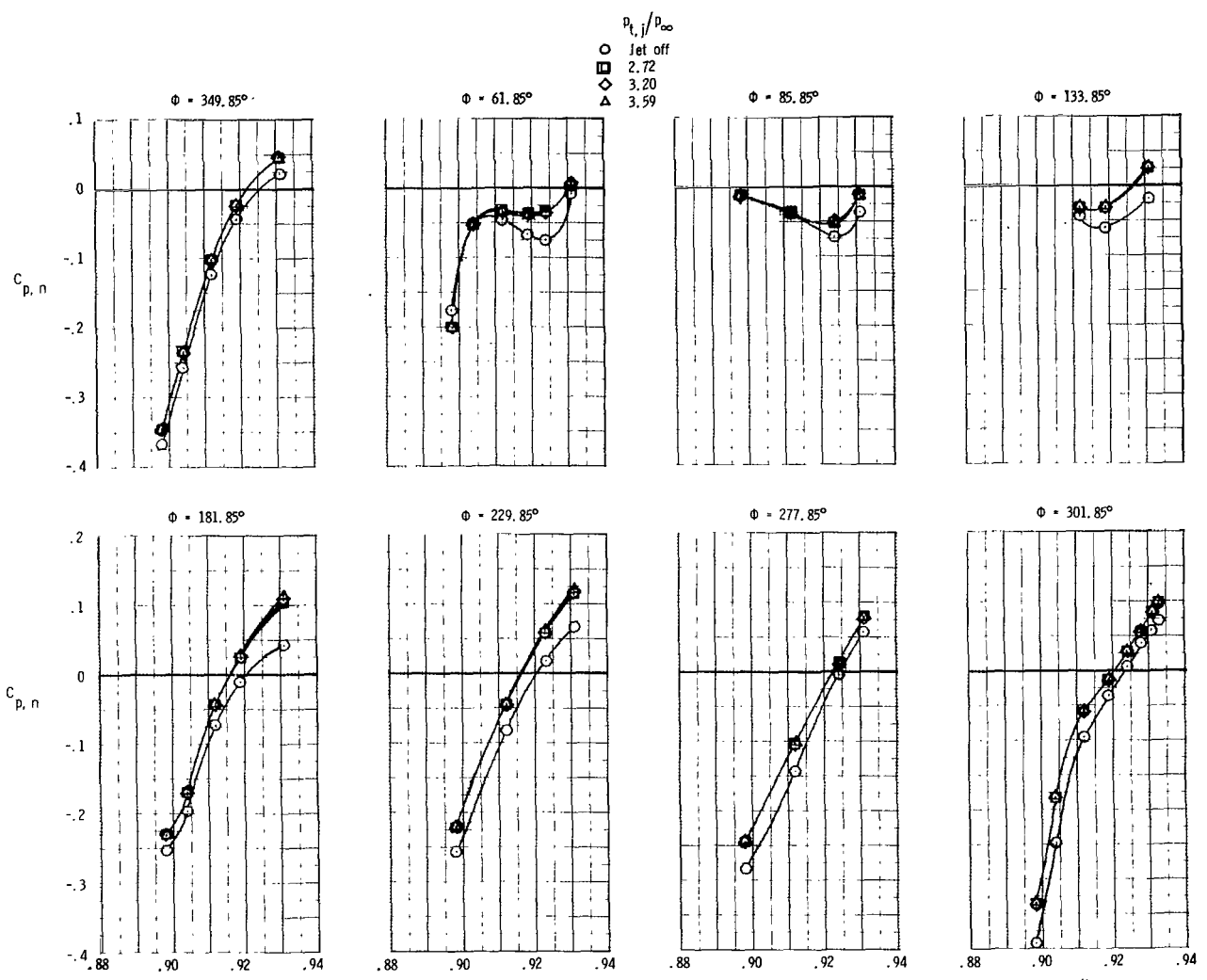
(a) $M = 0.601; \alpha = 1.06^\circ$.

Figure 11.- Static-pressure distributions on dry-power nozzle at several Mach number and angle-of-attack combinations for $\delta_h = 0^\circ$.



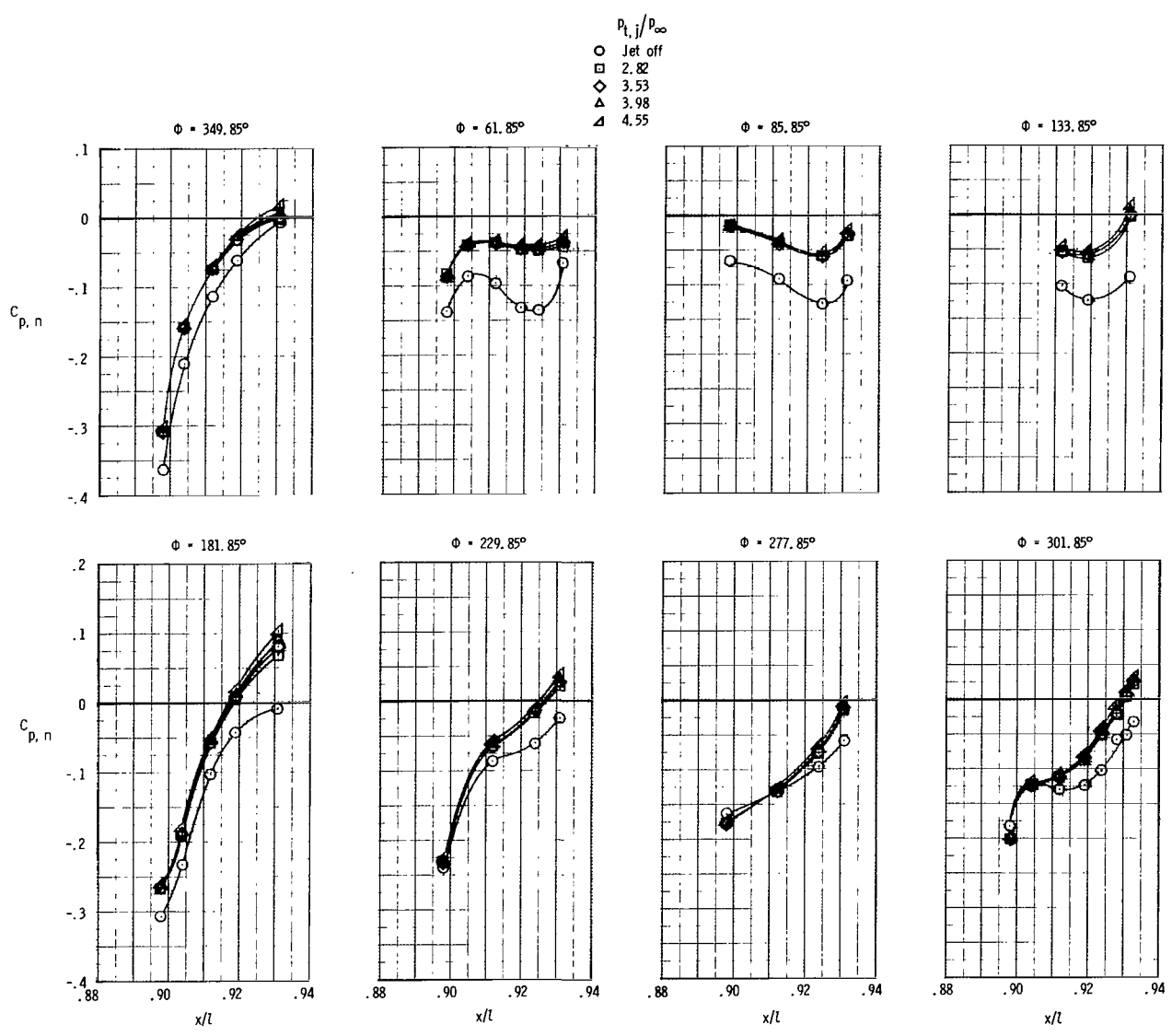
(b) $M = 0.600; \alpha = 3.08^\circ$.

Figure 11.- Continued.



(c) $M = 0.600; \alpha = 5.09^\circ$.

Figure 11.- Continued.



(d) $M = 0.800$; $\alpha = 3.09^\circ$.

Figure 11.- Continued.

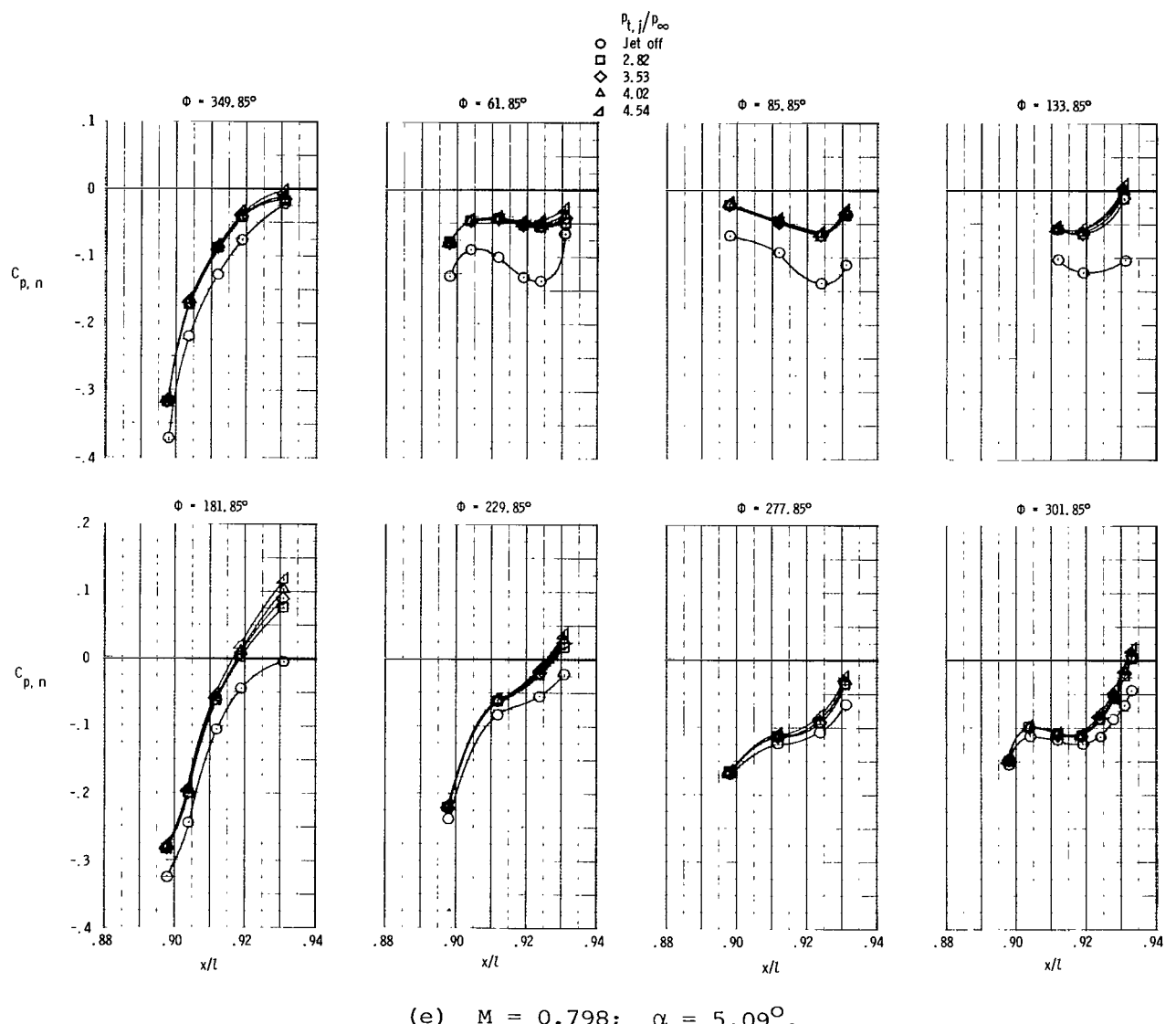
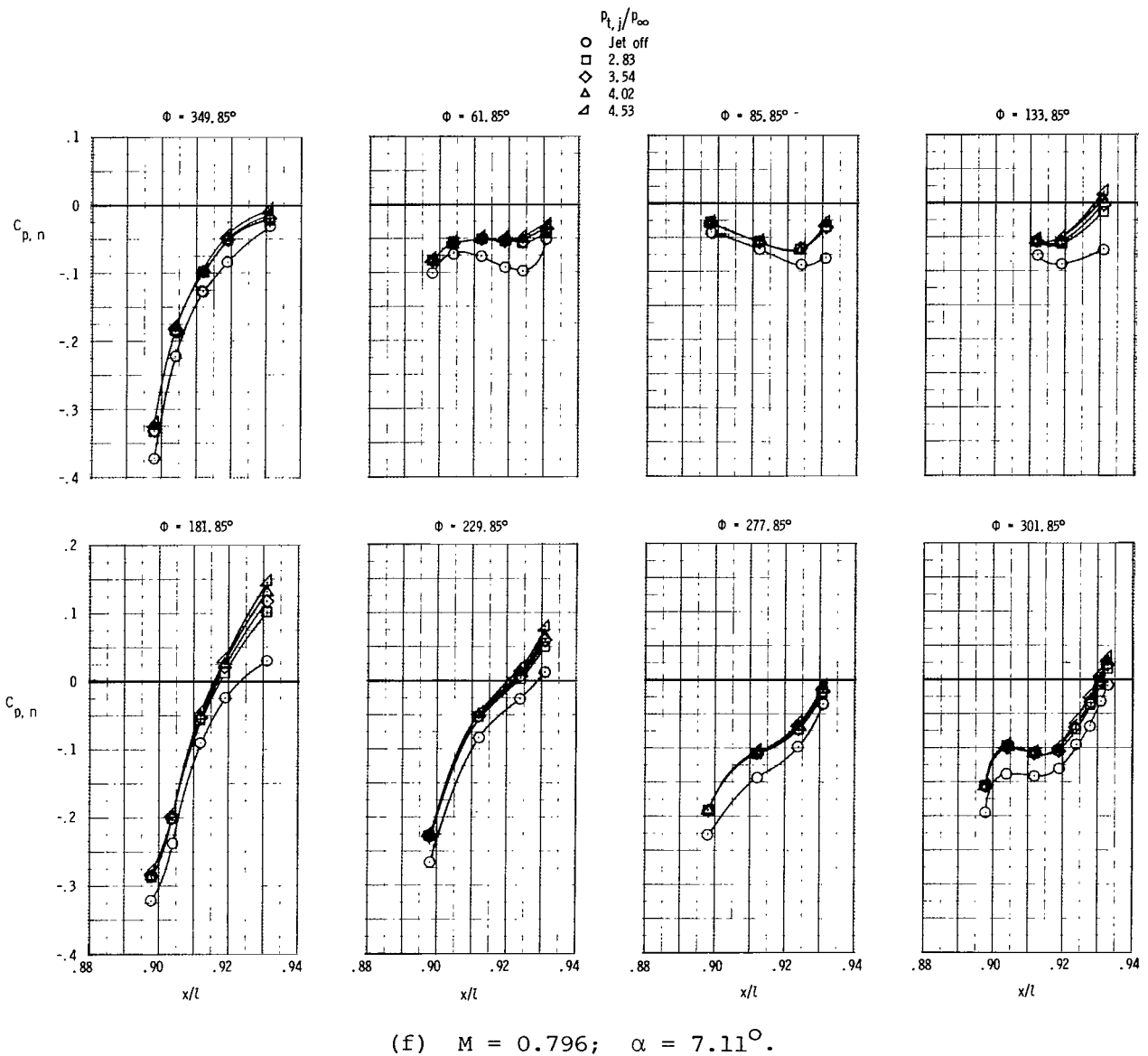
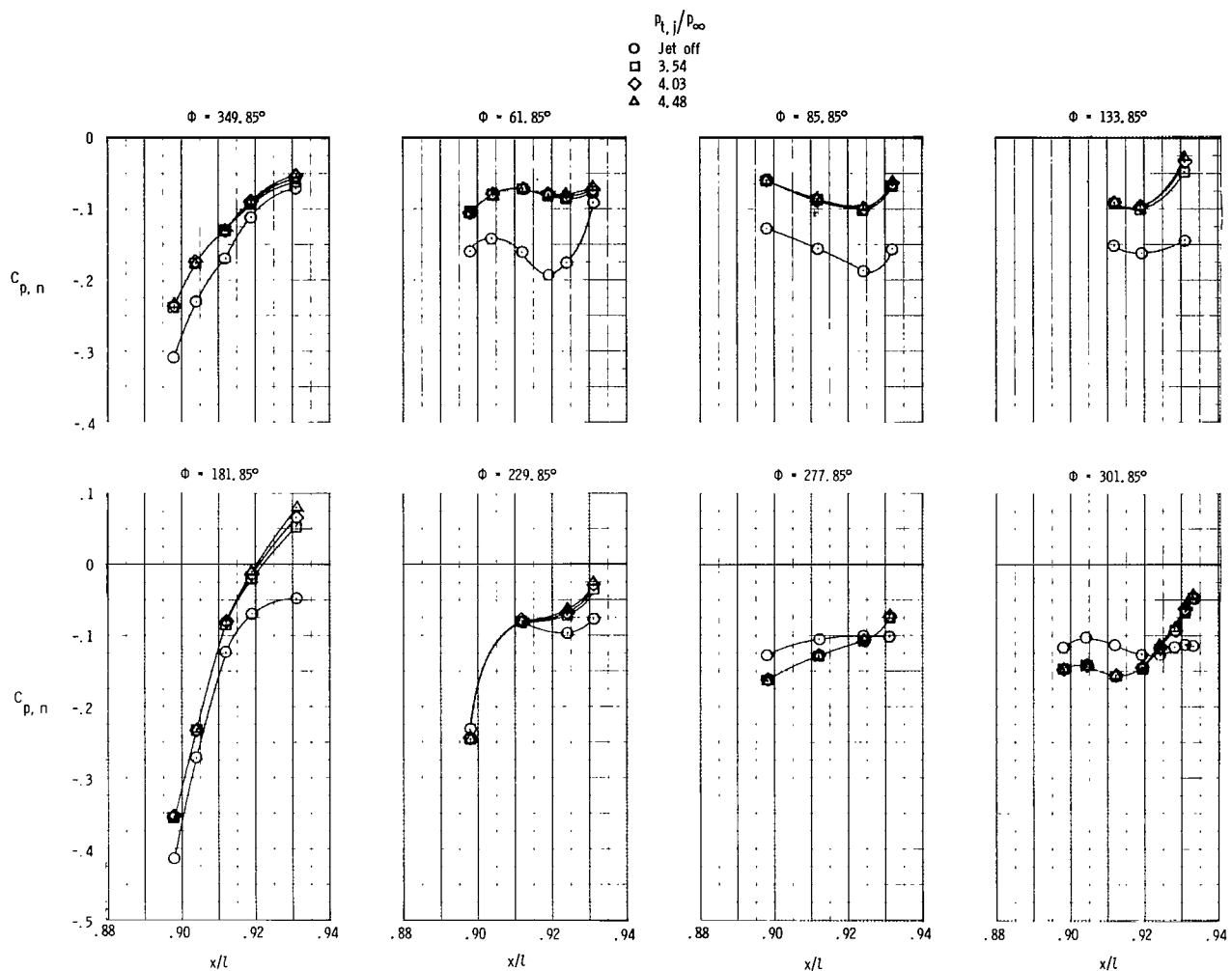


Figure 11.- Continued.



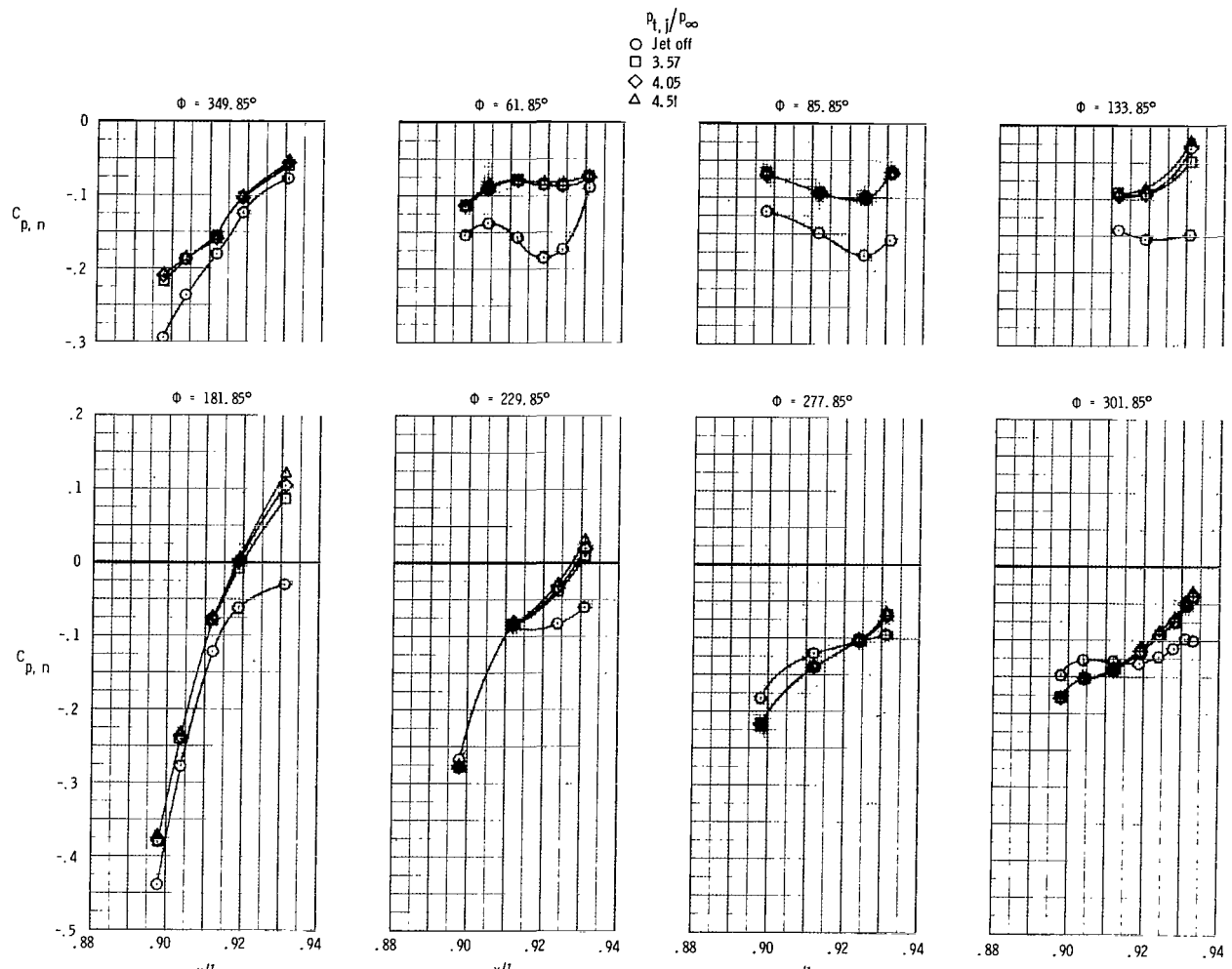
(f) $M = 0.796$; $\alpha = 7.11^\circ$.

Figure 11.- Continued.



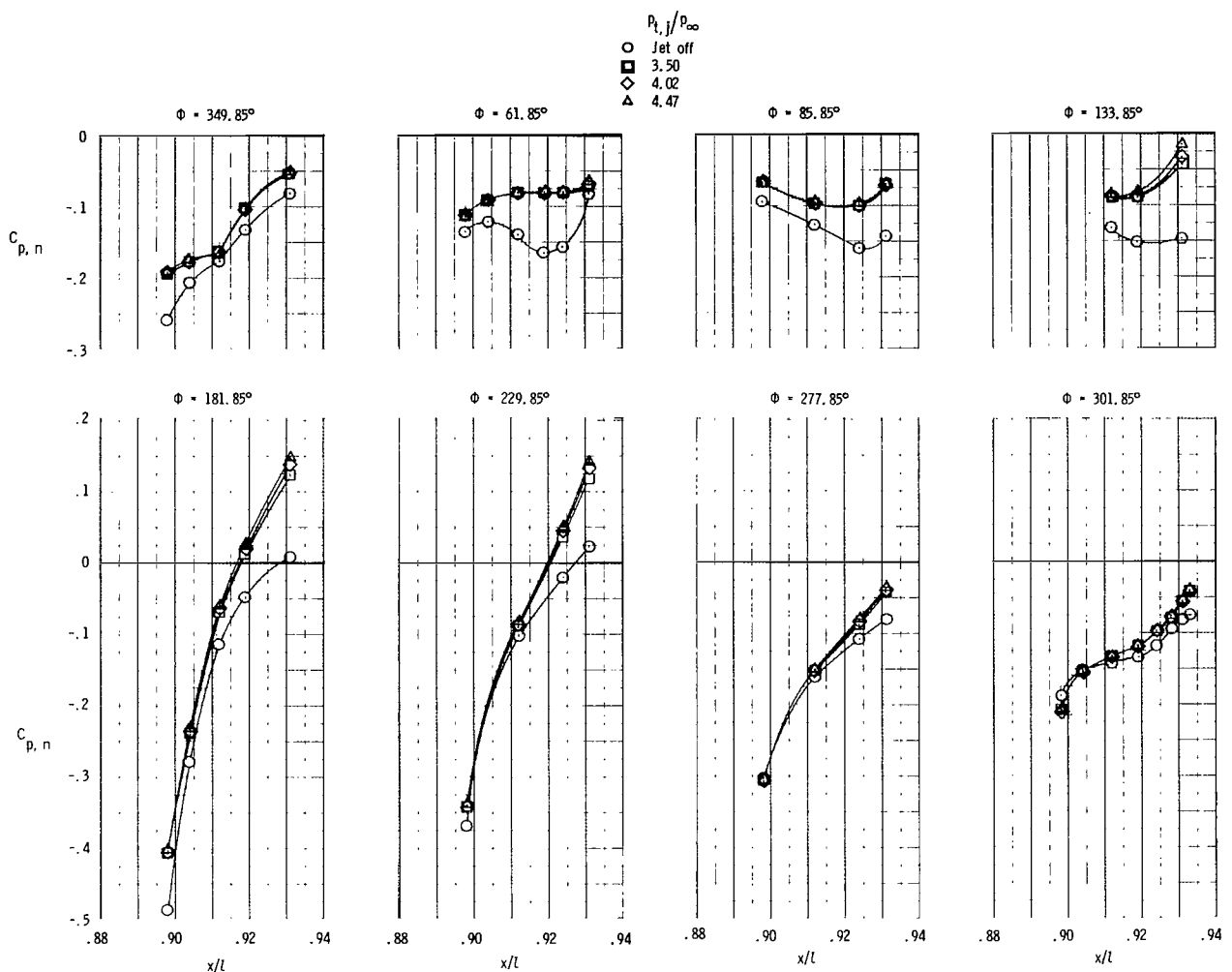
(g) $M = 0.870; \alpha = 5.10^\circ$.

Figure 11.- Continued.



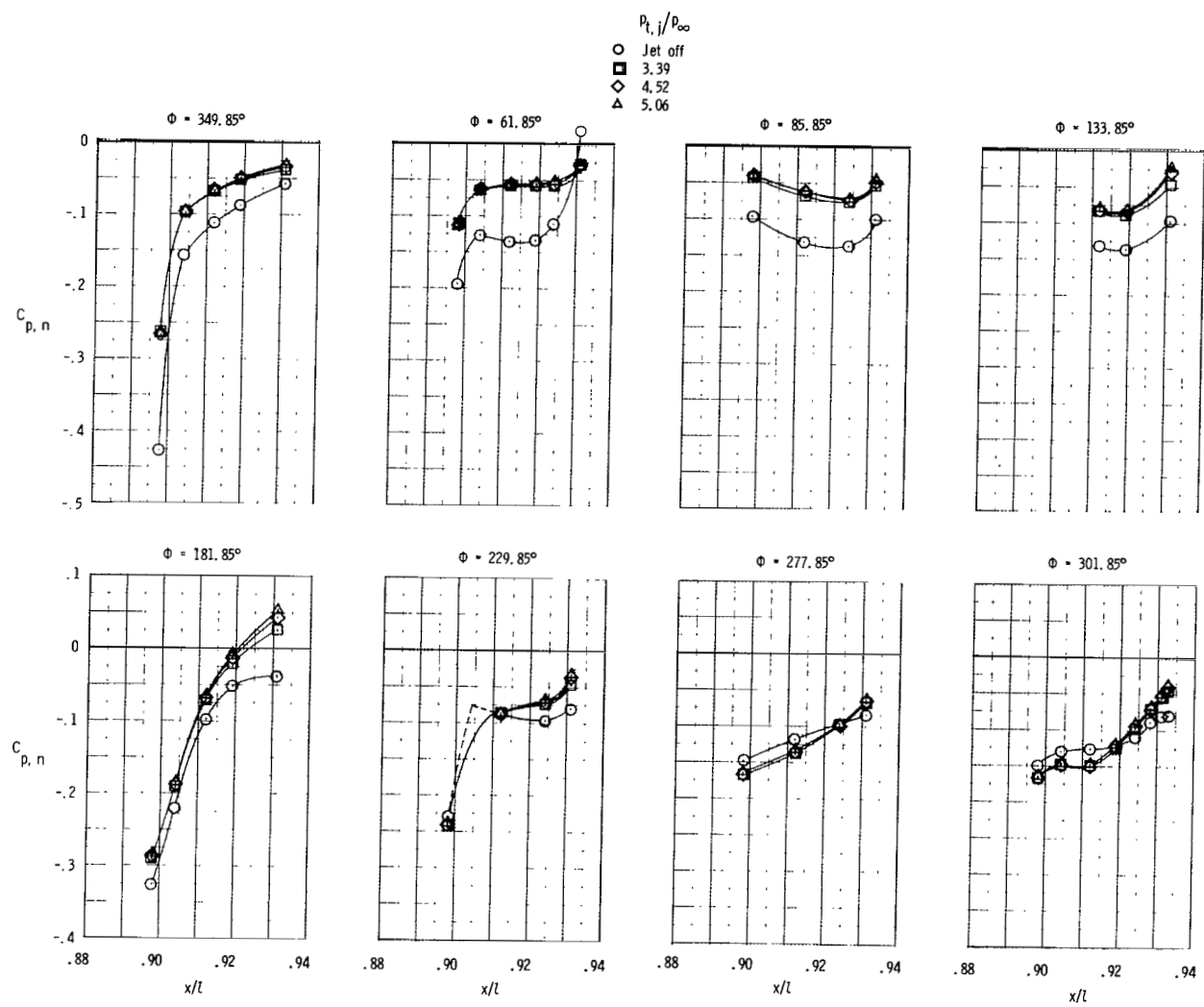
(h) $M = 0.870; \alpha = 7.12^\circ$.

Figure 11.- Continued.



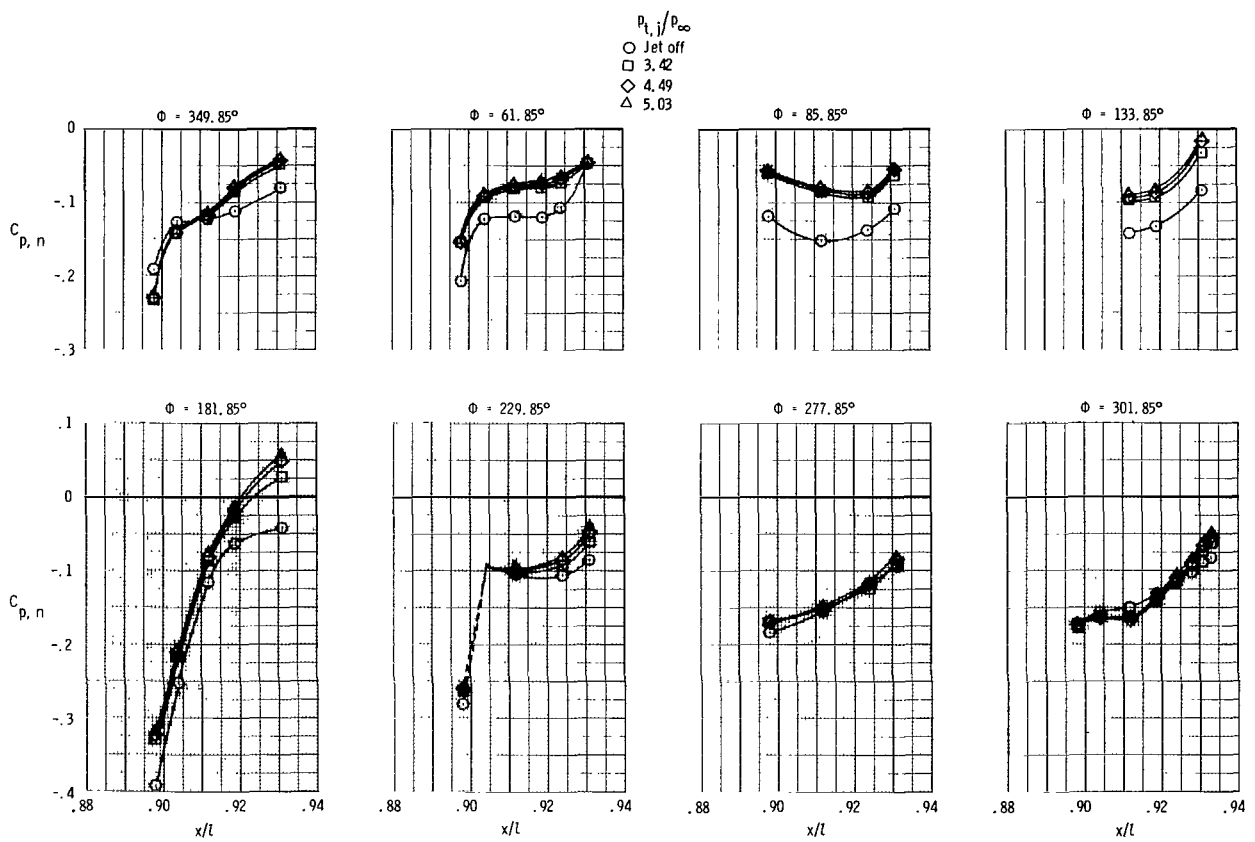
(i) $M = 0.869$; $\alpha = 9.13^\circ$.

Figure 11.- Continued.



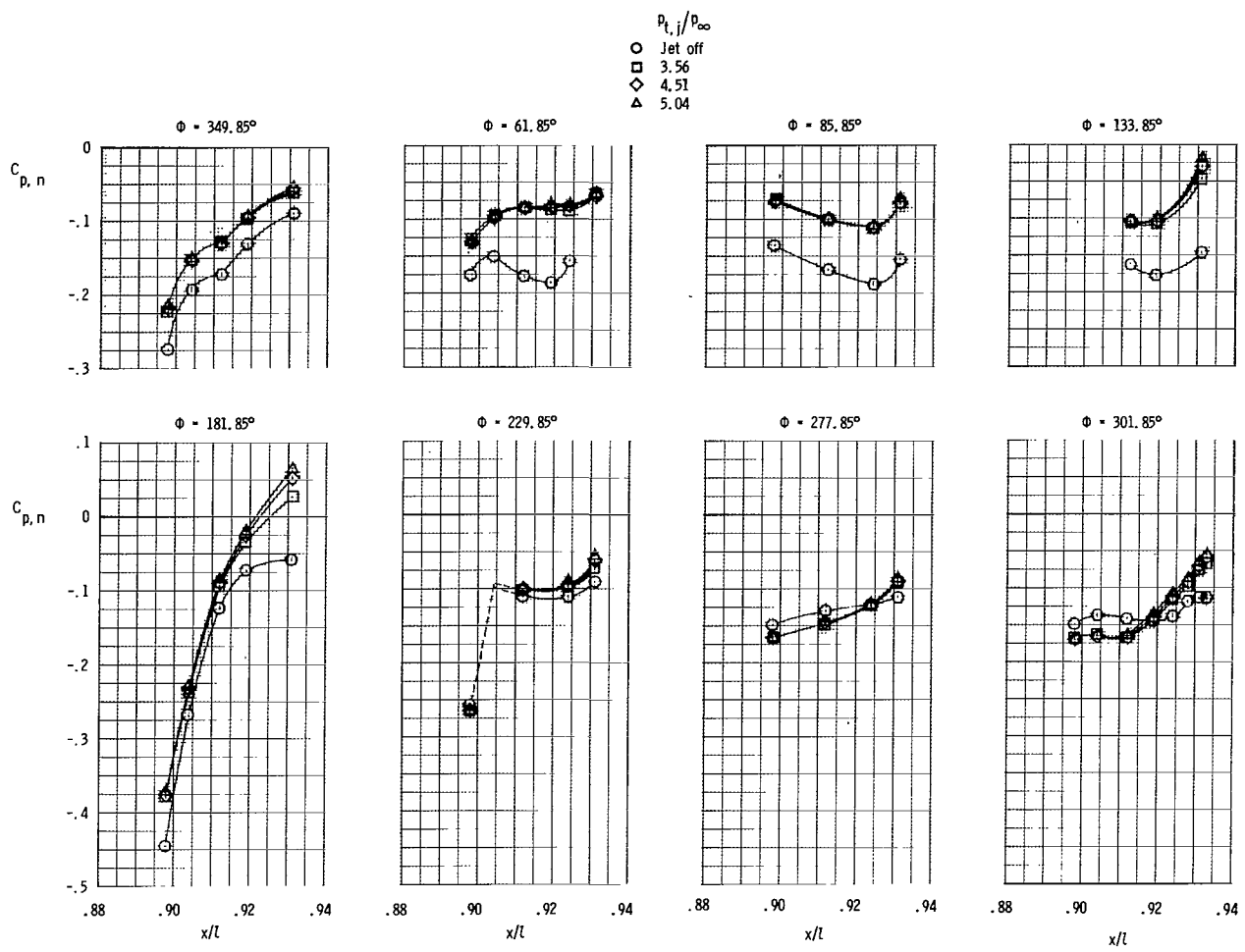
(j) $M = 0.896; \alpha = -0.87^\circ$.

Figure 11.- Continued.



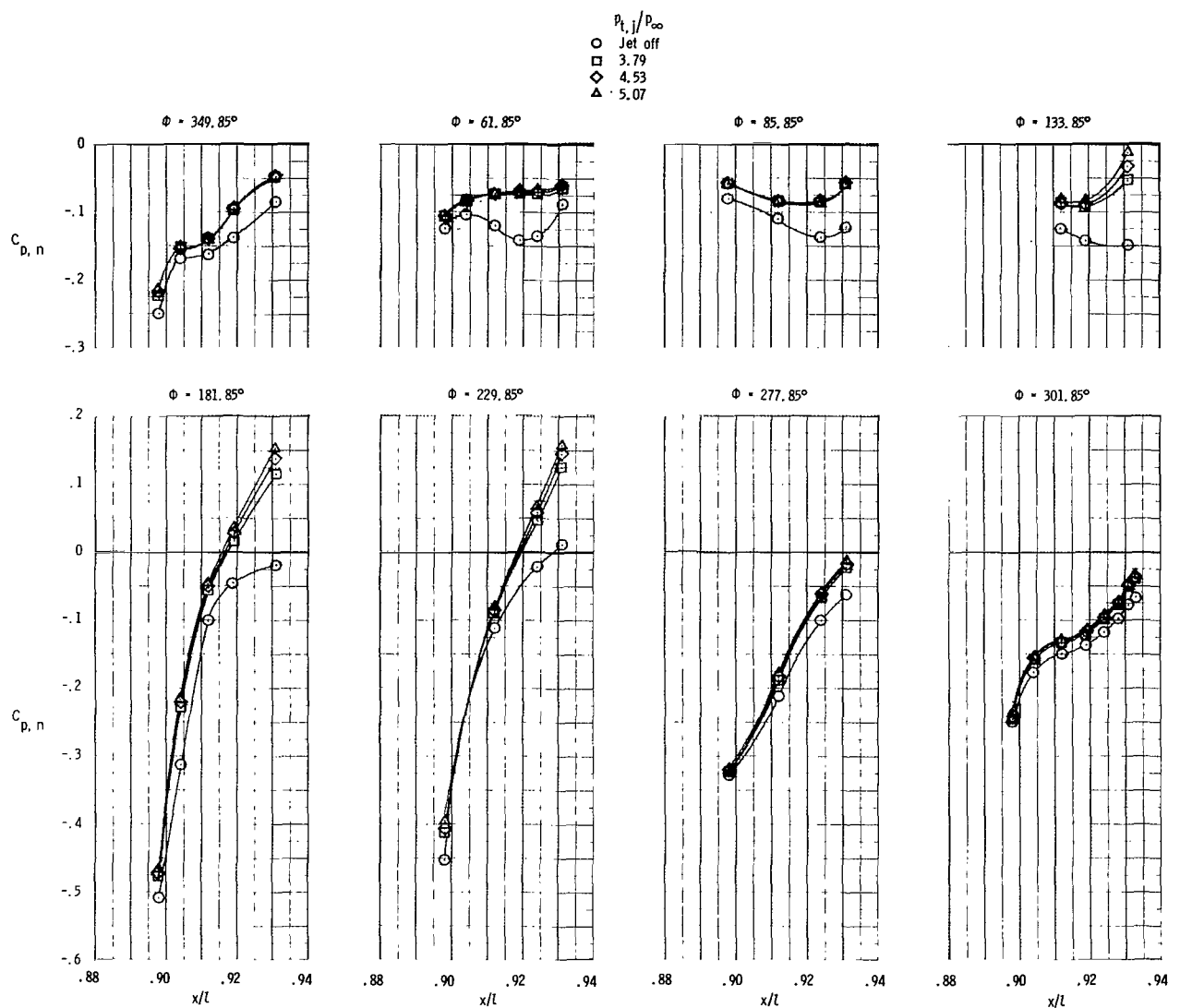
(k) $M = 0.893; \alpha = 1.11^\circ$.

Figure 11.- Continued.



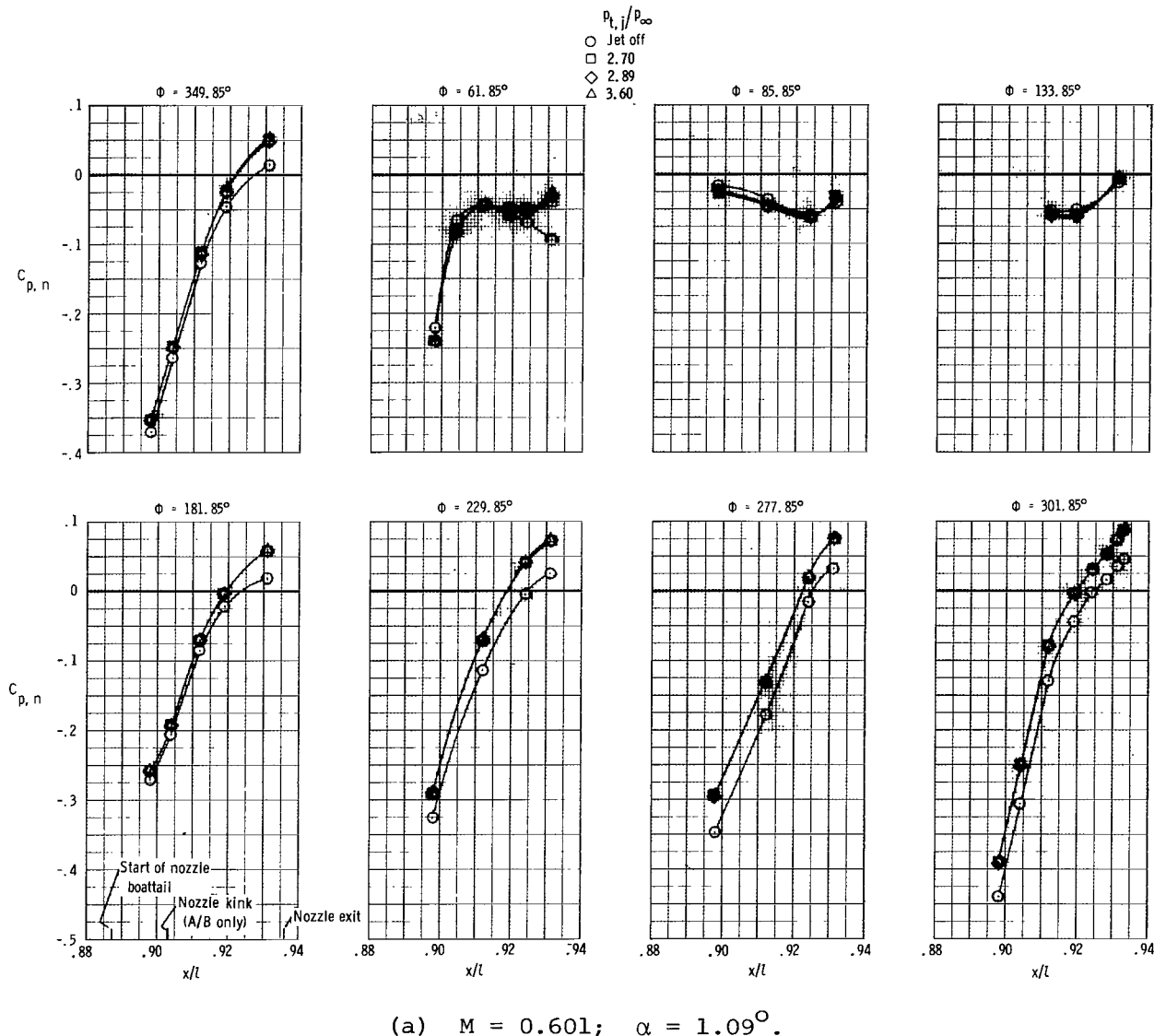
(1) $M = 0.895; \alpha = 3.11^\circ$.

Figure 11.- Continued.



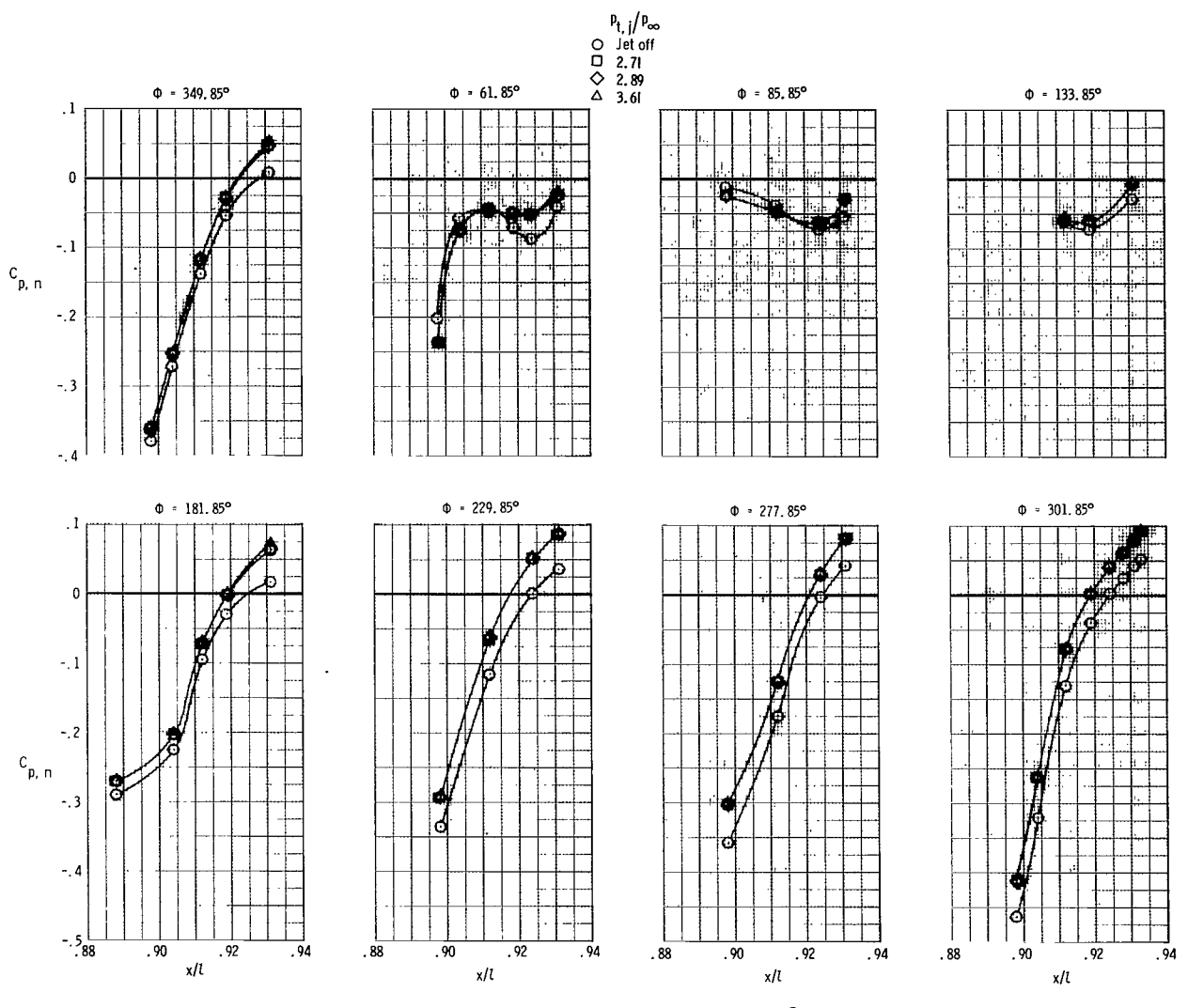
(m) $M = 0.897; \alpha = 9.14^\circ.$

Figure 11.- Concluded.



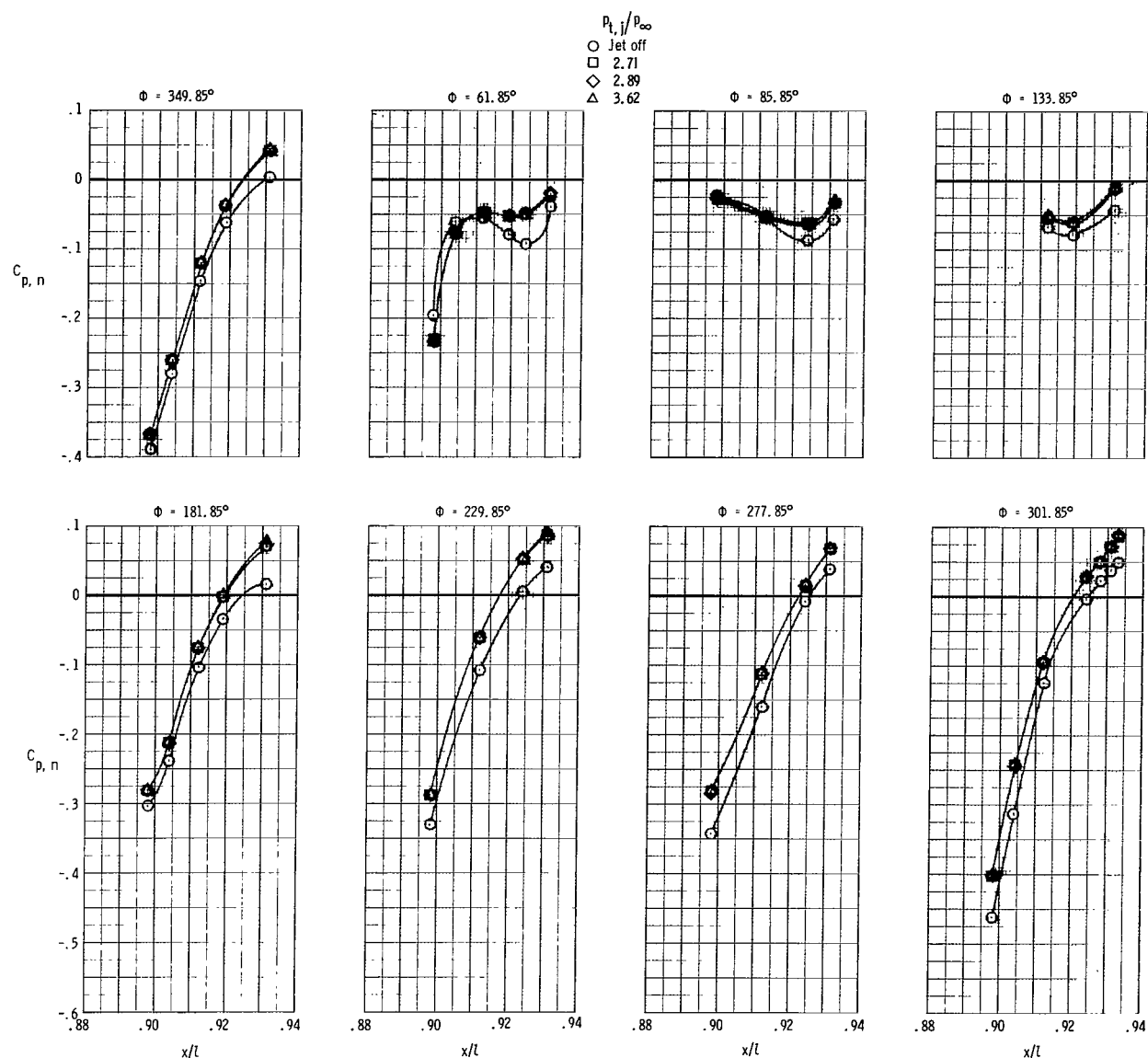
(a) $M = 0.601; \alpha = 1.09^\circ$.

Figure 12.- Static-pressure distributions on dry-power nozzle at several Mach number and angle-of-attack combinations for $\delta_h = -10^\circ$.



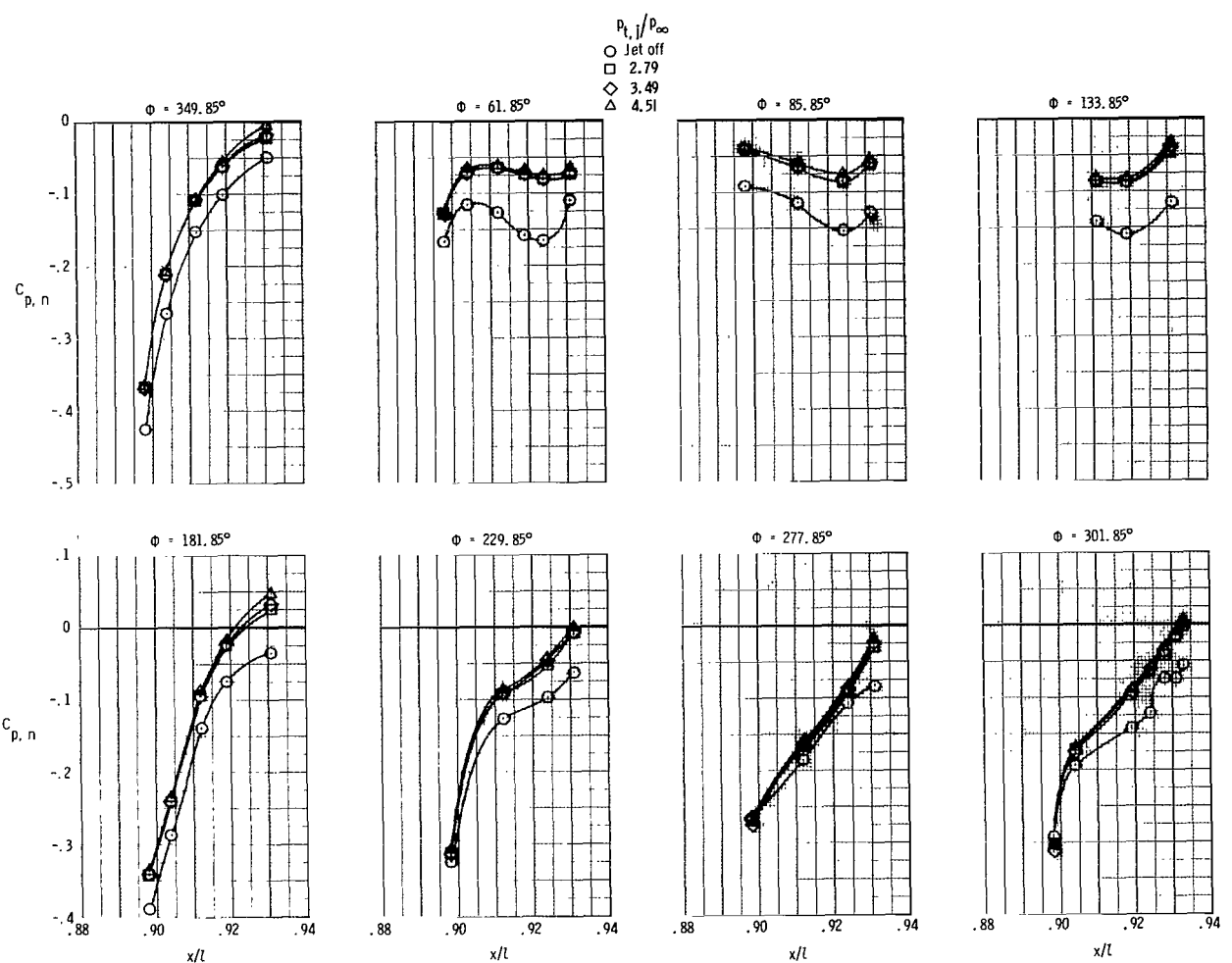
(b) $M = 0.600$; $\alpha = 3.11^\circ$.

Figure 12.- Continued.



(c) $M = 0.600$; $\alpha = 5.13^\circ$.

Figure 12.- Continued.



(d) $M = 0.797$; $\alpha = 3.12^\circ$.

Figure 12.- Continued.

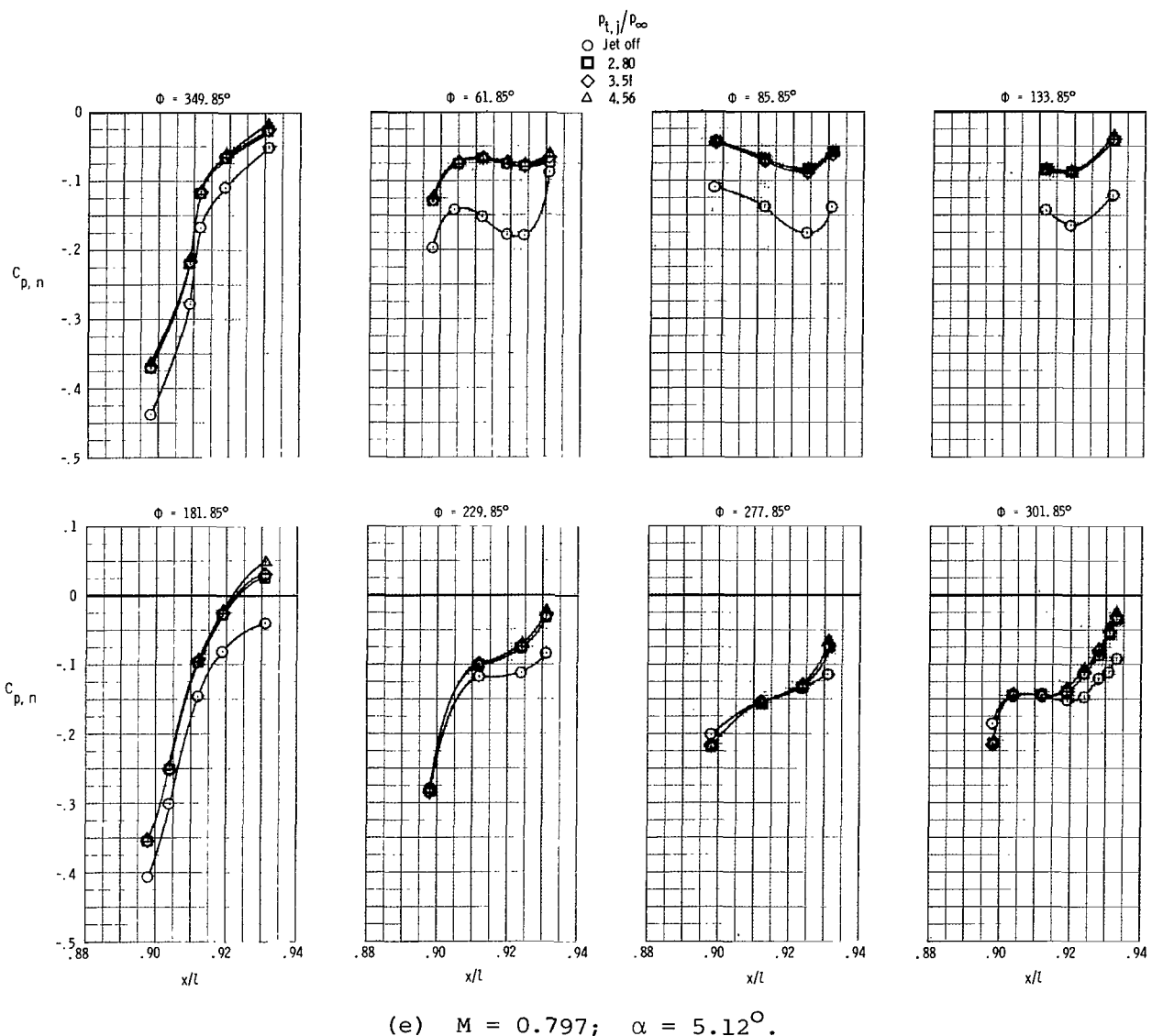
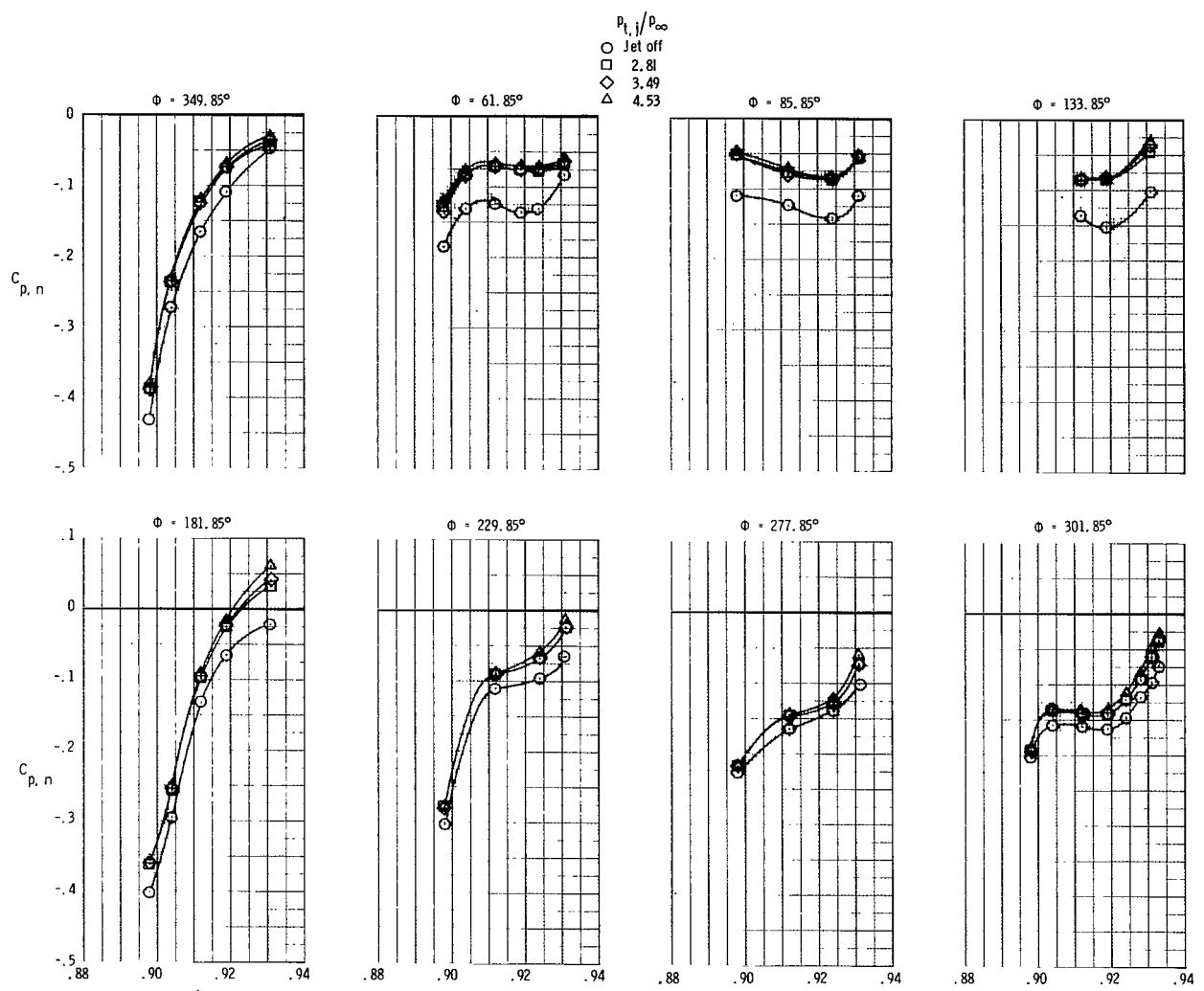
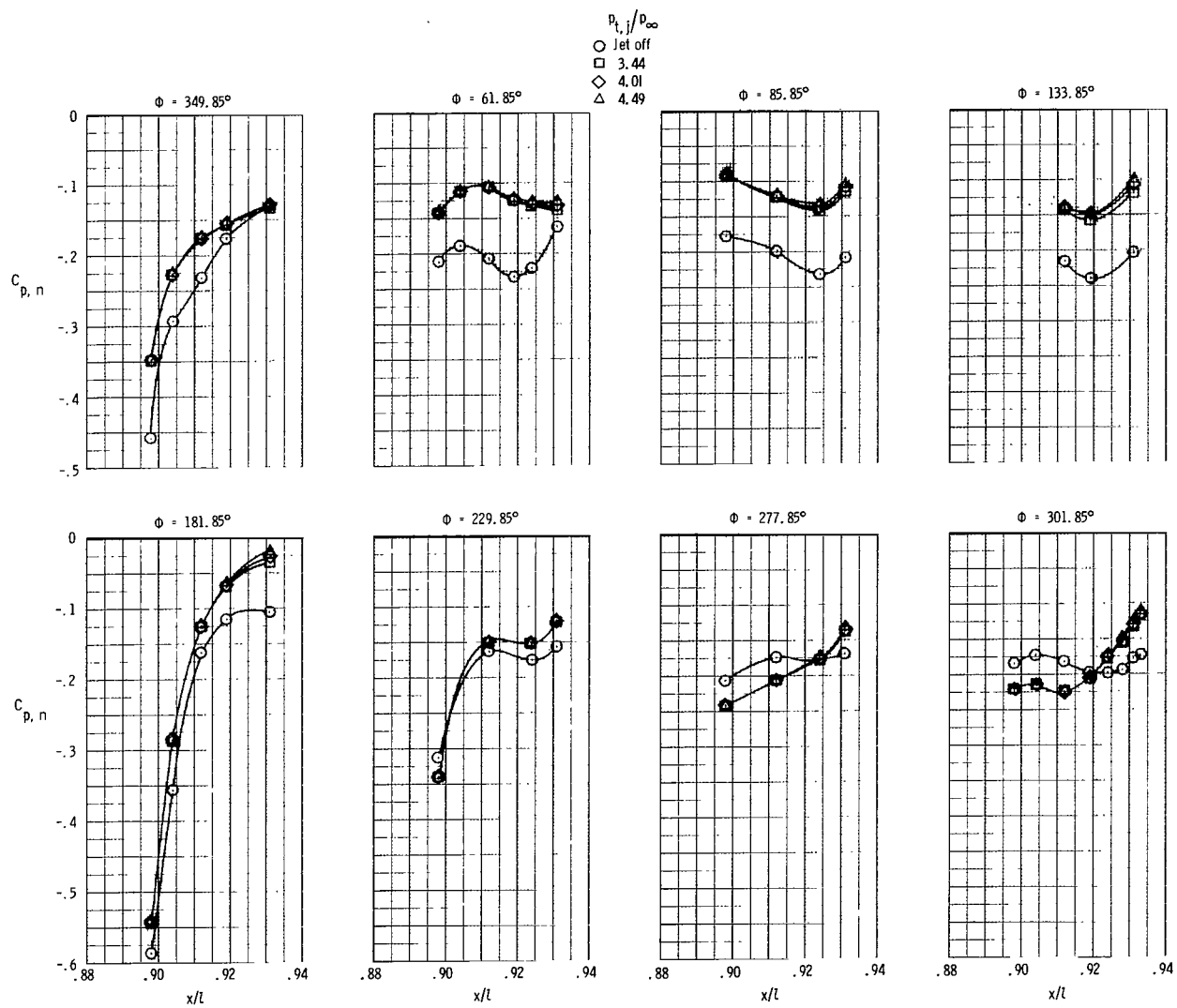


Figure 12.- Continued.



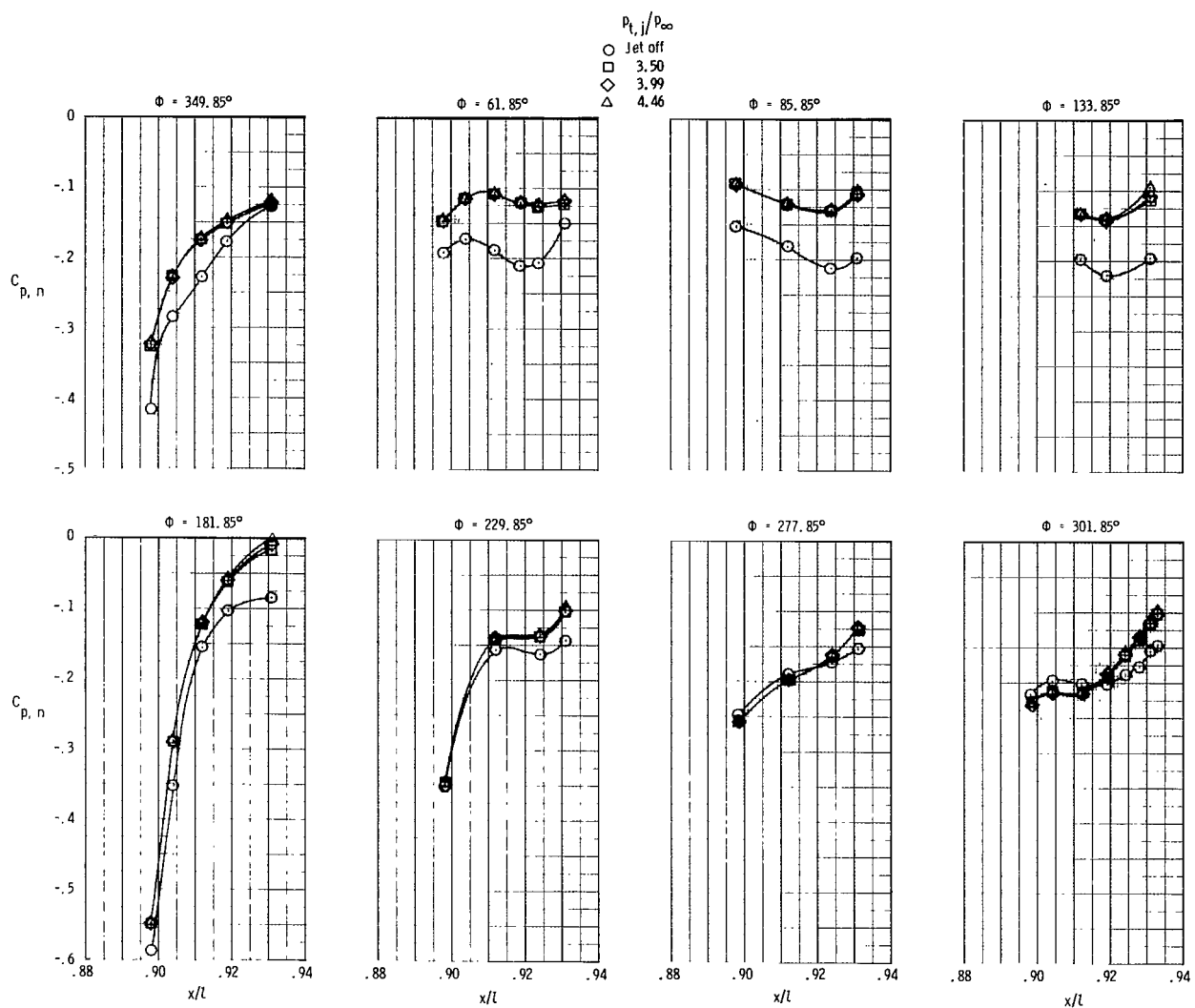
(f) $M = 0.796; \alpha = 7.14^\circ.$

Figure 12.- Continued.



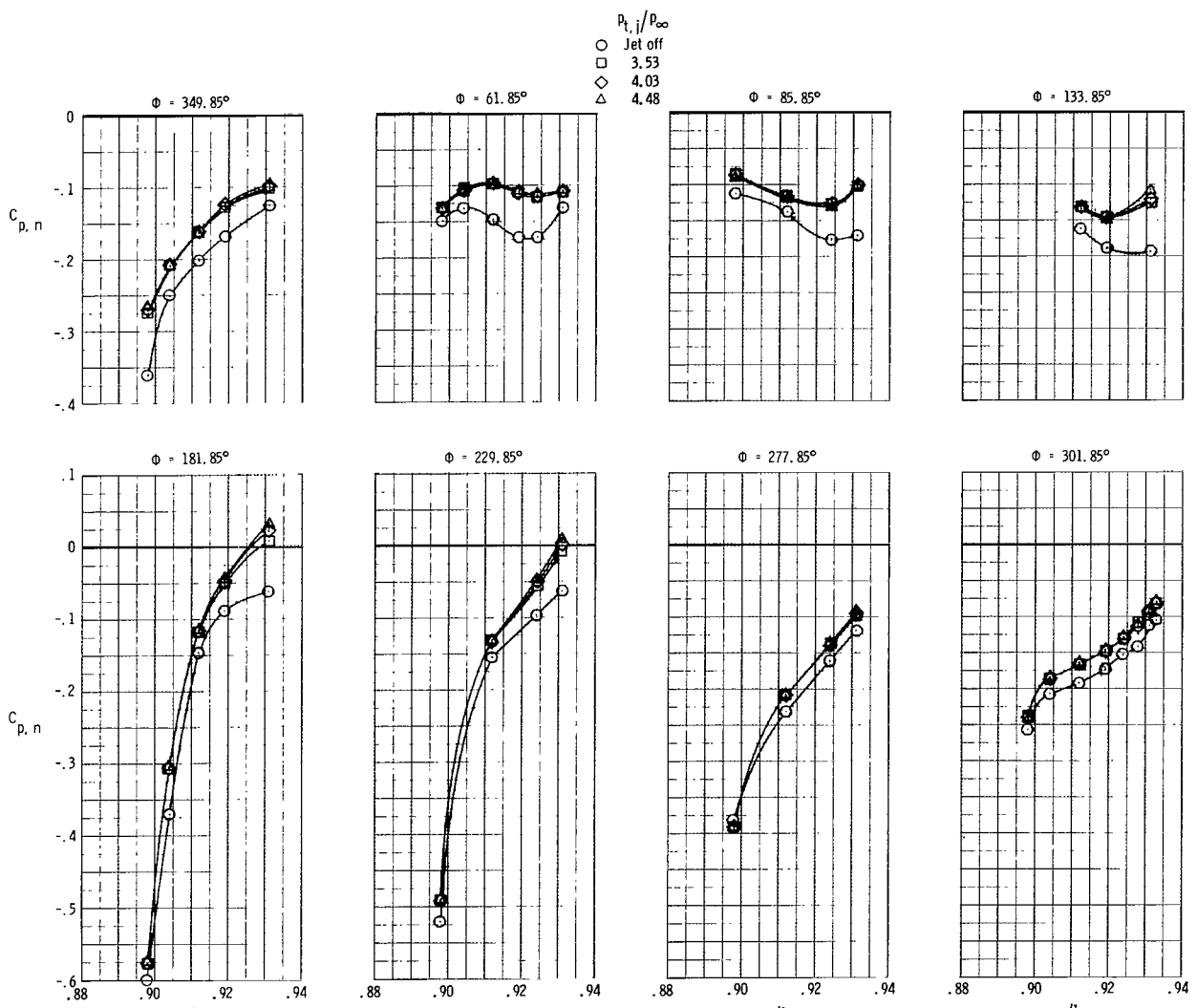
(g) $M = 0.872$; $\alpha = 5.13^\circ$.

Figure 12.- Continued.



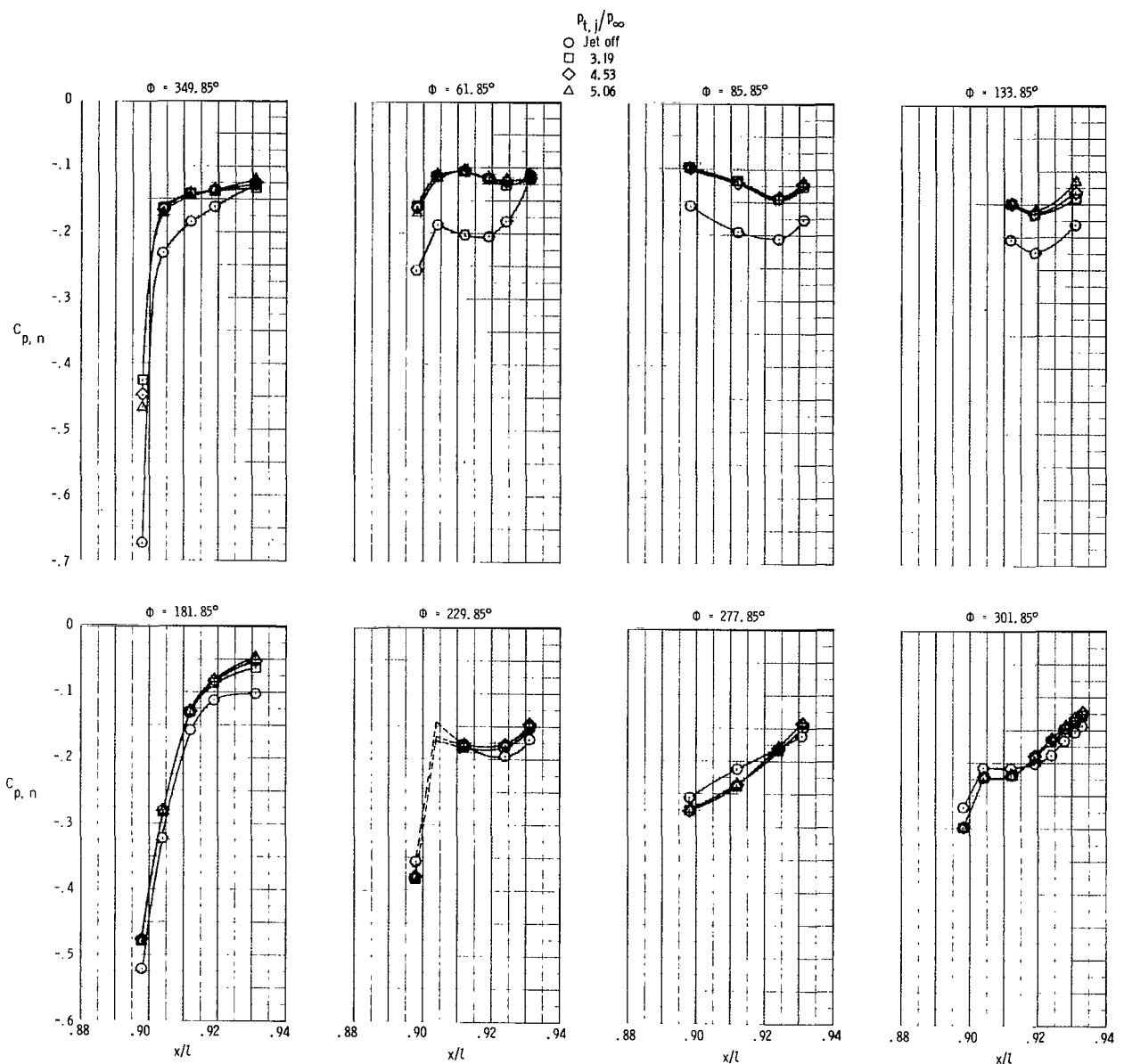
(h) $M = 0.868; \alpha = 7.14^\circ$.

Figure 12.- Continued.



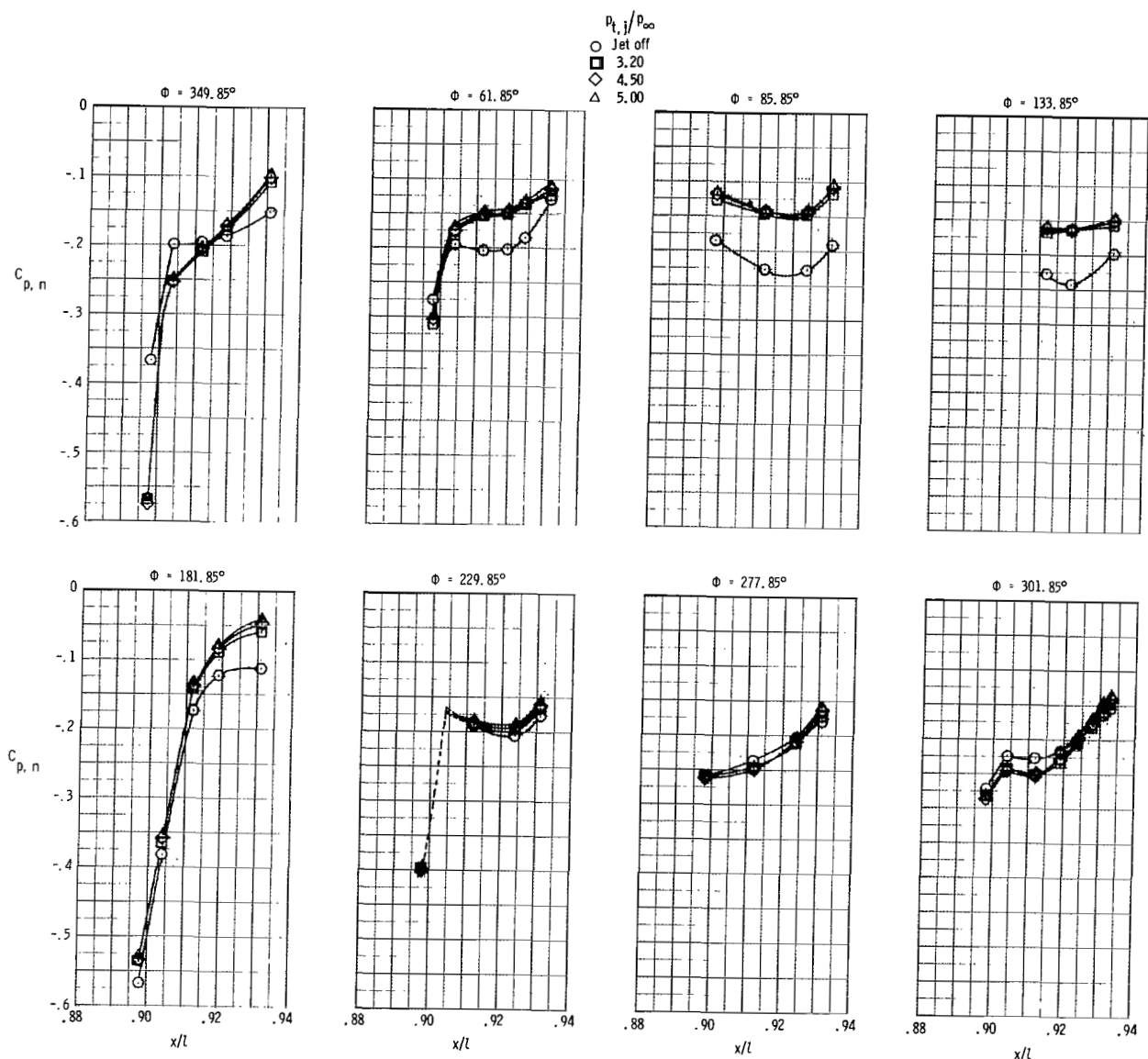
(i) $M = 0.868; \alpha = 9.16^\circ$.

Figure 12.- Continued.



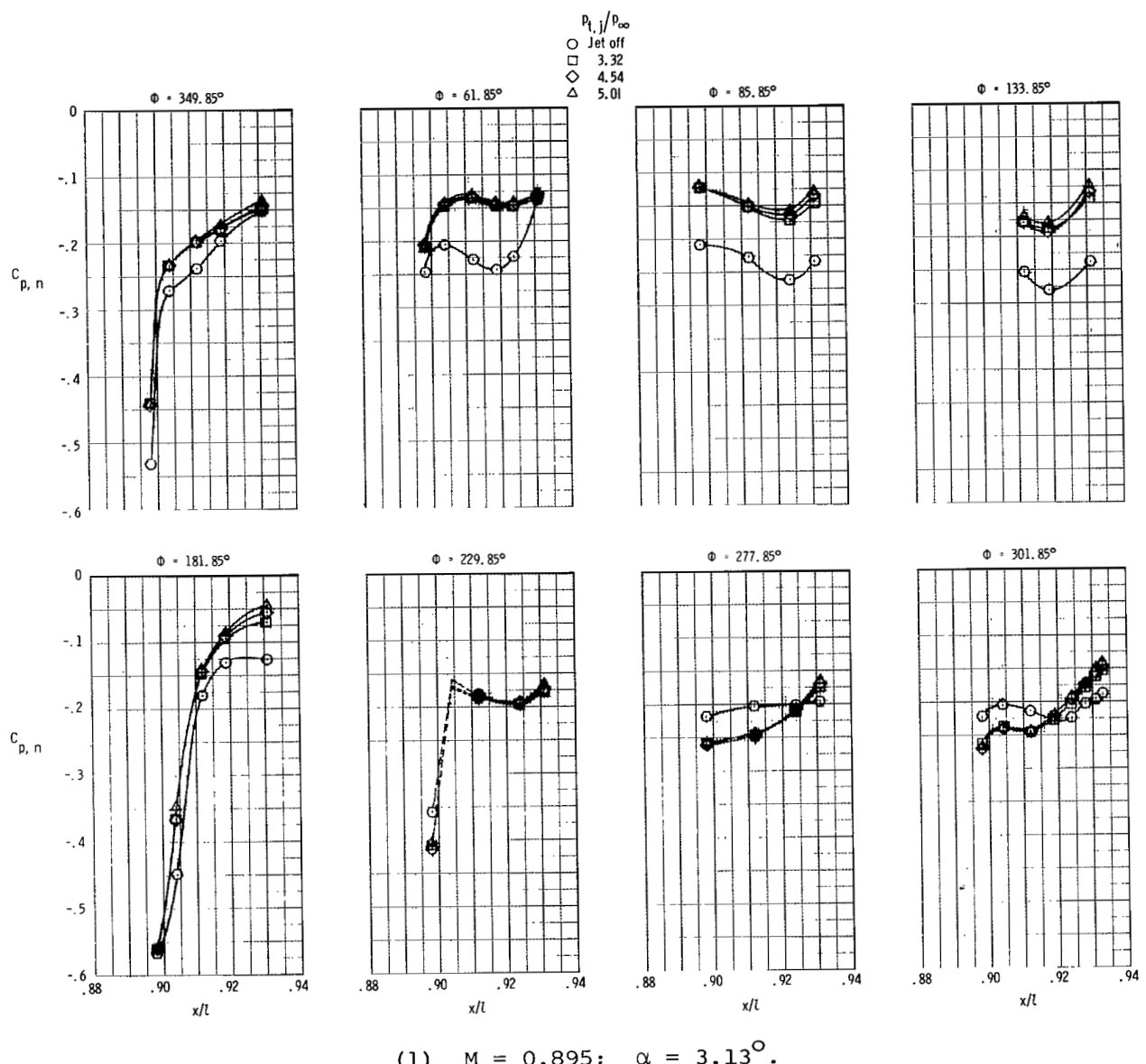
(j) $M = 0.893; \alpha = -0.89^\circ$.

Figure 12.- Continued.



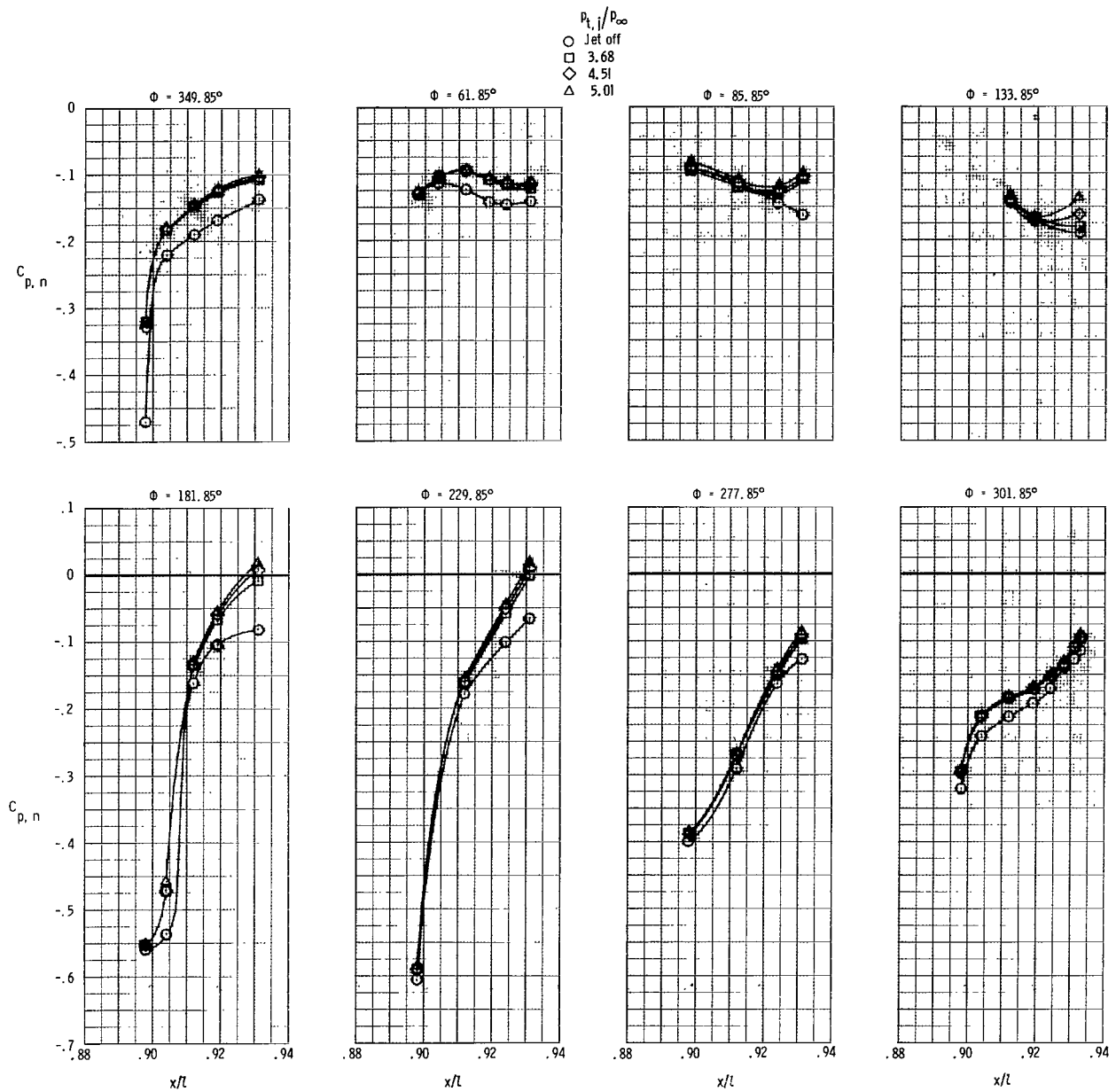
(k) $M = 0.892$; $\alpha = 1.11^\circ$.

Figure 12.- Continued.



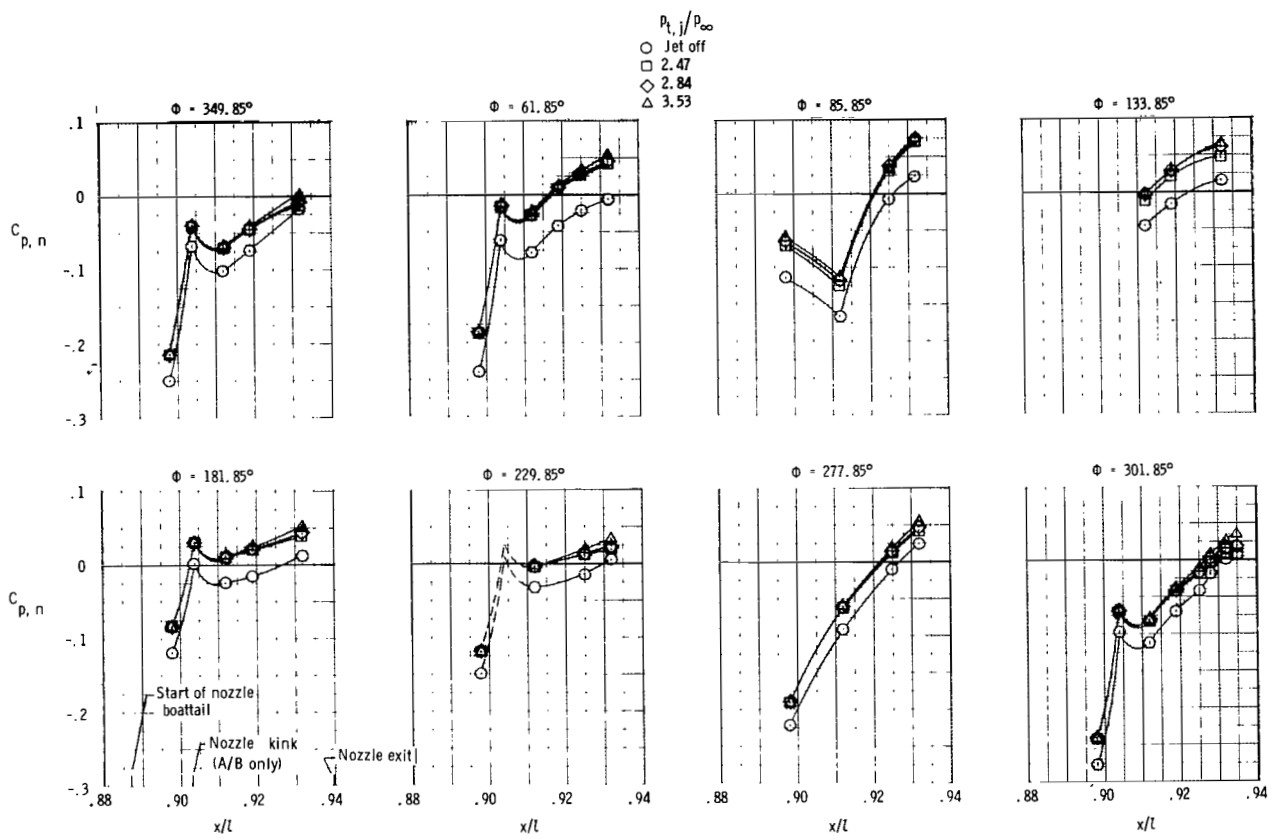
(1) $M = 0.895; \alpha = 3.13^\circ$.

Figure 12.- Continued.



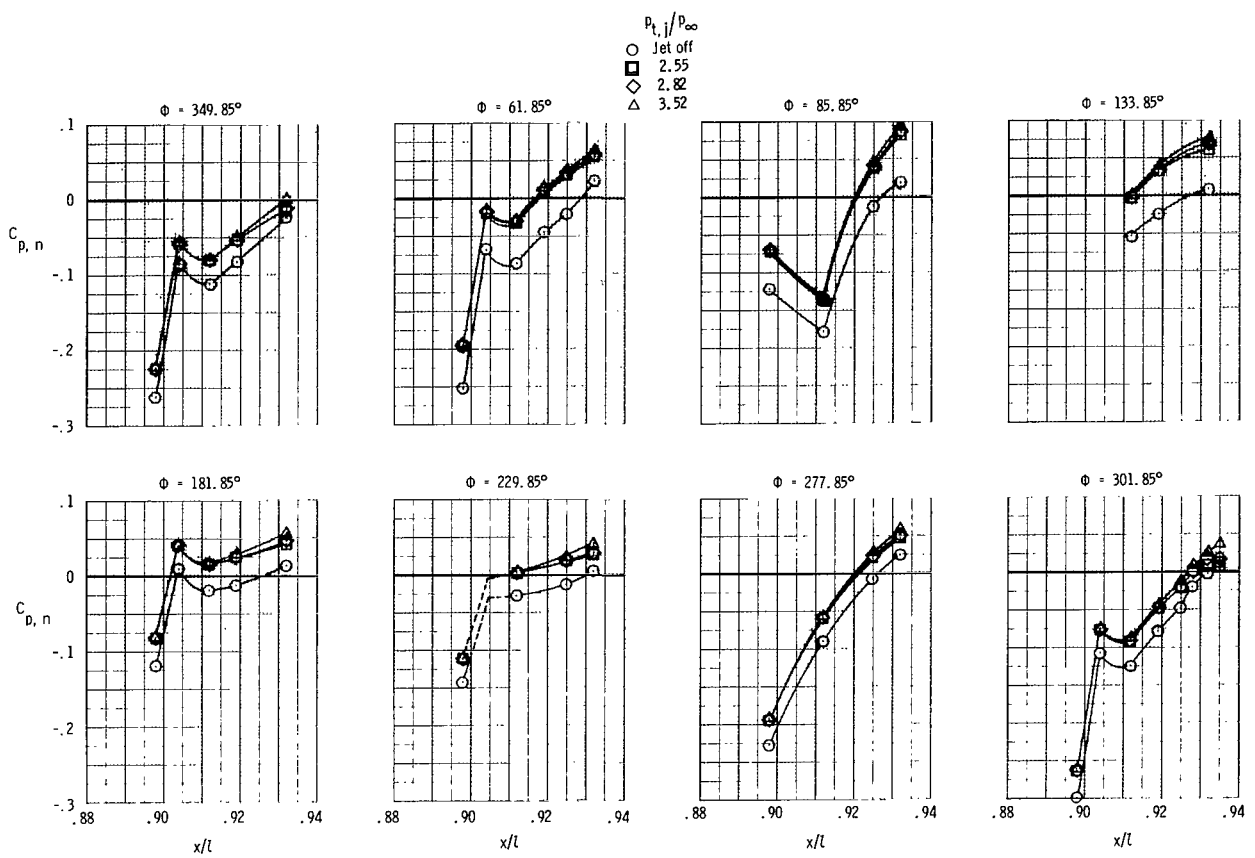
(m) $M = 0.895$; $\alpha = 9.17^\circ$.

Figure 12.- Concluded.



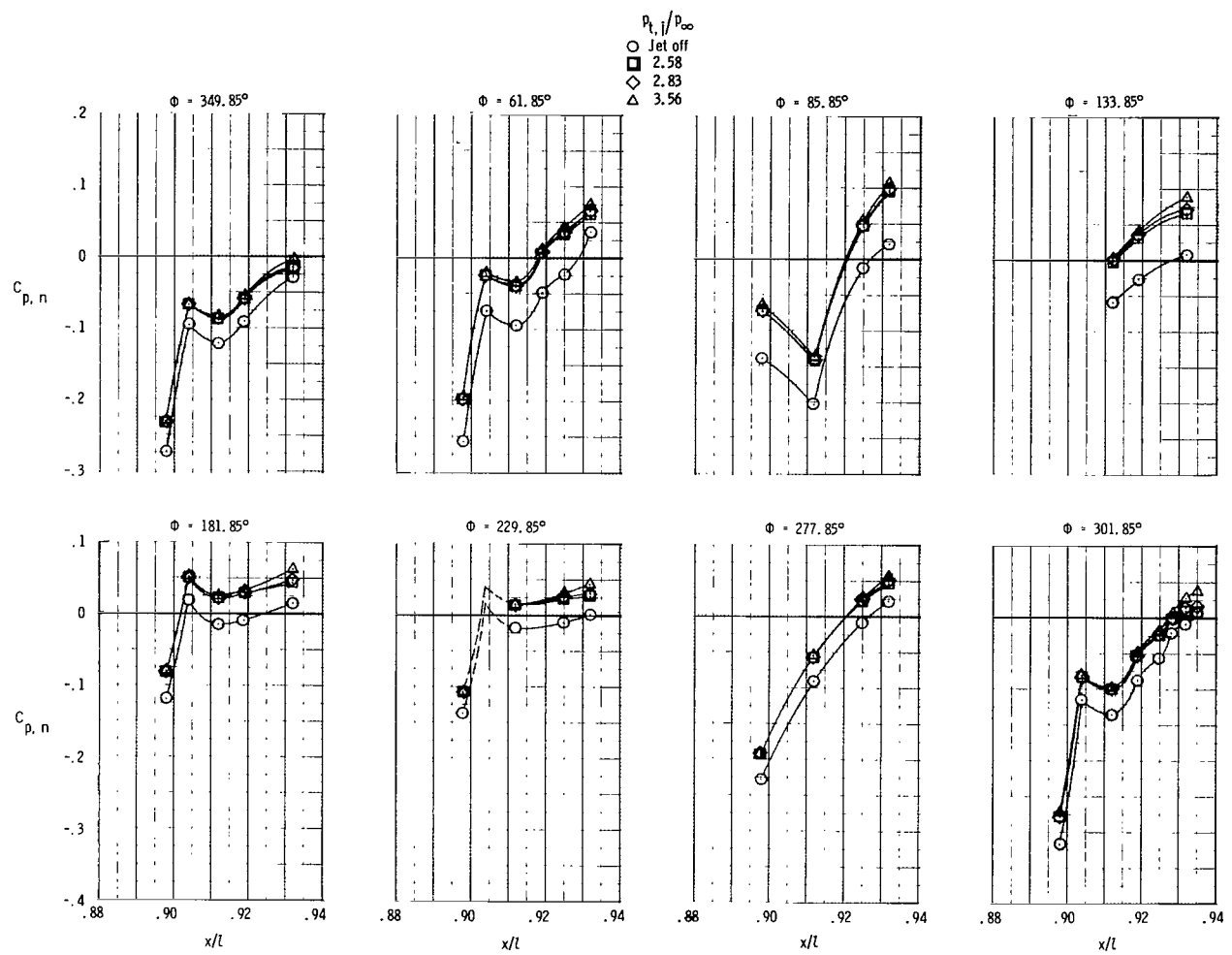
(a) $M = 0.600; \alpha = 1.08^\circ$.

Figure 13.- Static-pressure distributions on intermediate A/B power nozzle at several Mach number and angle-of-attack combinations for $\delta_h = 0^\circ$.



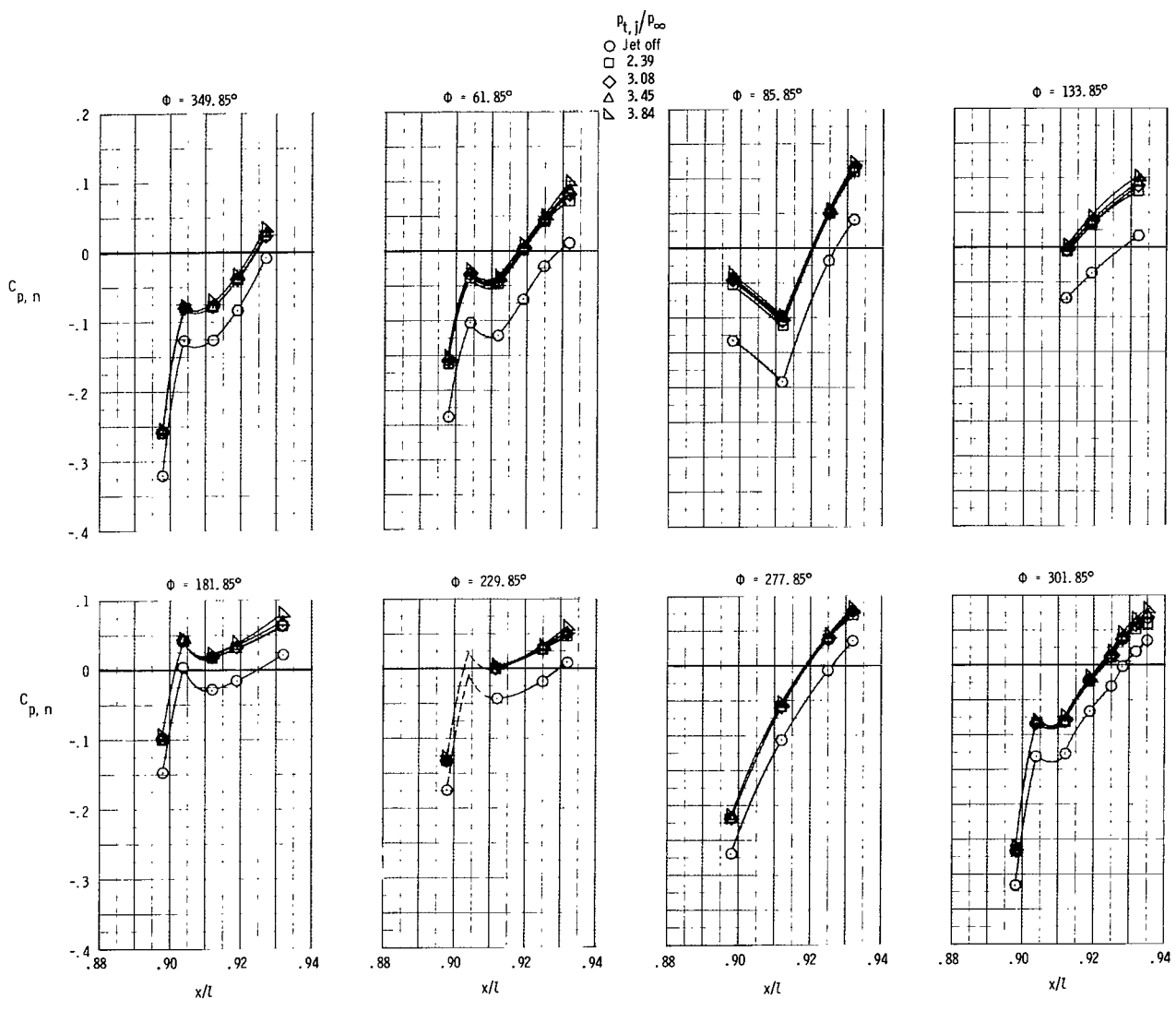
(b) $M = 0.599$; $\alpha = 3.08^\circ$.

Figure 13.- Continued.



(c) $M = 0.599$; $\alpha = 5.08^\circ$.

Figure 13.- Continued.



(d) $M = 0.798$; $\alpha = 3.08^\circ$.

Figure 13.- Continued.

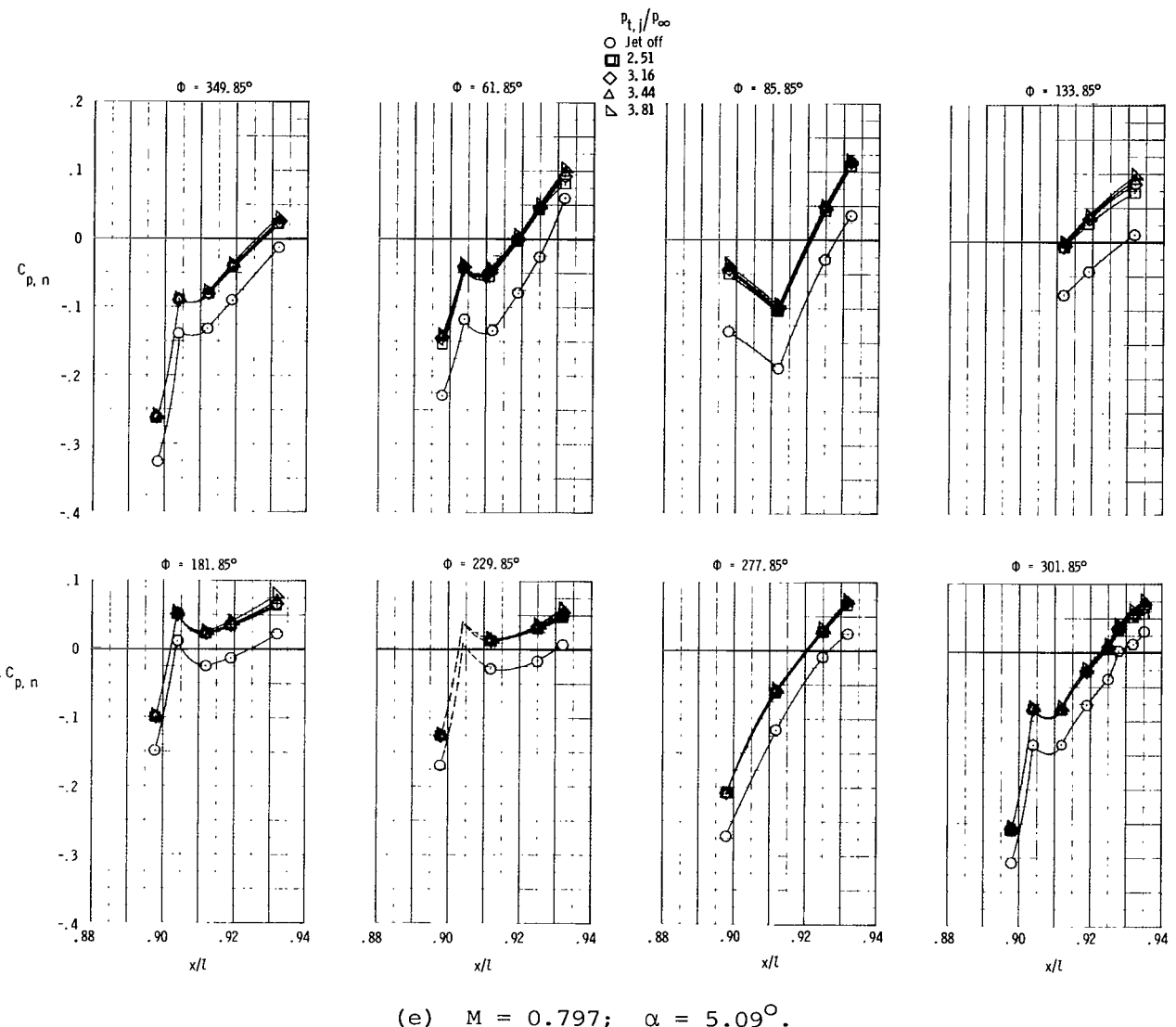
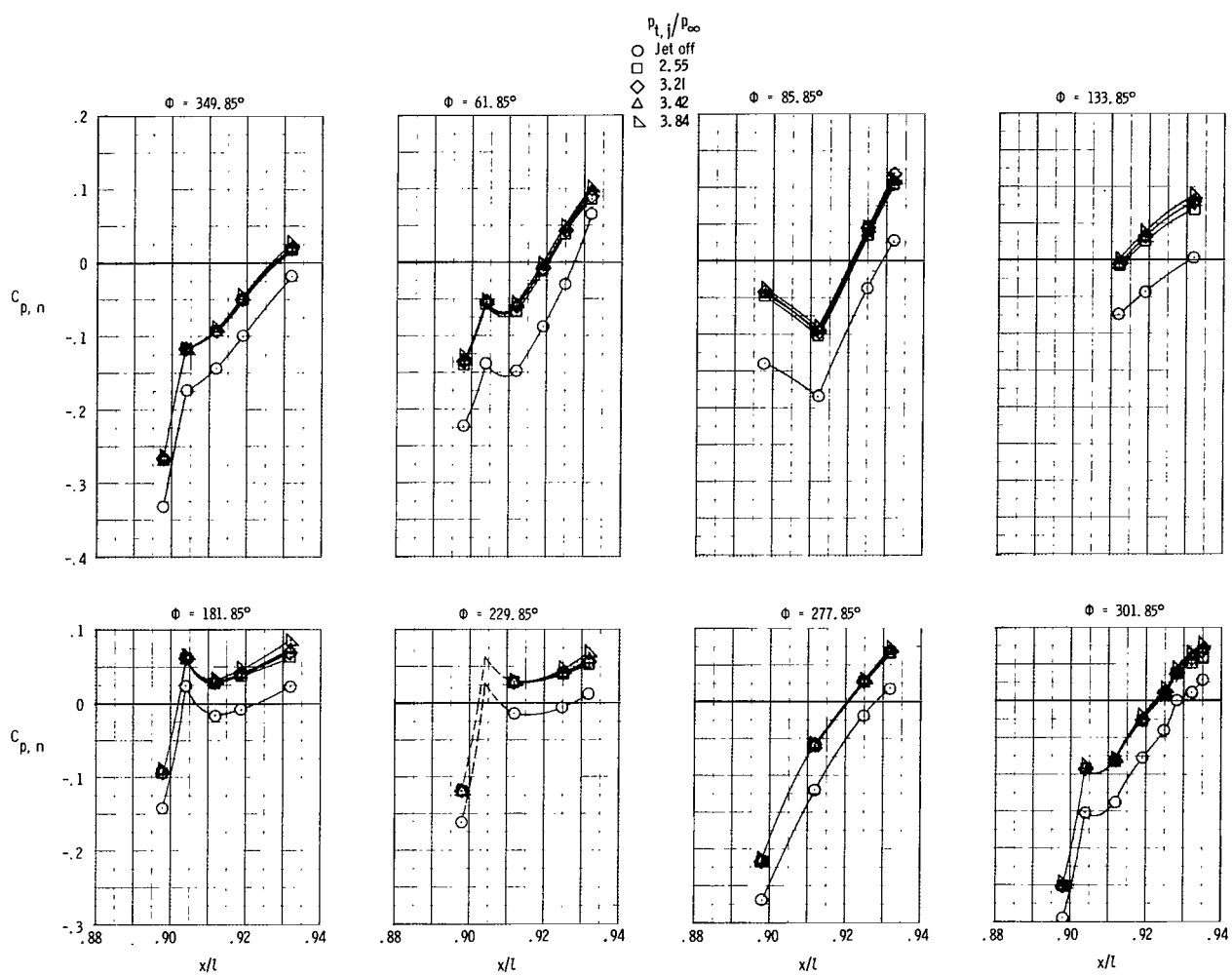
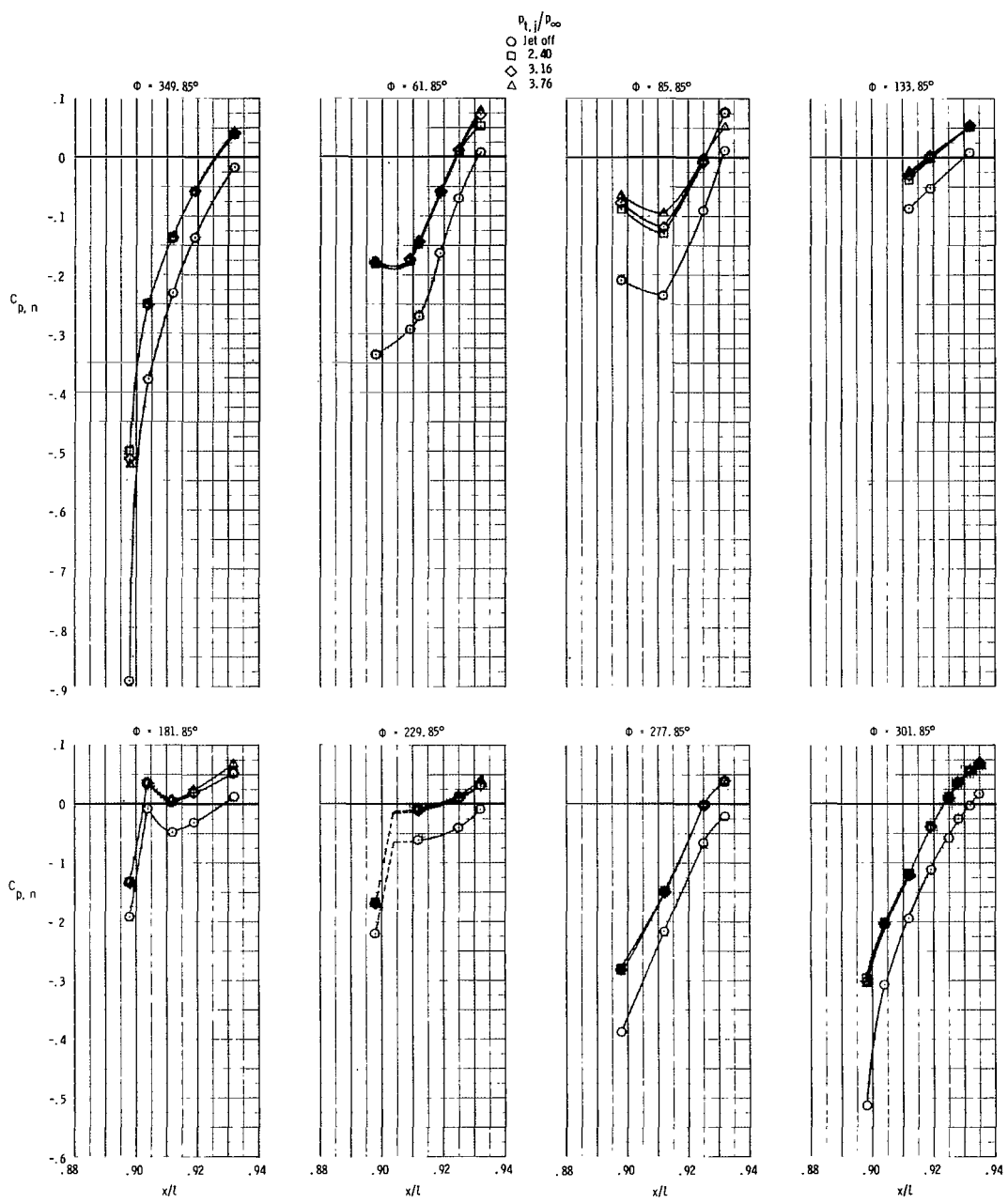


Figure 13.- Continued.



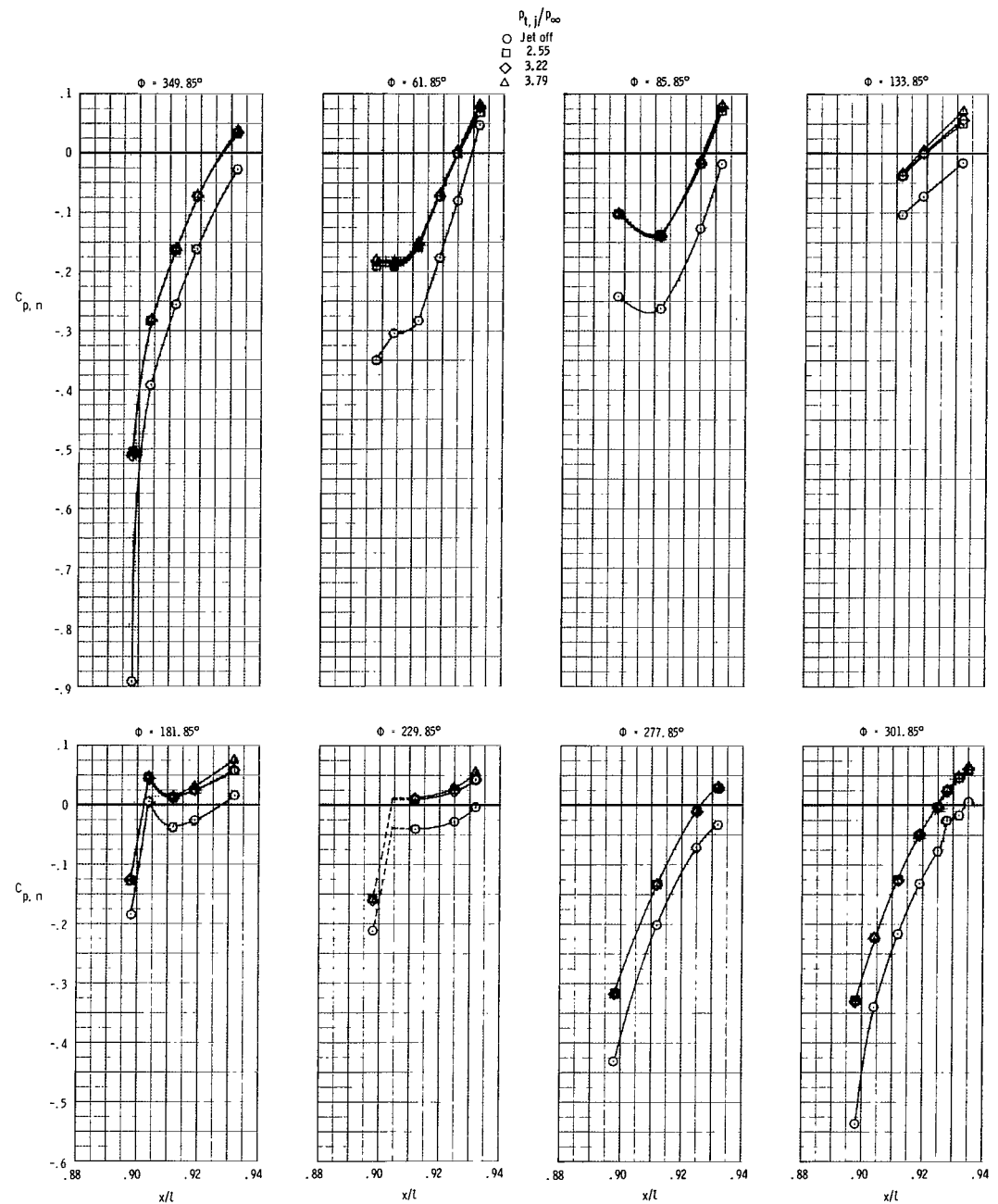
(f) $M = 0.797$; $\alpha = 7.09^\circ$.

Figure 13.- Continued.



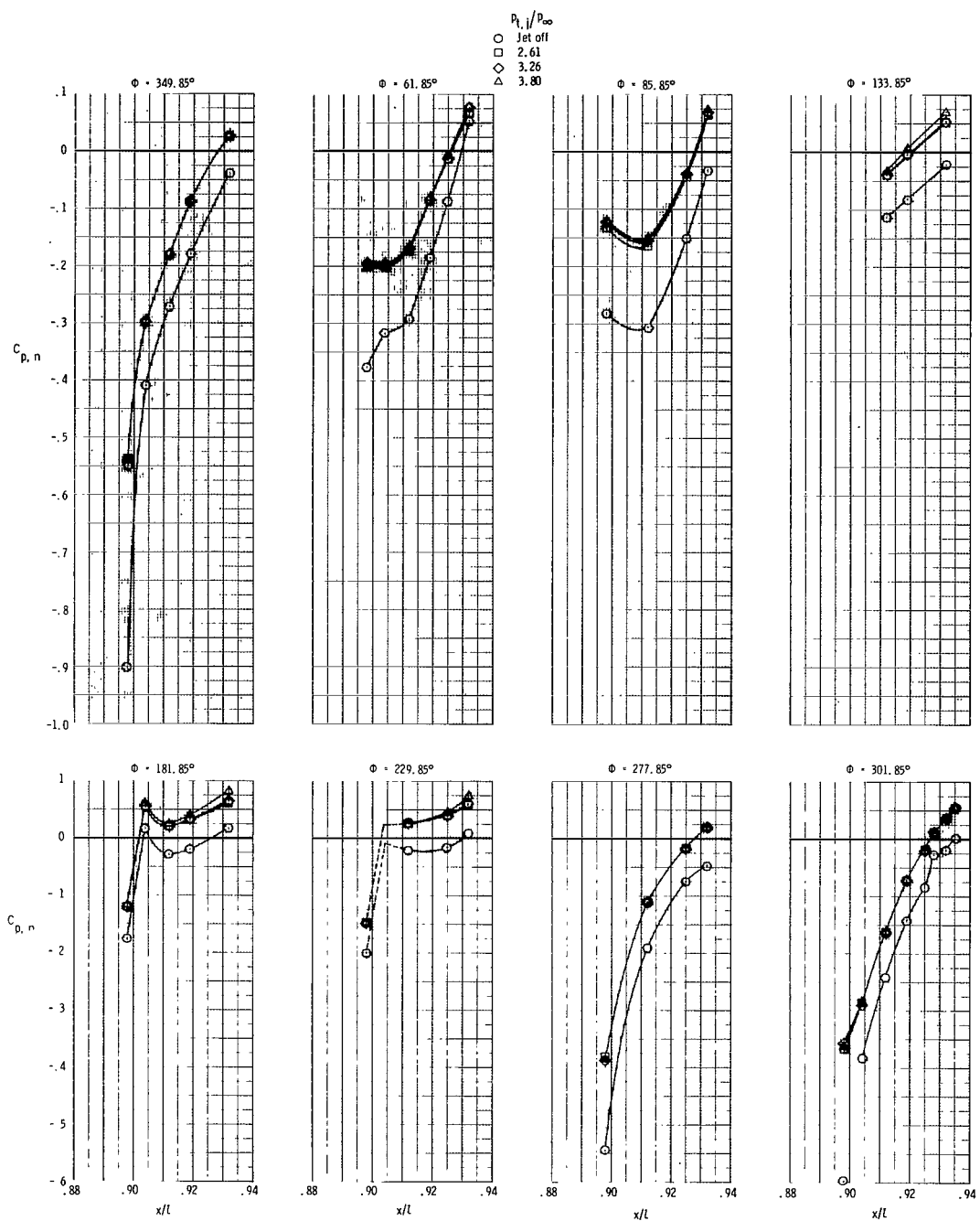
(g) $M = 0.870; \alpha = 5.08^\circ$.

Figure 13.- Continued.



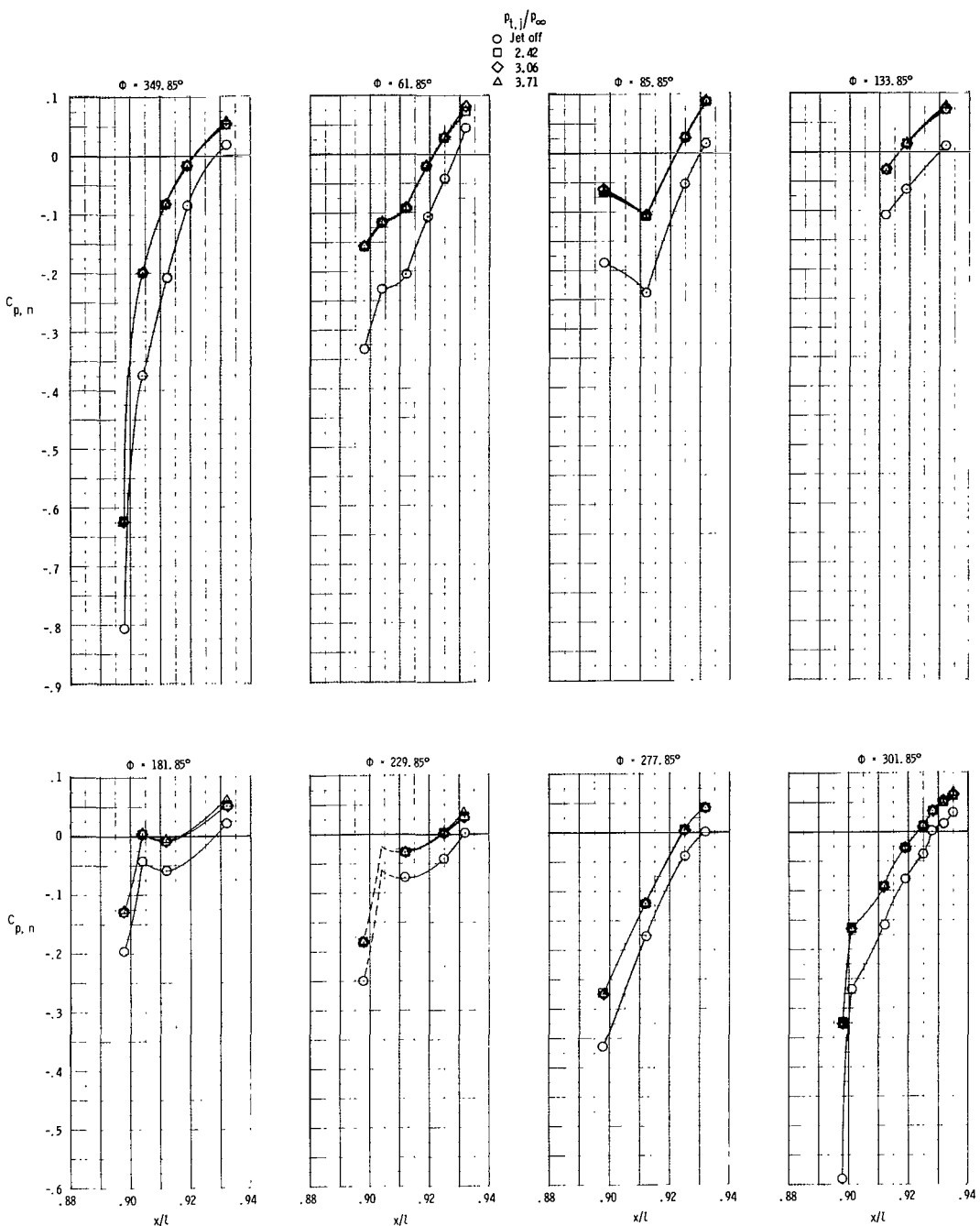
(h) $M = 0.870; \alpha = 7.10^\circ.$

Figure 13.- Continued.



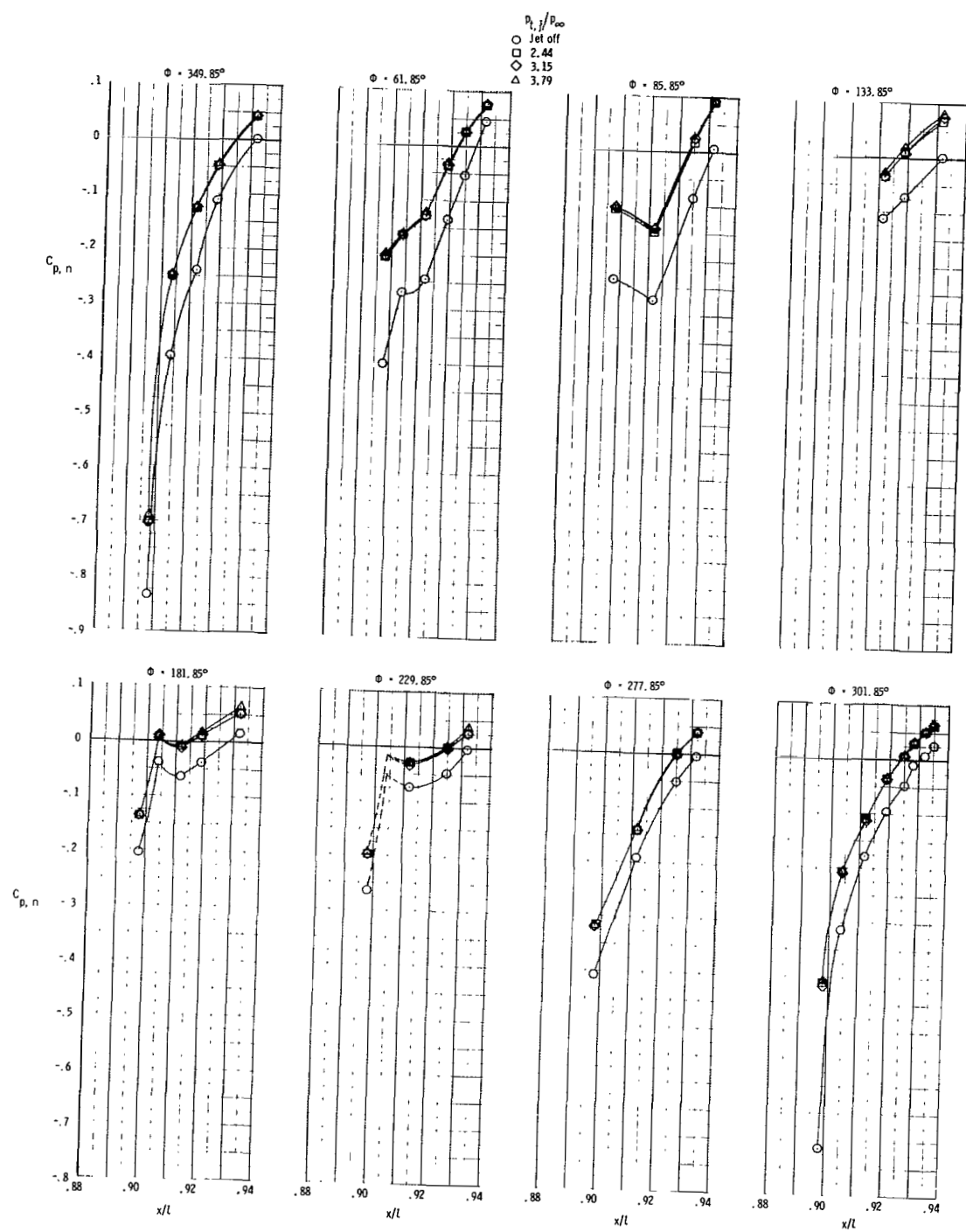
(i) $M = 0.870$; $\alpha = 9.11^\circ$.

Figure 13.-- Continued.



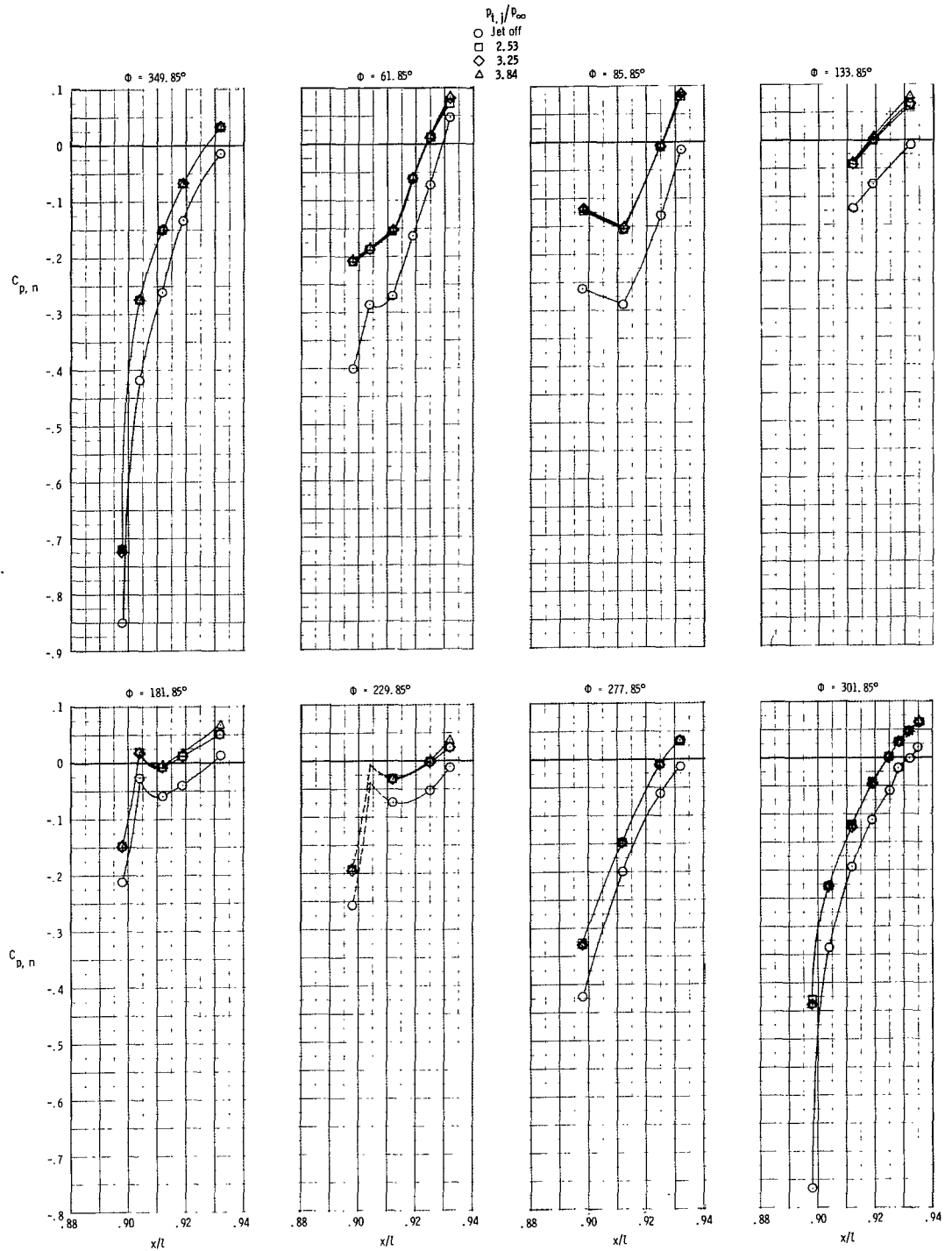
(j) $M = 0.897; \alpha = -0.88^\circ$.

Figure 13.- Continued.



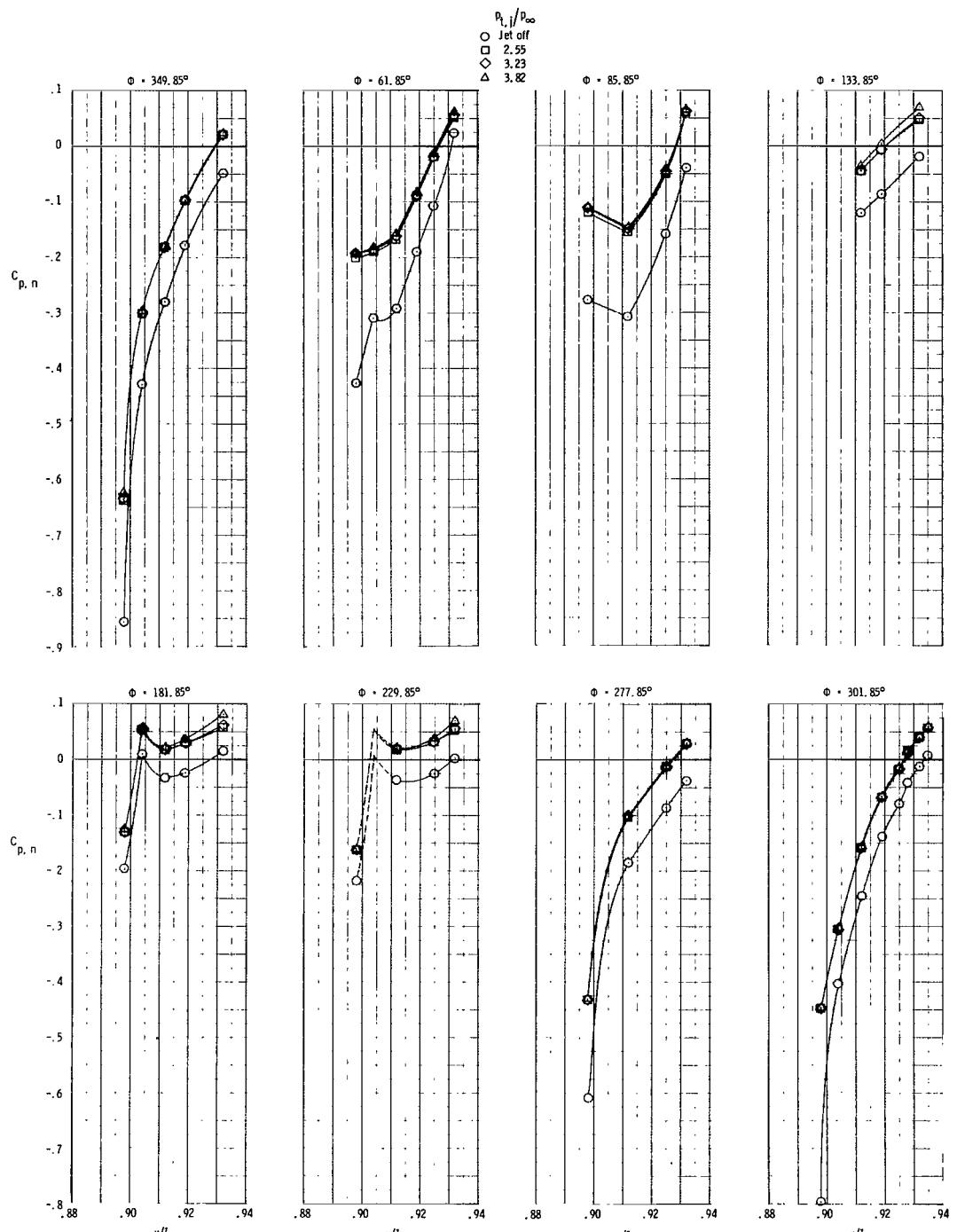
(k) $M = 0.897$; $\alpha = 1.12^\circ$.

Figure 13.- Continued.



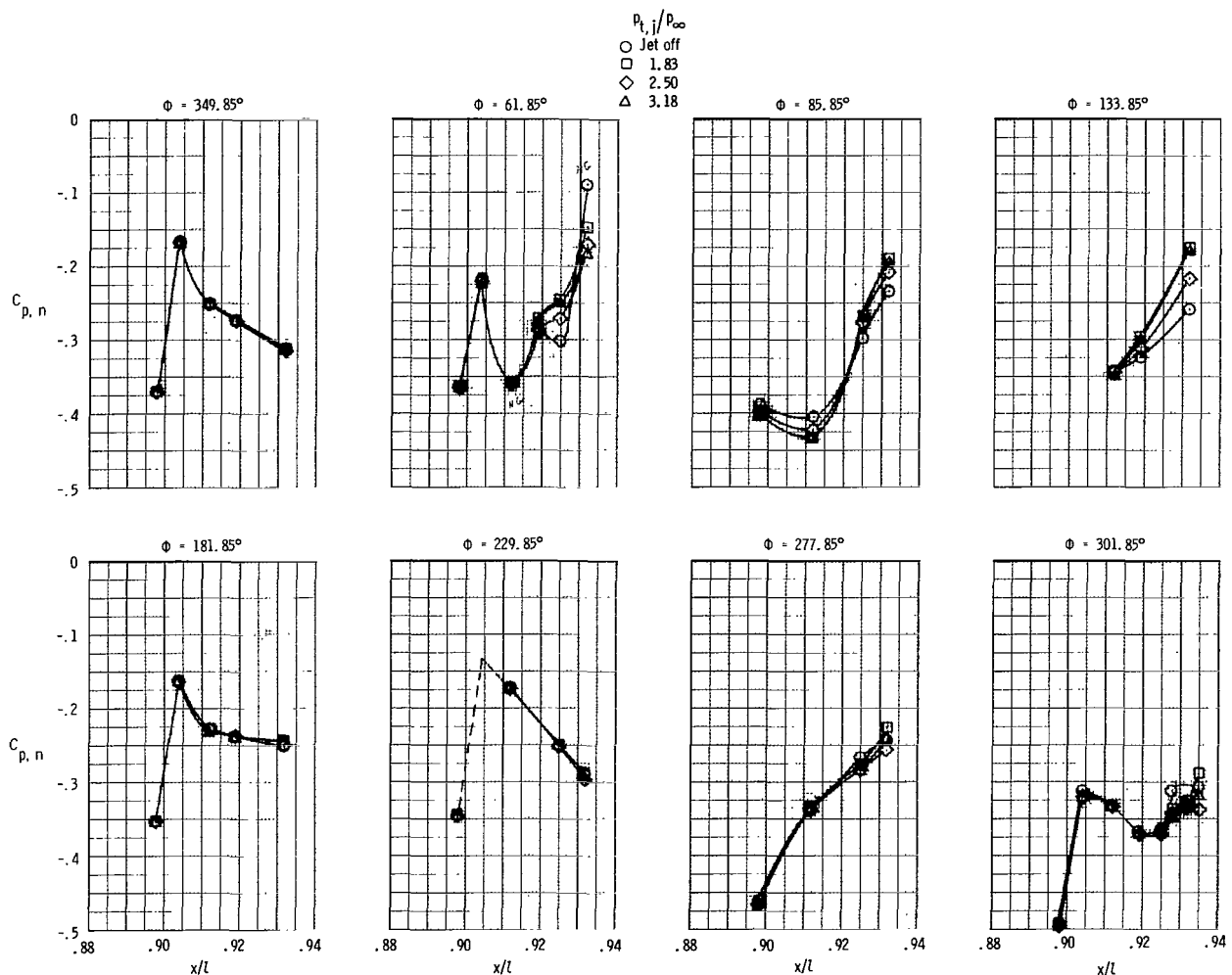
(1) $M = 0.896$; $\alpha = 3.11^\circ$.

Figure 13.- Continued.



(m) $M = 0.896; \alpha = 9.12^\circ$.

Figure 13.- Continued.



(n) $M = 1.190; \alpha = -0.68^\circ$.

Figure 13.- Continued.

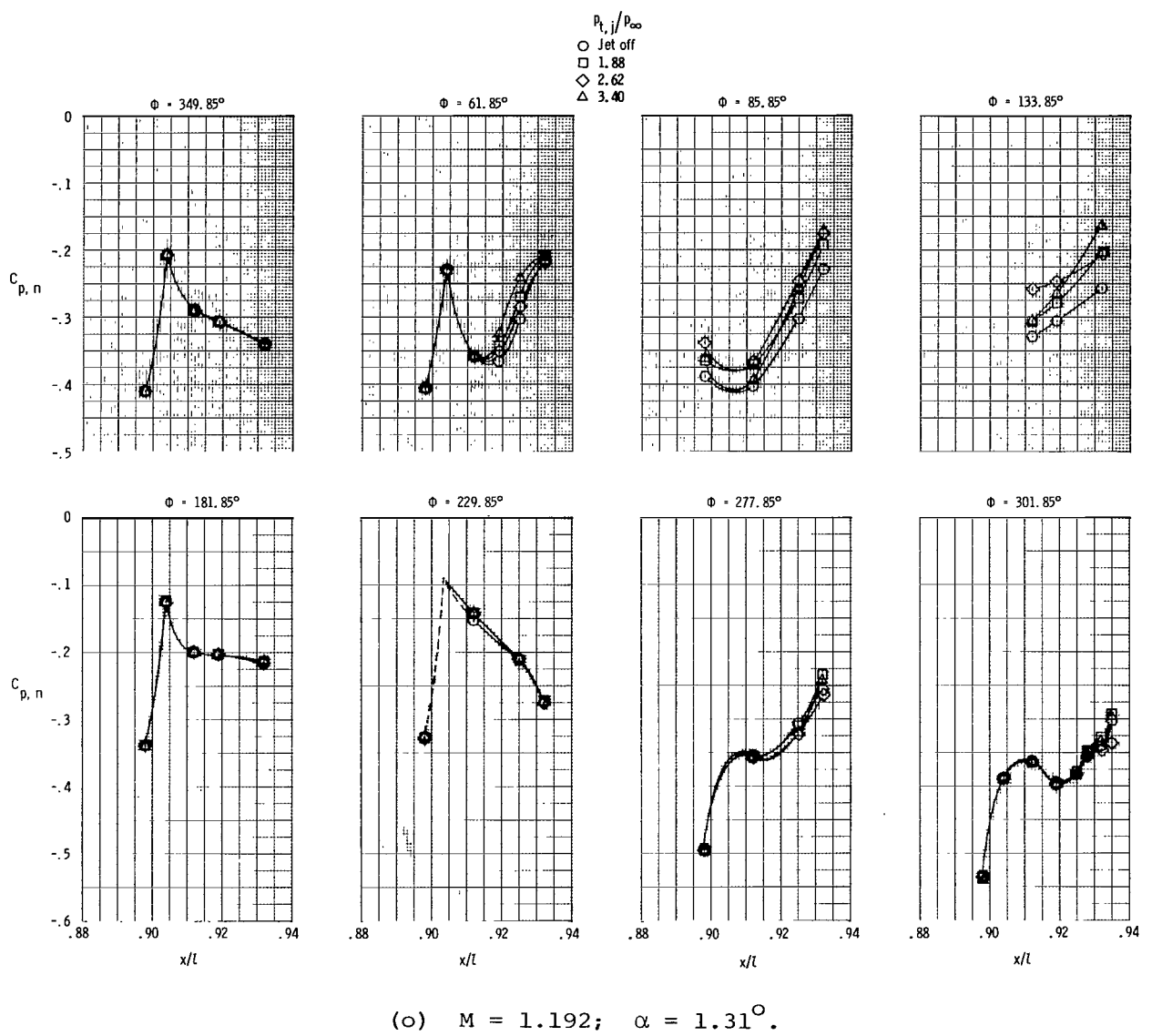
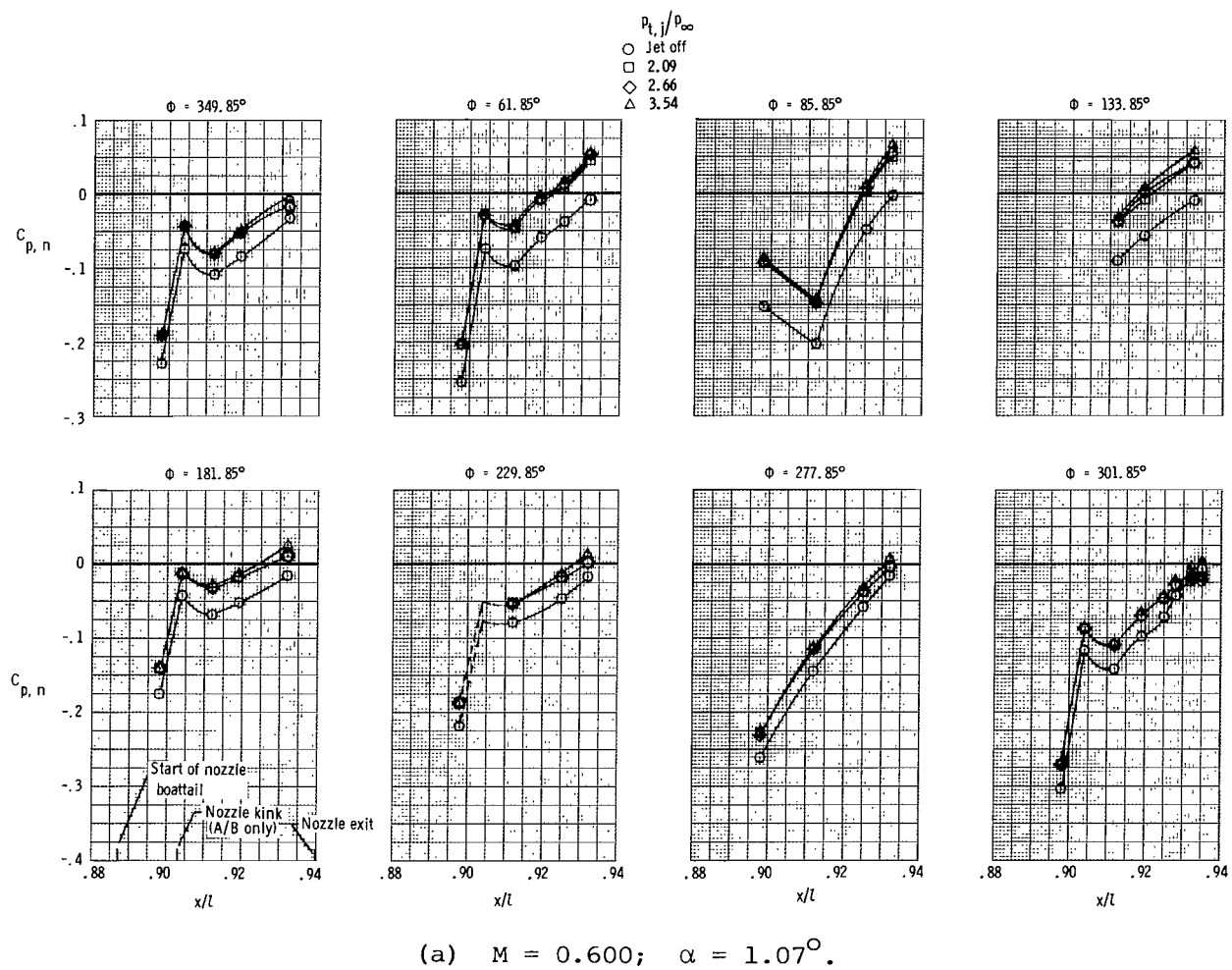
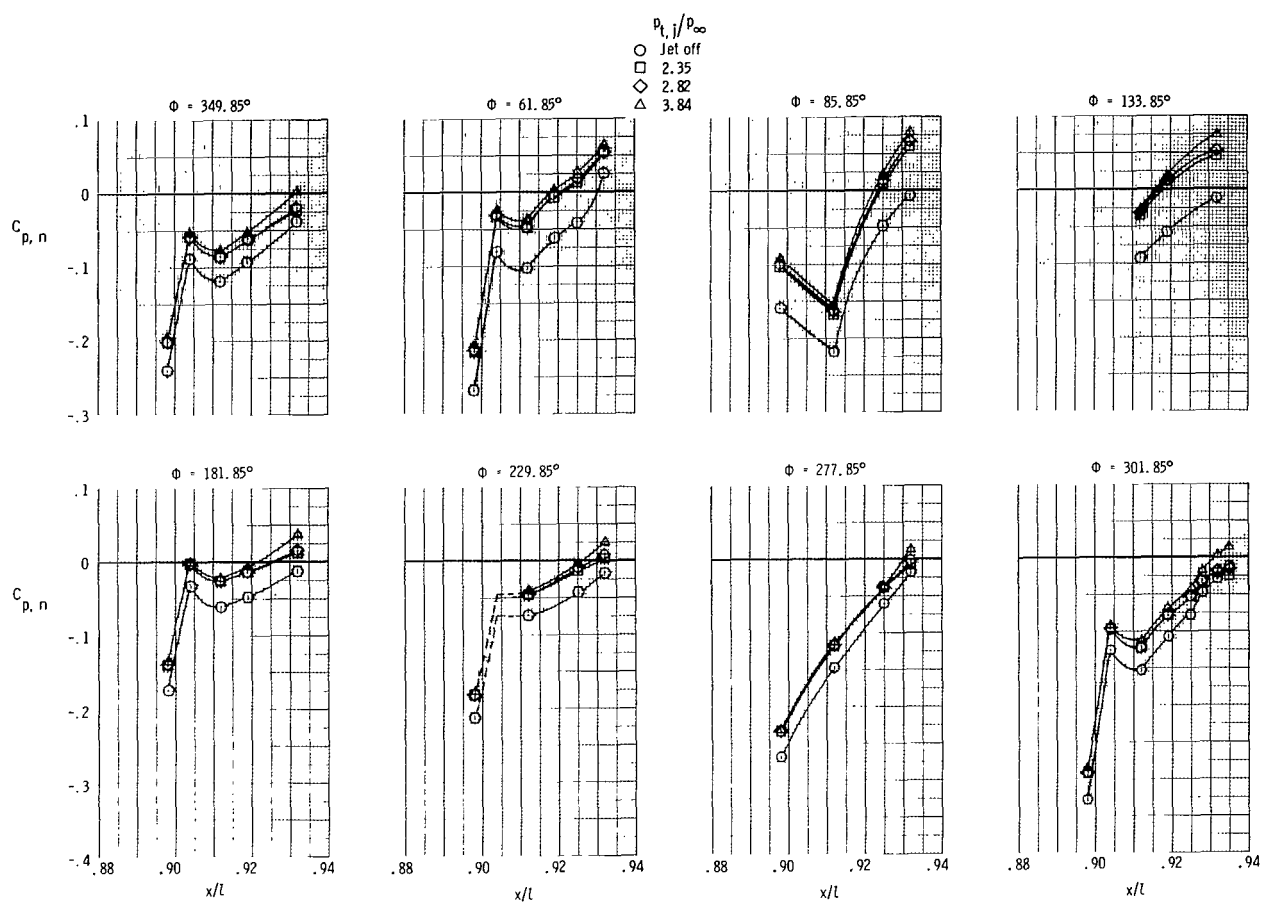


Figure 13.- Concluded.



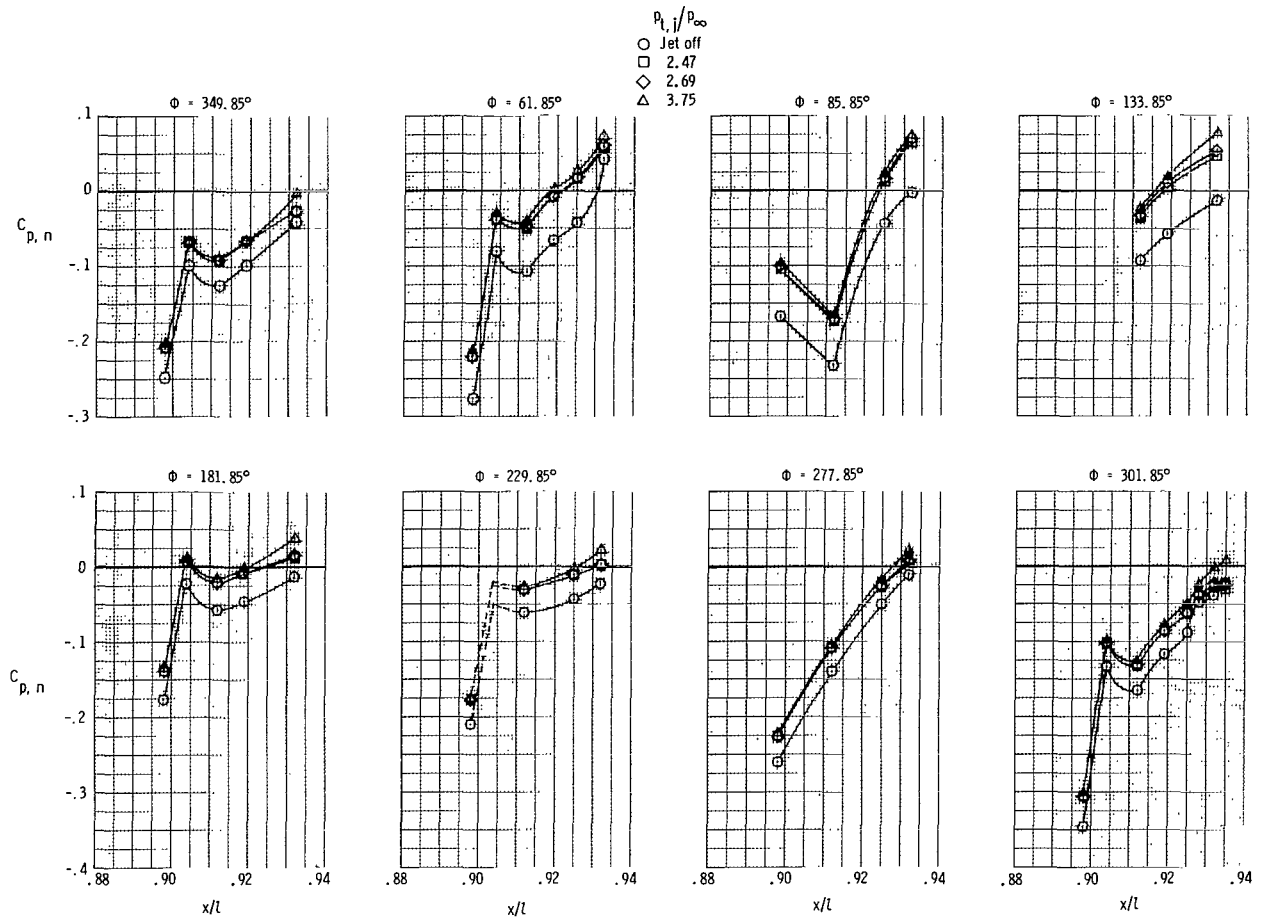
(a) $M = 0.600$; $\alpha = 1.07^\circ$.

Figure 14.- Static-pressure distributions on intermediate A/B power nozzle at several Mach number and angle-of-attack combinations for $\delta_h = -10^\circ$.



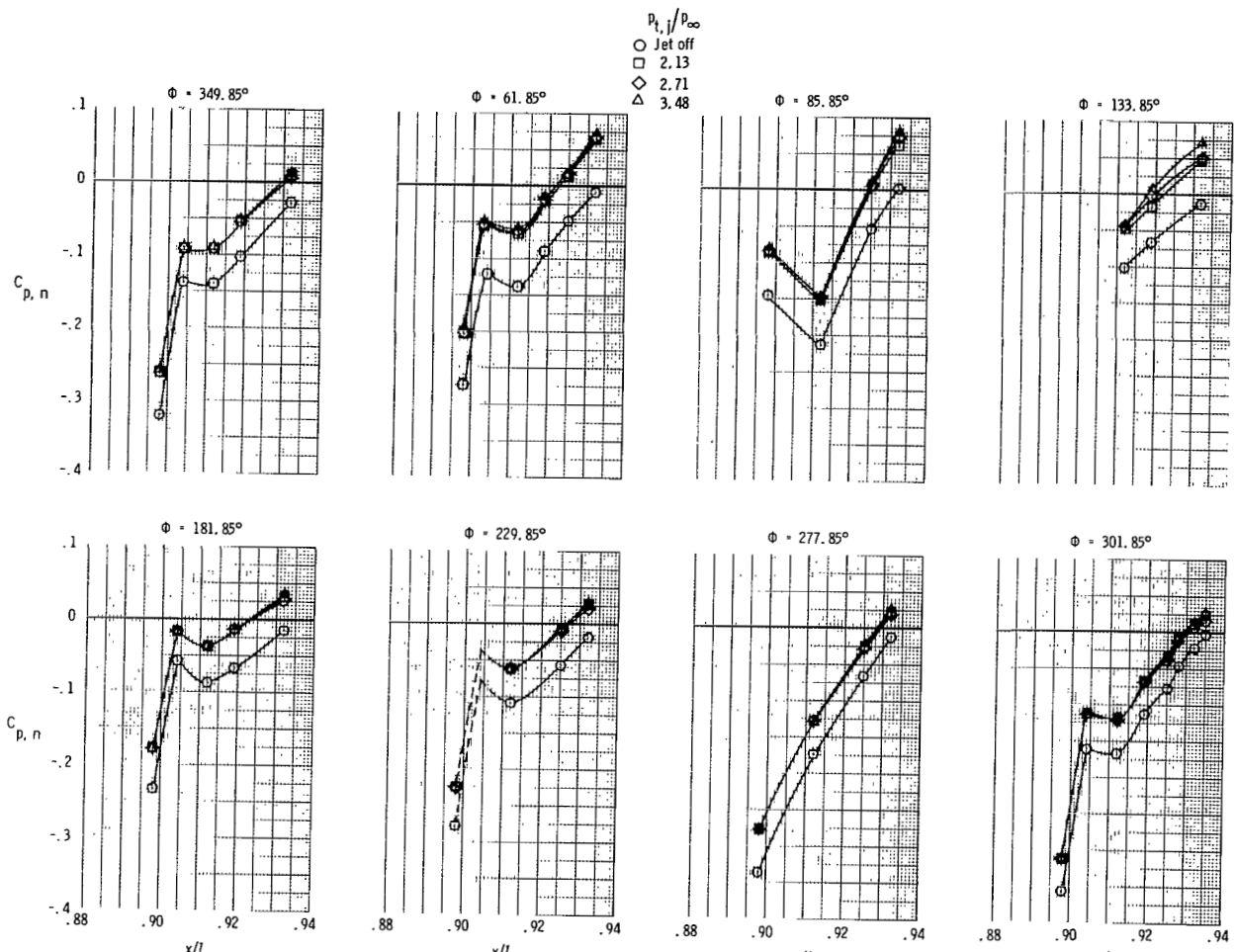
(b) $M = 0.600; \alpha = 3.08^\circ$.

Figure 14.- Continued.



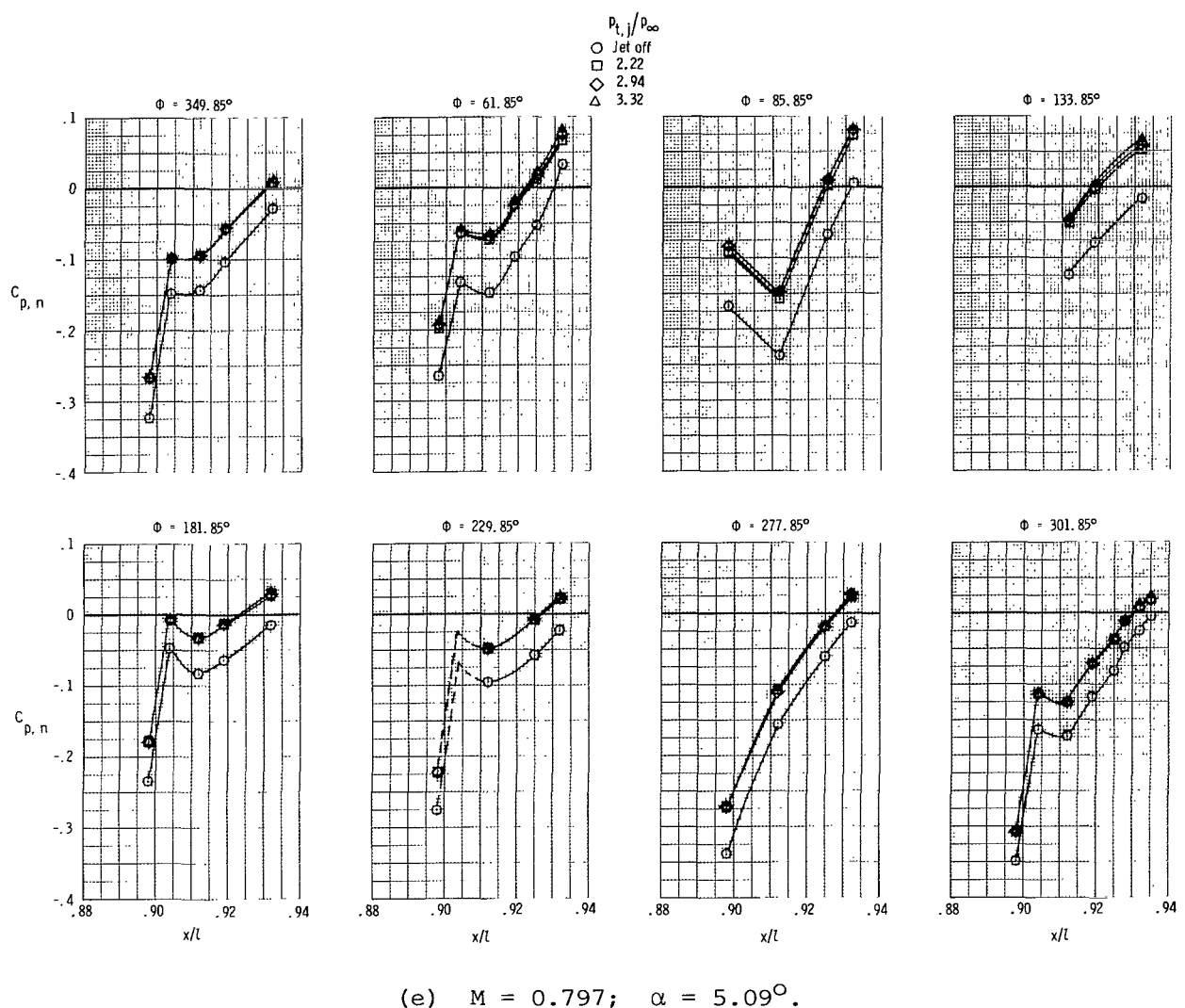
(c) $M = 0.600$; $\alpha = 5.09^\circ$.

Figure 14.- Continued.



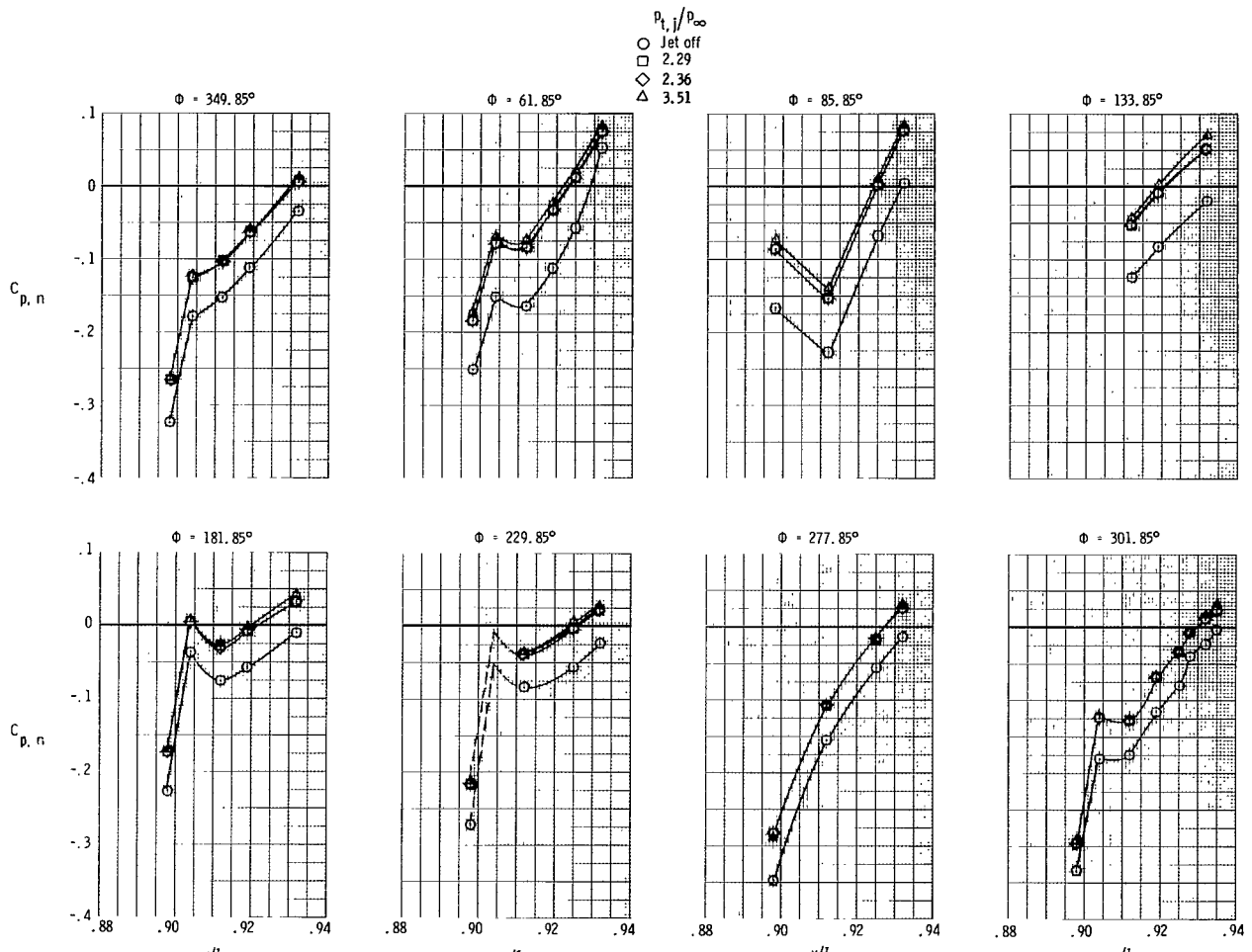
(d) $M = 0.798$; $\alpha = 3.08^\circ$.

Figure 14.- Continued.



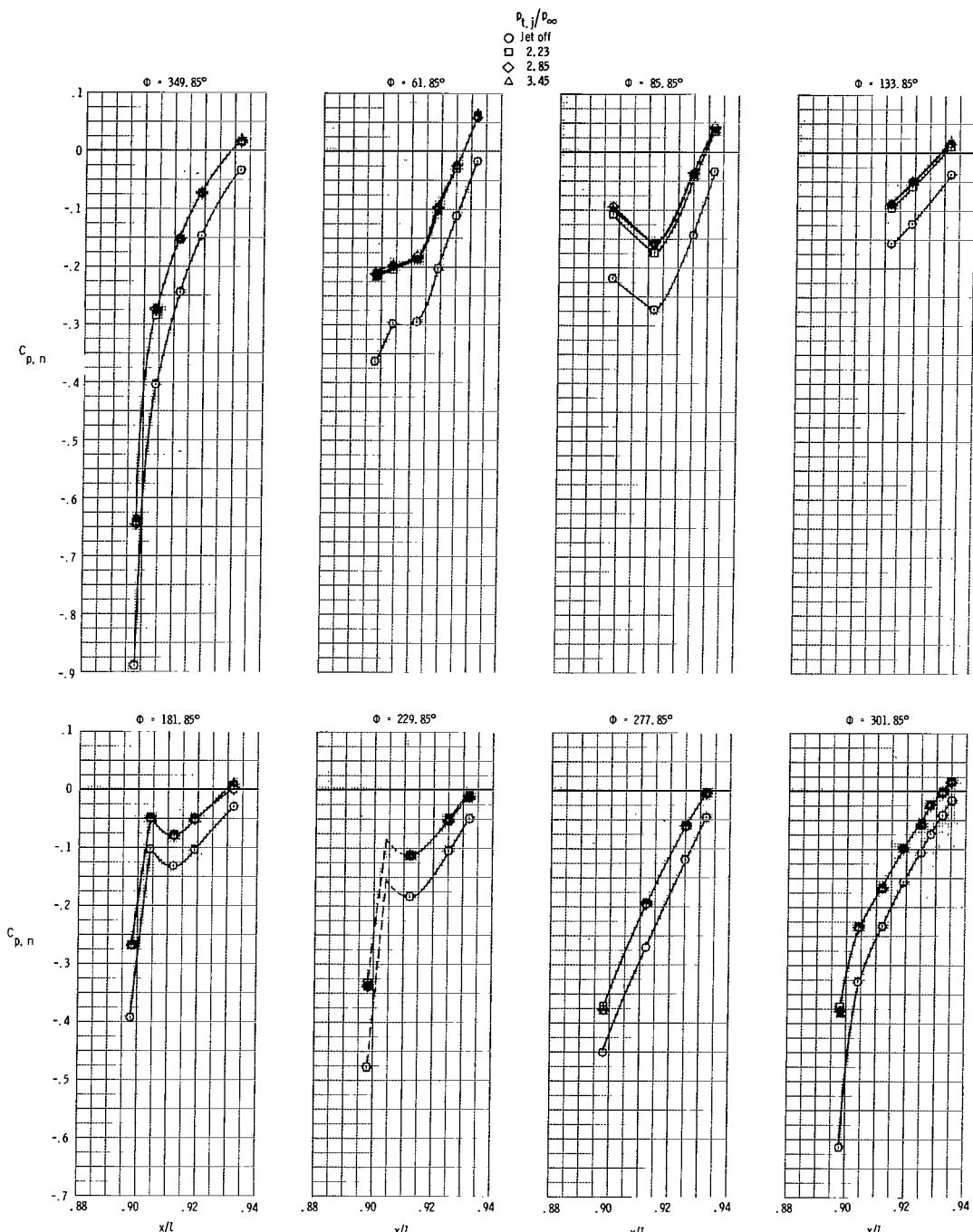
(e) $M = 0.797$; $\alpha = 5.09^\circ$.

Figure 14.- Continued.



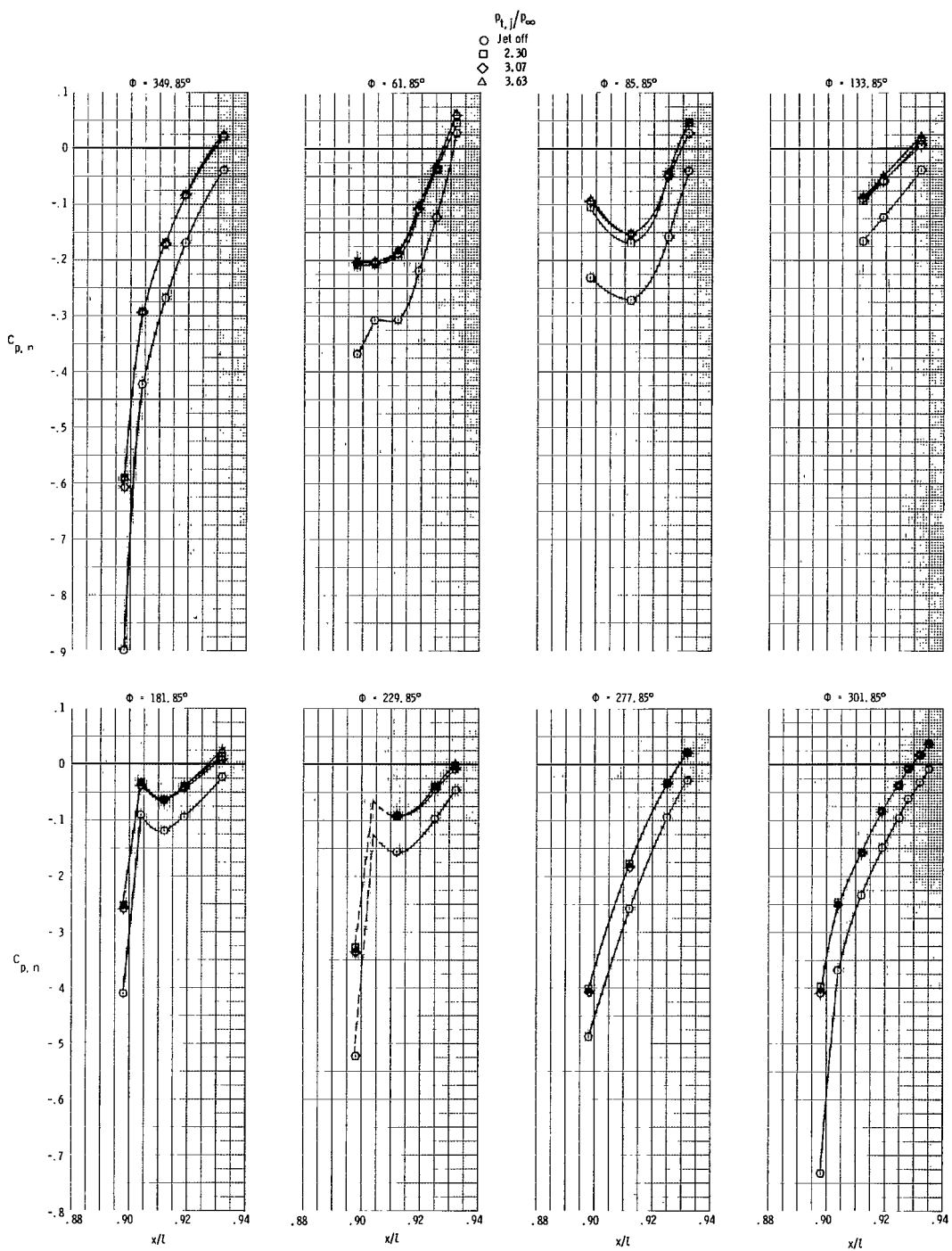
(f) $M = 0.798$; $\alpha = 7.11^\circ$.

Figure 14.- Continued.



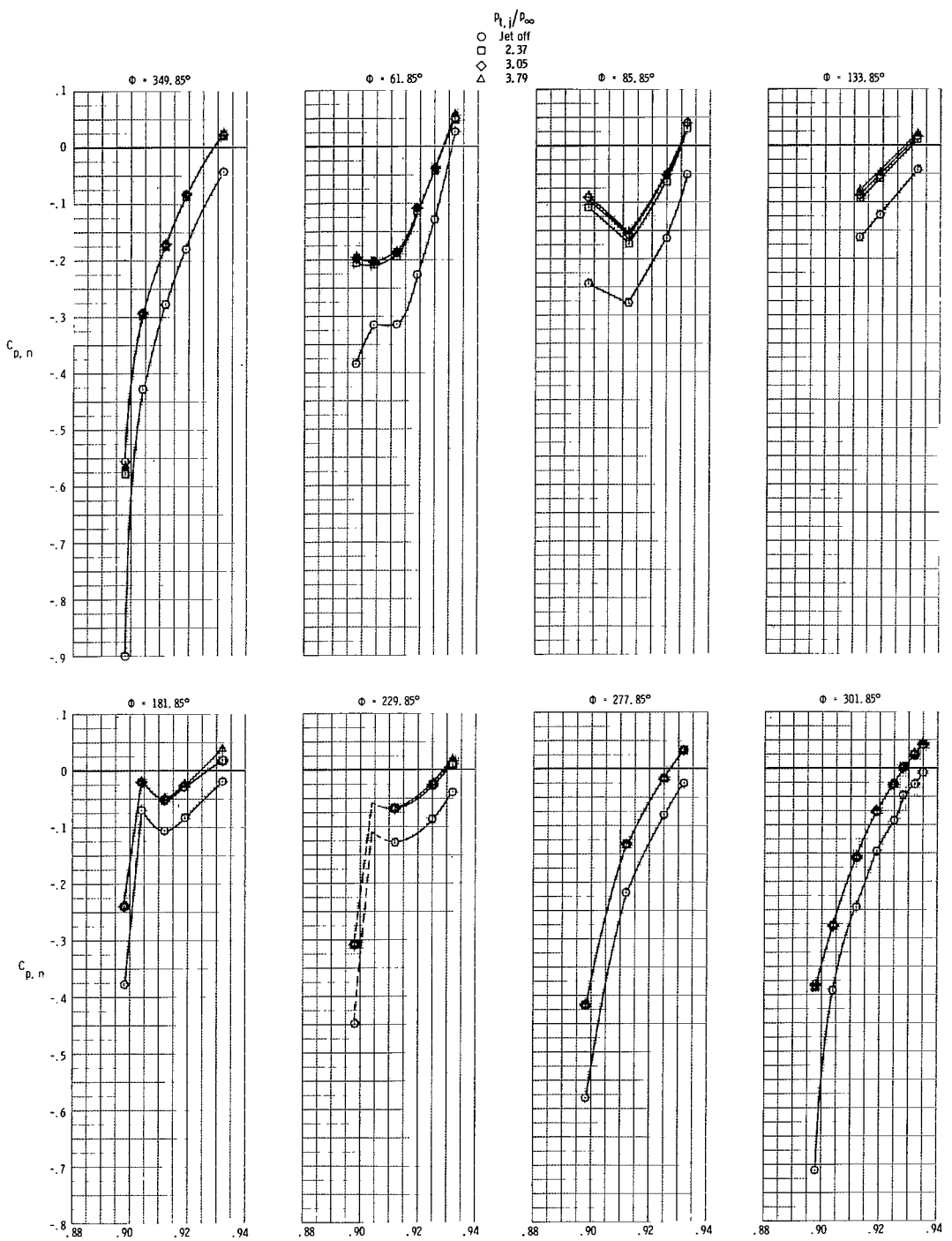
(g) $M = 0.870$; $\alpha = 5.09^\circ$.

Figure 14.- Continued.



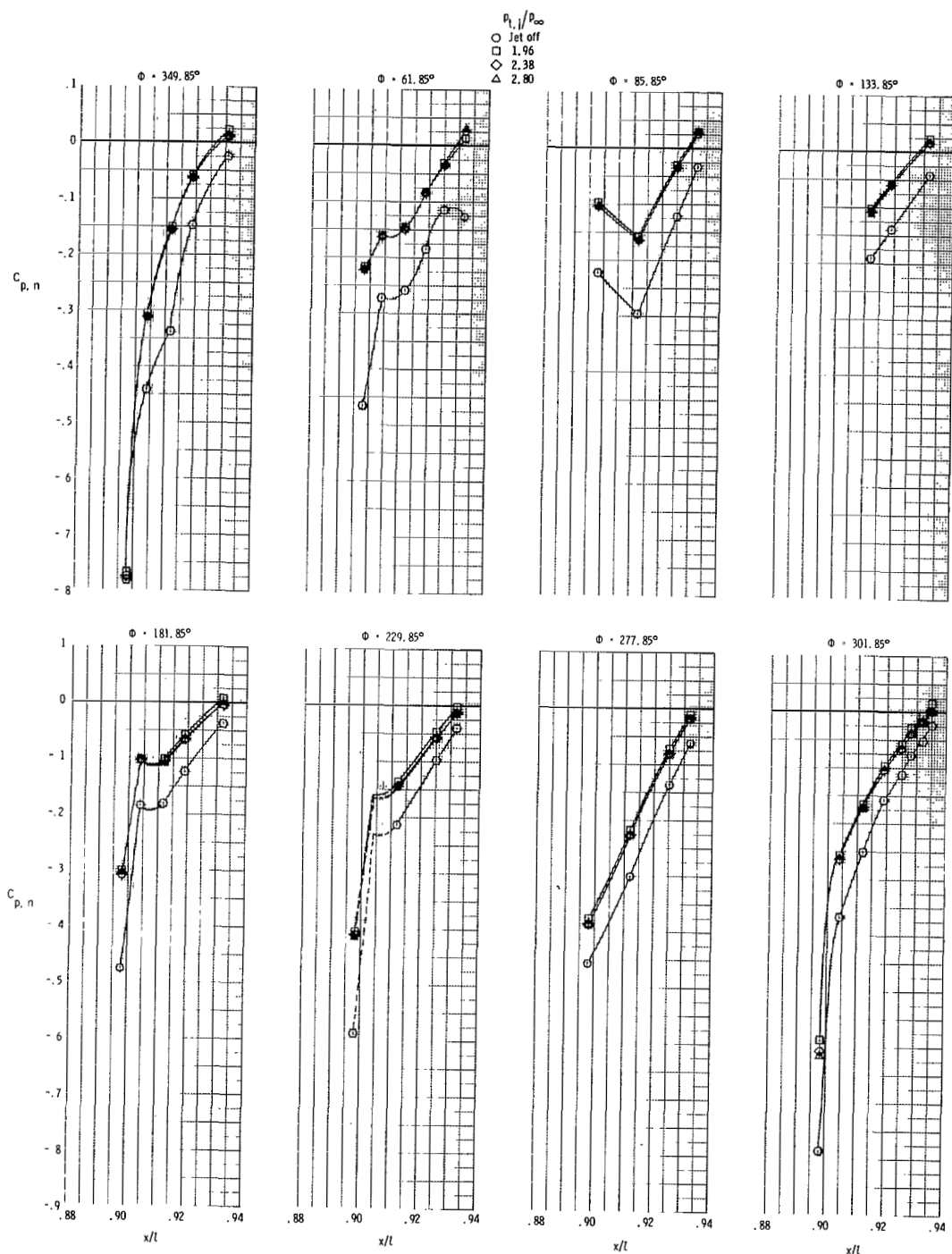
(h) $M = 0.870; \alpha = 7.11^\circ$.

Figure 14.- Continued.



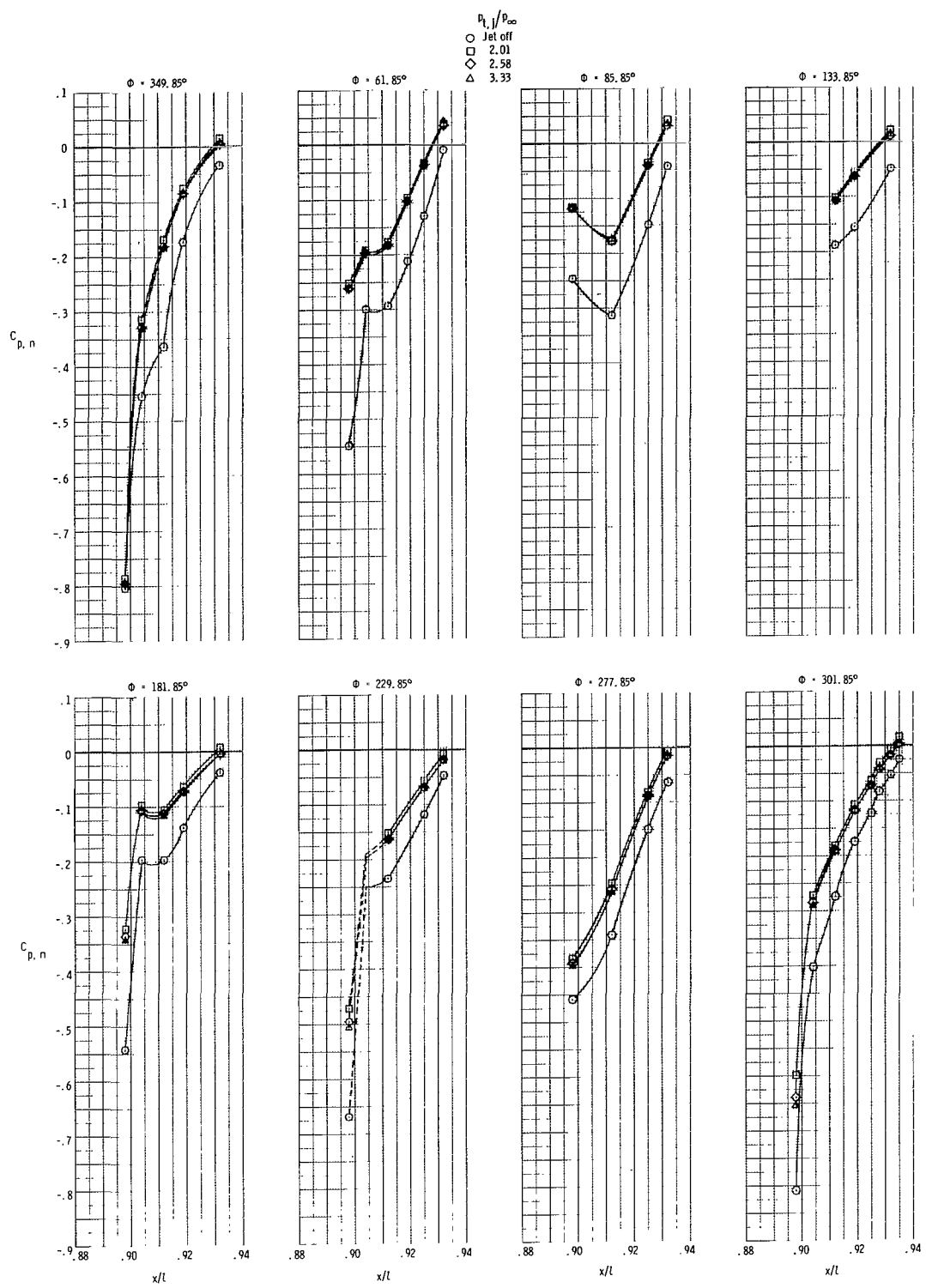
(i) $M = 0.870; \alpha = 9.14^\circ$.

Figure 14.- Continued.



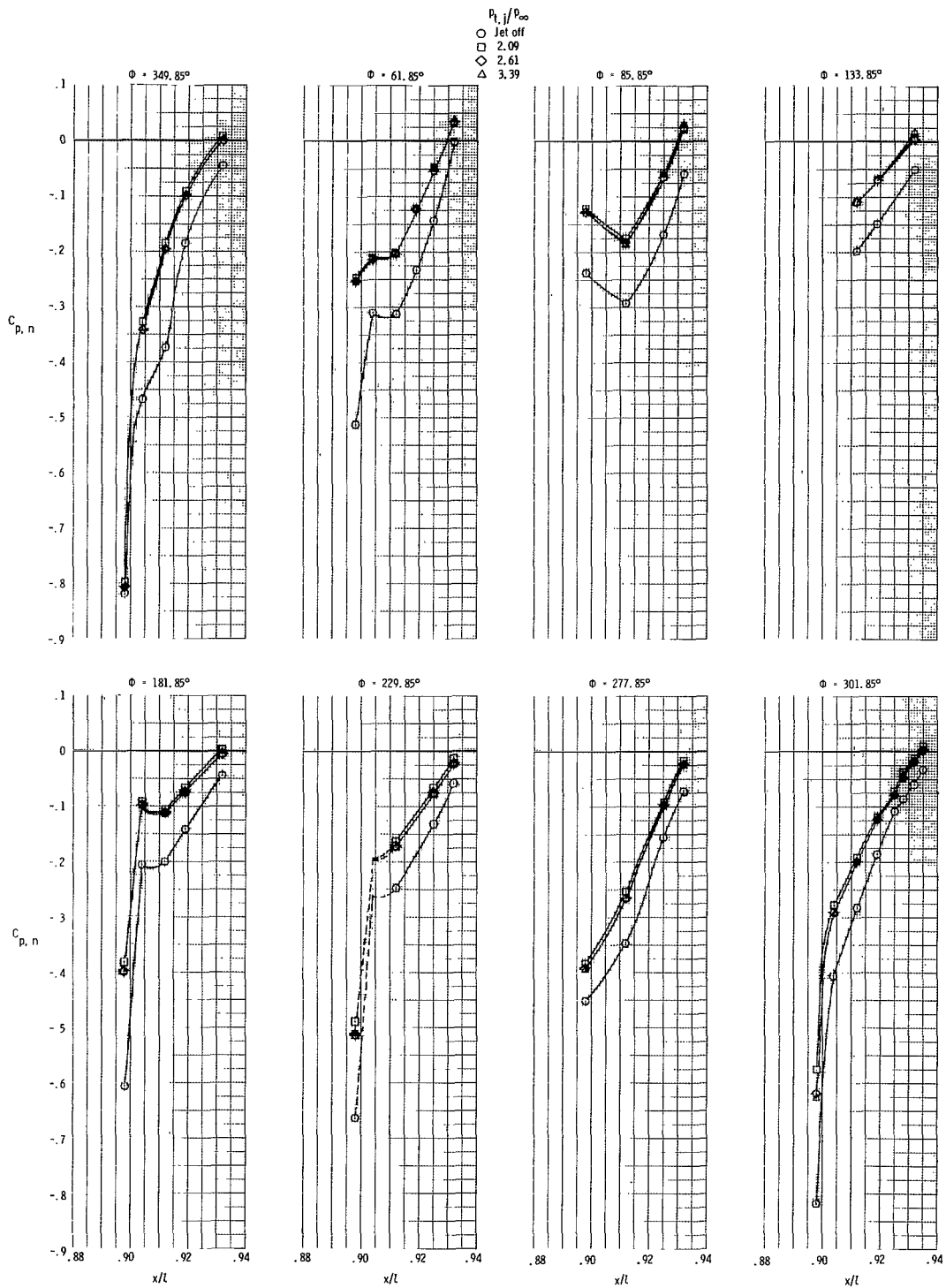
(j) $M = 0.896; \alpha = -0.92^\circ$.

Figure 14.- Continued.



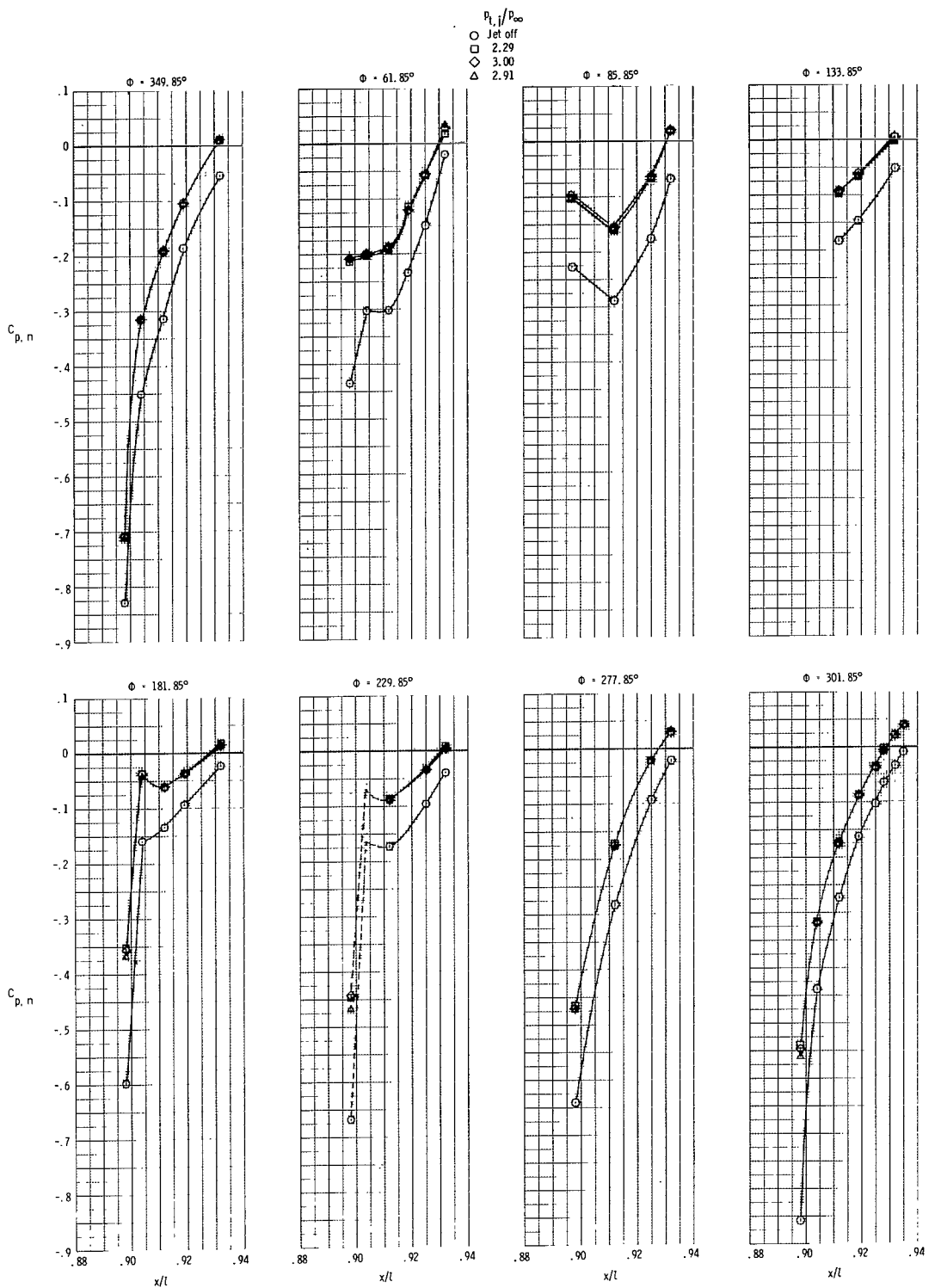
(k) $M = 0.896$; $\alpha = 1.08^\circ$.

Figure 14.- Continued.



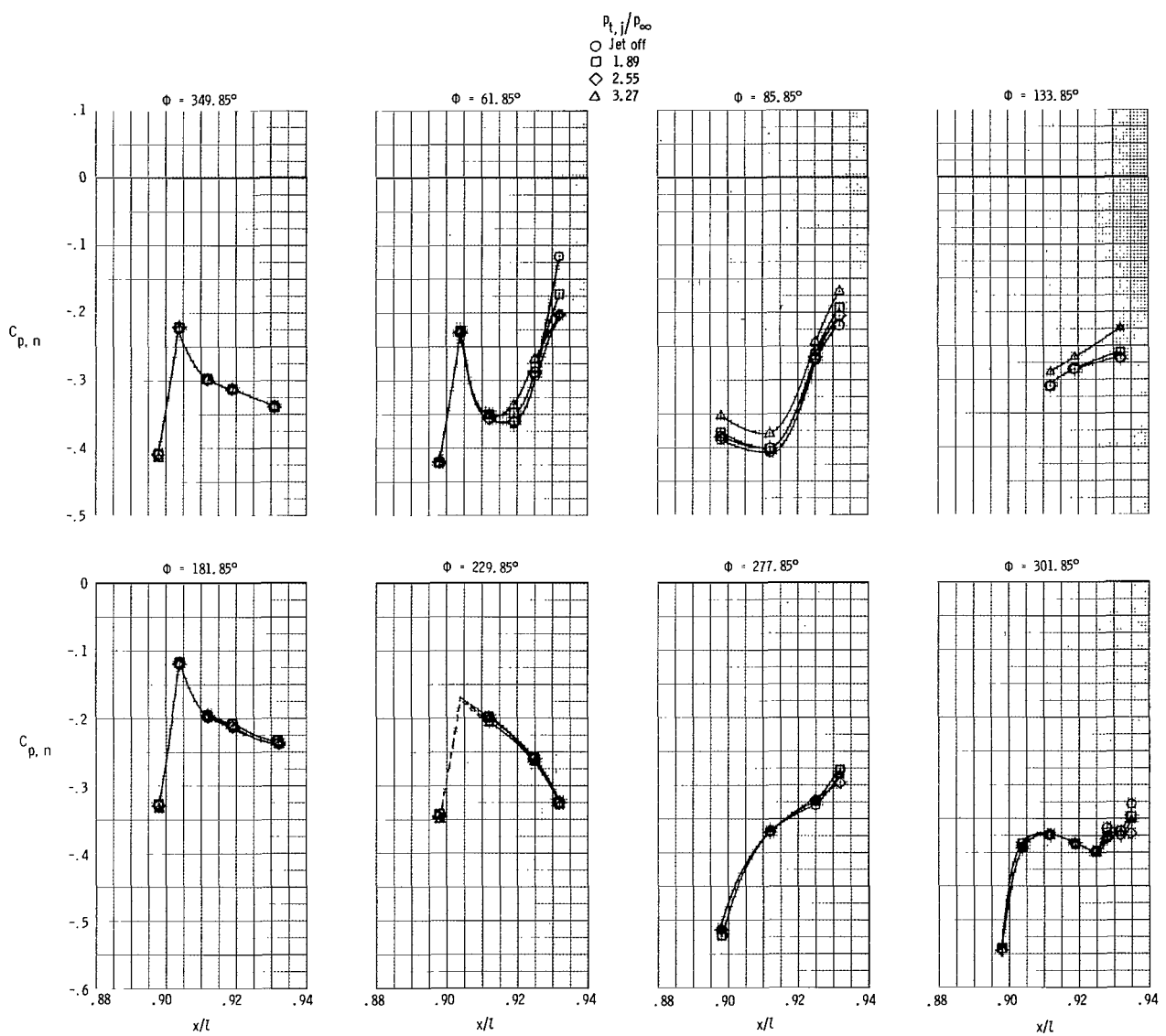
(1) $M = 0.897; \alpha = 3.08^\circ$.

Figure 14.- Continued.



(m) $M = 0.895; \alpha = 9.13^\circ.$

Figure 14.- Continued.



(n) $M = 1.190$; $\alpha = 1.85^\circ$.

Figure 14.- Concluded.

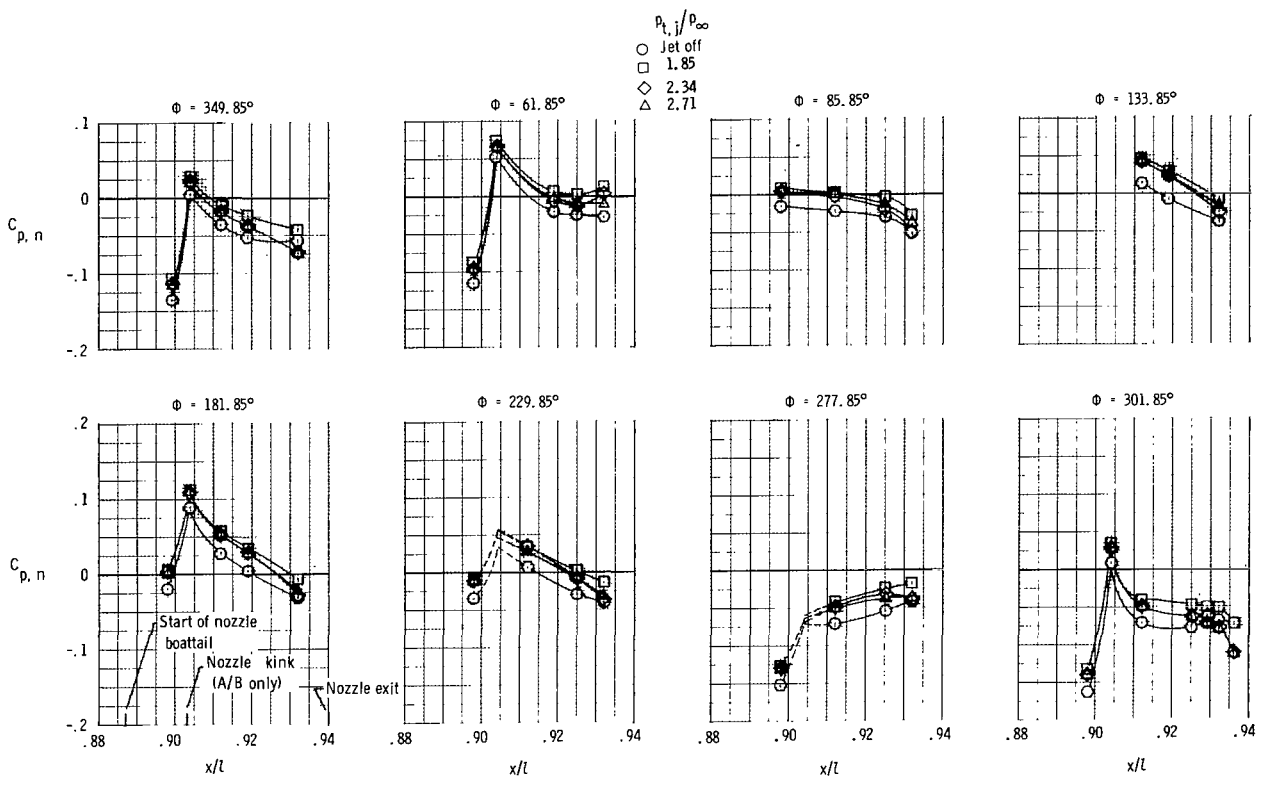
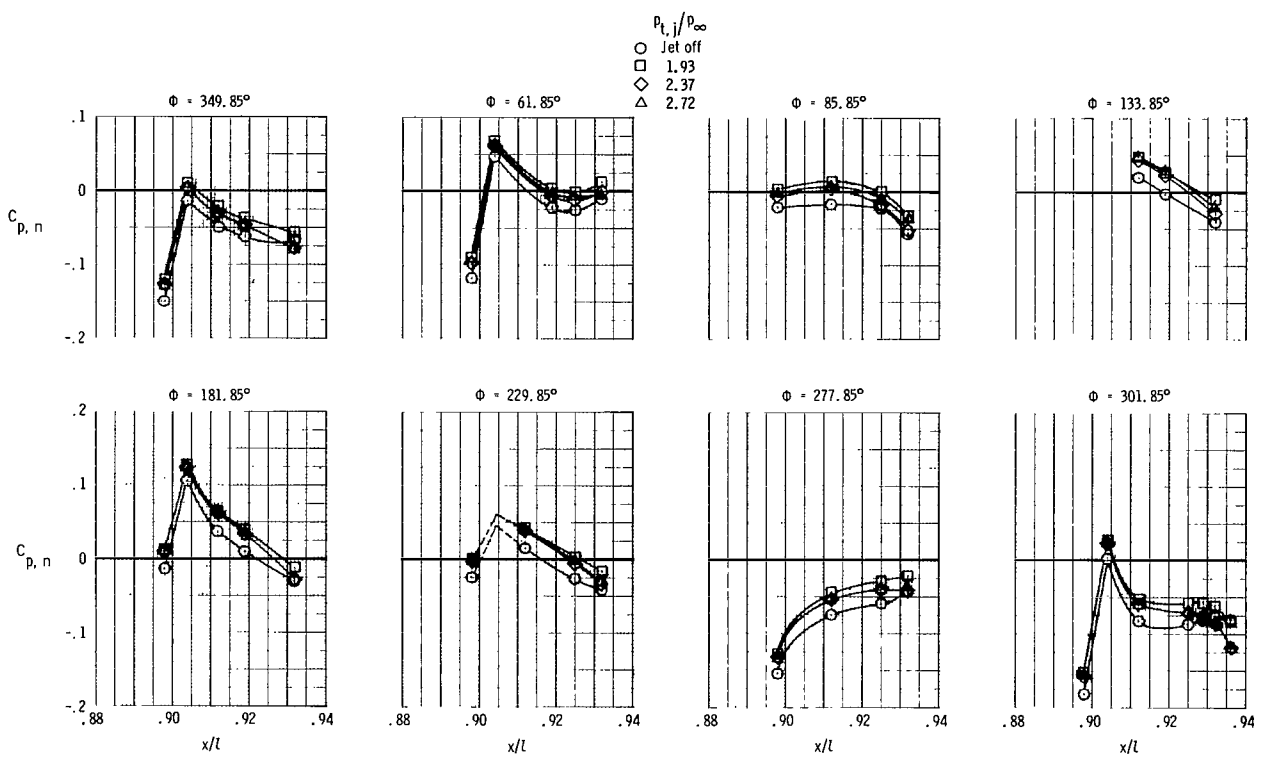
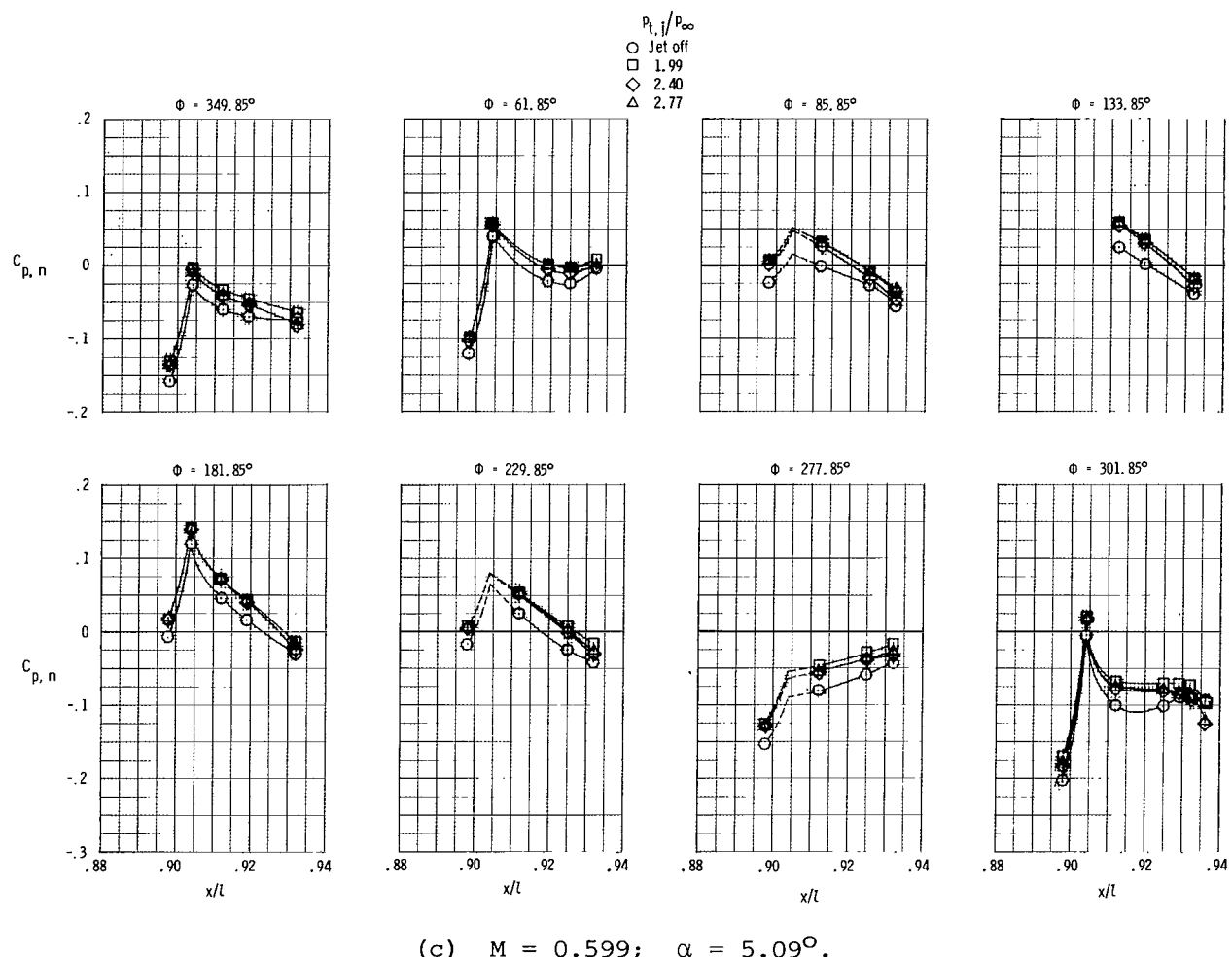


Figure 15.- Static-pressure distributions on max. A/B power nozzle at several Mach number and angle-of-attack combinations for $\delta_h = 0^\circ$.



(b) $M = 0.600$; $\alpha = 3.07^\circ$.

Figure 15.- Continued.



(c) $M = 0.599$; $\alpha = 5.09^\circ$.

Figure 15.- Continued.

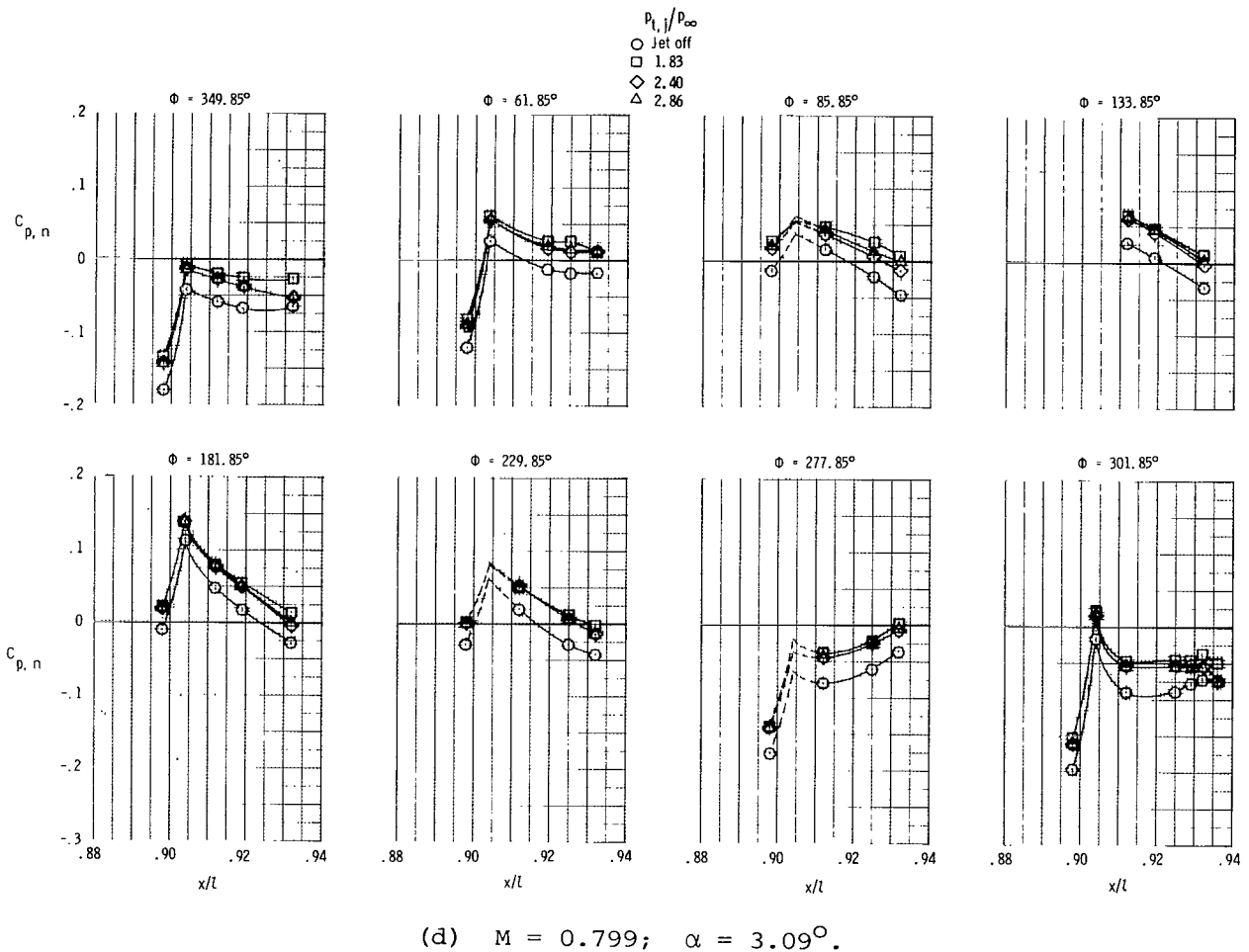


Figure 15.- Continued.

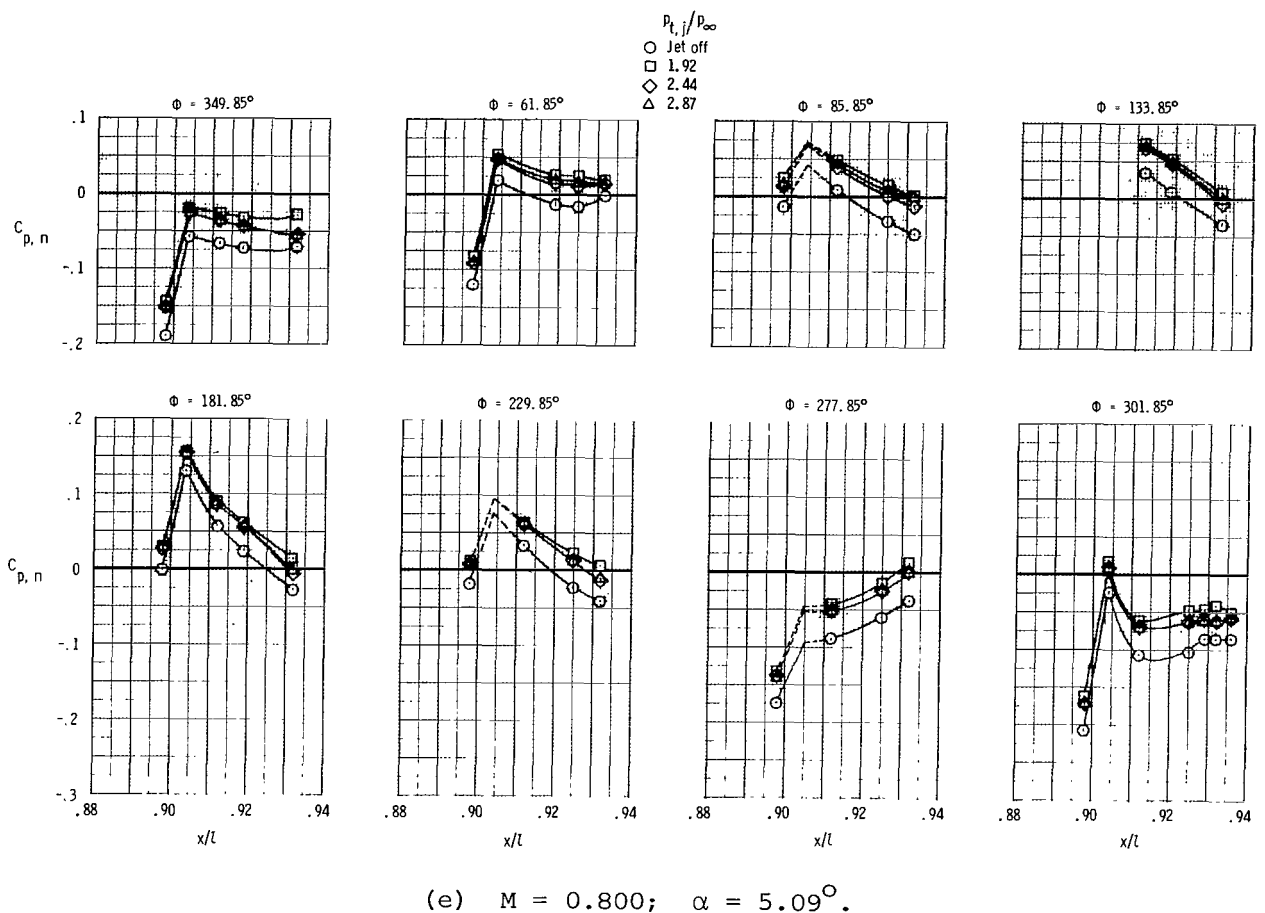
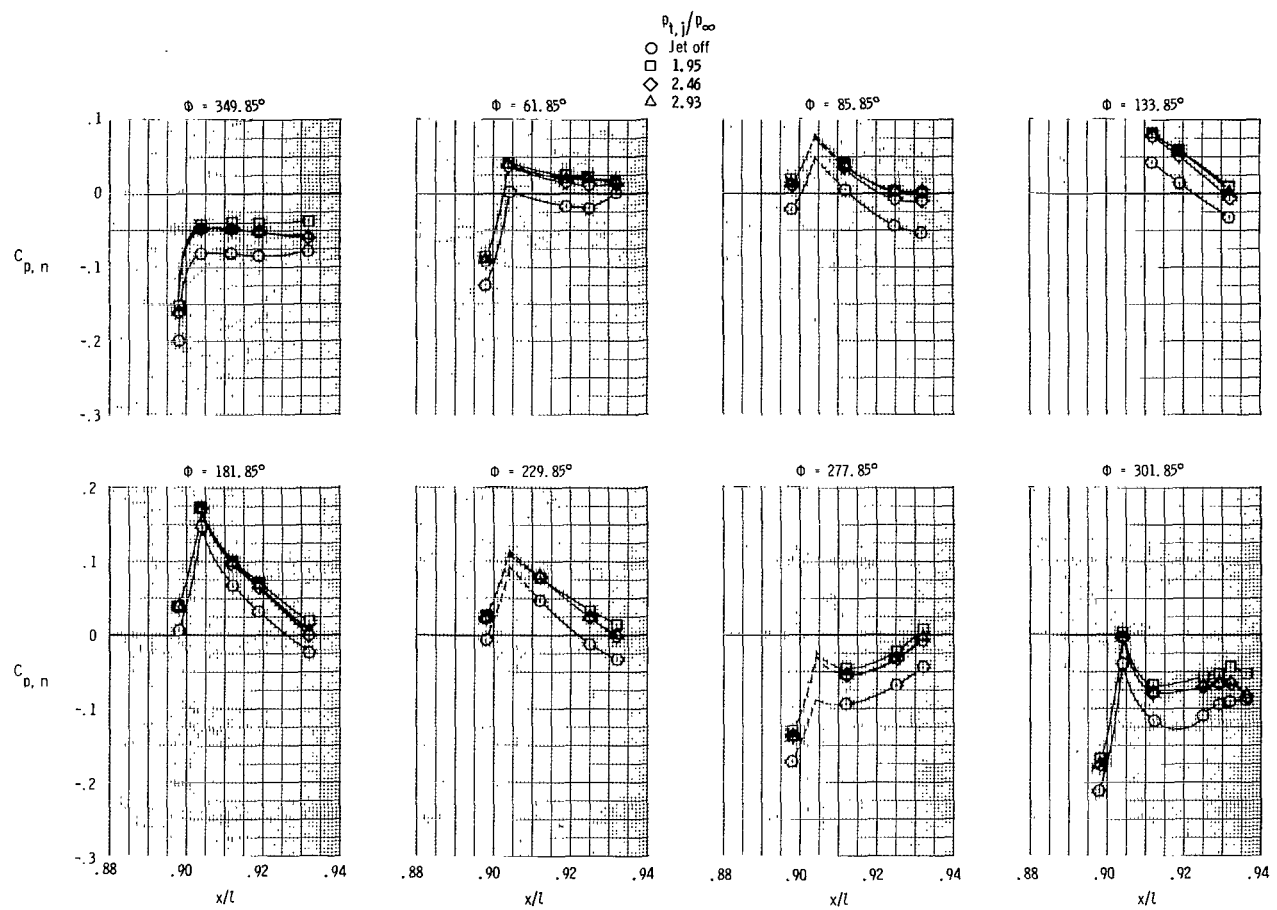
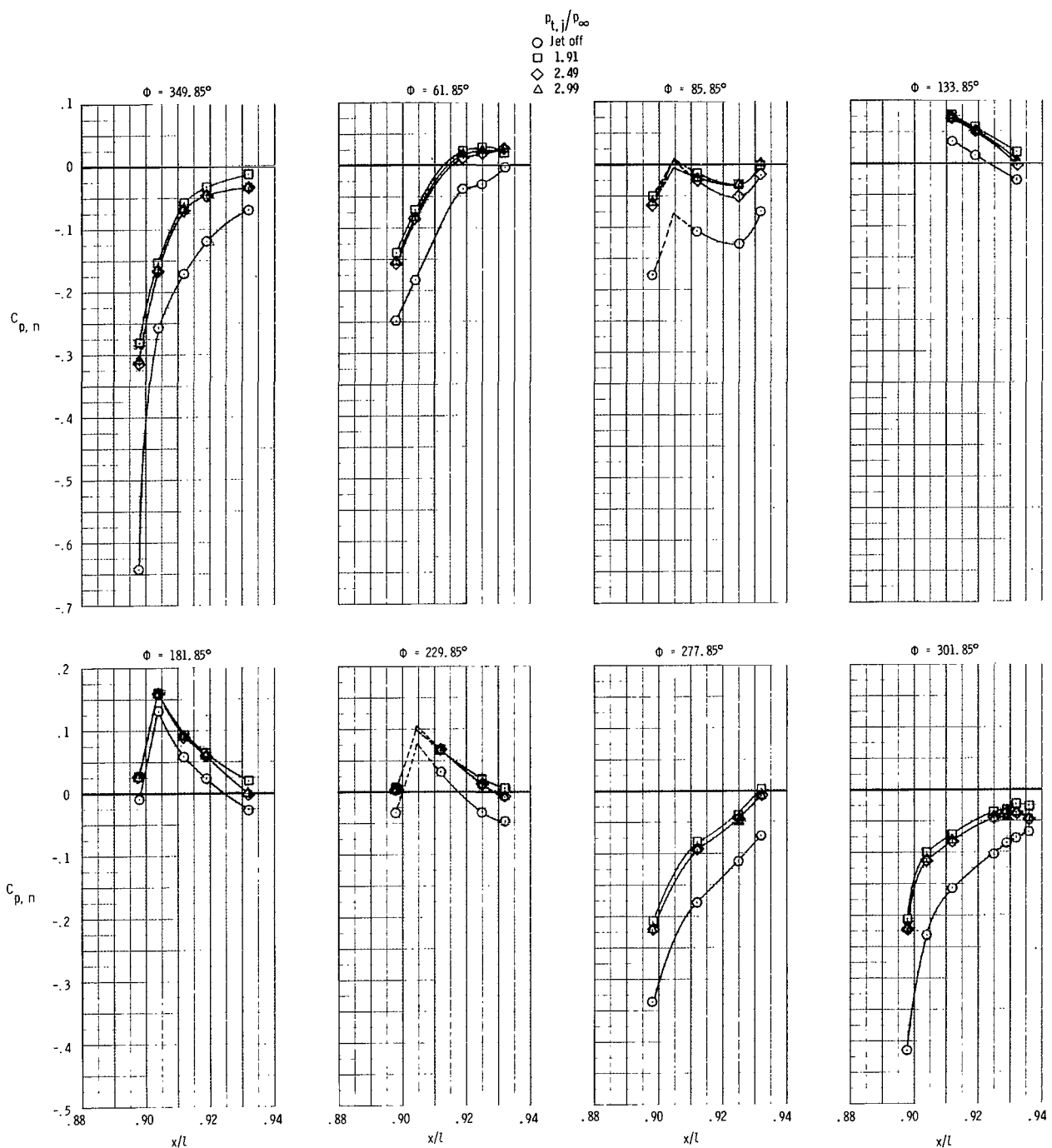


Figure 15.- Continued.



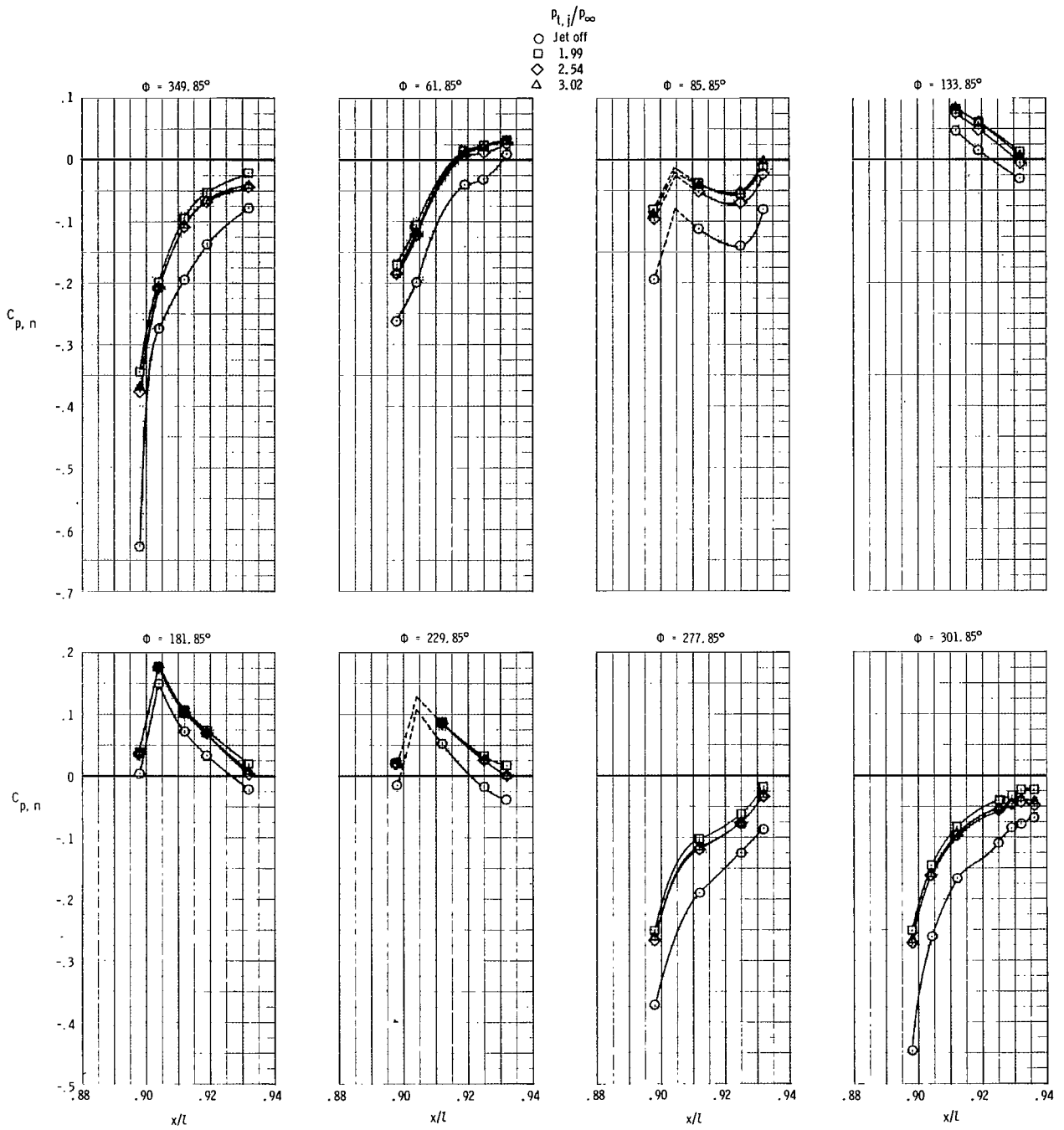
(f) $M = 0.796$; $\alpha = 7.10^\circ$.

Figure 15.- Continued.



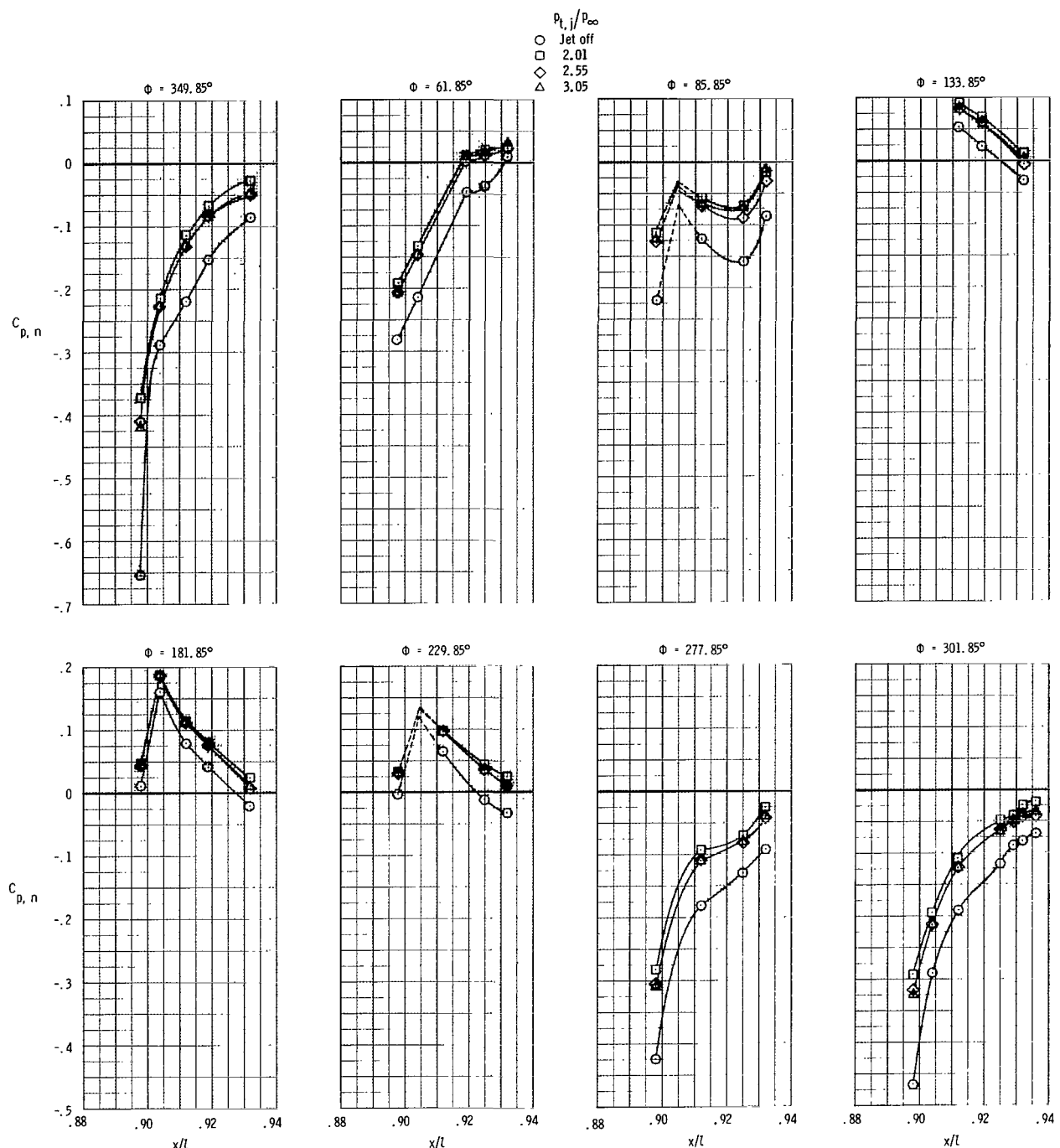
(g) $M = 0.870; \alpha = 5.10^\circ$.

Figure 15.- Continued.



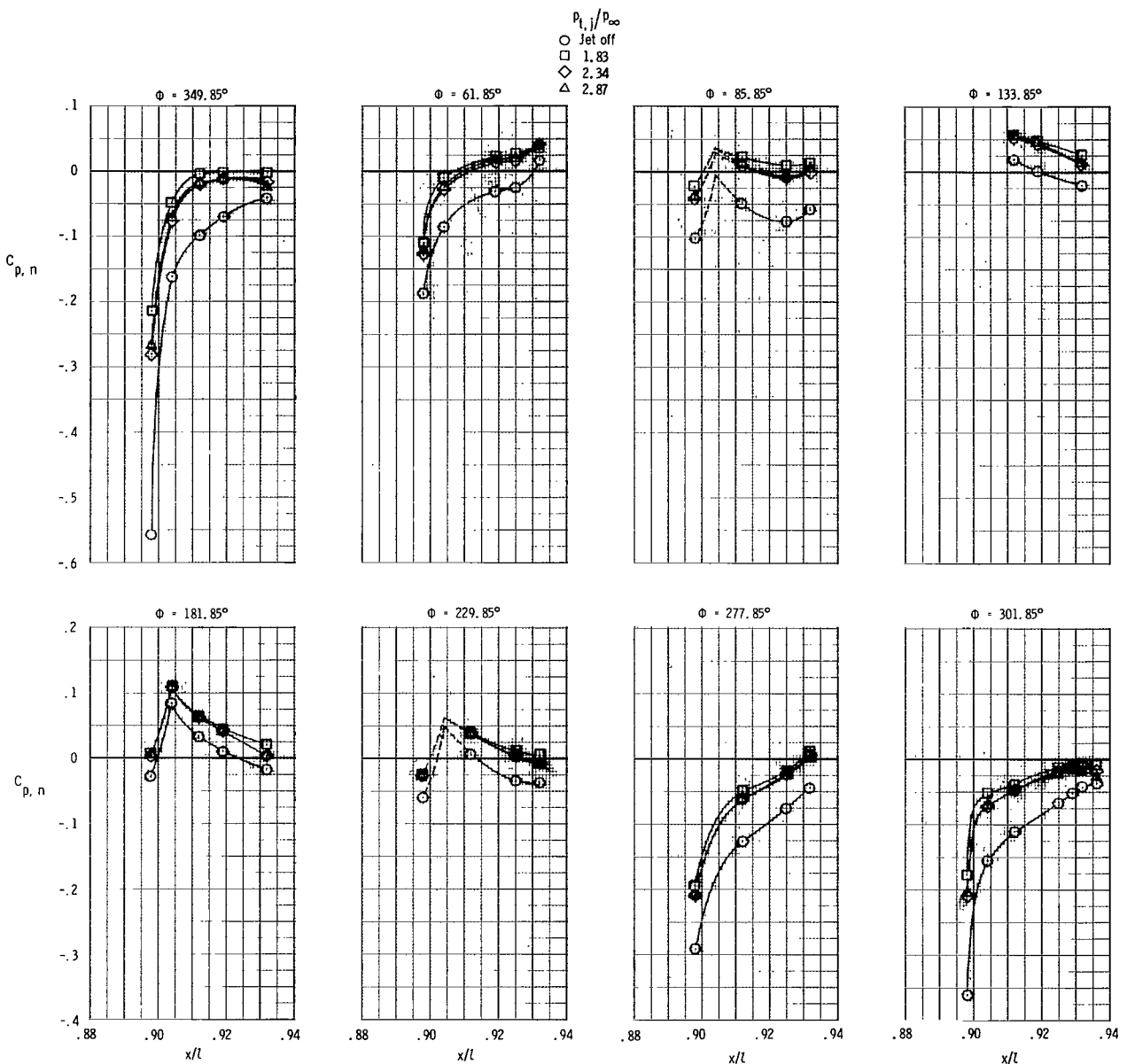
(h) $M = 0.870$; $\alpha = 7.11^\circ$.

Figure 15.- Continued.



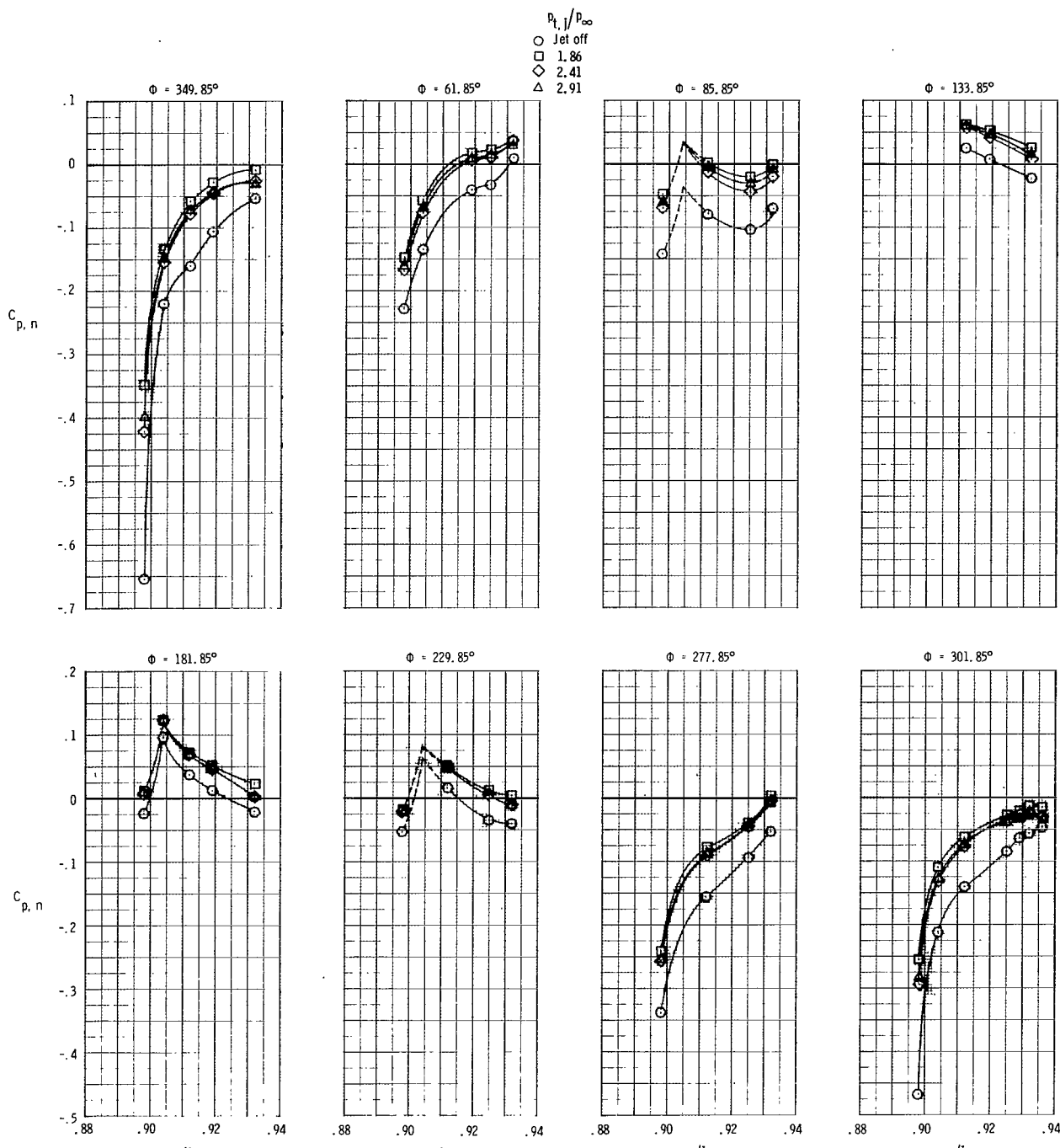
(i) $M = 0.870$; $\alpha = 9.12^\circ$.

Figure 15.- Continued.



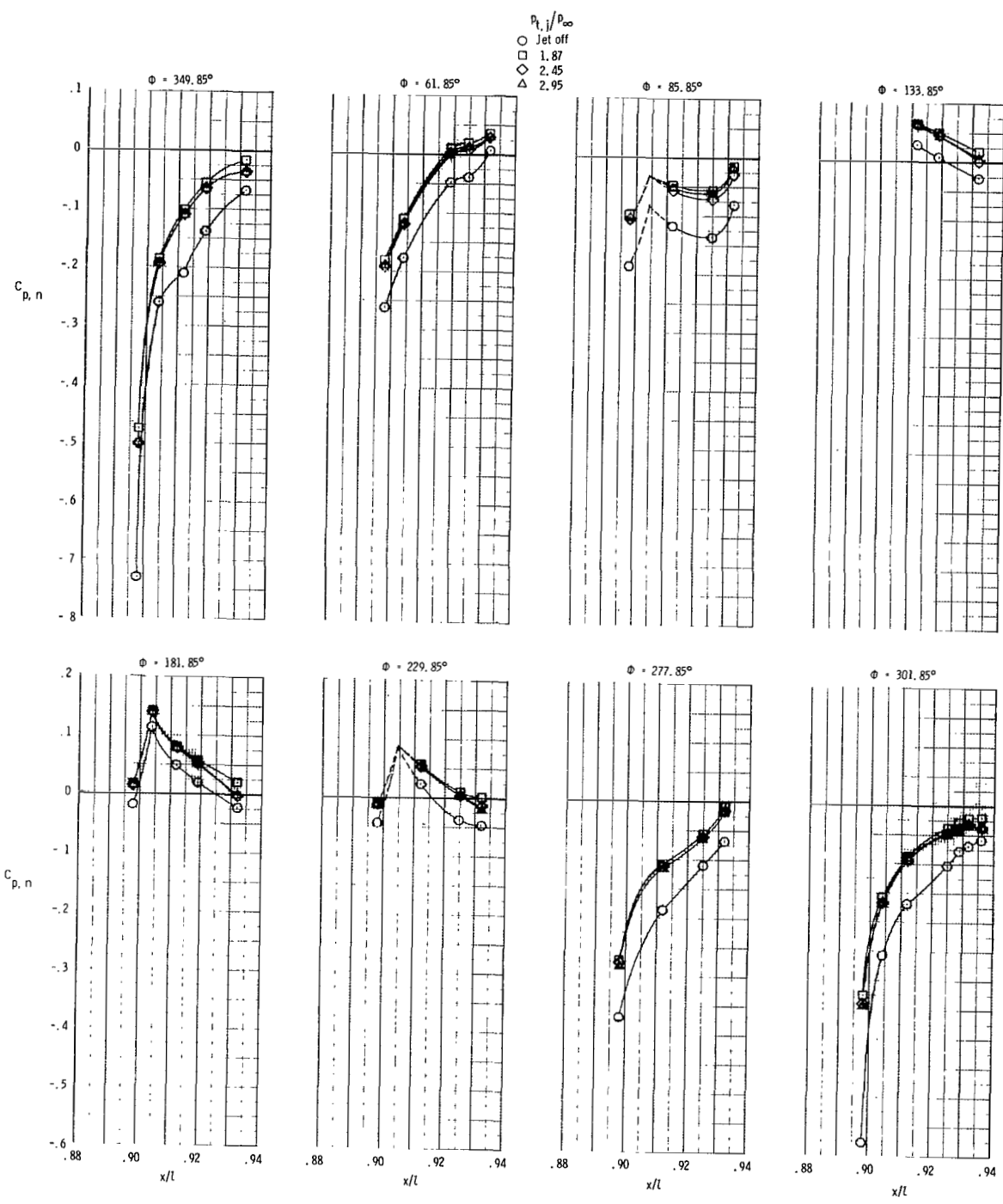
(j) $M = 0.896; \alpha = -0.87^\circ$.

Figure 15.- Continued.



(k) $M = 0.896$; $\alpha = 1.12^\circ$.

Figure 15.- Continued.



(1) $M = 0.897$; $\alpha = 3.11^\circ$.

Figure 15.- Continued.

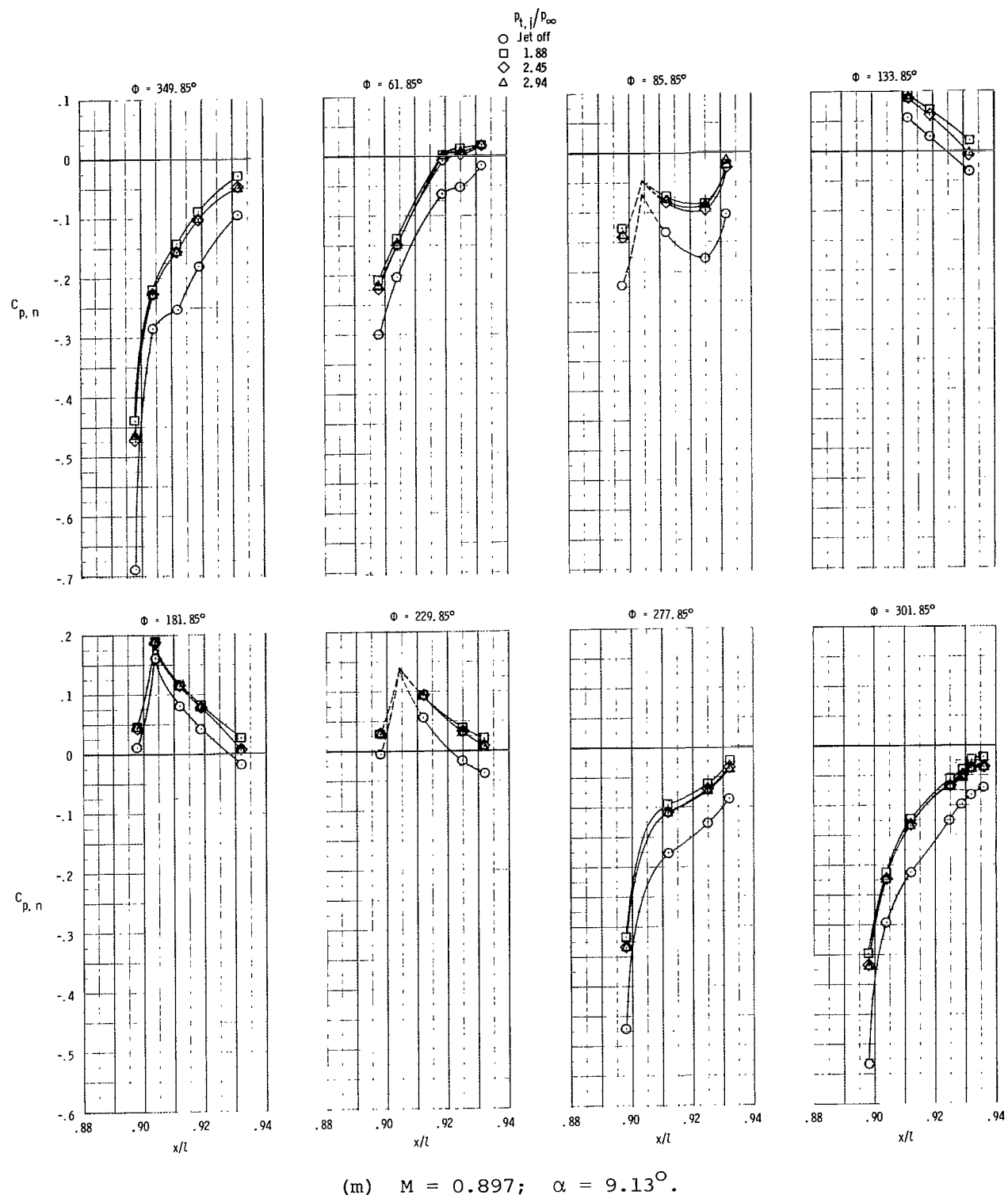
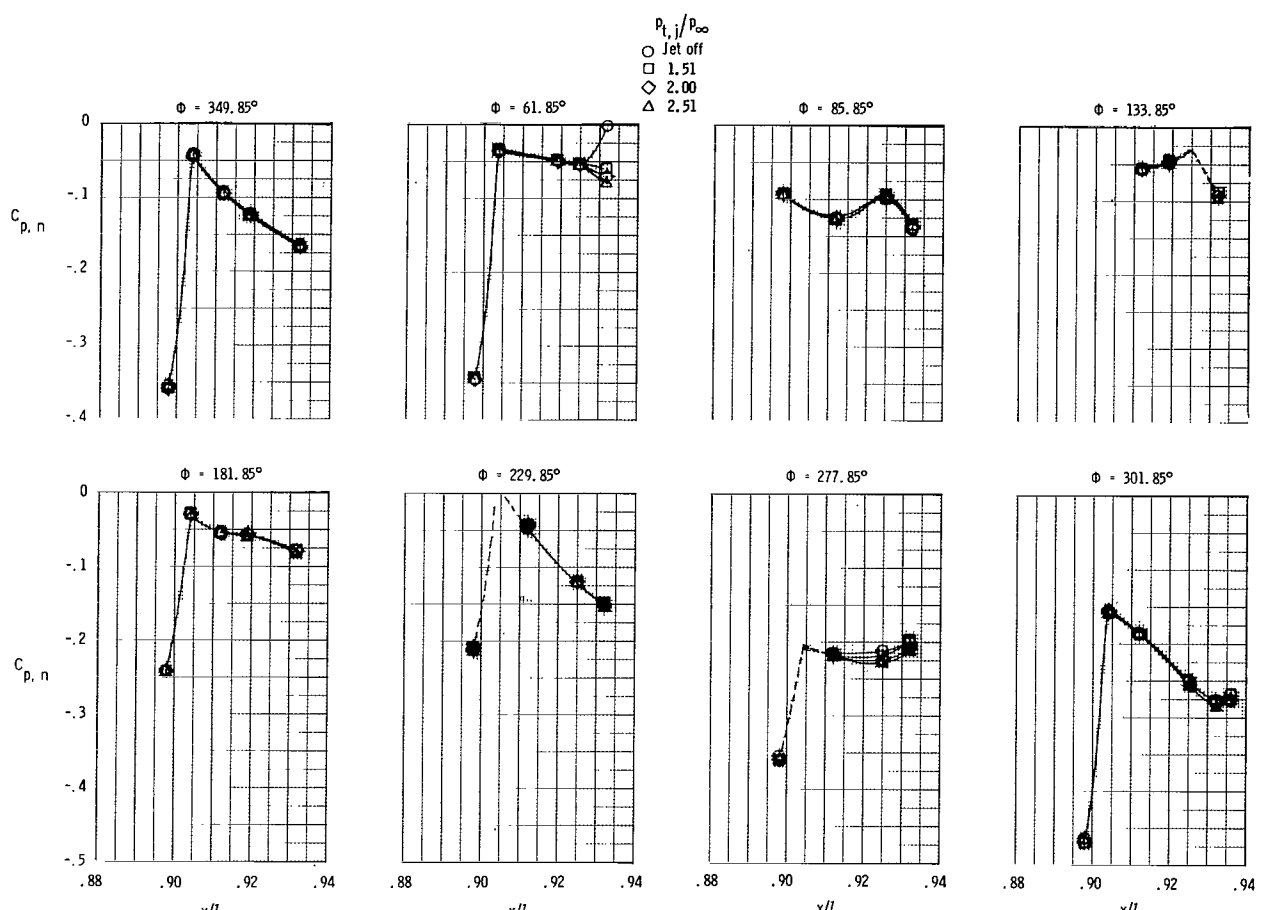
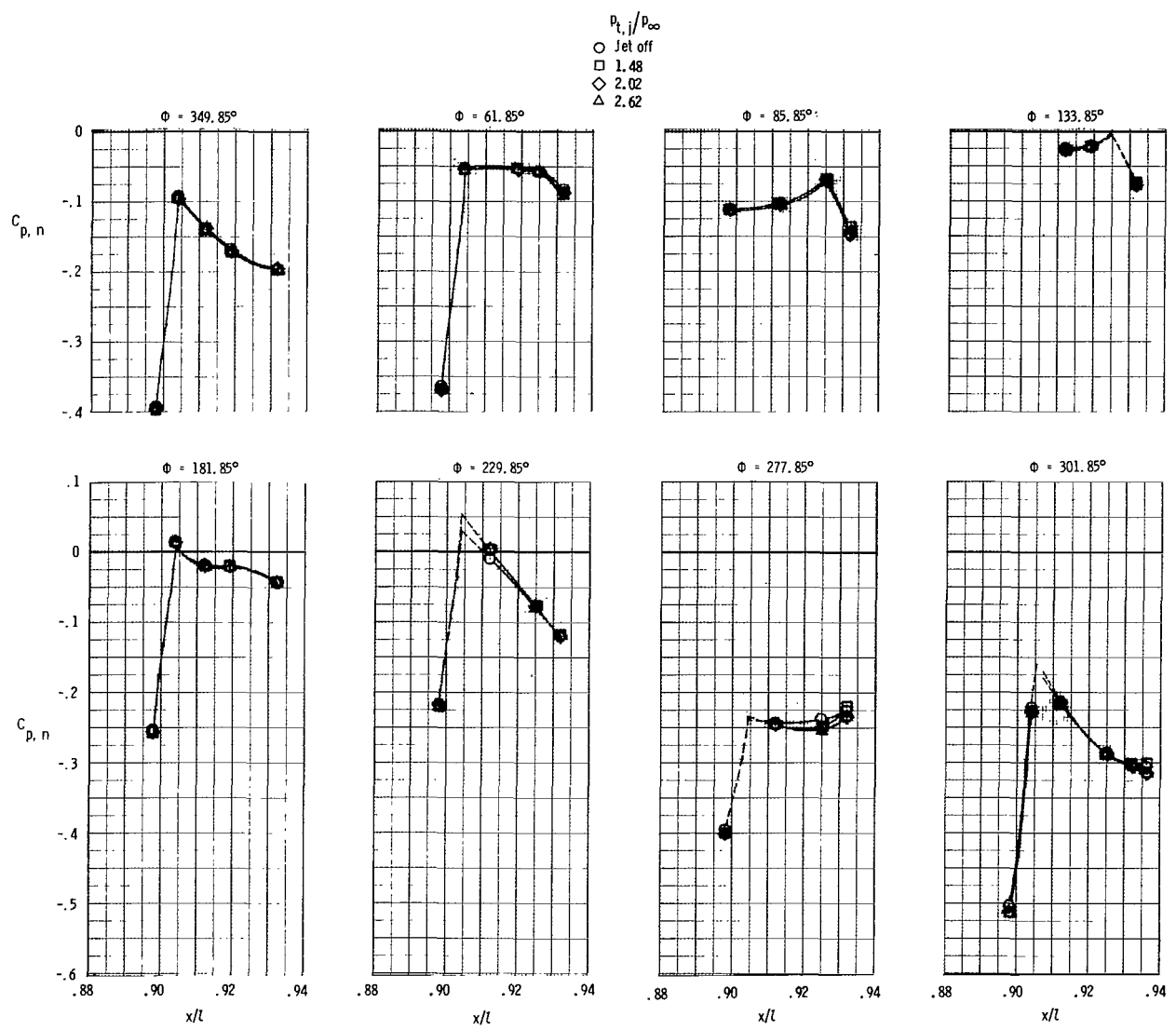


Figure 15.- Continued.



(n) $M = 1.19; \alpha = -0.67^\circ$.

Figure 15.- Continued.



(○) $M = 1.19; \alpha = 1.32^\circ.$

Figure 15.- Concluded.

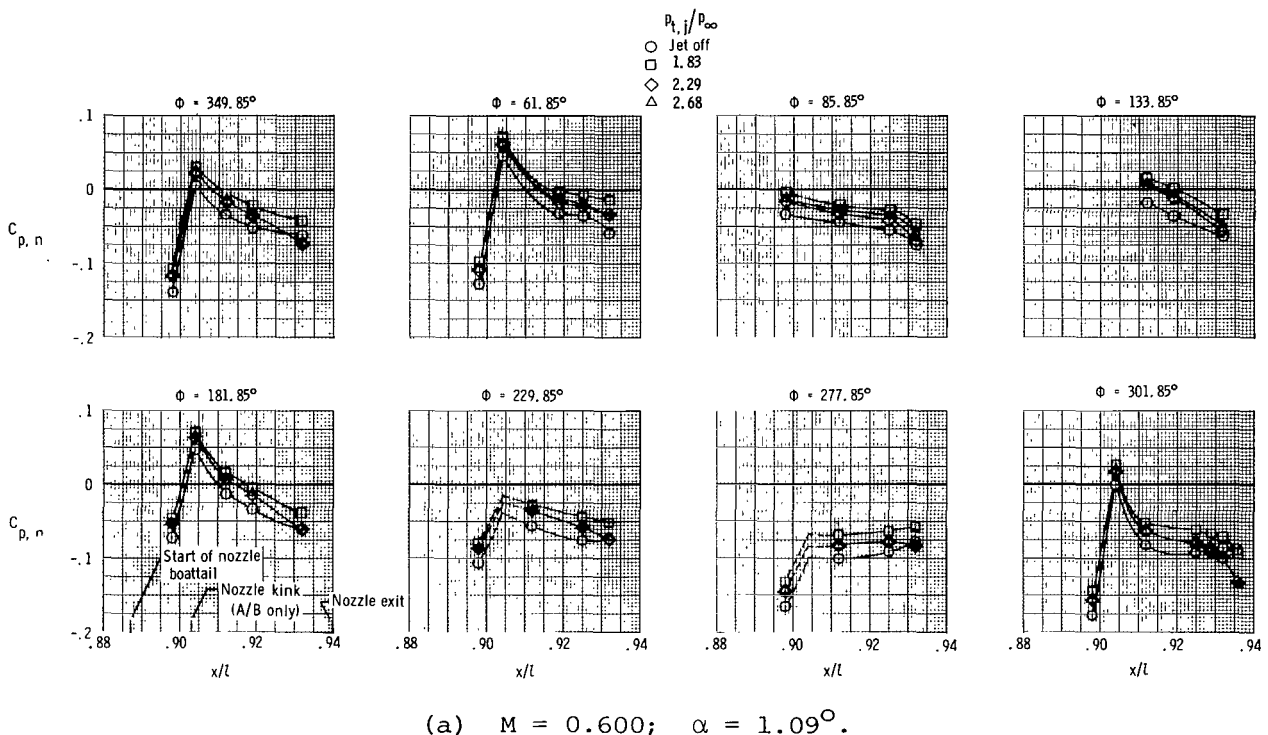


Figure 16.- Static-pressure distributions on max. A/B power nozzle at several Mach number and angle-of-attack combinations for $\delta_h = -10^\circ$.

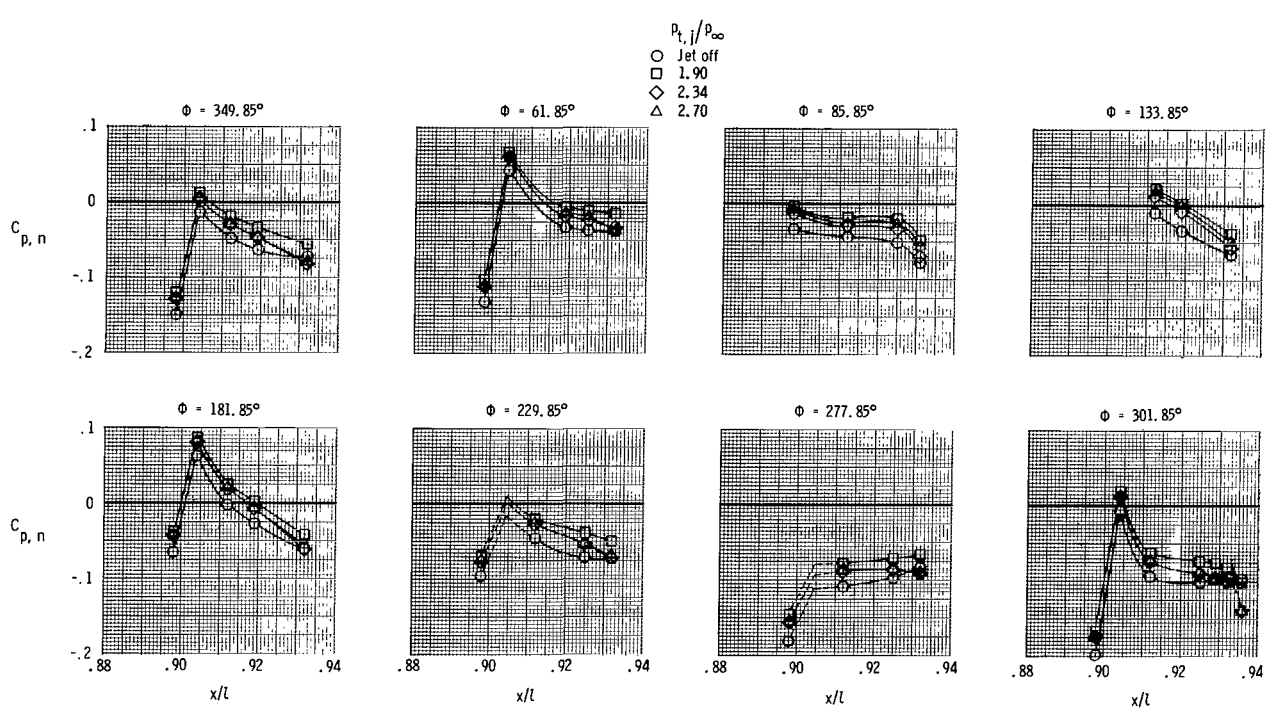
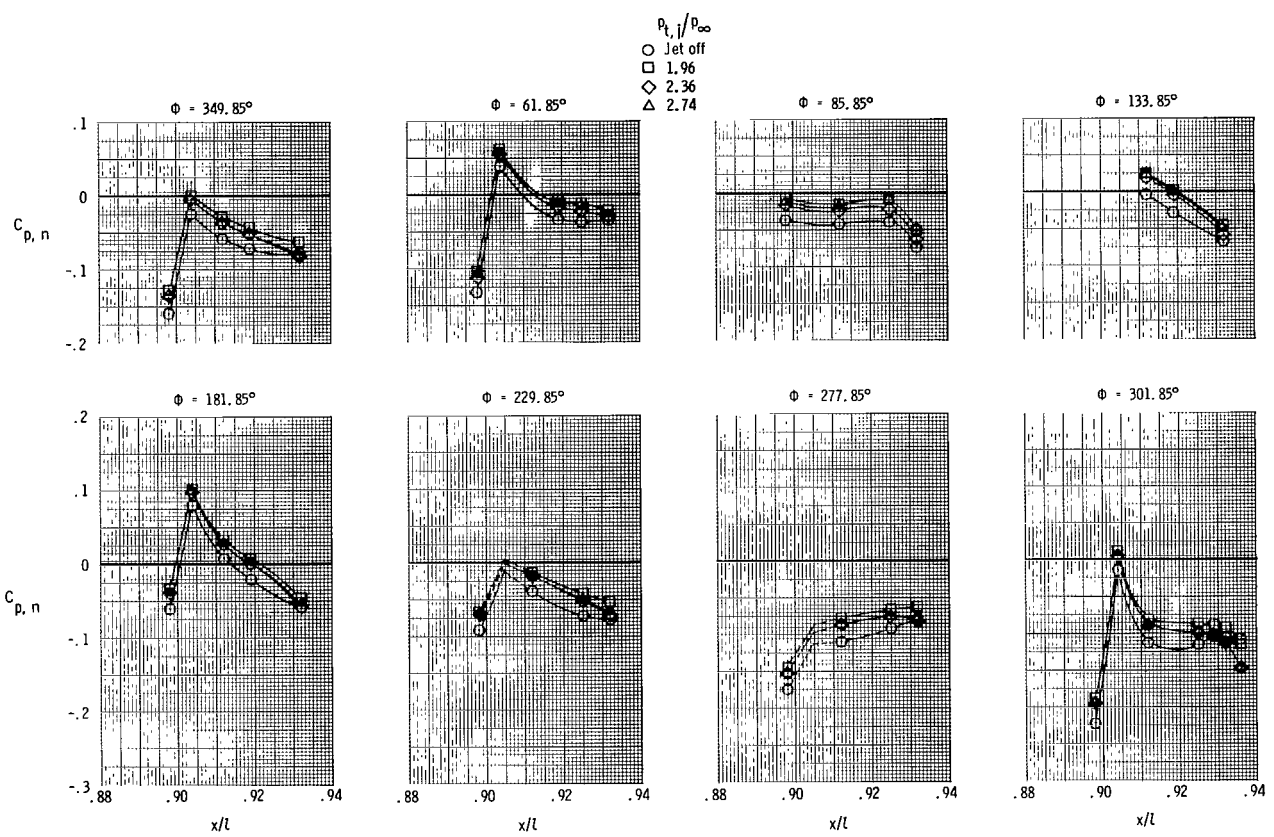
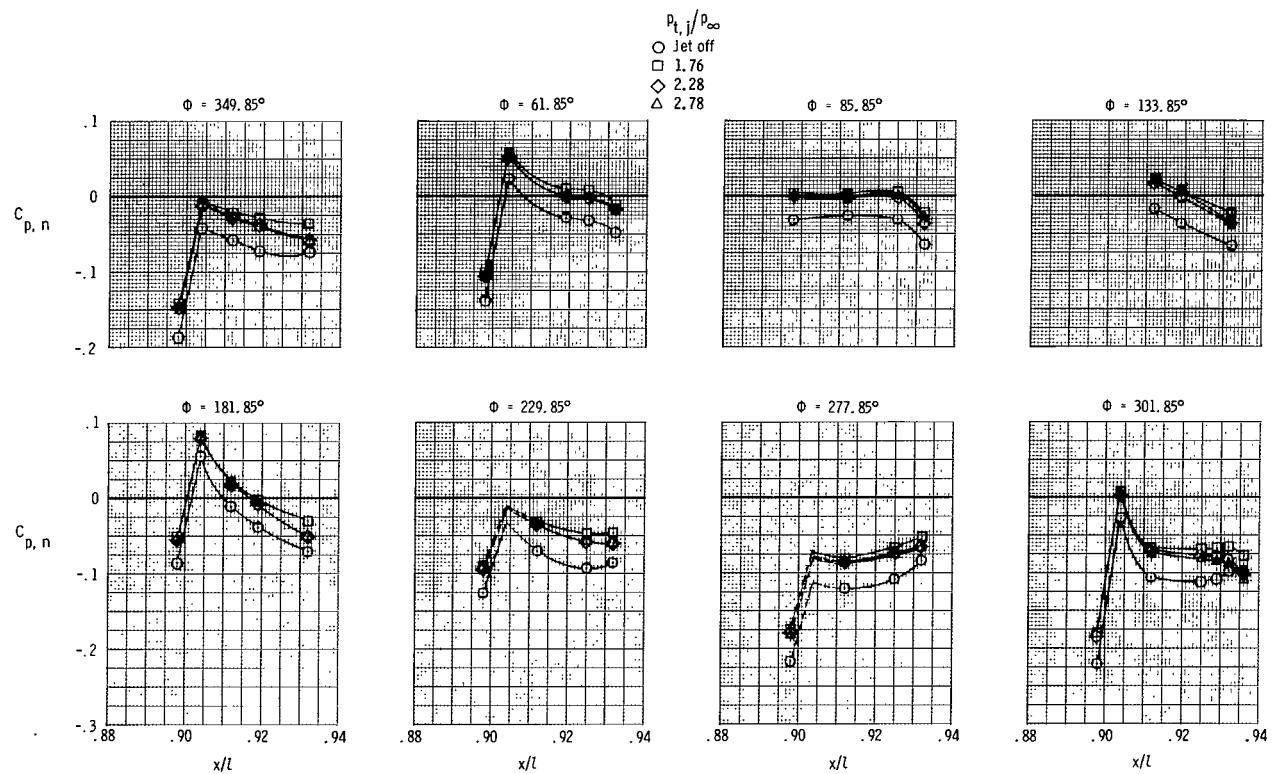


Figure 16.- Continued.



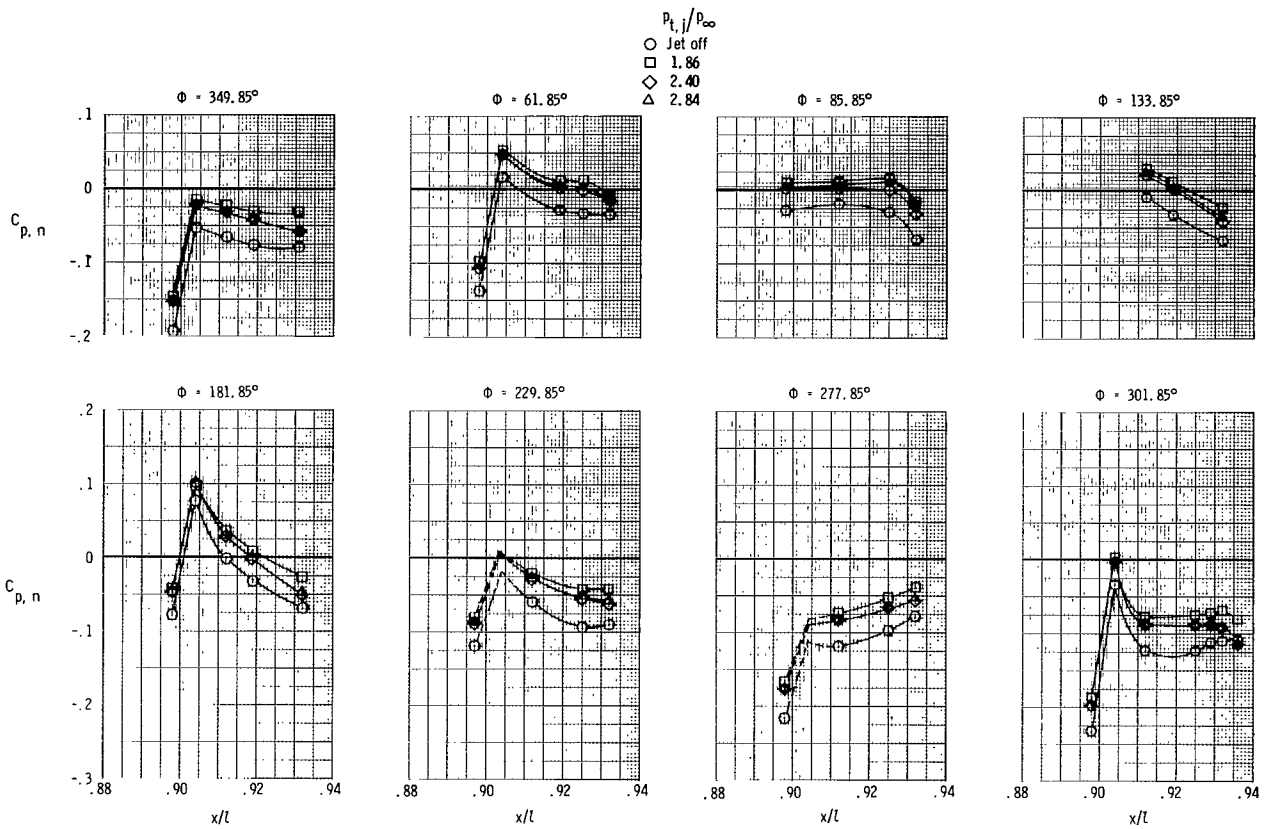
(c) $M = 0.600$; $\alpha = 5.09^\circ$.

Figure 16.- Continued.



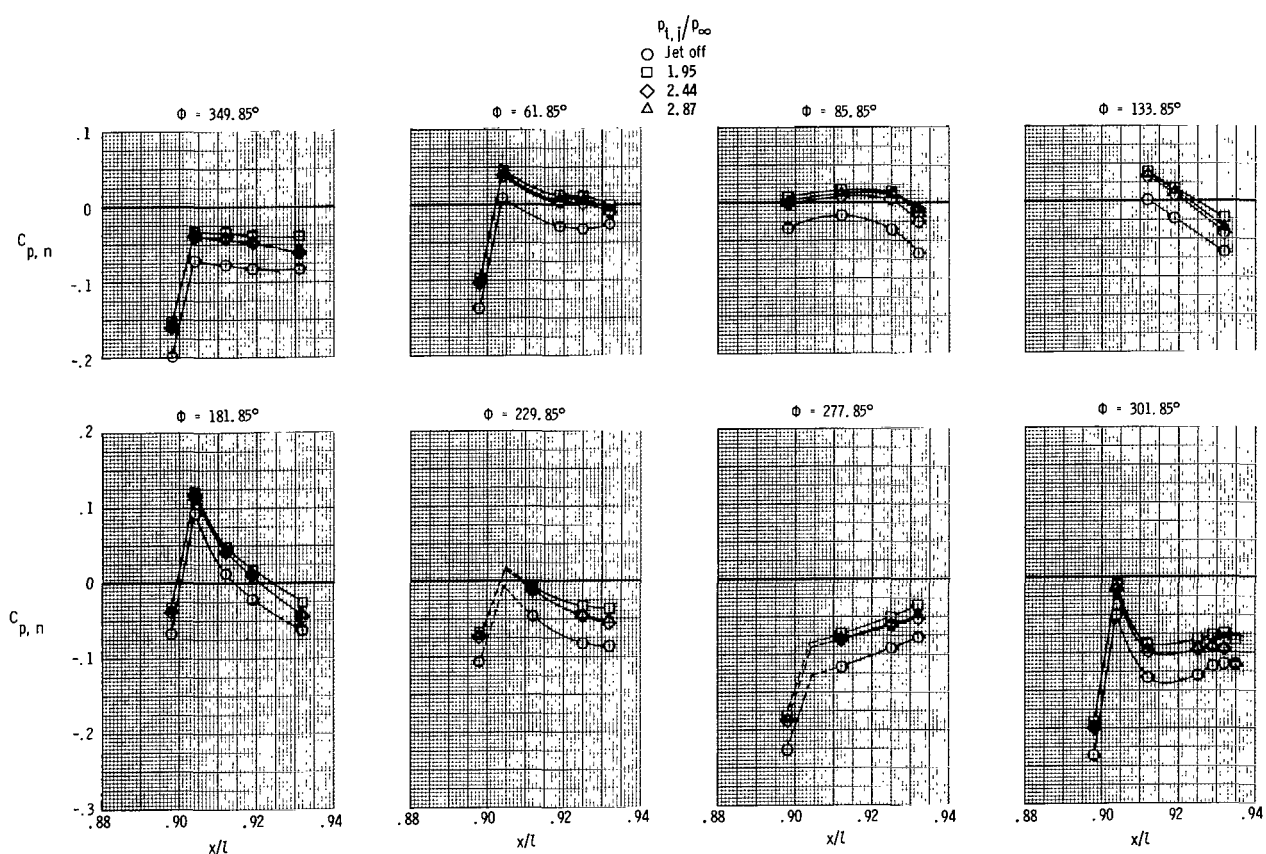
(d) $M = 0.795$; $\alpha = 3.09^\circ$.

Figure 16.- Continued.



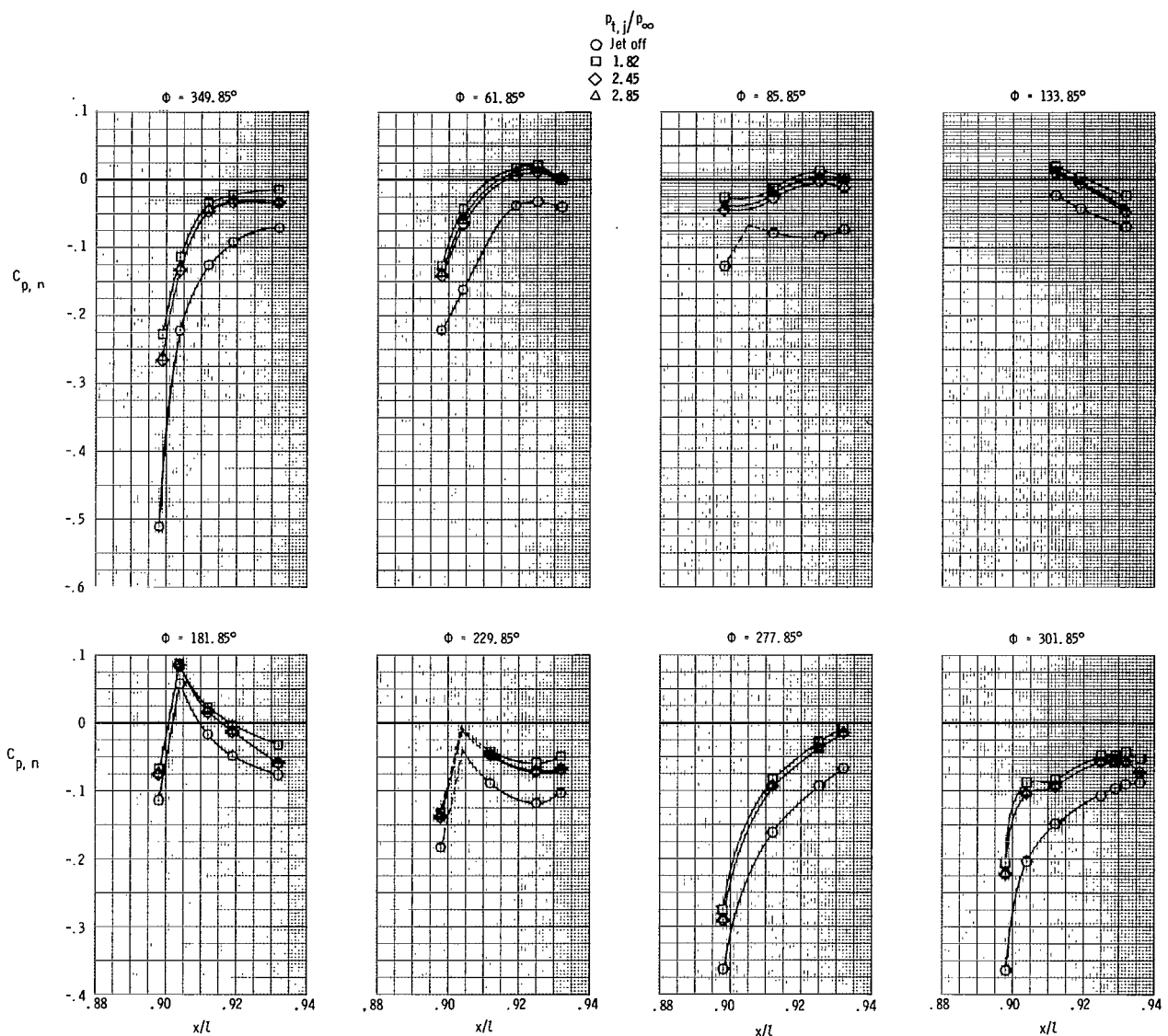
(e) $M = 0.795$; $\alpha = 5.10^\circ$.

Figure 16.- Continued.



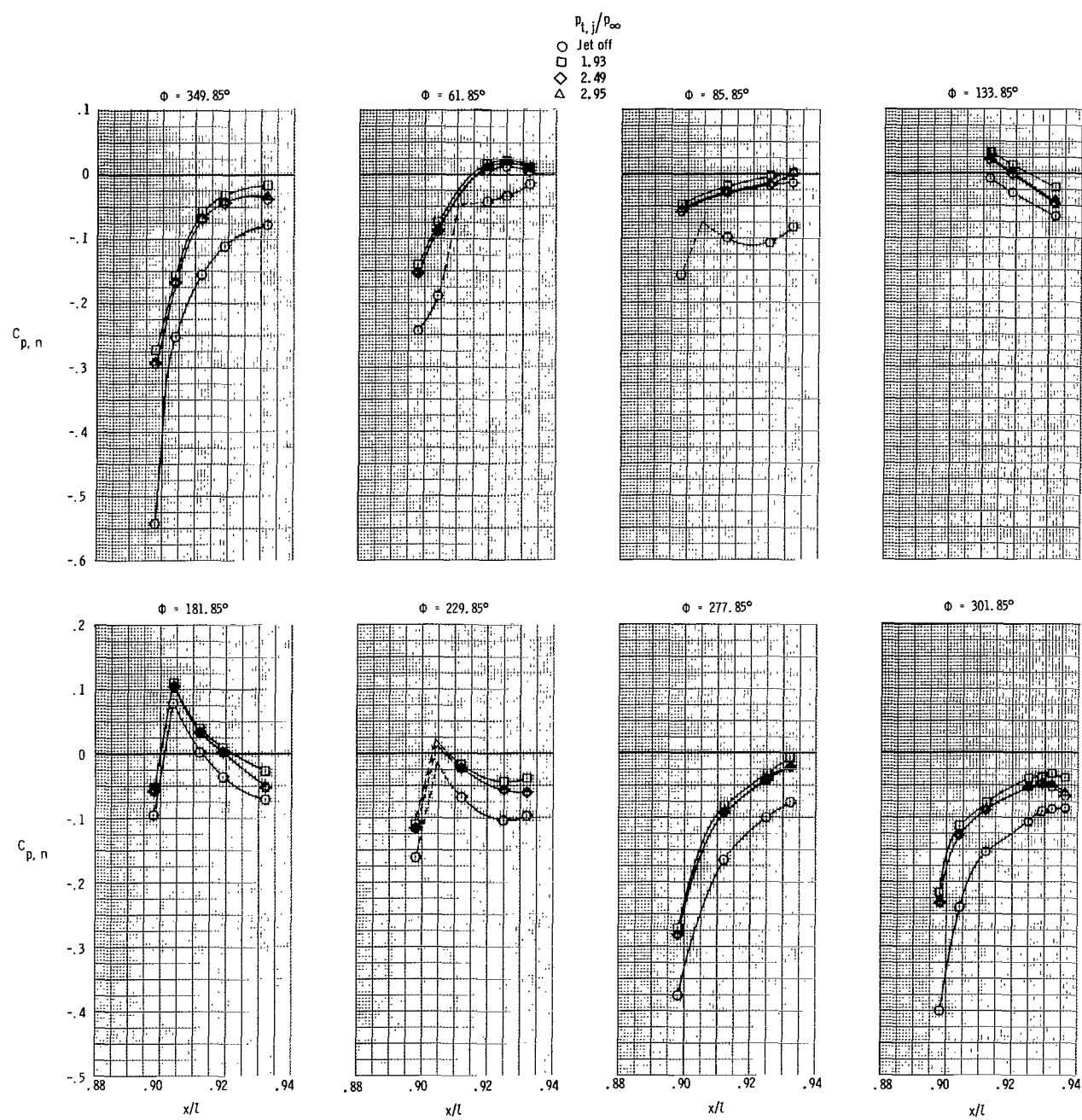
(f) $M = 0.795$; $\alpha = 7.10^\circ$.

Figure 16.- Continued.



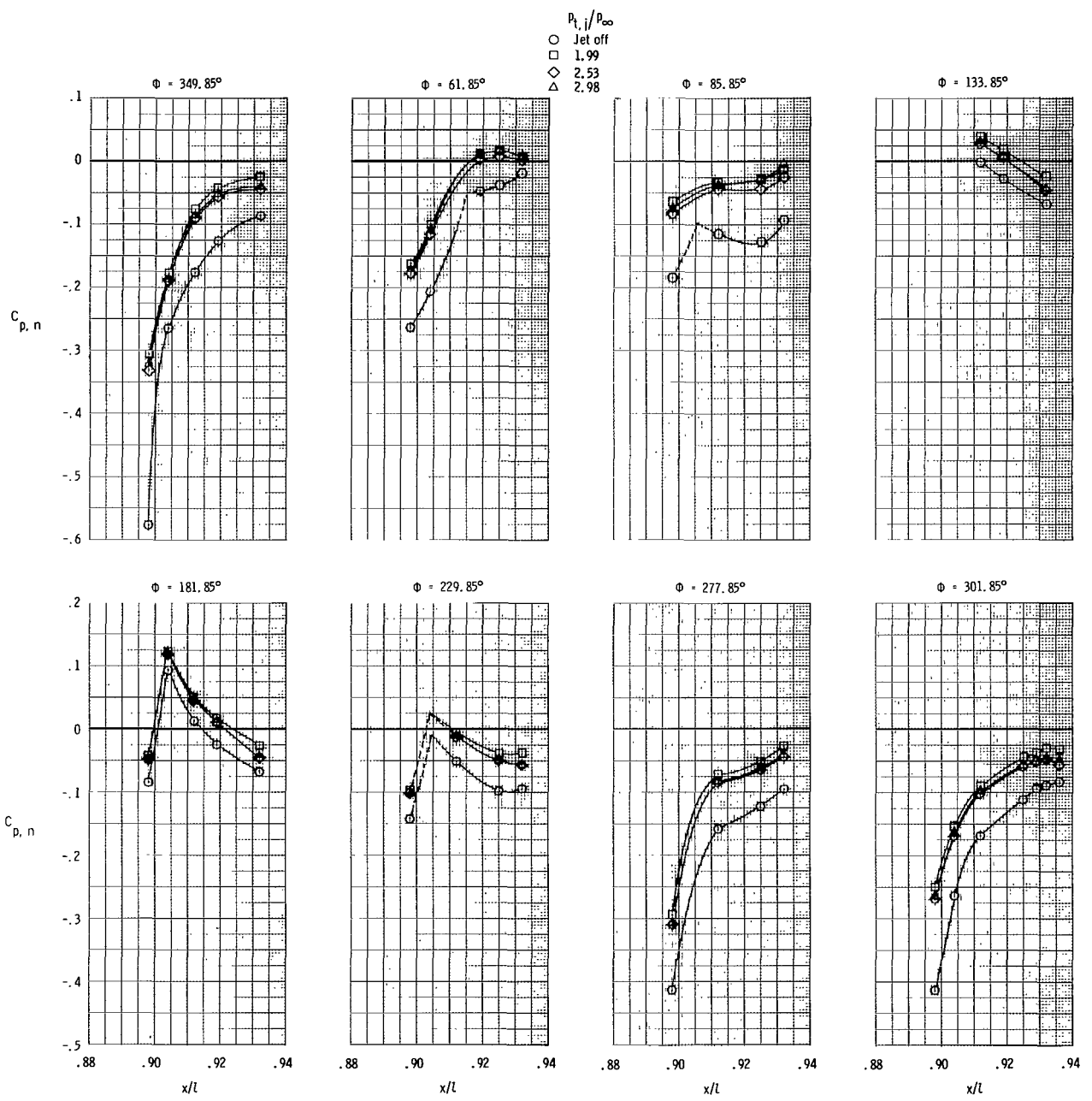
(g) $M = 0.869$; $\alpha = 5.10^\circ$.

Figure 16.- Continued.



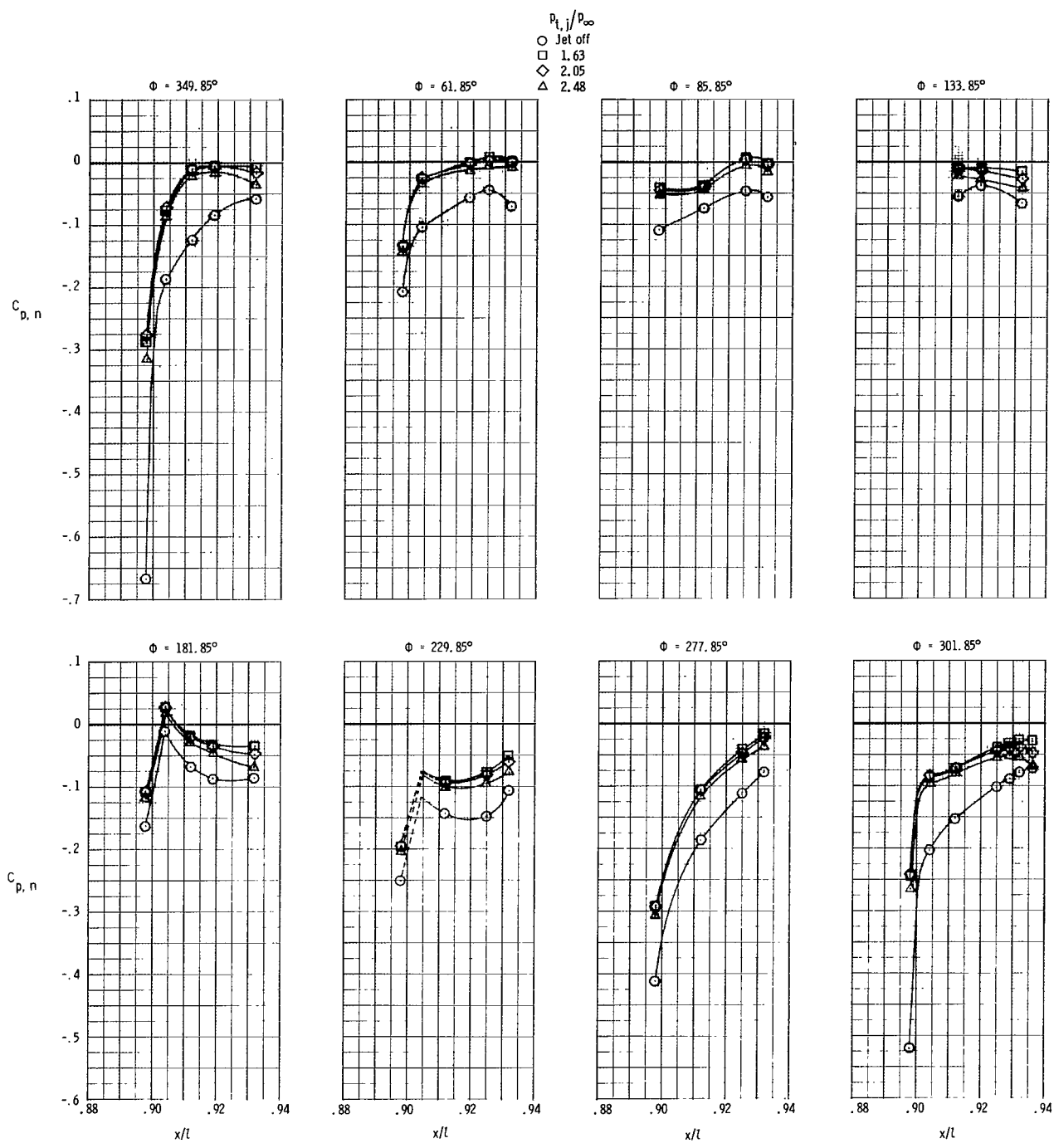
(h) $M = 0.868; \alpha = 7.11^\circ$.

Figure 16.- Continued.



(i) $M = 0.868; \alpha = 9.12^\circ$.

Figure 16.- Continued.



(j) $M = 0.899; \alpha = -0.90^\circ$.

Figure 16.- Continued.

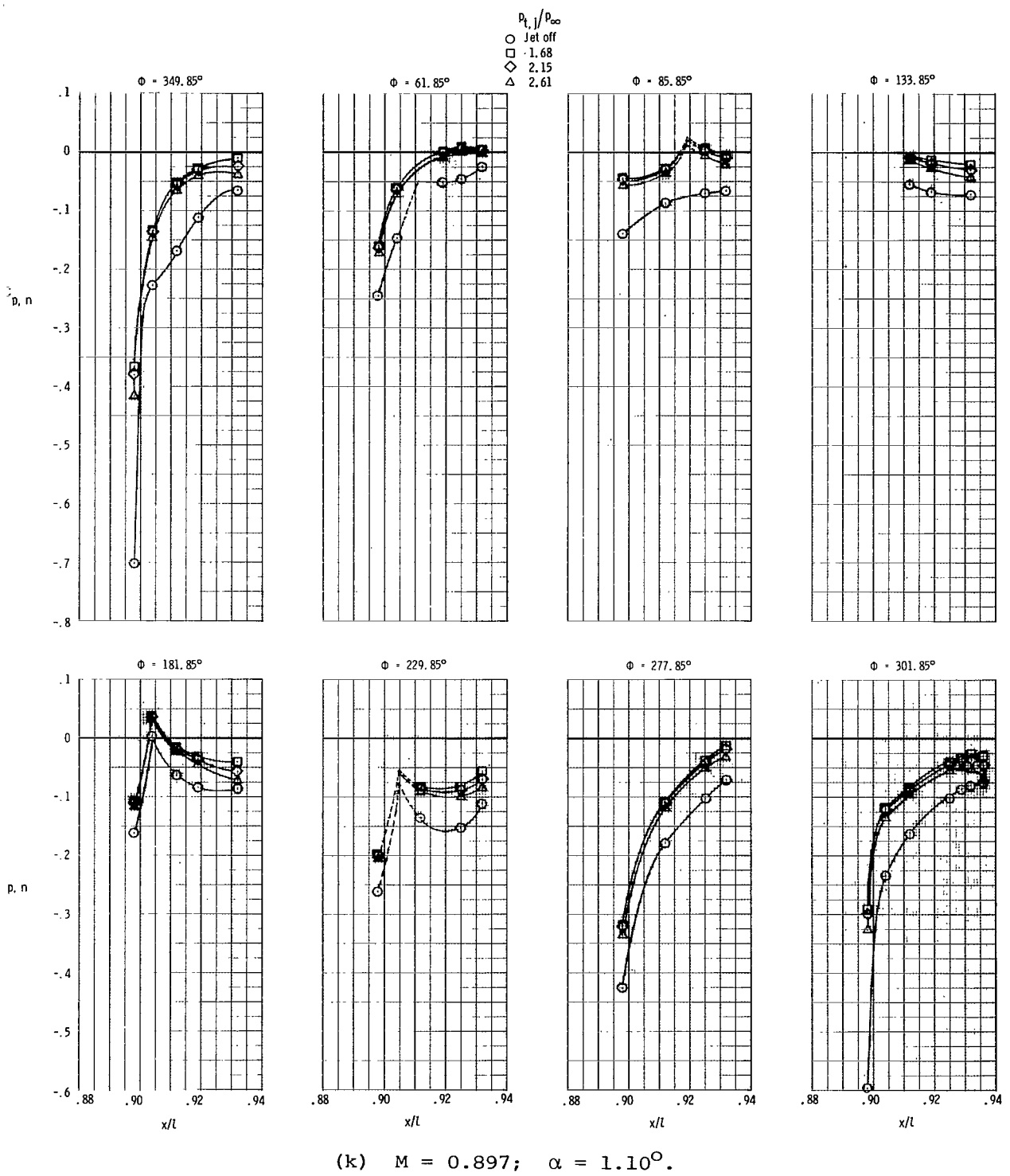
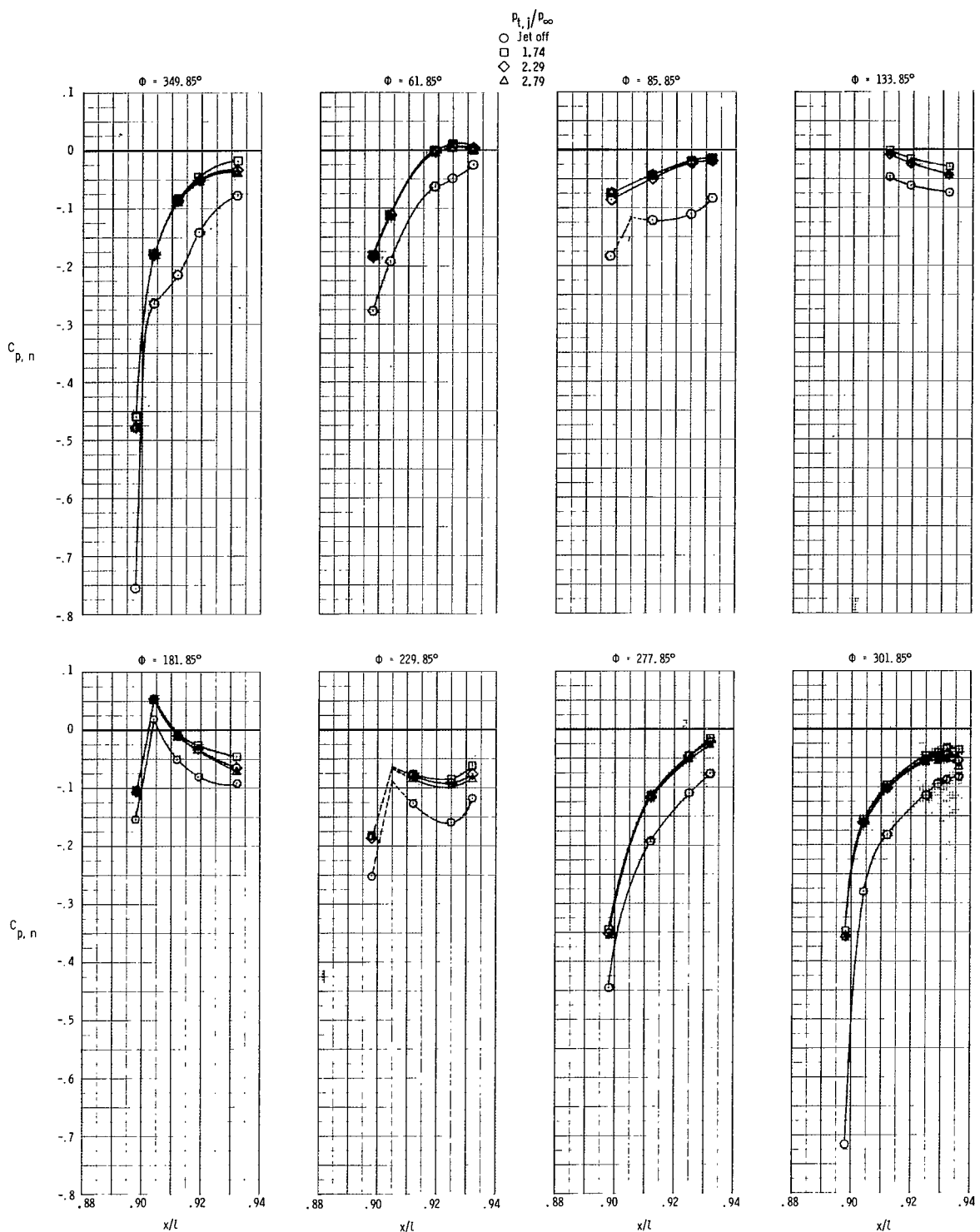
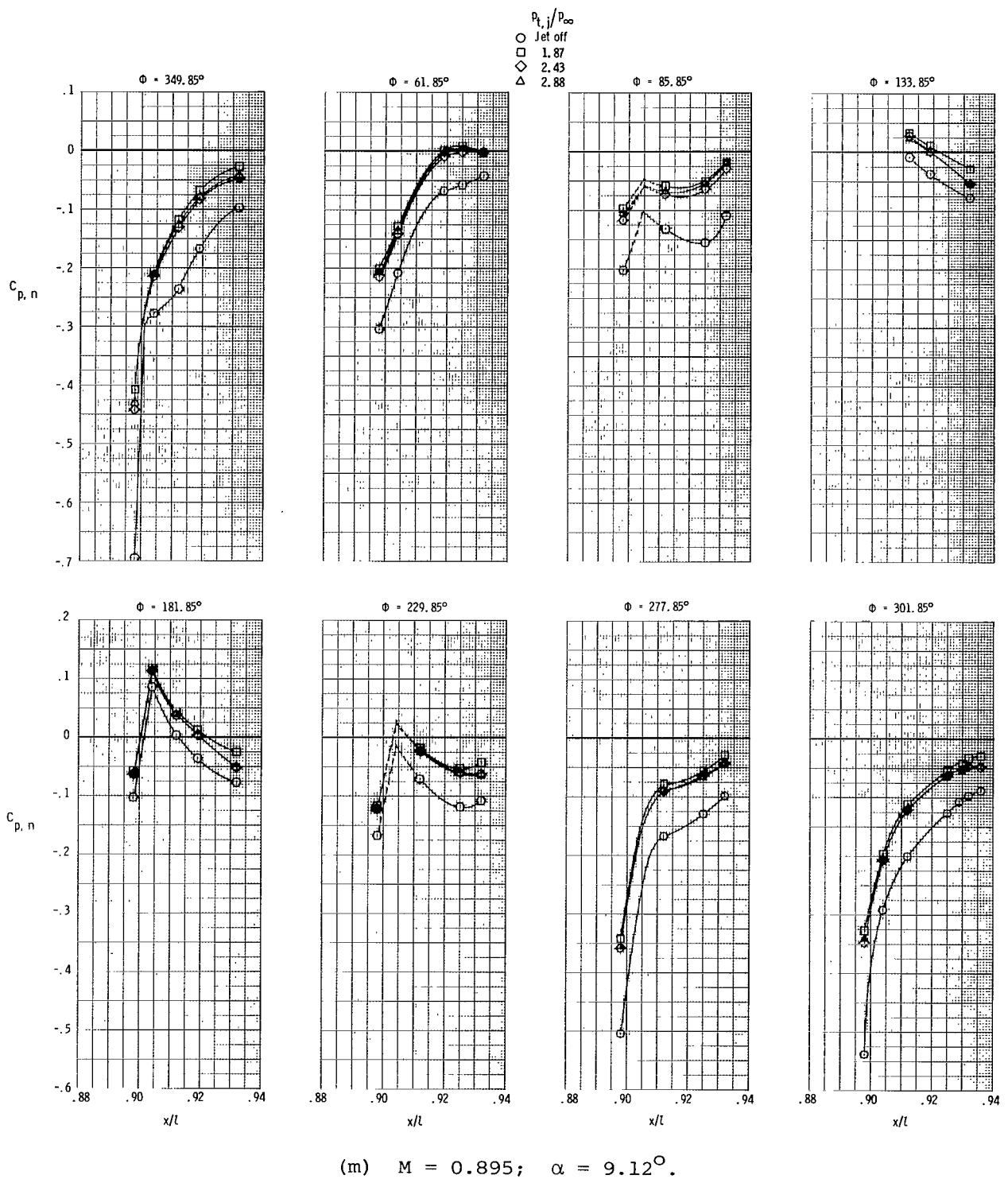


Figure 16.- Continued.



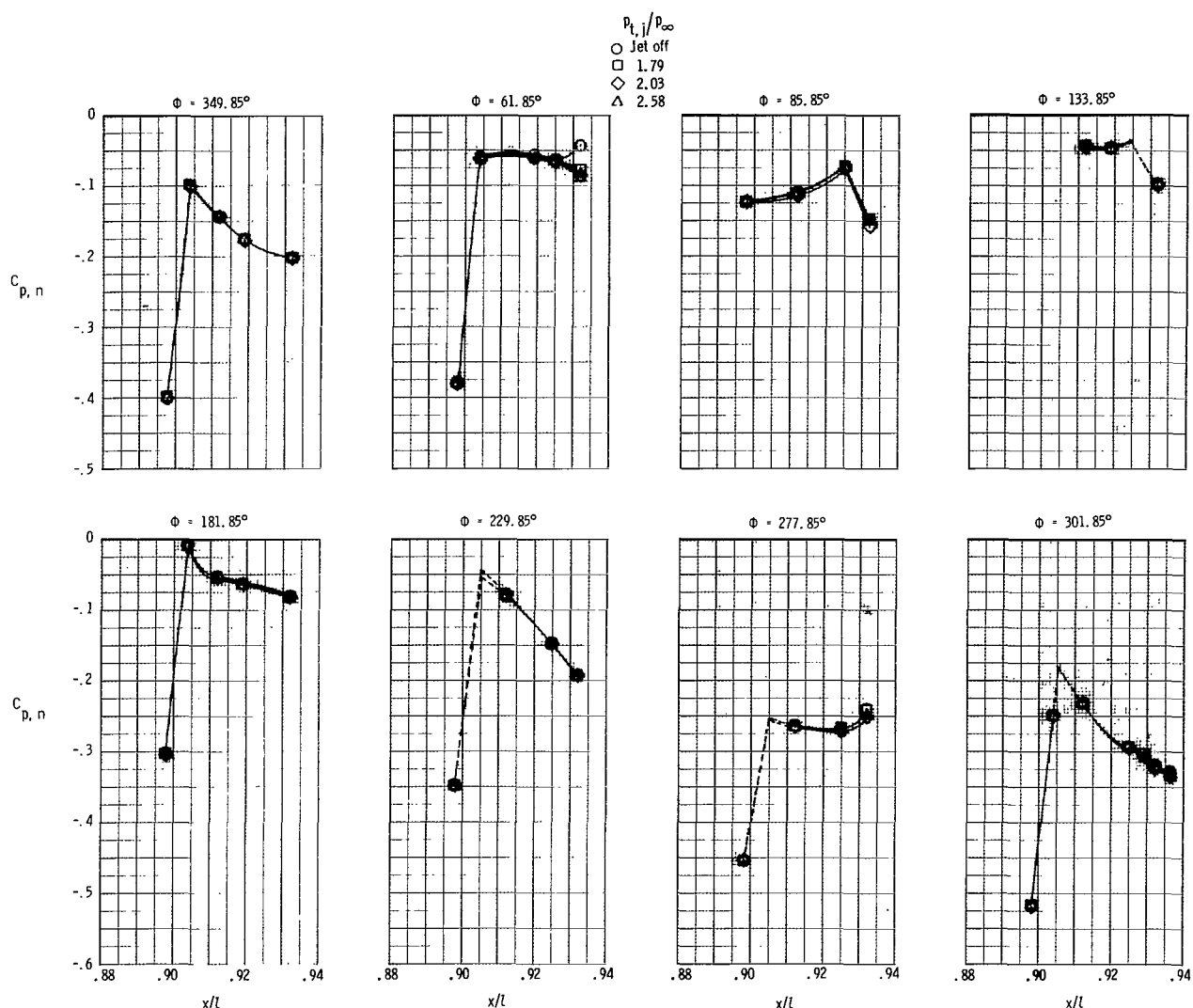
(1) $M = 0.896; \alpha = 3.10^\circ$.

Figure 16.- Continued.



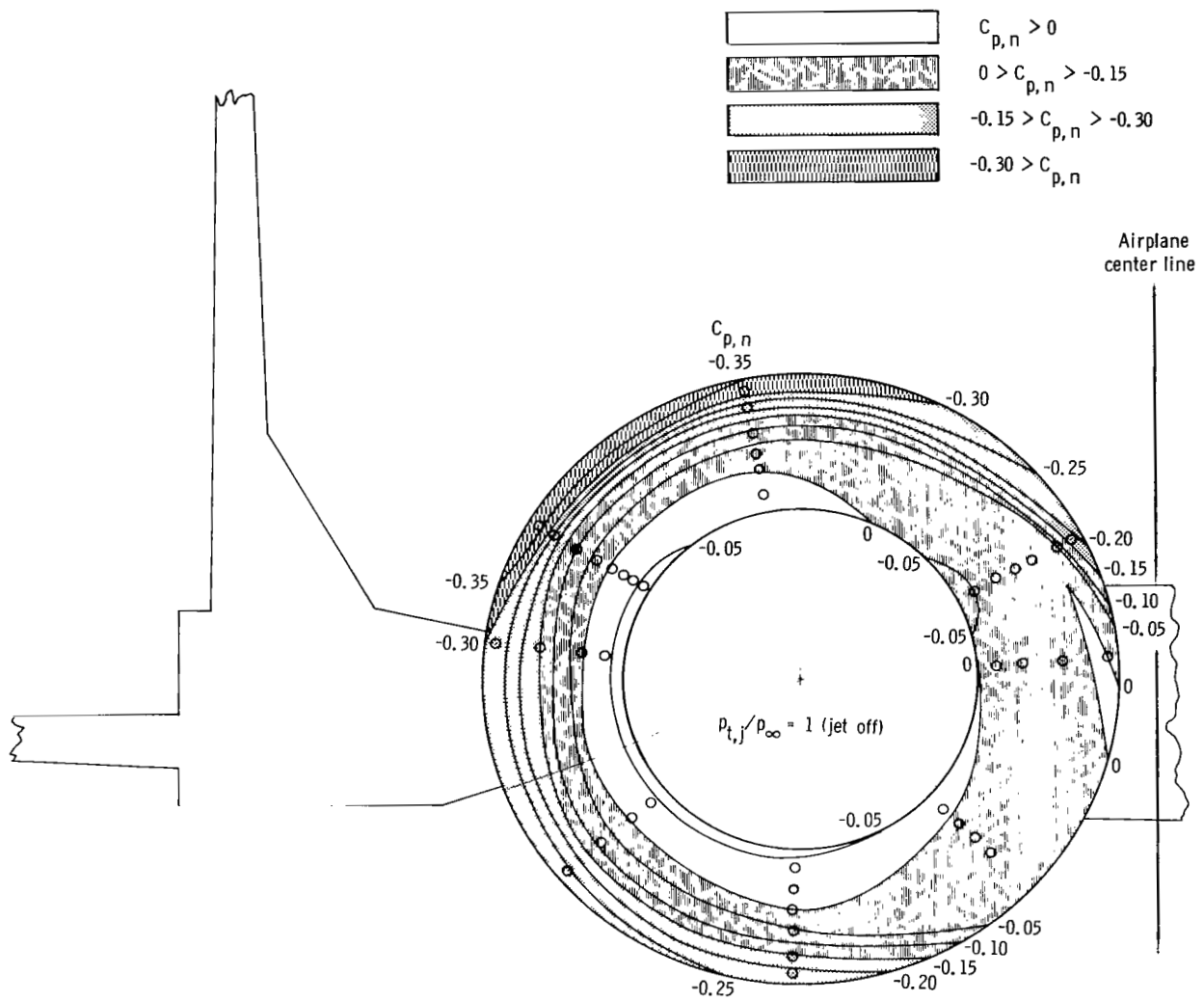
(m) $M = 0.895; \alpha = 9.12^\circ$.

Figure 16.- Continued.



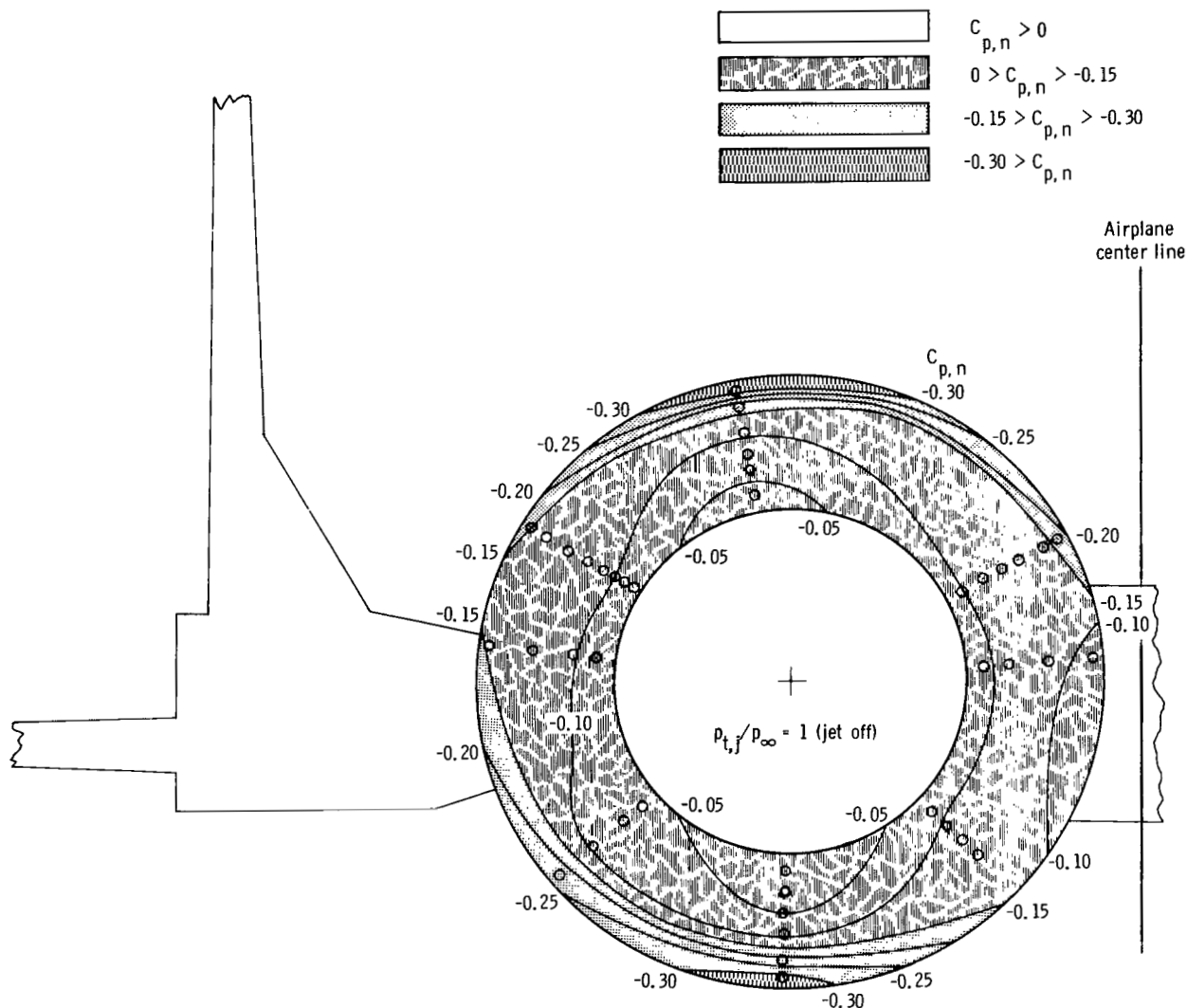
(n) $M = 1.19$; $\alpha = 1.32^\circ$.

Figure 16.- Concluded.



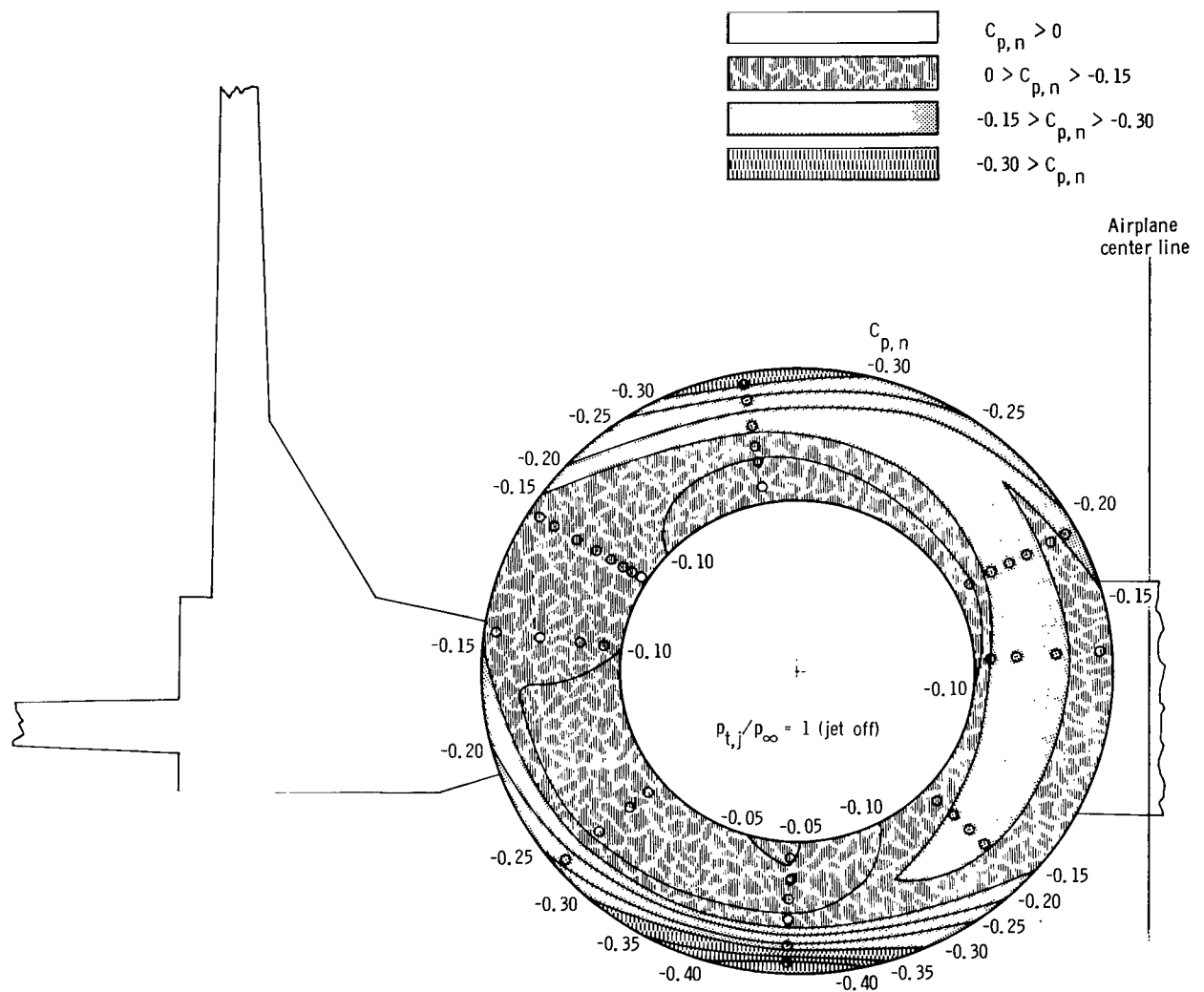
(a) $M = 0.60$; $\alpha = 0.07^\circ$; jet off.

Figure 17.- Isobar contours on dry-power nozzle (left-hand nozzle looking upstream). Ventral fins off; large vertical tails. $\delta_h = 0^\circ$.



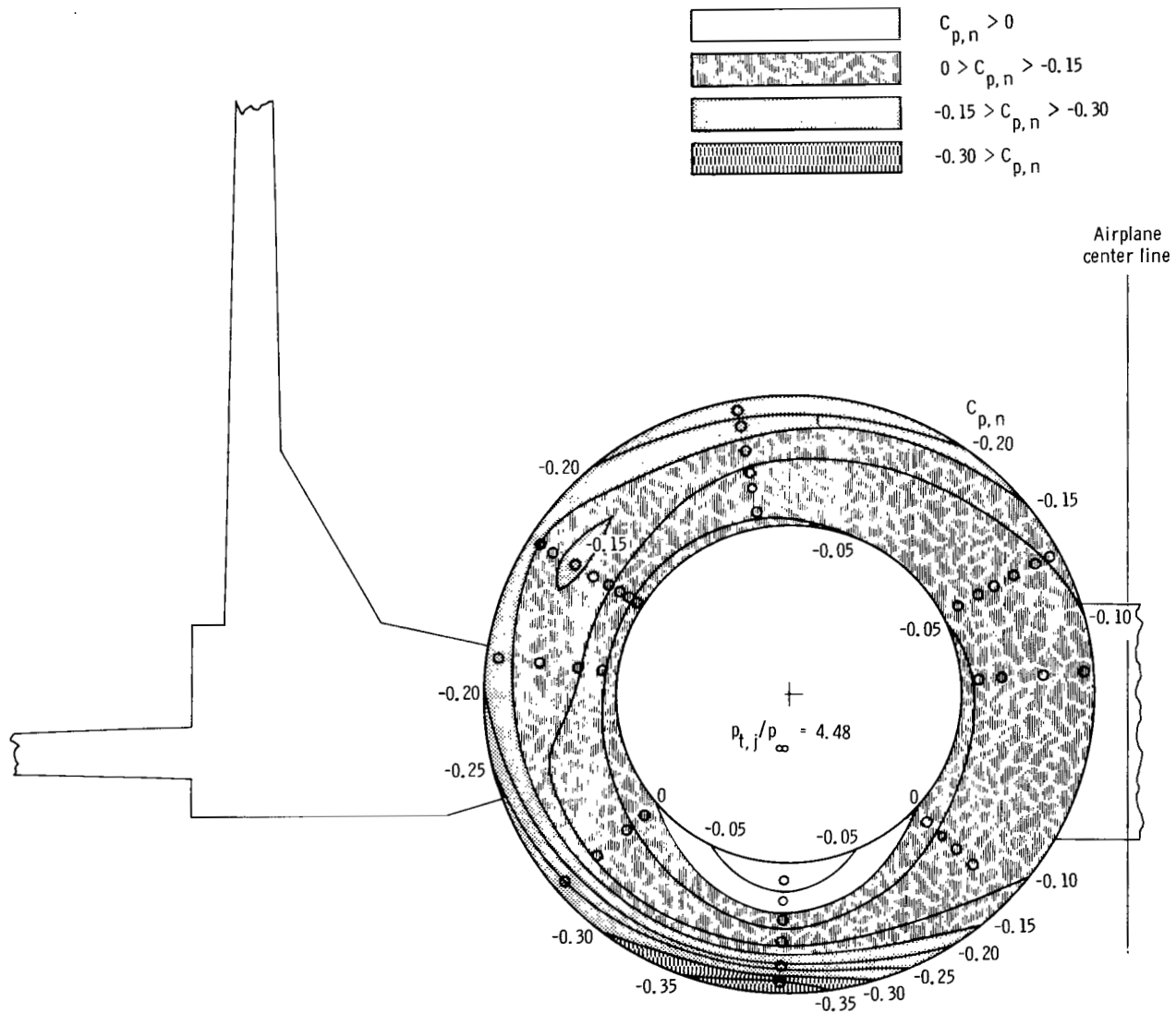
(b) $M = 0.87$; $\alpha = 0.08^\circ$; jet off.

Figure 17.- Continued.



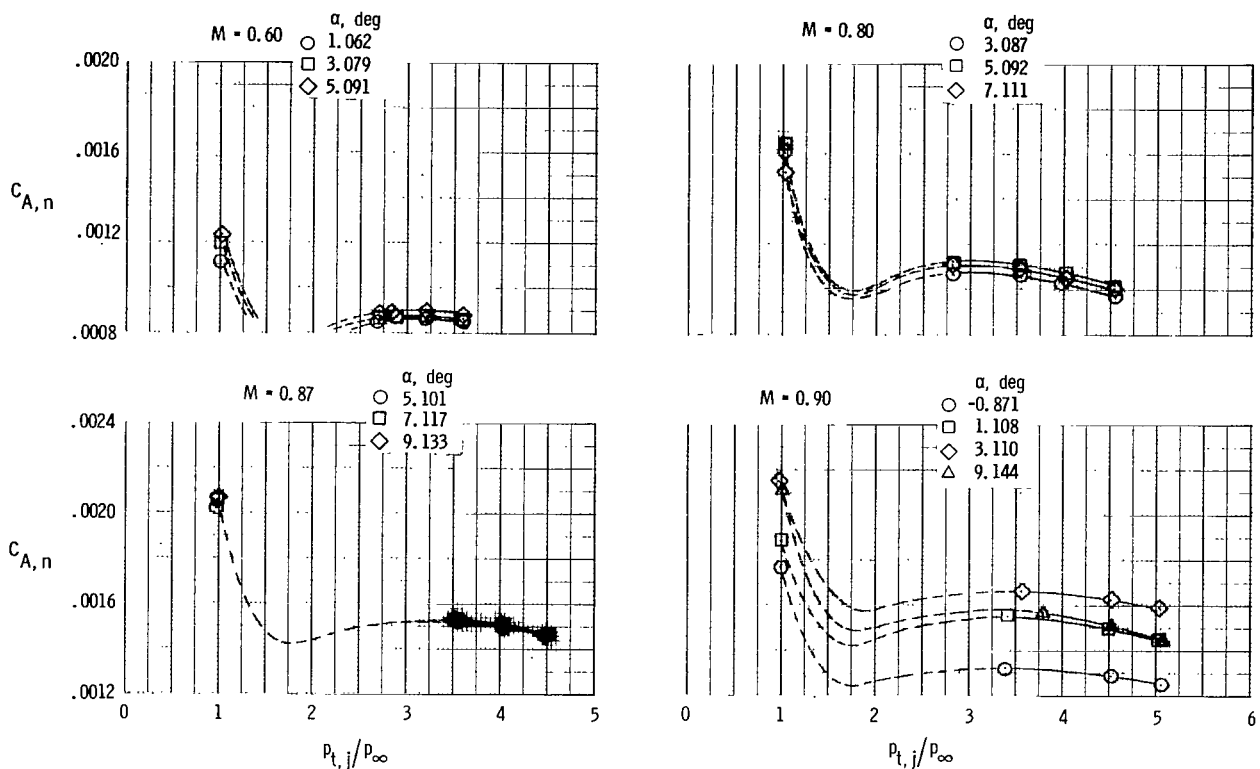
(c) $M = 0.87; \alpha = -5.10^\circ$; jet off.

Figure 17.- Continued.



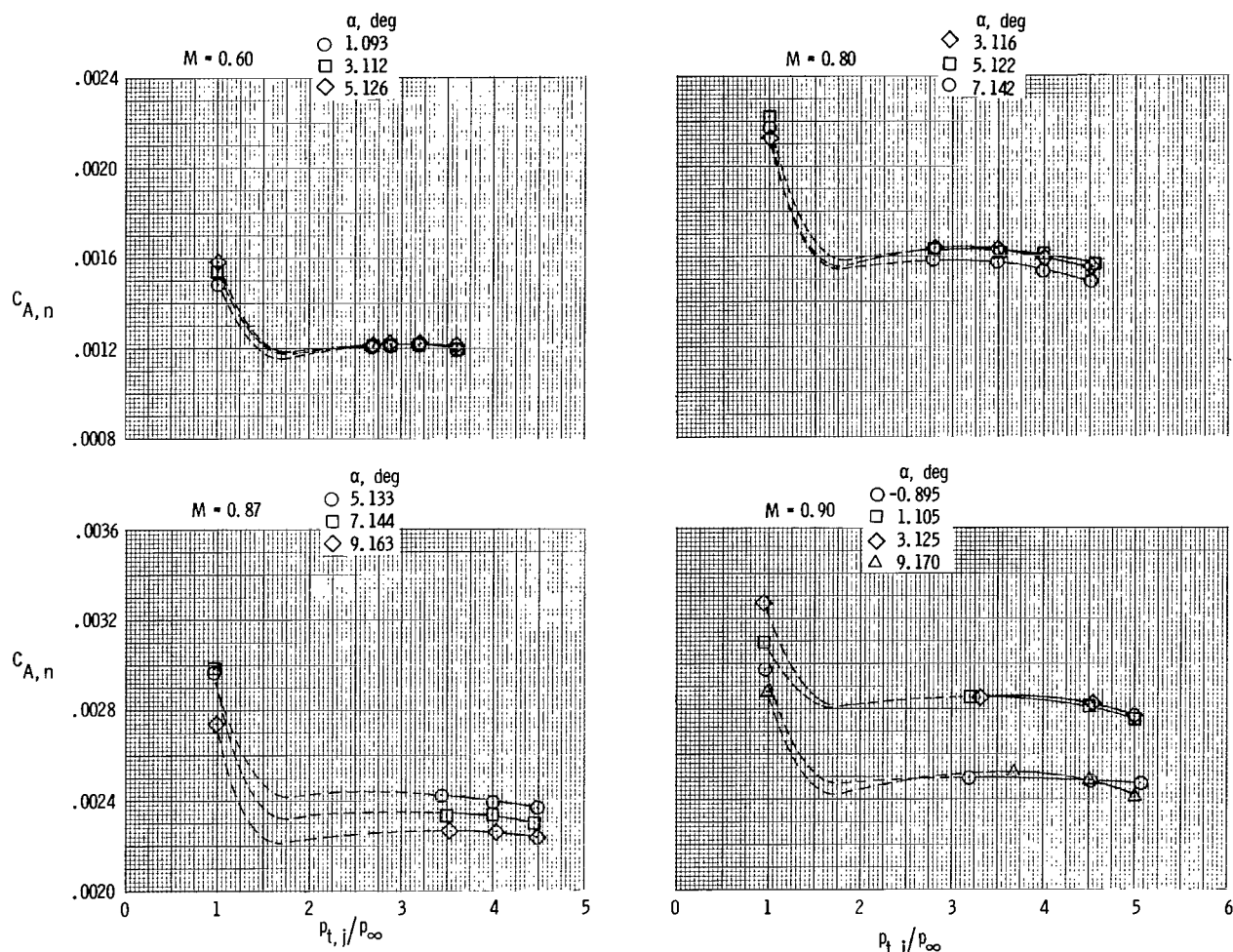
(d) $M = 0.87$; $\alpha = 5.10^\circ$; jet on.

Figure 17.- Concluded.



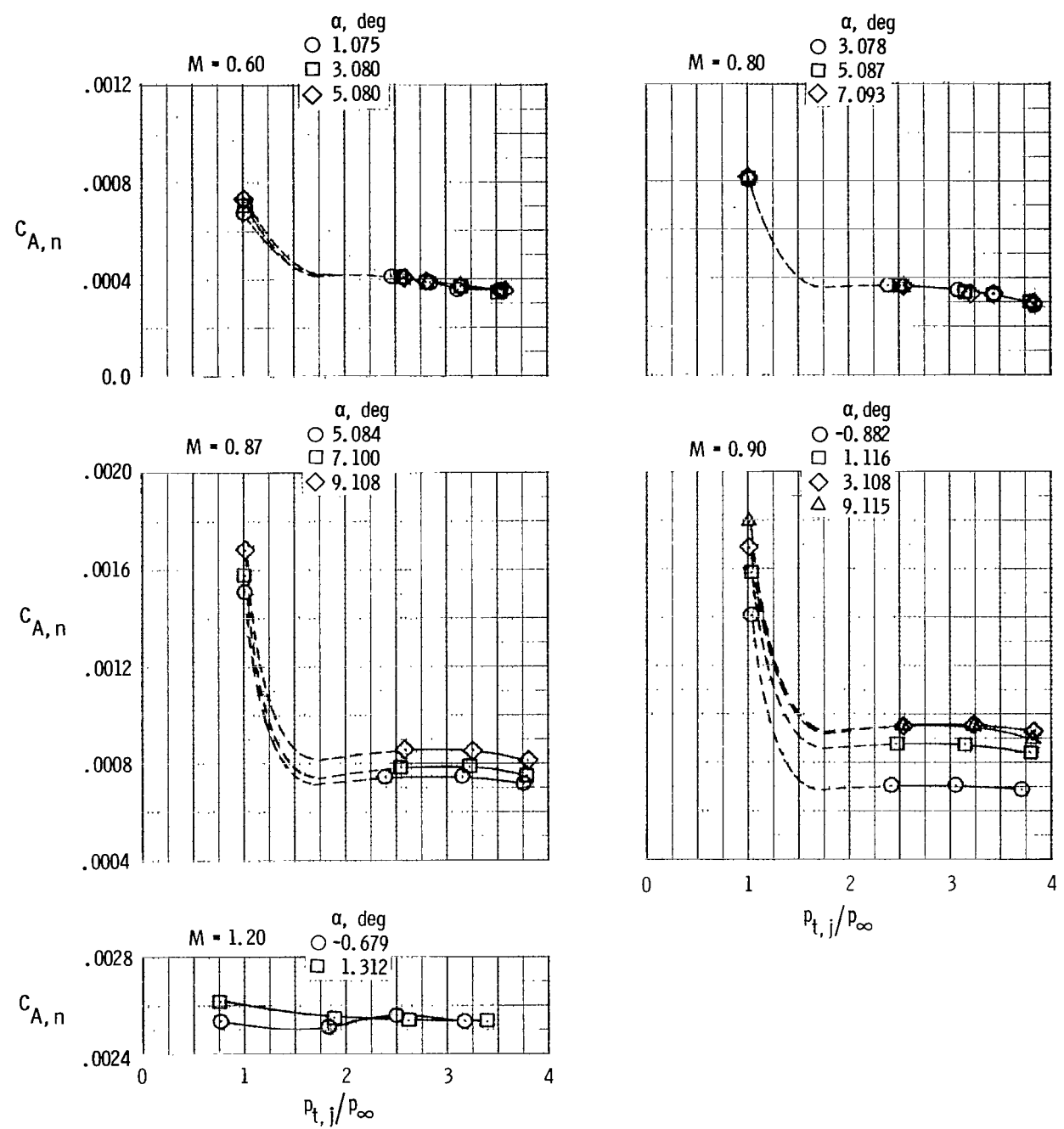
(a) Dry power; $\delta_h = 0^\circ$.

Figure 18.- Integrated axial-force coefficient for one nozzle.



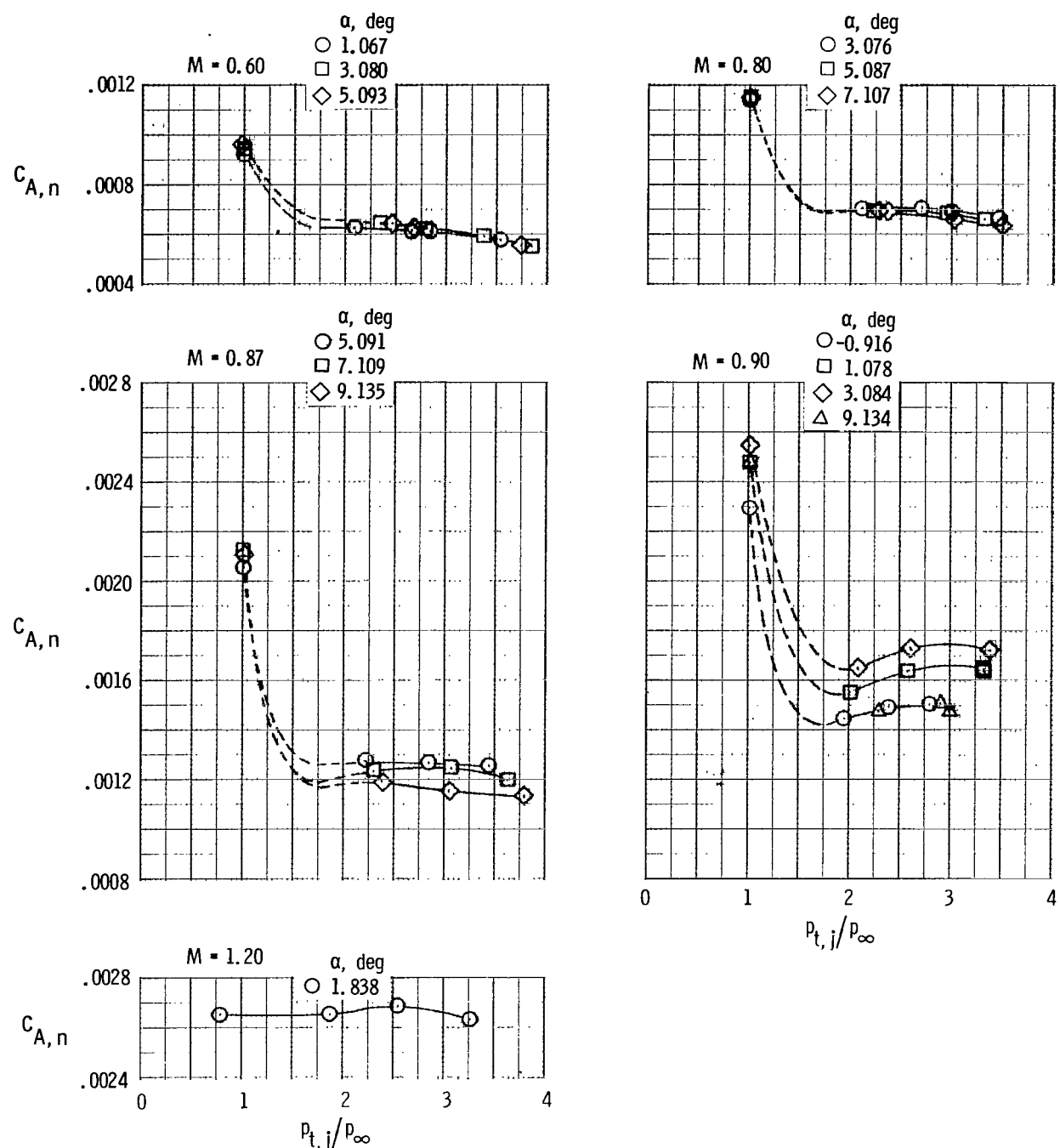
(b) Dry power; $\delta_h = -10^\circ$.

Figure 18.- Continued.



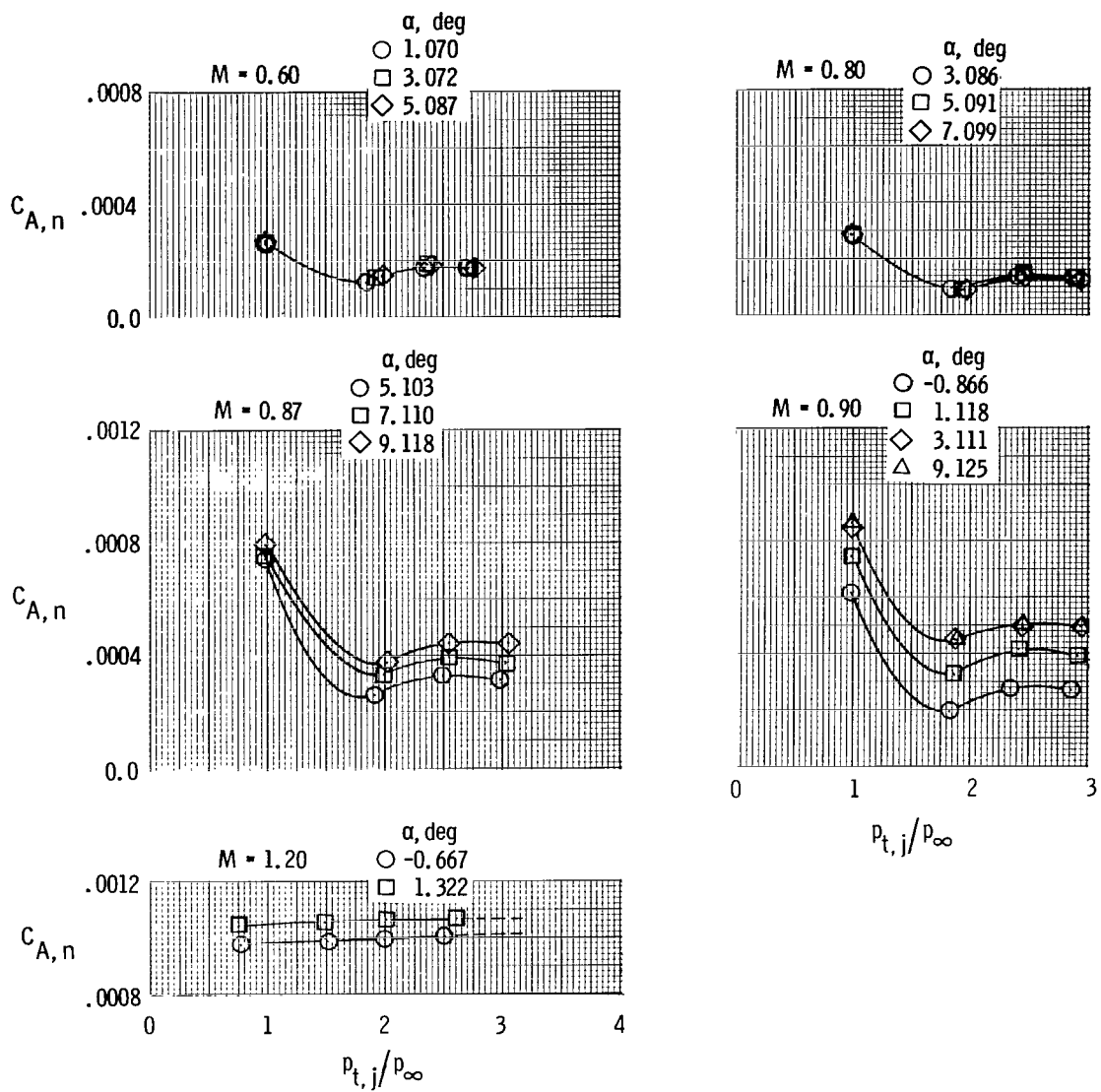
(c) Intermediate A/B power; $\delta_h = 0^\circ$.

Figure 18.- Continued.



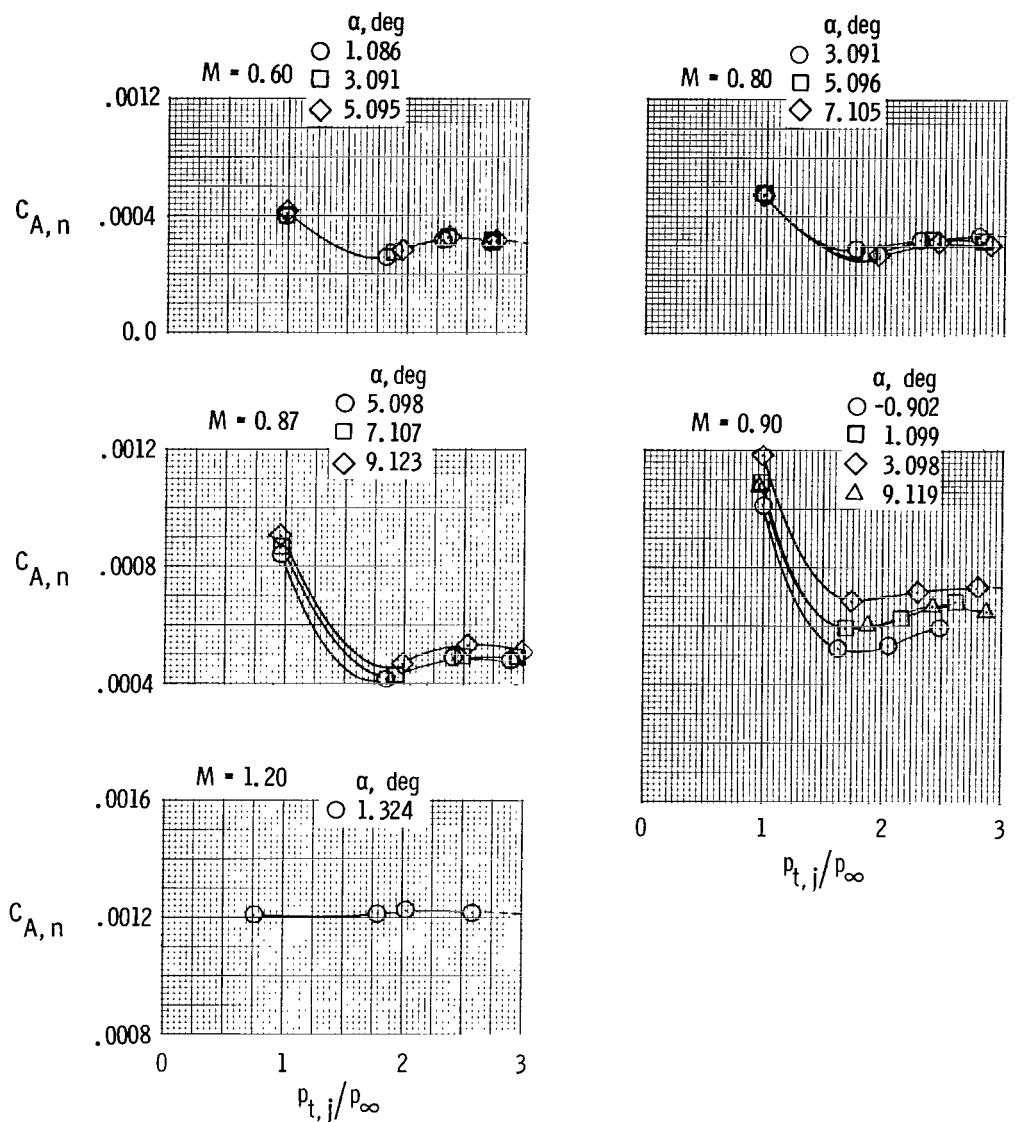
(d) Intermediate A/B power; $\delta_h = -10^\circ$.

Figure 18.- Continued.



(e) Max. A/B power; $\delta_h = 0^\circ$.

Figure 18.- Continued.



(f) Max. A/B power; $\delta_h = -10^\circ$.

Figure 18.- Concluded.

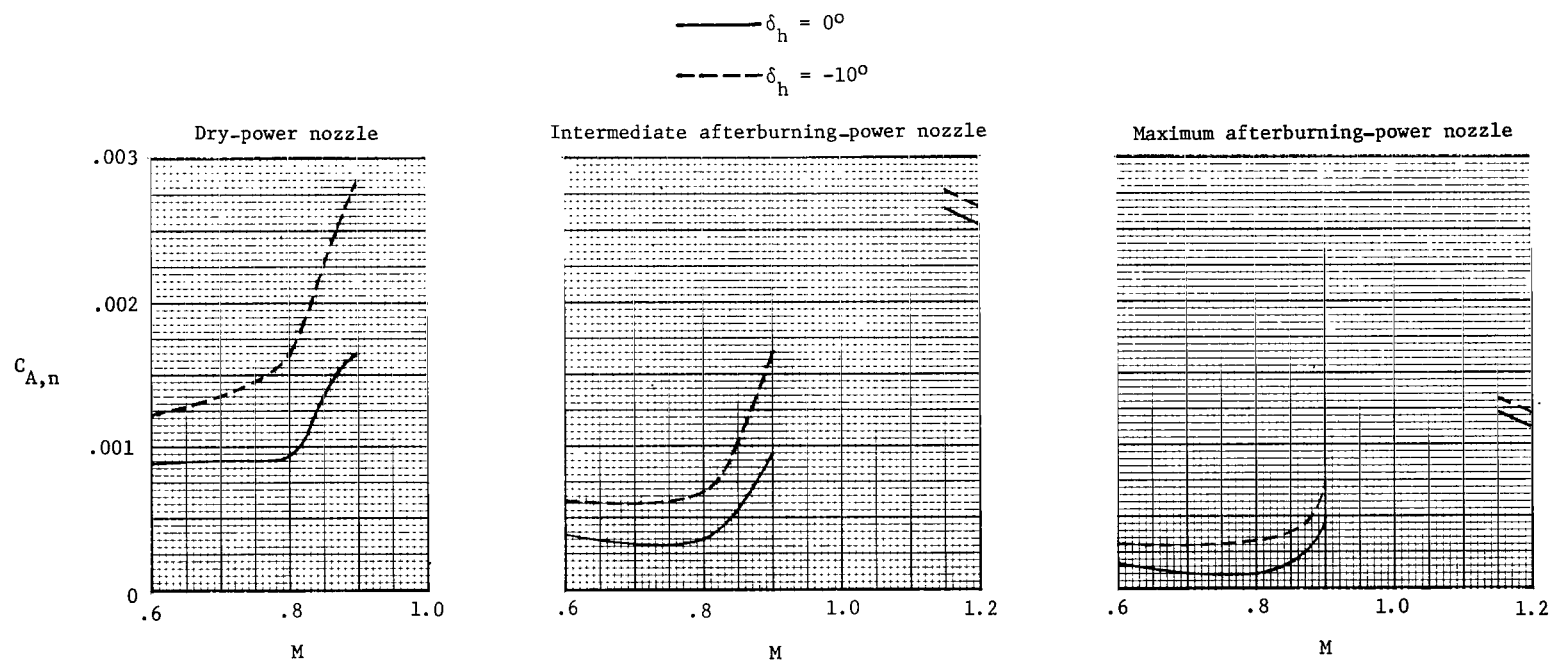


Figure 19.- Comparison of nozzle axial-force coefficients for two horizontal-tail angles.
 $\alpha \approx 3^\circ; p_{t,j}/p_\infty = 3.0.$

1. Report No. NASA TP-1521	2. Government Accession No.	3. Recipient's Catalog No.	
4. Title and Subtitle FUSELAGE AND NOZZLE PRESSURE DISTRIBUTIONS ON A 1/12-SCALE F-15 PROPULSION MODEL AT TRANSONIC SPEEDS		5. Report Date November 1979	
7. Author(s) Odis C. Pendergraft, Jr.		6. Performing Organization Code	
9. Performing Organization Name and Address NASA Langley Research Center Hampton, VA 23665		8. Performing Organization Report No. L-12948	
12. Sponsoring Agency Name and Address National Aeronautics and Space Administration Washington, DC 20546		10. Work Unit No. 505-31-43-04	
15. Supplementary Notes		11. Contract or Grant No.	
16. Abstract Static-pressure-coefficient distributions on the forebody, afterbody, and nozzles of a 1/12-scale F-15 propulsion model have been determined in the Langley 16-foot transonic tunnel for Mach numbers from 0.60 to 1.20, angles of attack from -1° to 9° , and jet total-pressure ratios from 1 (jet off) up to about 5, depending on Mach number. The effects of nozzle power setting and horizontal-tail deflection angle on the pressure-coefficient distributions were also investigated. Reynolds number per meter varied from about 1.0×10^7 to 1.3×10^7 , depending on Mach number.			
17. Key Words (Suggested by Author(s)) Nozzle afterbody static-pressure distribution Nozzle-power effects Horizontal-tail deflection effects Nozzle jet total-pressure ratio effects		18. Distribution Statement Unclassified - Unlimited Subject Category 02	
19. Security Classif. (of this report) Unclassified	20. Security Classif. (of this page) Unclassified	21. No. of Pages 137	22. Price* \$7.25

* For sale by the National Technical Information Service, Springfield, Virginia 22161

NASA-Langley, 1979

National Aeronautics and
Space Administration

Washington, D.C.
20546

Official Business
Penalty for Private Use, \$300

THIRD-CLASS BULK RATE

Postage and Fees Paid
National Aeronautics and
Space Administration
NASA-451



14 1 1U,A, 111979 S00903DS
DEPT OF THE AIR FORCE
AF WEAPONS LABORATORY
ATTN: TECHNICAL LIBRARY (SUL)
KIRTLAND AFB NM 87117

NASA



POSTMASTER:

If Undeliverable (Section 15
Postal Manual) Do Not Retu